Charles University
Faculty of Science

Study programme: Environmental Science

Mgr. Jan Bendl

Spatio-temporal distribution of atmospheric aerosol in urban and rural environment

Prostorově časová distribuce aerosolu v městském a venkovském prostředí

Doctoral thesis

Supervisor: RNDr. Jan Hovorka, Ph.D.

Prague, 2023

Prohlášení:

Prohlašuji, že jsem závěrečnou práci zpracoval samostatně a že jsem uvedl všechny použité informační zdroje a literaturu. Tato práce ani její podstatná část nebyla předložena k získání jiného nebo stejného akademického titulu.

V Praze, 30. 11. 2023

Jan Bendl

Dedicated to my family and to my colleague and friend Mgr. Miroslav Klán († 2021)

Table of Contents

Acknowledgement

I would like to express my gratitude to Jan Hovorka, who supervised my dissertation as well as my bachelor and master thesis. Thanks to him, I learned the scientific work - from designing the experiment, field work, to data processing, interpretations and presentations. I especially appreciate his creative way of solving scientific and technical problems, his endless enthusiasm, critical thinking and ability to improvise in the field, which I also tried to adopt. I am very grateful for allowing me to present my results at international conferences and involving me in interesting projects - from lab experiments such as testing air purifiers up to complex air quality measurements in cities and villages, to the most exciting measurement campaigns with remotely operated airship over coal mines, highway and industrial areas. He was always available and he also suggested and supported my internship in Germany, which later opened the door to my professional life.

Many thanks also to my university teachers, from my research focus especially to Jan Hovorka, Iva Hůnová, Vladimír Ždímal, Martin Braniš, Jan Bednář, Tomáš Cajthaml, Luboš Matějíček and many others.

I would also like to thank all my colleagues at the Institute for the environmental studies, especially Jaroslav Kukla, Miroslav Klán, Olga Vindušková, Petra Pokorná, Cecilia Leoni, Naděžda Zíková, Veronika Dočekalová, Jana Kozáková, Martina Píšová, Jolana Tátosová, Petra Benetková and many others for a pleasant time at the workplace and in the field.

I am grateful for the support by a STARS scholarship, and for funding my Charles University GA UK project no. 1474217, from which I could realize my experimental set-up. The work was supported also by the Czech Science Foundation project P503/12/G147, the SmartAQNet and the AeroHEALTH project. I am also thankful to the German Environmental Agency (DBU) for supporting my research project and allowing a one-year internship in the Comprehensive Molecular Analytics department (CMA) of Helmholtz Zentrum München. I am thankful to Dr. Jürgen Schnelle-Kreis for accepting and supervising my project, my CMA colleagues, and the Joint Mass Spectrometry Center (JMSC) group of Prof. Ralf Zimmermann.

I am especially grateful to the CMA deputy head Prof. Thomas Adam, who offered me at the end of my internship a research position in his department at the Bundeswehr University in Munich. I appreciate that he entrusted me for example with an organization and realization of the experimental set-up of the marine engine emission measurements, something I had no experience with before. Furthermore, he enabled me to carry out within the project MORE (part of dtec.bw project funded by EU) air quality measurements in the Munich subway and to write the paper, which I included in my PhD thesis.

And of course, the greatest thanks go to my family, I couldn't have done any of this if it weren't for the endless support of my mother Běla and father Jirka and my partner Barbara.

Abstract

Air quality in Europe remains a significant environmental concern, affecting the health and quality of life of its population. While stationary network ambient air quality monitoring allows for the observation of main trends, it is not fully representative of personal exposure of citizens due to high spatio-temporal variability of atmospheric aerosol. Therefore, highly time-and-space resolved measurements with state-of-the-art instruments and methods are needed to observe the aerosol variability, dynamics, identify hot-spots, and pollution sources, which are necessary for successful targeted mitigation measures.

This thesis addresses this gap focusing on the characterization of spatio-temporal distribution of atmospheric aerosol in inhabited environments. Novel mobile measurement systems were developed and employed to investigate diverse environments, including rural, urban and suburban area. Aerosol source-apportionment were conducted, and the toxicological effects associated with these environments were also investigated.

A novel mobile measurement system was developed for personal exposure measurements and pollution mapping in urban and rural environments. The system was used to measure air quality in the Munich subway, revealing high aerosol dynamics with significantly higher concentrations of mainly coarse particles – primarily iron oxides from rail and wheel abrasions – compared to ambient air (*Manuscript 1*). A similar mobile system also was used to explore the spatio-temporal distribution of emissions from local heating sources during the winter season in rural locations at the Czech-German border within two similarly sized villages. The study revealed a decrease of the air quality, especially in the Czech Republic in the afternoon and evening due to a combination of low-quality combustion processes, meteorological, and geomorphological conditions (*Manuscript 2*).

Innovative tethered-balloon measurements of vertical temperature-humidity profiles allowed the detection of the inversion layer's height, which prevented the dispersion of pollutants in suburban location (*Manuscript 3*). Source-apportionment using the Positive Matrix Factorization (PMF) method from both aerosol elemental composition and particle number size distributions, delineated key pollution sources and their contribution in urban and suburban air quality in the Ostrava region (*Manuscript 4*). Additionally, the use of a high-volume cascade impactor for the sampling into 4 particle size fractions allowed the monitoring of daily variability of carcinogenic polycyclic aromatic hydrocarbons (c-PAHs) and their toxicity, with the upper accumulation mode of the aerosol contained 44% of c-PAHs (*Manuscript 5*). Furthermore, in laboratory experiments, the toxicology effects of anthropogenic and biogenic secondary organic aerosol (SOA) typical for urban areas and remote locations were investigated, revealing a higher toxicity from anthropogenic SOA, typical of urban areas (*Manuscript 6*).

Abstrakt

Kvalita ovzduší v Evropě zůstává významným problémem v oblasti životního prostředí, který ovlivňuje zdraví a kvalitu života obyvatel. Stacionární síť monitorování kvality venkovního ovzduší sice umožňuje sledovat hlavní trendy, ale vzhledem k vysoké časoprostorové proměnlivosti atmosférického aerosolu není plně reprezentativní pro osobní expozici občanů. Proto jsou zapotřebí měření s vysokým časovým a prostorovým rozlišením, která umožní sledovat jak dynamiku aerosolu, tak identifikovat horká místa a zdroje znečištění. To je nezbytný předpoklad pro úspěšná cílená opatření ke zlepšení kvality ovzduší.

Práce se zaměřuje na charakterizaci časoprostorového rozložení atmosférického aerosolu v obydleném prostředí. Byly vyvinuty a použity nové systémy pro mobilní měření určené pro charakterizaci venkovských, městských a příměstských oblastí. Byly provedeny experimenty vedoucí k rozlišení zdrojů aerosolu a stanovení jeho toxikologických účinků.

Byl vyvinut nový mobilní měřicí systém pro měření osobní expozice a mapování znečištění v městském a venkovském prostředí. Systém byl použit k měření kvality ovzduší v mnichovském metru a odhalil vysokou dynamiku aerosolů s výrazně vyššími koncentracemi především hrubých částic – především oxidů železa z kolejnic a otěrů kol – ve srovnání s okolním ovzduším (*rukopis 1*). Podobný mobilní systém byl použit ke změření časoprostorového rozložení emisí z lokálních topenišť dvou podobně velkých obcí v zimním období na česko-německé hranici. Snížená kvalita ovzduší byla zejména v odpoledních a večerních hodinách v obci v České republice v důsledku kombinace nekvalitních spalovacích procesů, meteorologických a geomorfologických podmínek (*rukopis 2*).

Inovativní měření vertikálních teplotně-vlhkostních profilů pomocí připevněného balonu umožnilo v urbánním ovzduší zjistit výšku inverzní vrstvy, která limituje rozptyl znečišťujících látek v příměstské lokalitě (*rukopis 3*). Rozlišení zdrojů aerosolu pomocí metody PMF (Positive Matrix Factorization) z prvkového složení aerosolu a z velikostní distribuce počtu vymezilo klíčové zdroje znečištění a jejich podíl na kvalitě ovzduší měst a příměstských oblastí Ostravska (*rukopis 4*). Použití vysoko-objemového kaskádního impaktoru pro odběr vzorků do 4 velikostních frakcí částic navíc umožnilo sledovat denní variabilitu karcinogenních polycyklických aromatických uhlovodíků (c-PAH) a jejich toxicitu, přičemž horní akumulační mod aerosolu obsahoval 44 % c-PAH (*rukopis 5*). Dále byly v laboratorních experimentech zkoumány toxikologické účinky antropogenního a biogenního sekundárního organického aerosolu (SOA) typického pro městské oblasti a odlehlé lokality, přičemž byla zjištěna vyšší toxicita antropogenního SOA, typického pro městské oblasti (*rukopis 6*).

List of publications and manuscripts included in the doctoral thesis

Manuscript 1 (published): Bendl, J.; Neukirchen, C.; Mudan, A.; Padoan, S.; Zimmermann, R.; Adam, T. Personal measurements and sampling of particulate matter in a subway – Identification of hot-spots, spatio-temporal variability and sources of pollutants. *Atmospheric Environment* **2023,** *308*, 119883; DOI 10.1016/j.atmosenv.2023.119883.

Manuscript 2 (published): Liu, X.; Schnelle-Kreis, J.; Zhang, X.; **Bendl, J.**; Khedr, M.; Jakobi, G.; Schloter-Hai, B.; Hovorka, J.; Zimmermann, R. Integration of air pollution data collected by mobile measurement to derive a preliminary spatiotemporal air pollution profile from two neighboring German-Czech border villages. *The Science of the Total Environment* **2020,** *722*, 137632; DOI 10.1016/j.scitotenv.2020.137632.

Manuscript 3 (published): Bendl, J.; Hovorka, J. Temperature and Relative Humidity Vertical Profiles within Planetary Boundary Layer in Winter Urban Airshed. *IOP Conf. Ser.: Earth Environ. Sci.* **2017,** *95*, 52003; DOI 10.1088/1755-1315/95/5/052003.

Manuscript 4 (published): Pokorná, P.; Leoni, C.; Schwarz, J.; Ondráček, J.; Ondráčková, L.; Vodička, P.; Zíková, N.; Moravec, P.; **Bendl, J.**; Klán, M.; Hovorka, J.; Zhao, Y.; Cliff, S. S.; Ždímal, V.; Hopke, P. K. Spatial-temporal variability of aerosol sources based on chemical composition and particle number size distributions in an urban settlement influenced by metallurgical industry. *Environmental Science and Pollution Research International* **2020,** *27* (31), 38631–38643; DOI 10.1007/s11356-020-09694-0.

Manuscript 5 (published): Topinka, J.; Rossner, P.; Milcová, A.; Schmuczerová, J.; Pěnčíková, K.; Rossnerová, A.; Ambrož, A.; Štolcpartová, J.; **Bendl, J.**; Hovorka, J.; Machala, M. Day-to-day variability of toxic events induced by organic compounds bound to size segregated atmospheric aerosol. *Environmental Pollution* **2015,** *202*, 135–145; DOI 10.1016/j.envpol.2015.03.024.

Manuscript 6 (published): Offer, S.; Hartner, E.; Di Bucchianico, S.; Bisig, C.; Bauer, S.; Pantzke, J.; Zimmermann, E. J.; Cao, X.; Binder, S.; Kuhn, E.; Huber, A.; Jeong, S.; Käfer, U.; Martens, P.; Mesceriakovas, A.; **Bendl, J.**; Brejcha, R.; Buchholz, A.; Gat, D.; Hohaus, T.; Rastak, N.; Jakobi, G.; Kalberer, M.; Kanashova, T.; Hu, Y.; Ogris, C.; Marsico, A.; Theis, F.; Pardo, M.; Gröger, T.; Oeder, S.; Orasche, J.; Paul, A.; Ziehm, T.; Zhang, Z.-H.; Adam, T.; Sippula, O.; Sklorz, M.; Schnelle-Kreis, J.; Czech, H.; Kiendler-Scharr, A.; Rudich, Y.; Zimmermann, R. Effect of Atmospheric Aging on Soot Particle Toxicity in Lung Cell Models at the Air-Liquid Interface: Differential Toxicological Impacts of Biogenic and Anthropogenic Secondary Organic Aerosols (SOAs). *Environmental Health Perspectives* **2022,** *130* (2), 27003; DOI 10.1289/EHP9413.

Author’s contributions

Manuscript 1: Jan Bendl (JB) is first and corresponding author. He contributed to the main project ideas, built the new experimental setup (mobile system for mobile air quality measurements and sampling), performed most of the measurements used in the paper himself, organized the subway measurements and supervised 5 master students who conducted part of the measurements as part of their university practicum. JB analyzed and evaluated all on-line data, performed gravimetric analysis, processed raw ICP-MS data. JB prepared all graphs and tables and wrote the whole manuscript except the SEM-EDX part. JB presented the work as two oral presentations at the International Aerosol Conference (IAC) 2022 in Athens and at the European Aerosol Conference (EAC) 2023 in Malaga.

Manuscript 2: JB developed the new mobile measurement systems (3 experimental strollers equipped with portable instruments). JB planned and organized the Czech-German measurement campaign and led the measurements at the Czech site (about 6 student volunteers). JB contributed to the design of the experiment, participated in the data analysis and interpretations and presented the results as an oral presentation at the Helmholtz Zentrum München. JB popularized the results and the problematic of domestic heating emissions in Czech Television and within the European Commission (EC JRC) initiative project CONSPIRO.

Manuscript 3: JB performed all the balloon measurements and was involved in the whole winter campaign in Kladno – Švermov in 2016, which included stationary and mobile air quality measurements. JB analyzed the data, prepared all graphs and tables and wrote the whole manuscript. JB presented this work as a talk at the international conference of the Czech Aerosol Society (ČAS) 2016, at the Post-gradual Students Conference (PGS) 2016, and at the international World Multidisciplinary Earth Sciences Symposium (WMESS) 2017, where he chaired two environmental sessions.

Manuscript 4: JB was highly involved in the winter measurement campaigns in Ostrava, where he ensured the proper operation of the air quality monitoring station equipped with instruments for in-depth on-line particulate matter (PM) and gas measurements and PM sampling. JB was collecting samples during the campaign, and participated in the Czech TV investigation’s documentary “Nedej se! Ostravské ovzduší”.

Manuscript 5: JB participated in the field campaign measurements (1 month long campaign and additional preparations) and provided the sampling for this study, which included daily operation of the high-volume cascade impactor, preparation of polyurethane foam (PUF) substrates in the laboratory by successive leaching in de-ion water, methanol, dichloromethane, sample handling, complete gravimetric analysis of PUF and filters and evaluation of positive sampling artefact of polycyclic aromatic hydrocarbons outside the scope of this paper. JB wrote the related part of the methods.

Manuscript 6: JB participated in a measurement campaign at the Comprehensive Molecular Analytics (CMA) department of Helmholtz Zentrum München. JB was actively attending the campaign meetings and contributed to the design and performance of the experiments. JB mainly operated aerosol related instruments. For example, JB successfully repaired two faulty condensation particle counters (CPCs) during the on-going campaign.

The supervisor of the doctoral thesis, RNDr. Jan Hovorka, Ph.D. fully approves the contribution of Mgr. Jan Bendl as stated above.

Jan Hovorka

RNDr. Jan Hovorka, Ph.D.

List of Abbreviations

ALI	Air-Liquid Interface
AMS	Aerosol mass spectrometer
AQG	Air Quality Guidelines
BC	Black carbon
CAST	Combustion aerosol standard
CCN	Cloud condensation nuclei
CHMI	Czech hydrometeorological institute
COPD	Chronic obstructive pulmonary disease
C-PAHs	Carcinogenic PAHs
CPC	Condensation particle counter
DIP-HR TOFMS	Direct inlet probe-high-resolution time-of-flight mass spectrometry
DMA	Differential mobility analyzer
eBC	Equivalent black carbon
EC	Elemental carbon
EDF-XRF	Energy dispersive X-ray fluorescence
EDX	Energy dispersive X-ray spectroscopy
EEA	European Environment Agency
ELPI	Electrical low pressure impactor
EOM	Extractable organic matter
EPA	Environmental Protection Agency (United States)
GC-MS	Gas chromatography-mass spectrometry
GIS	Geographic information system
GPS	Global positioning system
GC	Gas chromatography
GC×GC-MS	Two-dimensional gas chromatography-mass spectrometry
HPLC	High performance liquid chromatography
HVCI	High volume cascade impactor
IARC	International Agency for Research on Cancer
ICP-MS	Inductively coupled plasma mass spectrometry
LC	Liquid chromatography
LDSA	Lung deposited surface area
MPPS	The most penetrating particle size
MS	Mass spectrometry
NEE	Non-exhaust emissions
NMHC	Non-methane hydrocarbons
NSD	Number size distribution

OC	Organic carbon
ONA	Optimized noise-reduction averaging
OPS	Optical particle sizer
PC	Polycarbonate
PAHs	Polycyclic aromatic hydrocarbons
PAM	Potential aerosol mass
PBL	Planetary boundary layer
PM	Particulate matter
PMF	Positive matrix factorization
PM_X	Particulate matter smaller than X μm in the aerodynamic diameter
PNC	Particle number concentration
PNSD	Particle number size distribution
PSD	Particle size distribution
PTR-MS	Quadrupole proton-transfer reaction mass spectrometer
PVC	Particle volume concentration
QFF	Quartz fiber filter
RDI	Rotating drum impactor
RH	Relative humidity
ROS	Reactive oxidative species
RT	Respiratory tract
SEM	Scanning electron microscope
SEM-EDX	Scanning electron microscopy with energy dispersive X-ray spectroscopy
SIA	Secondary inorganic aerosols
SMPS	Scanning Mobility Particle Sizer
SOA	Secondary organic aerosols
SP	Soot particles
SVOC	Semi-volatile organic compounds
S-XRF	Synchrotron XRF
TD	Thermal desorption
TEM	Transmission electron microscopy
TEOM	Tapered element oscillating microbalance
UFP	Ultrafine particles
UVPM	Ultraviolet absorbing particulate matter
VOC	Volatile organic compounds
VSD	Volume size distribution
WHO	World Health Organization
WMO	World Meteorological Organization
XRF	X-ray fluorescence

1. General introduction

1.1. Background and motivation

Air pollution is still an emerging global environmental problem. The World Health Organization (WHO) reports that over 90% of the world's population lives in areas where recommended levels of $PM_{2.5}$ (particulate matter with a diameter smaller than 2.5 µm) are exceeded (WHO, 2021). Therefore, air pollution is not only a problem in developing countries, but also in the most developed ones in Europe, where the quality of life, including available healthcare, quality of water and food, is of highest standards. Unlike other commodities, individuals have limited control over the air they breathe and often lack comprehensive information about its quality. Unfortunately, our perception system cannot detect nanoparticles containing mutagens or carcinogens and other harmful substances in the air. Some feedback, like coughing, typically occur only at extreme concentrations. Additionally, the health effects of air pollution often take years to manifest, adding a layer of complexity to the challenge. European Environmental Agency (EEA) estimates, that in the European Union, approximately 238 000 premature deaths are directly linked to exposure of fine particulate matter ($PM_{2.5}$) and 96% of the urban citizens were exposed to levels exceeding WHO Air Quality Guidelines (AQG). The consequences of air pollution are wide-ranging and severe, contribution to common respiratory diseases, chronic obstructive pulmonary disease (COPD), high blood pressure, ischemic heart disease, stroke and cancer (European Environment Agency, 2022). Especially old people, children and people with decreased health conditions are particularly vulnerable. Air pollution therefore has a significant impact on the economy, but also on ecosystems, especially vegetation, animals, insect and water and soil environments too. While there have been improvements in air quality over the past decades (European Environment Agency, 2022), not all processes and health effects are fully understood yet and new challenges are continuously arising. Furthermore, air pollution is linked to greenhouse gas emissions and processes causing climate change.

However, this work focuses on pollutants that directly affect the human health and the overall quality of life of the population through respiratory exposure. Nevertheless, addressing air quality from a health perspective may also be beneficial for addressing other environmental issues, such as climate change mitigation, while the health argument might be easier to grasp and defend.

Natural sources of air pollution, encompassing both particulate matter and gases, include occurrences like forest fires, biomass burning, volcanic activity, and dust storms. However, concerning health effects in European urban areas, anthropogenic sources of emissions play a pivotal role.

Importance of air pollution increased with the Industrial Revolution and gained major attention after 1952, when up to 12 000 people died during the Great Smog of London, clearly linked to air pollution from a coal combustion (Finlayson-Pitts and Pitts, 2000; Fowler et al., 2020). A major milestone in the Czech Republic (formerly Czechoslovakia) was the 1970s and 1980s, when extreme emissions of SO_2 and NO_X mainly from coal burning and industrial sources, led to acidification that damaged forests in the north and east of Bohemia and, through long-range transport, even affected life in Scandinavian lakes and contributed to the pollution of the Northern Hemisphere. For these reasons, and with contribution from the early environmentalists, measures such as desulfurization of large and medium-sized combustion plants were taken, which significantly reduced air pollution in the Czech Republic. Implementation of EU directives has led to a further decline in emissions (Hůnová, 2020). Currently, industrial sources in Europe are monitored and controlled on the basis of legislation (Marco and Bo, 2013). For example, in the Czech industrial city of Mladá Boleslav, it has been found that under unfavorable meteorological conditions, most of the air pollution in the city paradoxically originate from local heating sources from surrounding villages (Hovorka et al., 2015; Křůmal et al., 2017). The reason is, in contrast to industry, domestic heating is practically not controlled and monitored and its mitigation requires a complex approach, including the awareness raising and education. However, there are still places in Europe strongly affected by the industry, especially on a local scale, such as Ostrava-Radvanice district in the Czech Republic adjacent to the large metallurgical industrial complex (Pokorná et al., 2015). Nevertheless, ambient pollutant concentrations result from a mixture of various sources, often both from local and distant origin. There are several methods to apportion sources at location-receptor, from simple analysis or measurements of markers of specific source to a receptor modelling, such as positive matrix factorization (PMF) (Hopke et al., 2020). Measurements of background ambient concentrations can be also very useful, also for identification of long-range transport of pollutants.

Similar to industry, automotive transportation is currently subject to considerable regulations. New motor vehicles have to meet Euro standards, cars in use are subject to regular emissions checks and some variation of low emission zones are increasingly appearing in cities (Chamberlain et al., 2023). However, the situation is still problematic, mainly because emissions, especially from old diesel engines in poor technical conditions, can contain soot nanoparticles with adsorbed carcinogenic polycyclic aromatic hydrocarbons (PAHs) and other hazardous chemical compounds such as NOx (Hooftman et al., 2018). Relatively few high emitters can affect the air quality significantly (Vojtisek-Lom et al., 2020).

With increasing electromobility and alternative fuel cars, non-exhaust emissions, mainly abrasion of tires, brakes and other surfaces, become more significant. Brake wear accounts for about 55% of non-exhaust emissions and form up to 21% of traffic-related PM_{10}

emissions (Grigoratos and Martini, 2015). The estimated PM_{10} emission factor from tires is 6.3 $mg.km^{-1}$ and from brakes 6.7 $mg.km^{-1}$ per vehicle (Grigoratos and Martini, 2015). Tires are considered as one of the largest sources of microplastics in the environment (Järlskog et al., 2022) and brakes are significant source of heavy metals, such as Fe, Cu, Zn, Sb and Ba (Grigoratos and Martini, 2015). Non-exhaust emissions can be generated even by railway traffic, including trams and subway systems, due to abrasion of rails, wheels, catenaries and brake pads. In closed poorly ventilated environments such as subway tunnels, concentrations of metal-containing particles can increase to high levels (Xu and Hao, 2017).

In terms of personal exposure to harmful PM in the ambient air, meteorological dispersion conditions and proximity to the source are important factors affecting the overall concentrations. Since studies have shown large spatio-temporal differences in ambient pollutant concentrations at the urban microscale (Wu and Boor, 2021), scarcely positioned state air quality monitoring stations may produce data relevant for only part of the urban population. Further misinterpretation by public and even air quality models based on this data could underestimate local sources, such as domestic heating. Therefore, a useful way to get information on actual personal exposure of citizens is through mobile personal measurements, which are now increasingly possible in both outdoor and indoor environments thanks to advances in aerosol instrumentation and analytical techniques in past decades (Ensor, 2011).

In summary, stationary air quality measurements play a crucial role, especially for identifying long-term and large-scale trends, offering advanced and detailed measurements with extensive instrumentation, and serving as a reference. However, there is a recognized need for new approaches to identify pollution sources and hot-spots effectively. These new approaches can lead to effective measures to mitigate the personal exposure of citizens on daily basis, thereby ensuring compliant air quality for all.

Within this context, the present thesis focuses on the investigation of novel approaches to explore the spatio-temporal variability of aerosols in inhabited environments. Subsequent chapters offer a fundamental introduction to the topics, measurement parameters and techniques discussed in the papers of this study. For more in-depth explanations, readers are encouraged in the cited literature.

1.2. Atmospheric aerosol and its basic physical properties

Atmospheric aerosol is defined as a suspension of solid/liquid particles in the air and is ubiquitous component of the Earth's atmosphere (Hinds et al., 2022). It is of great importance for the existence of the water cycle, since aerosol particles form **cloud condensation nuclei (CCN)** and play also a significant role in the Earth's temperature balance and visibility (Finlayson-Pitts and Pitts, 2000; Seinfeld and Pandis, 2016). As highlighted in *Section 1.1.*, aerosols can be also highly health relevant, since they can act as a carrier of harmful compounds (*Section 1.3.*). They can also negatively affect plants, buildings and various ecosystems (Hinds et al., 2022).

Aerosols, with a particle diameter ranging from ~ **1 nm to 100 µm**, include subsets such as dust (micrometer size range of particles); smoke (sub-micrometer range); smog; fume; haze; spray and other subclasses, which are determined mostly according to particle forms and its generation. Particles with biological origin, **bioaerosol,** include viruses (10–200 nm), bacteria (200 nm – 20 µm), spores (around 1–50 µm), pollen (20-100 µm) and other biological material (Hinds et al., 2022).

The basic differentiation is into **primary and secondary aerosol**, where primary aerosols are directly emitted and secondary aerosols are formed in the atmosphere through chemical and photochemical reactions. Secondary aerosol can be distinguished between **secondary organic aerosol (SOA)** and **secondary inorganic aerosol (SIA)** (Colbeck, 2008).

Since aerosol particles have various shapes and densities (e. g. long asbestos fibers, dense iron oxide particles, hollow pollen particles, carbon spheres) and can even form clusters, which behave in the air like a single particle, it is necessary to determine the **equivalent particle diameter** for correct descriptions and quantifications of aerosol particles and their size classes. For example, one of the most important **aerodynamic particle diameter,** d_a , is diameter of the sphere with a density of 1 g.cm^{-3} that settles in still air at the same velocity as the particle (Hinds et al., 2022). For particles larger than 1 µm applies following equation:

$$d_a = d_p \chi \sqrt{\frac{\rho_p}{\rho_0}} \tag{1}$$

where d_a is the particle aerodynamic diameter, d_p or ρ_p is it's physical geometric diameter or the density and ρ_0 is the standard particle density (1 g.cm^{-3}) and (Hinds et al., 2022) and χ is a dynamic shape factor (Wang et al., 2022).

Aerodynamic diameter may be noticeably different from the **geometric diameter** in case of irregular shape (Finlayson-Pitts and Pitts, 2000) and different densities. The usual particle density in urban environments is on average around 1.5 g.cm^{-3} but for example, iron oxide particles have effective density 5.2 g.cm^{-3} (Hinds et al., 2022). Aerodynamic diameter is relevant in terms of aerosol penetration into lungs and to most of the atmospheric processes. Another equivalent diameter is for example **electrical mobility diameter** (d_m), which is based on the behavior of charged aerosol particles in the electric field. Several common aerosol measurement techniques are using this phenomenon and therefore the different equivalent diameters have to be taken into account when interpreting the data (Baron et al., 2011).

Due to a 5 order of magnitude difference in size between the smallest (1 nm) and largest (100 µm) aerosol particles, the physical behavior of particles in the air cannot be described universally. The smallest particles, with size close to the average molecule in the air (0.37 nm), are moving by **Brownian motion (diffusion)**, while the relatively large particles are moving and settling by **Stokes's and Newton's laws** (Hinds et al., 2022).

To illustrate importance of the d_a, in case of aerosol particle sedimentation in still air, particle of d_a = 10 µm settles a height 1 m about 6.1 minutes, while 1 µm particle 7.5 hours and 100 nm particle for 304 hours (Hinds et al., 2022). However, due to turbulences and airflows in the atmosphere and indoor environments, the real sedimentation can take even longer time. On the other hand, particles can be removed in relatively short time by various processes mentioned in the *Section 1.3*.

The difference between the physical behavior of micrometer- and nanometer-range particles can be also illustrated with the **filtration theory**. There are numerous types of filters, from quartz fiber filters (QFF) consisting of quartz microfibers with a certain thickness to polycarbonate (PC) filters, which are composed of a thin membrane with precisely defined holes, for example 2 µm in diameter. In this case, it might be intuitive to conclude that particles larger than 2 µm are captured while the smaller particles pass through, however, the second part of this hypothesis is not exactly correct. If we would simplify air filtration to a basic physical process, it is a stream of air that bypasses an obstacle, for example an edge of the hole or a single fiber of the filter. Large particles > 0.5 µm can be collected on filter by **gravitational forces**, while other particles tend to follow the air streamline around the obstacle. However, some of them are captured due to their shape within the particle radius of a fiber, which is called **interception**, other cannot follow the streamline due to their mass and resulting inertia and impact the fiber - **impaction**, and only certain fewer heavy particles can go through the filter. However, the smallest particles <100 nm (ultrafine particles, UFP) are constantly moving in all directions by Brownian motion, so even though they're several orders of magnitude smaller than the diameter of the fiber or a hole, they are effectively collected on the fiber as well by the **diffusion** mechanism. Another mechanism for collecting especially small particles are by electrical or electro-statical forces (Dilamian et al., 2021).

A typical minimum for **particle collection efficiency** of filtration is at around d_a = 300 nm, meaning particles of these sizes are collected the least effectively. It is referred as the most penetrating particle size (MPPS). Filtration efficiency is influenced by a flow velocity, diameter of fiber and other factors (Bai et al., 2021).

In the **human respiratory tract (RT)**, inertial impaction, settling and Brownian diffusions are the most important processes of aerosol particle deposition and besides physio-chemical properties of particles, physiology of the person plays an important role (Colbeck and Lazaridis, 2014). RT is divided into three main regions: extrathoracic, tracheobronchial and alveolar (Sierra-Vargas and Teran, 2012). *Figure 1* shows which sizes of particles are typically collected in which regions. Similar to the case of particle capture by a fiber filter, the most penetrating particle size (MPPS) in the human respiratory system is in the region of about 0.3 – 0.5 µm (Hinds et al., 2022).

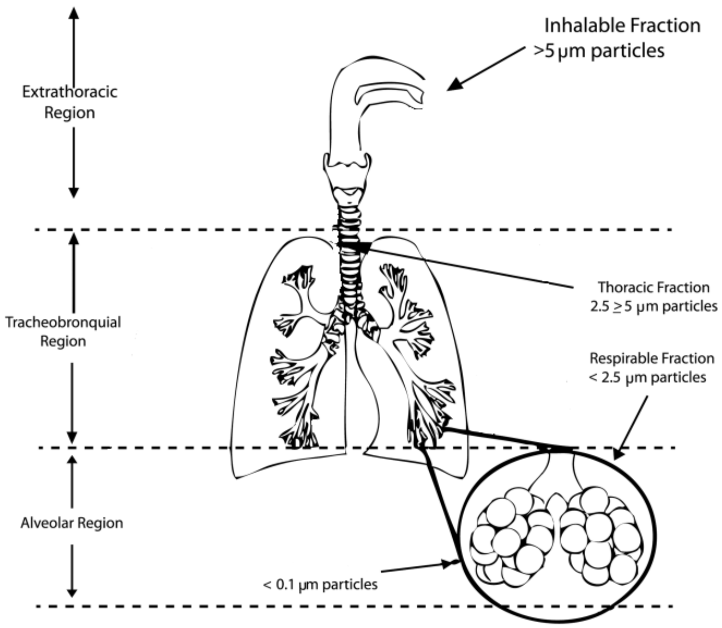

Figure 1: Deposition of particles in the human respiratory tract. Adapted from Sierra-Vargas and Teran (2012).

Respirability, different physical behavior, composition and sources are one of the reasons, why we generally distinguish between **coarse particles** larger than 2.5 µm and **fine particles** smaller than 2.5 µm, alternatively 2 µm according to Whitby (Baron et al., 2011). **Ultra-fine particles (UFP)** are a subdivision and cover particles smaller than 100 nm. The commonly used term **Particulate Matter (PM)** represents solid or liquid particles and abbreviations **PM_{10}, $PM_{2.5}$, PM_1**, are often used for expressing PM lower than 10, 2.5 and 1 µm in aerodynamic diameter, respectively (Baron et al., 2011). Historically, mainly 24-hour mass concentrations of PM_{10} were quantified using samplers and gravimetry (Colbeck, 2008), but PM_1 and $PM_{2.5}$ are nowadays more important metrics, because of the ability of particles in these fractions to penetrate in the tracheobronchial and alveolar region of lungs. The differences in mass between PM_{10} and $PM_{2.5}$ or even PM_1 can be very significant, given that the larger diameter particles form the most of the total aerosol mass (Baron et al., 2011), which is explained in the following chapter.

1.3. Aerosol size distribution and its health effects implications

Atmospheric aerosol is usually formed by a large number of particles. There can be 100 to 10 million particles with a diameter ranging from 1 nm up to 100 µm in one cubic centimeter of ambient air. The distribution of particles at a given time and a given location changes dynamically depending on many factors. It is therefore useful to measure in time the **particle size distributions** (PSD) (Baron et al., 2011; Hinds et al., 2022). The most commonly used are particle number, mass and volume size distribution (*Manuscript 4*). The PSD of the surface is also relevant for health effects because harmful chemical compounds can be bonded to the surface of the particles.

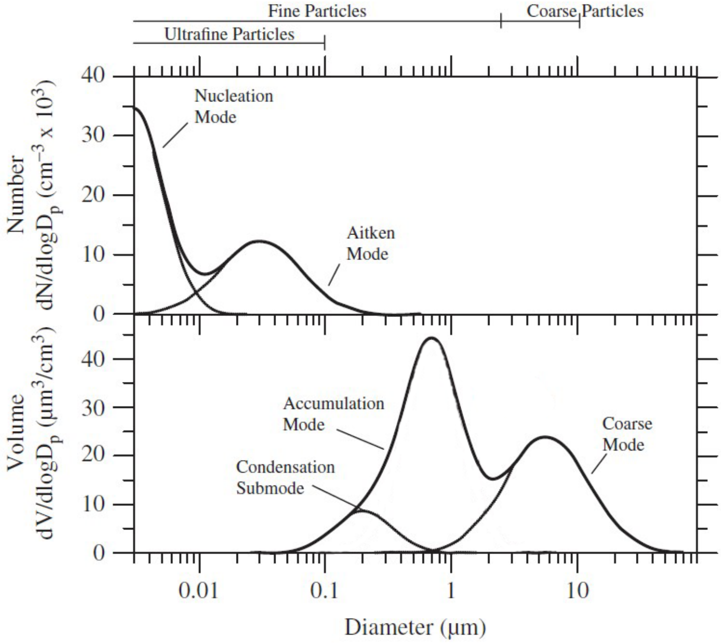

Figure 2: Comparison between particle number and volume size distribution with highlighted modes, adapted from Colbeck and Lazaridis (2014).

Figure 2 illustrates the difference between **particle number** (up) **and volume** (down) **size distribution** of the same set of particles. Generally, the smallest particles in nanometer range naturally account for most of the particle number, while having a negligible volume and mass, and the largest particles in micrometer range are usually responsible for most of the volume and mass but do not have high number. Consequently, the size distributions of aerosol are essential information for the study of urban or rural air quality, identification of sources and its impact on health.

Atmospheric aerosol shows in the size-distribution modal structures with distinct peaks in certain size ranges, that have physical-chemical basis and are the result of sources and sinks. The main modes in urban air are the **nuclei (nucleation) mode** (0.005-0.1 µm) and the **accumulation mode** (0.1-2 µm), commonly named as fine aerosol particles, and the **coarse particle mode** (>2 µm) (Baron et al., 2011). Sometimes the **Aitken mode** (0.01-0.1 µm) (Colbeck and Lazaridis, 2014) and the **inter-modal fraction** (1-2.5 µm) (Kozáková et al., 2017) are also distinguished. The particles of the **nuclei mode** are formed by condensation of super-saturated gases in the troposphere or emitted directly by combustion. Their residence time in the troposphere ranges from seconds to tens of minutes due to their high reactivity (Baron et al., 2011). The **Aitken mode** includes primary particles emitted by combustion processes, such as soot particles, but can also contain condensed particles of nuclei mode. **Accumulation mode** is mainly formed by gas-to-particle conversion and from coagulation of smaller particles, which can also condense on particles from this mode. Accumulation mode contains most of the fine particle mass and the residence time is from days to weeks (Baron et al., 2011). **Coarse particles** are usually originated from mechanical processes, such as dust particles from agriculture, mining, sea spray, or from for example biomass burning emissions. Due to gravitational sedimentation, coarse particle residence time range in the troposphere usually from hours to two days. Important removal process of atmospheric aerosols is by the rain and other wet and dry deposition (Baron et al., 2011; Colbeck and Lazaridis, 2014; Hinds et al., 2022).

Especially for the **urban aerosol** are typical anthropogenic sources and concentrations from tens of $\mu g.m^{-3}$ up to $mg.m^{-3}$ in heavily polluted cities and during smog situations. The horizontal spatial distribution is mainly determined by sources and atmospheric conditions. The size distribution of urban aerosol is complex due to the various size distribution of sources which are mixed. Moreover, the atmospheric processes described above, such as particle growth, evaporation and removal are affecting the size distribution. It is typically tri-modal with nuclei, accumulation and coarse mode (Hinds et al., 2022). Since distribution from each source are overlapping, it is normally not possible to distinguish the sources based on the overall ambient particle size distribution. Aerosols and $PM_{2.5}$ are distributed unevenly in both urban and rural environments, and also within Europe (Trechera et al., 2023; Yu et al., 2023). Locally, the highest concentrations are usually near the sources and hot-spots.

1.4. Atmospheric aerosol chemical composition

Generally, chemical composition of particles is very diverse and complex, with both organic and inorganic compounds. The composition is depending mainly on the sources and atmospheric conditions, so it is often linked with location and the particle physical characteristics, such as particle size distribution. Dominant chemical compounds of PM are

sulfates, nitrates, ammonium (**secondary inorganic compounds** generated mostly by oxidation in the atmosphere), **mineral dust** (aluminosilicates and carbonates), **sea salt**, **organic and elemental carbon** (Colbeck, 2008).

Individual particles composition can be uniform within the population of particles and then it's referred as **internally mixed** aerosol (all particles contain the same species in the same mass fractions), or it may vary within an ensemble of particles and then it's called **externally mixed** aerosol (each particle contains specific species). Aerosol mixing state therefore refers to the distribution of properties across the population of particles. However, aerosol mixing state is in reality in between of these two extremes and is evolving over time. For example, addition of new particles to the population might shift the mixing state towards "externally mixed", while aerosol aging process or addition of dominating particle type might shift the population of particles towards "internally mixed" state and make the population more homogenous. Therefore, it is important to distinguish between populations of particles and single-particles due to high diversities of particles and their distribution within the population (Riemer et al., 2019).

Coarse particles >2.5 μm formed mainly by mechanical processes often contain naturally occurring earth elements, minerals, soil, sea salt and elements such as Ca, Fe, Si, Al, Mg, Na, K (Colbeck, 2008). Due to adsorption processes they can act as a carrier of other compounds, including toxic PAHs. **Fine particles** <2.5 μm contain typically carbonaceous particles, sulfates, ammonium and nitrate ions and other compounds including trace elements and toxic compounds, such as PAHs (Colbeck, 2008; Lv et al., 2016).

Carbonaceous aerosols are divided between **organic carbon (OC)**, a mixture of thousands of organic compounds, and **elemental carbon (EC)**. EC contains pure carbon in the form of chain aggregates of **soot** globules and is formed during the high-temperature combustion processes, such as incomplete burning of fossil fuels. On the other hand, primary source of OC are often fossil fuel and biomass burning, industrial, automotive and other sources. OC can be also produced from atmospheric oxidation of **volatile organic compounds (VOC)**. VOC in the troposphere can originate from biogenic processes, such as α-pinene, β-pinene, isoprene, formic acids and others, or from anthropogenic sources, such as benzene, naphthalene and other volatile aromatics, and alkanes (Finlayson-Pitts and Pitts, 2000; Rissanen, 2021).

OC typically consists of carbon, hydrogen, oxygen, nitrogen and other elements. OC and EC measurements are often used for characterization and identification of sources (Colbeck, 2008). Sometimes, **non-methane hydrocarbons** (**NMHC**) are monitored as compounds possibly contributing to the smog formation (Finlayson-Pitts and Pitts, 2000).

Black carbon (BC) then represents carbonaceous particles strongly absorbing the visible light and therefore contribute to the warming of the atmosphere and is often used as a synonym to EC (Rönkkö et al., 2023). BC is formed by EC but can contain also OC with similar light absorbing properties. **Brown carbon (BrC)** is absorbing light at shorter wavelengths of the visible spectrum and is mainly formed by organic compounds and from photochemical reactions of VOCs. VOCs, such as alkanes, alkenes, alkynes, aromatics, carbonyls, react with oxidizing agents in the atmosphere, such as O_3, OH and NO_3 radicals and form **SOA**. Precursors of SOA with low vapor pressure can be both anthropogenic and biogenic origins (Colbeck, 2008; Fan et al., 2022; Koppmann, 2007).

Generally, there is a large variety of **organic compounds** in aerosol particles, significantly contributing to their mass, as primary components or mainly through low-vapor pressure condensates. Besides above-mentioned carbonaceous particles and SOA and VOC, other organic compounds can be present such as macromolecules "humic-like substances" (HULIS) (Colbeck, 2008; Schneider et al., 2023). Some analyzed organic compounds can be used also as molecular markers for identification of pollution sources, or using specific diagnostic ratios (Mikuška et al., 2015).

The most health relevant organic compounds in the urban and suburban airshed are **Polycyclic aromatic hydrocarbons (PAHs).** PAHs are composed of multiple aromatic rings and are most commonly formed as products of incomplete combustion and pyrolysis. PAHs can be found both in gas and particle phase. Generally, PAHs with 2-3 rings have low vapor pressures are dominantly in the gas phase, while 4-ring PAHs are both in gas and particle, depending on the vapor pressure of the compound and the atmospheric temperature. They can be condensed on the aerosol particles of various fractions (Dat and Chang, 2017; Finlayson-Pitts and Pitts, 2000; Kim et al., 2013). Their health effects are discussed in *Section 2.7*. Common methods used in this work for organic compounds characterization are described in *Section 2.3.1*.

Minerals, trace elements and metals are also important components of aerosol from environmental and sometimes also health perspective (*Section 2.7.*). Their monitoring can be used as a tracer of their specific sources. For example, for coal burning are typical elemental constituents As, Se, and specific ratios Mn to Fe and Fe to Mg. Fine particulate emissions from refineries and oil power plants typically contain specific relative concentrations of earth elements. Source apportionment models, such as Positive Matrix Factorization (PMF, *Section 2.4.*) are often using elements to identify the pollution sources (Finlayson-Pitts and Pitts, 2000; Hopke et al., 2020). Health effects of selected elements and heavy metals are described in *Section 2.7*. Methods used in this work for inorganic compounds characterization are described in *Section 2.3.2*.

Water is often also contained in particles. The water soluble compounds can absorb atmospheric water and turn from solid particles to liquid droplets (Colbeck, 2008).

Almost ubiquitous **bioaerosols** include pollen, fungal spores, bacteria, viruses and other material of both plant and animal origin (Xie et al., 2021).

1.5. Aerosol sources and their composition in urban and rural areas

The sources and composition of aerosol in urban and rural areas can vary significantly, however, some typical sources and patterns can be observed.

Urban areas often contain higher levels of combustion related particles (OC, EC) and SOA, such as nitrate, sulfate, ammonium. The combustion sources are **typically transportation, industrial processes, domestic heating** and other ambient sources such as **cooking emissions, cigarette smoke** etc. Coarse particles can be originated for example from **dust storms** (e.g., Saharan dust), **resuspension of the street dust**. From traffic are typical soot particles with adsorbed organic compounds such as PAHs, but also **non-exhaust emissions (NEE)** are significantly emitted, mainly from **brake and tire wear** and from road surfaces (Fussell et al., 2022; Grigoratos and Martini, 2015). NEE emissions also occur in rail transport and can reach high concentrations, especially in enclosed, poorly ventilated areas such as subway tunnels (Cusack et al., 2015; Martins et al., 2015). A significant problem, particularly in port cities, is **emissions from ships**, which are currently subject to only relatively light regulation and can be a significant contributor to pollutants and health hazards such as PAHs and other products of oil combustion (Anders et al., 2023; Jeong et al., 2023; Schneider et al., 2023). Other sources may also be present, such as **airports** with jet-engine emissions (Rohkamp et al., 2023). The composition of the aerosol depends on the location and the representation of typical sources varies and cannot be completely generalized. Photochemistry plays also an important role and vary in time and among specific locations (Sadanaga et al., 2003), as well as long-range transport (Martins et al., 2018).

Rural areas normally do not contain such a large variety of local sources as urban areas, however, for example typical **domestic heating, biomass burning, traffic and other local sources** can contribute on high pollution levels. Particularly in the winter months, during temperature inversions, PM concentrations can increase significantly above those in developed cities with central heating and gasification. In the coarse particle mode, there may be resuspended dust from agriculture, for example from fields, which may contain pesticides (M Figueiredo et al., 2022). There may be a higher incidence of **bioaerosols** in areas close to natural environment such as forests, grasslands and there can be an influence of **agricultural emissions**. Rural environment can be dominated by a long-range transport and the **new particle formation (nucleation)** can be observed (Hock et al., 2008). Nucleation occurs usually in a relatively clean air during sunny days and when the precursors (sulfur dioxide) are available (Jorga et al., 2023).

In 2022 in the EU, the highest concentration of $PM_{2.5}$ were detected in Po Valley (northern Italy), where is a combination of high levels of anthropogenic emissions with unfavorable morphological and meteorological conditions, and in eastern and central Europe, mainly due to solid fuel combustion and older vehicle fleet. Due to energy crisis and higher gas prices in 2023, higher consumption of wood and coal as a fuel is expected. Traditionally high PM_{10}

and $PM_{2.5}$ concentration are reported from central-eastern Europe, mainly from solid fuels combustions for domestic heating, industrial activities, agriculture and road transport. (European Environment Agency, 2023). Typical example is Ostrava region in the Czech Republic, which is the European hot-spot for $PM_{2.5}$ and benzo[a]pyrene (Sram et al., 2013b). A common issue for all populated areas is the **indoor air quality**, where people often spend most of their time during the day. The largest problem in houses and buildings is emissions from smoking and other combustion processes, including emissions from cooking and candles. In addition, the exchange between the outdoor and indoor environment, which can introduce emissions from the outside, is significant (Morawska et al., 2013; Talbot et al., 2016). On the other hand, controlled air exchange is desirable because, for example, furniture can release significant amounts of VOCs, including harmful formaldehyde (Morawska and Salthammer, 2003).

2. Aerosol measurements and analytical techniques

The classic method for determining PM mass concentration, and estimating the air quality, is filter sampling followed by gravimetric analysis to calculate the average aerosol mass concentration in the air over the sampling period (US EPA, 2016). As the analysis must be performed retrospectively, it can be referred to as offline analysis. The need for sufficient aerosol mass on the filter for the subsequent filter weighing is the main limiting factor in capturing intra-day and spatio-temporal dynamics. From this reason, cumulative samples of 24 or 12 hours are commonly used. The similar limitation applies to sampling for chemical analysis, where shorter times are possible depending on the analytical technique. Another limitation is that the sample is usually taken from a single aerosol size fraction, commonly PM_{10}, $PM_{2.5}$ or PM_1, so information on the size of the particles to which the hazardous substances are bonded may be lacking. This could have a major impact on health risks (*Section 1.2.*) and the interpretations would be limited for standalone sampling. It is therefore advantageous to complement off-line cumulative sampling with on-line measurements of aerosol size distributions and other variables with high temporal resolution that can reveal sources, physicochemical processes, personal exposures and contribute to a better understanding of aerosol behavior in the atmosphere. On-line measurements provide instantaneous data and nowadays, fully automated monitoring stations are available. In all cases of aerosol measurements, care must be taken to ensure proper methodology, e. g. avoidance of aerosol losses in the duct, avoidance of losses of volatile compounds, and minimization of sampling artefacts, such as by appropriate drying of moisture droplets. The instrumentation and methods for air quality measurements and analysis have made substantial advancements in recent decades. However, the utilization of different techniques is frequently constrained by the financial, material, and manpower requirements associated with specific instruments, measurements, and analyses. Subsequent chapters will provide background information on the methods encountered in this thesis.

2.1. On-line measurements

On-line measurements are performed in real time, or near-real time, providing typical outputs such as the concentration of PM or other monitored parameters (Baron et al., 2011). The choice of the appropriate instrumentation and measurement strategy is crucial for the correct interpretation of the measured data. It is often possible to select the integration time of the measurement, i.e., the period over which the data are averaged. For mobile measurements, it is essential that the time is short enough to match the time frequency of the process or movement. For instance, one-second data (1 Hz acquisition) is required for cycling, 5-seconds may be sufficient for walking, while one- or several minute data acquisition may be sufficient for stationary measurements. In this case is often advantageous to choose a longer integration time to remove unwanted noise and make the main trend visible. This can also be achieved by post-processing the data, for example by averaging using central moving average or other statistical methods (Liu et al., 2021).

2.1.1. Optical particle sizers

For on-line measurement of PM with high temporal resolution, **optical particle sizers (OPS)** are most commonly used. OPS exploit the scattering of light on the aerosol particles, which is proportional to the particle size (Hinds et al., 2022). Based on this principle, particles are assigned to size classes (bins), the range of which can be predefined. However, most spectrometers measure particles from about 300 nm in diameter due to limitations of visible light scattering (Baron et al., 2011).

The number size distribution of the aerosol can then be plotted from the observed time period. Particles are classified according to their optical diameter, regardless of their shape, which can lead to inaccuracies, especially for certain aerosol types. It is often desirable to calculate the aerosol mass distribution based on the raw counts and average effective particle density. An average density of 1 or 1.5 $g.cm^{-3}$ is usually used as the most typical for urban ambient air, but the best results are obtained by correcting the data using gravimetric analysis from a back-up filter. For simultaneous measurements with multiple spectrometers, collocation of the instruments is required, where the instruments measure the same aerosol over a certain period of time and concentrations and the data are mutually corrected using a regression equation to make them comparable.

In the *Manuscript 1*, **OPS 3330 (TSI, USA**) was used for both stationary and mobile measurements. The theory of operation of OPS 3330 is following: aerosol entering through the inlet nozzle is mixed with a laminar stream of particle-free air (sheath air) to properly direct the particles into the measuring cell and avoid the coincidence of multiple particles at the same time during laser measurements. A laser diode is used as a light source, and the scattered light from the particles is directed through a mirror onto the photodetector which detects the signal. The filter cartridge downstream the detector can be used for gravimetric correction. This can be done by simply comparing the concentration of the measured OPS and gravimetric analysis. However, since the OPS has a relatively low flow rate of 1 lpm, it is often preferable to use an external sampler with a higher flow rate for gravimetric correction. Since the instrument also measures coarse particles, which is susceptible to losses in the pipeline, it is advisable to keep the distance between the inlet and the instrument as short as possible, ideally without any bends, and to position the inlet vertically for low velocity measurements. For flight measurements with a horizontal inlet, the OPS 3330 can then be placed in the vertical position as the optical detection is independent of the instrument orientation. The instrument is also not significantly susceptible to vibration. At high humidity it is necessary to dry the aerosol or use a heated inlet and insulation of the instrument to prevent condensation in the device. An advanced dust monitor **DustTrak DRX 8533** (**TSI, USA**; *Manuscript 2*) works on a similar principle to the OPS 3330, but is tailored for higher concentrations of dust particles, which it measures in three size fractions PM_1, $PM_{2.5}$, PM_{10} only.

For long-term outdoor measurements, the Fidas 200s (Palas, Germany), identical to the **APDA-372 (Horiba, Japan**; *Manuscript 1*), is a suitable type of OPS system. It includes a conditioned environmental enclosure, heated inlet with the Sigma-2 sampling head, external temperature and humidity sensors, and the ability to calibrate on site using the test dust. The system is also EN 15267 certified.

2.1.2. Ultrafine particle counters and sizers

For particles of d_a<300 nm, the intensity of scattered light declines with λ^4 of wavelength (Baron et al., 2011). But controlled particle condensational growth to supermicron size overcomes such a difficulty. This principle is used by **condensation particle counters (CPC)**. In an **UCPC 3076 (TSI, USA)**, aerosol particles are injected into a sheath flow saturated with butanol vapor at 39 °C, then they enter a 10 °C condenser, where they enlarge their size to about d_a=10 μm in diameter by butanol condensation and are easily detected by a laser. The CPC can therefore only determine the total **particle number concentration (PNC)** of the aerosol for specific size range. An example of a commercial CPC suitable for mobile measurements is the **P-Trak 8525 (TSI, USA**; *Manuscript 2*) or the **CPC 3007 (TSI)**. However, as there is a risk of butanol flooding the optics if the instrument is tilted, it is important to secure the system against tilting and excessive vibrations.

In order to obtain the particle size distribution, it is necessary to first separate particles by size and count only the particles of the same size (monodisperse aerosol) in a narrow range and at the shortest possible time. The **Differential Mobility Analyzer (DMA)** works on the principle that a polydisperse aerosol enters an electric field through which only monodisperse aerosol passes to the exit. Prior to a DMA the aerosol passes through charge **neutralizers** based on weak radioactive or X-ray sources to equilibrize particle charge. The entire system including DMA and CPC is called the **Scanning Mobility Particle Sizer (SMPS)**. Size distribution spectra are measured by increasing the voltage in the DMA from units to tens of thousands of volts (up-scan), so that one full spectrum takes up to several minutes, and then a scan in the reverse direction can be measured without a time delay (down-scan). The use of SMPS is problematic when atmospheric processes to be measured are faster than the scan time. Therefore, traditional SMPS are not entirely suitable for mobile measurements and a partial solution may be to limit the size range and therefore the time, or to use a DMA with a fixed setting to monitor only the mode of interest. It should also be noted that the DMA classifies particles according to the mobility diameter of particles and not the aerodynamic diameter. In this work, SMPS consisting of 3082 DMA and 3750 CPC (TSI, USA) and SMPS 3936 (TSI, USA) were used (*Manuscript 4, 5*).

Diffusion size classifiers provide size-segregation on a different principle. One of the commercial handheld instruments suitable for mobile measurements is the **DISCmini** (**Testo, Germany**, *Manuscript 1*). The aerosol enters the device, where it mixes with the positive ions generated in the corona discharge. The charged particles are then first detected on a metal grid, where the smallest nanoparticles are captured by diffusion, and they are detected as an electric current. The remaining particles pass through the grid to the filter stage, where they are also detected as an electric current. The ratio between these two fractions is then estimated by the size mode in nanometers according to the calibration. From the sum of the two currents, the instrument calculates the concentration of the aerosol in the 10-700 nm fraction. The upper limit is given by the impactor, which does not allow larger particles to enter and contaminate the instrument. Larger particles are almost negligible in terms of particle number. The instrument can measure total PNC with a time resolution of up to 1 second (DISCmini, Testo, Instruction manual v1.12). Compared to the CPC/P-Trak, the DISCmini can quantify the **lung-deposited surface area** (**LDSA**), a relatively new metric that combines alveolar particle deposition efficiency with particle surface area and thus proves to be highly relevant for epidemiology (Lepistö et al., 2023; Salo et al., 2021).

The **Electrical Low-Pressure Impactor** (**ELPI; Dekati, Finland;** *Manuscript 6*) also works on the principle of particle electric charge detection, but is capable of measuring real-time aerosol size distributions in the range of 0.03-10 µm. It is a 12-stage impactor (*Section 2.2.1.*) with a high-sensitivity detector on each impaction plate, electrically isolated from each other (Marjamäki et al., 2000).

Nowadays, sub-10 nm aerosol particles are still challenging to measure reliably (Kangasluoma et al., 2020).

2.1.3. Aethalometers

Aethalometers are semi-continuous instruments that can measure usually both **Black Carbon (BC)** and **Brown Carbon (BrC)**. The measurement principle involves collecting aerosol on a white tape for the measurement time, the shortest possible time being usually 10 seconds, and then a laser beam of different wavelengths is passed through the spot and its attenuation is measured. The tape is then moved and the measurement is repeated. In the case of the portable micro-aethalometer **MA200 (AethLabs, USA**; *Manuscript 1, 2*), five wavelengths are used: 880 nm, 625 nm, 528 nm, 470 nm, 375 nm, where 880 nm corresponds to the BC concentration and 375 nm to the ultra-violet absorbing PM (UVPM), which corresponds to brown carbon (BrC; Operating Manual, MA200, Aethlabs). For stationary measurements, benchtop aethalometers are available, such as the **AE33 (Magee Scientific, Slovenia**; *Manuscript 6*), which even measures at 7 wavelengths. In order to differentiate between BC measured by different methods, which can lead to discrepancies and misinterpretations, Petzold et al. proposed to use the term equivalent BC (eBC) for optically measured BC (Petzold et al., 2013).

2.1.4. Other on-line instrumentation

A number of commercial and experimental instruments are available for on-line characterization of aerosol physical properties and individual variables, and it is necessary to carefully evaluate which technique is appropriate for each application, as many devices have their specific limitations and advantages. In this work, in addition to the instruments mentioned above, the following were used: **Aerosol Particle Sizer** (**APS 3321, TSI**, **USA**; *Manuscript 4*), which measures the aerosol size distribution using a time-of-flight method in the range of 0.542 – 20µm) (Vincent, 2007); semi-continuous **OC/EC analyzer** (**Sunset Laboratories, USA**; *Manuscript 4*); **tapered element oscillating microbalance** (**TEOM, 1400a, Rupprecht Pataschnik, USA**; *Manuscript 6*), which analyses the aerosol mass online based on the oscillation of the captured aerosol on the pendulum, and others (Vincent, 2007). An important part of the ambient air monitoring stations are on-line gas analyzers (in our case from the manufacturer Horiba, Japan), which are not emphasized in this work. In *Manuscript 6*, we used **ozone** monitor in emission concentration range **APOA 350 E** (**Horiba, Japan**), while during stationary measurements (*Manuscripts 3, 4, 5*), we used monitors designed for the ambient air for **NOx, O_3, CO, SO_2, non-methane hydrocarbons (NMHC) and CH_4 (APNA-360, APOA-360, APCA-360, APSA-360, APHA-360; Horiba, Japan**) with integration time of 5 min. In addition, meteorological data, especially temperature, humidity, pressure, solar radiation, wind speed and direction, and precipitation, are usually required for all ambient air measurements. This can be achieved using portable stations, such as **Vantage 2 Pro (Davis, USA**; *Manuscript 1*) or **WMR 300** (**Oregon**

Scientific, USA; *Manuscript 2*). In *Manuscript 3*, it was necessary to use temperature and humidity sensors with extremely fast response times (**Vaisala, Finland**), which are usually used in weather balloons, but in our case, they were custom adapted to log the data for re-use.

Almost all on-line analyzers require regular leak checks with HEPA filters and flow calibrations, for example with a **mass flow meter** (**4043 H, TSI, USA**; *Manuscript 1, 6*). There are also many instruments that do not measure aerosols but are necessary for desired experiments in conjunction with other instruments, such as GPS units, data-loggers, computers, multimeters, etc. Some of the analytical instruments from the *Section 2.3.* can be used also on-line or semi-online.

2.2. Off-line measurements

Off-line measurement refers to the collection of aerosols on a filter followed by laboratory analysis. A simple sampling device consists of a filter holder and pump controlled by a mass flow controller or a critical orifice. To determine the concentration of the monitored substance or aerosol mass, it is necessary to know the exact flow rate and time of sampling, from which the volume of air sampled is simply calculated. In ambient air quality measurements, this volume is most often given in terms of actual values for a given ambient air temperature and pressure. However, sampling recommendations for individual pollutants may vary according to ISO standards. For emissions sampling, the volume of air sampled is most often converted to a normal volume according to duct temperature and pressure. Another important factor is the choice of a suitable filter material or substrate on which to collect the aerosol. It is important that all particles within the observed size range are collected quantitatively. In most cases, filters with a particle collection efficiency close to 100% are used (Baron et al., 2011). The choice of suitable filter material and its laboratory preparation is mainly determined by the method of chemical or gravimetric analysis. To ensure the quality of the sample collected, it is necessary to consider potential contamination, loss of volatiles, sampling artefacts, and sample preparation.

2.2.1. Stationary samplers

Before the actual aerosol collection, the particles are usually pre-separated into PM_{10}, $PM_{2.5}$, PM_1 or other size fractions. This is done using impactors or cyclones. In the case of impactors, an air stream bypasses the impaction plate and particles larger than the cut-off size are trapped on the plate by impaction (*Section 1.2.*), while the remaining particles continue on the filter. In the case of a cyclone, the air creates a vortex and the larger particles are collected by centrifugal action according to the calibrated cut-off. The impactors and cyclones must be selected according to the flow rate, which must remain constant, so the potential pressure drop due to the aerosol loading on the filter must be compensated. For this reason, the pumps must be regulated and capable of handling the increased under-pressure. Tubing must be of conductive materials and ideally vertical and as short as possible to prevent aerosol loss in the duct (Baron et al., 2011; Hinds et al., 2022) and the inlet should be omni-directional to not discriminate between wind directions. The standard stationary **low-volume sampler** with selectable sampling head as a pre-impactor is the **SEQ-47/50** or **LVS-3** (Leckel, Germany, *Manuscript 4*) with a flow rate of 2.3 $m^3.h^{-1}$, which contains a **47 mm filter-holder** that automatically changes filters according to the selected protocol (Leckel SEQ-47/50, Operation Manual). Similarly, the **Digitel DHA-80 high-volume sampler** (*Manuscript 1, 4*) operates at a higher flow rate of typically 30 $m^3 \cdot h^{-1}$. A special case are **cascade impactors**, where several impactors are cascaded below each other and the aerosol is collected on a filter or substrate that is part of the impaction plate. This allows the different aerosol size-fraction to be separated. In the *Manuscript 5*, the **BGI-900 High Volume Cascade Impactor (HVCI)** was used, which separates aerosol into fractions of 10-1 µm, 1-0.5 µm, 0.5-0.17 µm, and a back-up filter captures all remaining particles smaller than 0.17 µm. A porous **polyurethane foam** (**PUF**) is used as the substrate in each stage and the last stage is a PTFE-coated glass fiber filter. To achieve sufficient mass on each stage at common ambient air concentrations, it samples 54 $m^3.h^{-1}$. When analyzing semi-volatile organic compounds (SVOC) such as some PAHs, it should be considered a positive sampling artifact of the gas phase on the PUF (Bendl, 2014). The **Davis Rotating-drum Uniform-size-cut Monitor** (**3DRUM, Delta Group UC-Davis, USA**; *Manuscript 4*), works on the principle of particle impaction on a **Mylar tape** placed on a slowly rotating cylinder, with 3 cylinders in a cascade, similar to cascade impactors. The advantage, however, is that the aerosol can be analyzed for example for elemental composition by synchrotron X-ray fluorescence (S-XRF, *Section 2.3.2.*) with a high time resolution of up to 1 hour, which is not common with most samplers (Bukowiecki et al., 2008).

2.2.2. Portable samplers

Miniaturized portable samplers suitable for personal exposure monitoring function in a similar way to the stationary samplers described in the previous section. They can be used, for example, by a worker in a hazardous occupation to collect daily exposure samples during an 8-hour shift. For this reason, portable sampler pumps typically contain rechargeable batteries and the size of the whole system is such that it can be clipped to a belt. A pre-impactor and a simple **filter holder** can be used. The **Sioutas five-stage cascade impactor** (**SKC Ltd., USA**) with 25 mm upper-stage filters and 37 mm back-up filter was used in the *Manuscript 1* together with the **SG10-2 mobile sampler** (**GSA, Germany**). Sioutas impactor was also used as a 2.5 µm pre-impactor in front of a 47 mm filter-holder to achieve a larger filter area.

2.3. Chemical analysis and analytical techniques

The analysis of samples, e.g. PM samples collected on filter, through chemical and analytical methods enables precise identification and quantification of airborne substances. This plays a crucial role in the understanding of air quality and its implications for health and the environment. Such analyses are pivotal for assessing health risks associated with organic substances such as carcinogenic PAHs (Mikuška et al., 2015; Topinka et al., 2015), toxic metals (Font et al., 2019), asbestos (Klán et al., 2018) and others. Moreover, the characterization of substances in the air enables for a deeper understanding of complex atmospheric processes and facilitates source-apportionment. These analyses can broadly be divided into organic, inorganic or elemental and shape analyses.

2.3.1. Organic analysis

Aerosol samples typically contain a complex mixture of both inorganic and organic compounds. The wide variations in the chemical composition of aerosols and their concentrations often require the application of several analytical methods to gain a deeper understanding of their chemical profile. This often involves the combination of separation methods and diverse detection techniques (Heard, 2006).

In this thesis, both **high performance liquid chromatography (HPLC)** and **gas chromatography-mass spectrometry (GC-MS)** methods were used to explore the chemical composition of organic aerosol.

Specifically, a standard methods based on the use of HPLC was employed to quantify PAHs in accordance with the US Environmental Protection Agency (EPA) guidelines (Wise et al., 2015) and following the norm ISO 11338-2 (*Manuscript 5*).

Organic substances, including PAHs, collected on filter often involves the use of GC-MS based methodologies (*Manuscript 6*) (Wise et al., 2015). However, conventional GC-MS is often not enough for resolving the high complexity of aerosol samples. Thus, the use of higher resolution GC-MS techniques such as **comprehensive two-dimensional GC (GC×GC)** became essential (Tranchida et al., 2022) (*Manuscript 6*). The process of sample introduction is crucial as it involves transferring compounds from the filter samples to the analytical GC column. Typically, extraction methods using suitable solvents are employed for this purpose. In recent years, thermal extraction methods such as **thermal desorption (TD)** have gained popularity as well. Methods based on **direct thermal desorption (DTD)** from filter, has been used in this thesis in combination with GC / GC×GC -MS for the analysis of volatile and semi-volatile organic compounds (VOCs and SVOCs) (*Manuscript 6*). The use of direct MS based methodology such as, **direct inlet probe-high-resolution time-of-flight MS (DIP HR-TOF-MS)** and **quadrupole proton-transfer reaction mass spectrometer (PTR-MS)** has been explored for the chemical characterization of aerosol samples (*Manuscript 6*). However, this topic is not further discussed in the current thesis, as it is beyond the scope of the research.

2.3.2. Elemental analysis

A common method of elemental analysis is a combination of 24 h aerosol sampling on filter using a low- or high-volume sampler followed by **inductively coupled plasma mass spectrometry** (**ICP-MS**) analysis (*Manuscript 1*). While quartz fiber filters (QFF) are commonly used for sampling, other suitable filter materials, such as polycarbonate filter, can also be employed for coupling with ICP-MS analysis.

Sample extraction procedure is a crucial step for ICP-MS analysis (Ogrizek et al., 2022). According to standard method EN 1234:2014, microwave digestion of filters using HNO_3 and H_2O_2 is commonly used, but for specific elements, alternative extraction methods may provide better recoveries (Aldabe et al., 2013). In *Manuscript 1*, samples were digested by **Microwave speedwave ENTRY** (**Berghof, Germany**) according to DIN 14902 and analyzed by **ICP-MS 8900** (**Agilent, USA**).

Another method for elemental analysis of aerosol samples is by **Energy dispersive X-ray fluorescence (ED-XRF)**, which, while less sensitive than ICP-MS, offers the advantage of not requiring sample preparation (Ogrizek et al., 2022). Higher precision for complex aerosol samples is provided by **Synchrotron XRF (S-XRF)**, that uses an excitation source of synchrotron radiation that is less accessible (Bukowiecki et al., 2008; Ogrizek et al., 2022). S-XRF was used in *Manuscript 4* to analyze Mylar stripes from the rotating drum impactor (RDI, *Section 2.2.1.*) to provide concentrations of 24 elements in 3 size fractions and 1 h time resolution.

Elemental composition can also be determined using the **Energy dispersive X-ray (EDX)** probe of a scanning electron microscope (SEM, *Manuscript 1*), which is the subject of the following section.

In *Manuscript 4*, **cations and anions** from the aerosol sample were analyzed using **Dionex ICS-5000 system** (**Dionex. USA**), which operates on the principle of ion chromatography (Pokorná et al., 2020).

2.3.3. Shape and single-particle analysis

Due to the size of aerosol particles ranging from nanometers to hundreds of micrometers in diameter, classical optical microscopy is insufficient for visualization of the particle shape. High resolution is achievable using **Scanning electron microscopy (SEM)** and **Transmission electron microscopy (TEM)**. SEM uses reflected electrons to create the image, while TEM uses electrons that pass through the sample. From this reason, TEM is more suitable for small particles, lower than 0.5 μm (Baron et al., 2011). These techniques can provide with appropriate detectors information on the morphology, physical properties and even the chemical composition of individual particles. The **Energy-dispersive X-ray spectroscopy** (**EDX**) detector is used for the elementary analysis of individual particles within the SEM. For SEM-EDX analysis, filter sputtering is usually necessary to minimize the charging effects (Bendl et al., 2023). The choice of metal for sputtering the filter or matrix with the sample must be consistent with the elements to be analyzed with respect to interferences. The same applies to the filter or matrix itself. In the *Manuscript 1*, we sampled aerosol simultaneously on the polycarbonate (PC) filters and silica wafers. Sampling was performed in the total aerosol fraction and several times in the $PM_{2.5}$ fraction to verify the cut-off of the Sioutas impactor, which was used for ICP-MS samples. Representative 12 mm circular PC filter punches were then sputtered with a thin carbon layer using the **Q150T ES Plus** sputter device (**Quorom technologies, UK**). The subsequent analysis was performed using the **Inlens and SE2 detectors** of the **Gemini SEM 360** (**Carl Zeiss, Germany**) and the EDX detector **ULTIM Max 40** (**Oxford instruments, UK**). In addition to the conventional manual analysis of samples with mapping, automatic classification of particles in individual samples was also performed.

Analysis by SEM-EDX can also be performed in individual aerosol fractions, for example separated by the high-volume cascade impactor, which is useful to characterize physical properties of particles and their elemental composition used for in-vitro toxicological or other analyses (Marvanová et al., 2018).

2.3.4. Gravimetric analysis

Gravimetry is the most reliable method of determining aerosol mass concentration and is often used as a reference in on-line aerosol measurements. On-line methods typically do not directly measure mass, with exceptions such as TEOM (*Section 2.1.4.*); instead, aerosol mass is calculated based on number concentration and typical specific density of particles. Gravimetry for determination of PM_{10} and $PM_{2.5}$ mass concentration is commonly performed as part of monitoring according to European Standard EN 1234:2014.

Basically, it is the weighing of filters or other collection materials before and after sampling exposure, where the difference in mass represents the weight of the aerosol. Based on the volume of sampled air, the mass concentration of a given aerosol size fraction can then be calculated. The temperature and humidity of the filter and the conditioned gravimetry chamber or room must be always the same, usually 45 or 50% of relative humidity (RH) and 22 °C for accurate weighing and filters must be preconditioned for 24 hours. It is also necessary to remove the charge from the filter, for example by corona-discharge and perform blank and replicates weighing. If the filter is subsequently analyzed, precautions must be taken to avoid contaminations. Furthermore, losses and cross-contamination of volatiles during equilibration must be taken into account (Baron et al., 2011).

In *Manuscript 1*, we used an ultra-micro balance **Cubis MCA2.7S-2S00-F** (**Sartorius, Germany**) with a scale interval 0.0001 mg, inside the weighing chamber with corona discharge **PureGMC18** (**pure engineering GmbH, Germany**) set to 45 % RH and temperature 22 °C. Quartz, polycarbonate and Teflon filters were used. In *Manuscript 5*, we used an air-conditioned weighing room to 50 % and 21°C with a weights **MC 210S** (**Sartorius, Germany**) for weighing of PUF substrates and PTFE-coated glass micro-fiber filters. For PUF equilibration to 50% RH, desiccator with $Mg(NO_3)_2.6H_20$ was used.

2.4. Stationary monitoring of air pollutants

In most developed countries around the world, air pollution levels are regularly monitored through ambient air quality monitoring. Subsequently, it is checked whether the legal limits for individual pollutants are being exceeded. In the EU, these limits are generally not as strict as the guideline values recommended by the World Health Organization (WHO, 2021), which are often difficult to meet. Long-term stationary monitoring is also important in terms of source identification, public awareness, detection of long- and short-term trends, ecosystem exposure and more. Long-term monitoring in Europe is established by legislation, including the distribution of ambient monitoring stations. A common methodology has an advantage of making the data comparable within and between countries and ensuring quality control of measured data. The results are published in the regular yearbooks and synthesis reports of the European Environment Agency (European Environment Agency, 2023).

Although long-term ambient air quality monitoring as required by law has undeniable value for observing and improving air quality, it is advisable to combine it with the scientific approach of short-term air quality measurements for detailed identification of pollutant sources and dynamics. Such measurements are typically carried out in multi-week campaigns using moveable air quality stations, where typically many more air quality parameters are measured and analyzed at a shorter time resolution. Based on these data, it is then possible to evaluate pollution sources using statistical methods such as **Positive Matrix Factorization** (**PMF**) (Hopke et al., 2020; Hopke et al., 2022). In the *Manuscript 4*, such measurement campaign was carried out in the city of Ostrava - in the European air-pollution hot-spot. In order to make the results comparable with the monitoring stations, it is appropriate to perform a co-measurement of PM or to use a same calibrated PM reference instrument to which the data from the other instruments (e.g., SMPS and APS) are compared using linear regression. In the *Manuscript 4*, a mobile air quality monitoring station of the Laboratory of the Air Quality Research (Institute for Environmental Studies, Charles University), was used in the measuring site in Ostrava-Radvanice district in 2014 (*Figure 3*). **Continuous PM_{10} monitoring** instrument **FH 62 I-R** (**Thermo ESM Andersen, Germany**) was used for the comparison and data quality verification. For PM on-line data, instrument comparisons are particularly important to verify the accuracy of the chosen particle density, which is used to calculate mass concentrations from the number concentrations measured by SMPS and APS and eventually make corrections (*Section 2.1.2.*). In order to determine for which area is the station location representative, it is useful to complement the stationary measurements with a network on-line measurement of PM by portable monitors with a short acquisition time. In the case of *Manuscript 4*, seven monitors **DustTrak 8520 (TSI, USA**, *Section 2.1.1.*) were used to monitor $PM_{2.5}$ in 1 min. resolution in an area of several square kilometers (Pokorná et al., 2015). The instruments were also collocated prior to measurement to correct any off-set and verify the accuracy of the measurements.

The basic equipment of state's air quality monitoring stations are monitors of gases, especially NO_x, NO, NO_2, O_3, SO_2 and CO (*Section 2.1.4.*). In the case of on-line aerosol monitoring, PM_{10} measurements still predominate at state air quality monitoring stations, although it is not the most relevant metric from a health perspective (*Section 1.2., 1.3.*). However, more appropriate on-line measurements of $PM_{2.5}$ and PM_1 are becoming more widespread. The measured parameters are mainly corresponding to the current European Directive 2008/50/EC (European Parliament, 2015), which also sets the concentration limits of various pollutants in ambient air. For subsequent data interpretation, a meteorological observation at a given location with a proportional integration time to other parameters is an essential part of each stationary measurement (*Section 2.1.4.*), ideally according to the guidelines and recommendations of the World Meteorological Organization (WMO, 2021). In addition, measurements of aerosol size distributions and other on-line parameters (*Section 2.1.*) and sampling (*Section 2.2.*) are essential for scientific source-apportionment studies based on short intensive measurement campaigns (*Manuscript 4*). Figure 3 is an Air Quality Laboratory station showing isolated inlets (left) to individual instruments within the station (right).

Relatively inexpensive "low-cost" gas sensors and OPCs are increasingly available on the market. For professional use, however, they may suffer from offsets, interferences, detection and other data quality issues. Low-cost OPCs tend to fail especially at high relative humidity. However, they can be very useful and advantageous in enriching the network measurements, especially if the sensors are regularly calibrated and data are properly post-processed. Their quantity within the network can then be statistically corrected to compensate for the inaccuracies of individual sensors. They can be also useful for citizen science and basic occupational exposure monitoring (Li et al., 2018; Liu et al., 2020; Siouti et al., 2023; Zikova et al., 2017). Satellite remote sensing can also provide useful information on spatio-temporal variability of air pollutants, but primarily at larger scales (Tian et al., 2023).

Since meteorology significantly influences the aerosol distribution, PM sources from the long-range transport can be identified using backward air trajectories, such as Hybrid Single Particle Lagrangian Integrated Trajectory (HYSPLIT) and other modelling approaches, such as cluster analysis (Abdalmogith and Harrison, 2005).

Figure 3: Air quality monitoring station of the Laboratory of the Air Quality Research (Institute for Environmental Studies, Charles University) in Ostrava-Radvanice, 13. 2. 2014; photo: Jan Bendl

2.5. Mobile measurements

As discussed in *Section 1.3.-1.5.*, both aerosol and gaseous pollutants are not uniformly distributed in the atmosphere and, therefore, it is not possible to ensure that stationary monitoring stations are representative for all different urban and rural **micro-environments**. Although air quality models based on these measurements can be applied according to various parameters, the actual concentrations can vary considerably from the prediction. The **spatio-temporal variability of aerosol concentrations** in the study area can be resolved by mobile measurements. This method can help to directly identify individual pollution sources, areas of elevated concentrations and the dispersion of pollutants. By systematically repeating mobile measurements, **hot-spots** (locations where the concentrations are commonly elevated) can be identified. It should be considered that the monitoring stations are usually not located in the immediate vicinity of the sources, whereas by mobile measurements it is possible to measure even almost undiluted emissions in short time events, e.g. from car exhausts, chimney plumes, cigarette smoke, cooking emissions etc. (Liu et al., 2021). Therefore, maximum particle number concentrations (peak values) up to several orders of magnitude higher can be measured and thus the route and measurement strategy are important factors. Especially for people who are frequently or permanently in pollution hot-spot areas, exposure to pollutants can be dramatically higher than the average concentrations according to stationary monitoring (Jeong et al., 2019; Sullivan and Pryor, 2014; van Nunen et al., 2020).

By choosing a typical walking or cycling route, it is possible to assess the personal exposure of people, i.e., to capture the real concentrations of pollutants that are inhaled and for example compare different traffic modes of transportation (Cepeda et al., 2017; Kumar and Gupta, 2016) Since the background concentration naturally changes during the walk or ride, it is advisable to choose the length of one walk/ride to avoid misinterpretations. In the

Supplementary Information of the *Manuscript 1* are described following general recommendations regarding the mobile measurements: (1) The route must be around 1h long to observe enough micro-environments and have enough sample material on filter but, at the same time, the ambient PM background should not change significantly over the measuring time, (2) The route should start and end at the same location to observe the change of background concentrations, (3) the route should be close to the long-term air quality monitoring station to allow data comparison, (4) Typical urban micro-environments should be included, e.g., busy and non-busy streets, highways, parks, residential areas, sports facilities, restaurants or kiosks (cooking emissions), schools, kindergartens, public buildings, etc. (5). It should be possible to repeat the same route for spatio-temporal variability, ideally several times a day (Bendl et al., 2023).

In terms of instrumentation, portable on-line instruments (*Section 2.1.*) and portable samplers (*Section 2.2.*) are usually the most suitable. *Manuscript 1* describes the experimental set-up and measurement methodology using a self-constructed mobile measurement system specifically for investigation of a subway air quality (*Section 5.2.*), but it is applicable also for other micro-environments. Concept of mobile walking/cycling measurements is not new (van Poppel et al., 2013), however, *Manuscript 1* and *Manuscript 2* bring notable improvements and novel solutions, which are described in the results in *Section 4*. The system and methodology presented in *Manuscript 1* is one of the most comprehensive portable platforms for personal exposure to particle number and mass concentration, for personal sampling and hot-spots and aerosol sources identification using the professional instrumentation.

In the case of an outdoor mobile measurements, the easiest way to assign each measured point in space is to use the **GPS** coordinates recorded continuously in 1 Hz. In *Manuscript 1*, **GPS 64s** (**Garmin, USA**) was used for walking reference measurements. However, during the subway measurement, the GPS signal is not present and, therefore, the signal is not available and therefore it is necessary to **assign the location according to the notes**. In the case of *Manuscript 1*, the door opening and closing times at each station were recorded with one second accuracy. The prerequisite was to set the exact time of all instruments and GPS in a one second accuracy before the start of each measurement.

The **integration time of the measurement** must then be adjusted in proportion to the speed of the walk or ride and observed processes so that all changes in concentrations are clearly visible on the graph. On the other hand, choosing the short integration time may cause higher measurement noise, which makes interpretation more difficult. Therefore, **averaging** of some variables are beneficial, for example eBC values from micro-aethalometer MA200 using the Central Moving Average (Liu et al., 2021).

The resulting concentrations of the individual variables can then be plotted on maps, for example in **ArcGIS Pro** (**ESRI**). A **geographic information system (GIS)** enables further analysis of mobile data.

Another approach of mobile measurements is characterization of real-driving emissions of motorized vehicles using Portable Emission Measurement System (PEMS) (Kousoulidou et al., 2013). PEMS can measure tailpipe emissions of cars, trucks and other vehicles but now even two-wheelers (Vojtisek-Lom et al., 2020). Gaseous pollutants, such as NOx can be measured for example using miniaturized FTIR system. Such measurements are capable to identify excess emitters (Vojtíšek-Lom et al., 2018). Therefore, it can be used also as a tool for the law enforcement.

Other types of mobile measurements are **aerial measurements** which can observe spatio-temporal variability in three dimensions. They can be more complex and also demanding due to many limitations, especially the limited weight of the payload. In *Manuscript 3*, **Helium-filled tethered-balloon** (custom built) was included to air quality campaign in the city of Kladno (*Section 2.4.*) to monitor the temperature inversion layer height using fast temperature and relative humidity sonde (*Section 2.1.4.*). In this case, not only the acquisition rate is important, but also the reaction time of the sensor to changes in temperature or humidity since the balloon is freely launched. Choosing the suitable instrumentation and setting is therefore crucial for correct mobile measurement. However, without critical manual inspection of the measured data, such an error of inappropriate experimental setup can hardly be detected. Despite the numerous possibilities of automating data processing, a scientific approach is always required, including data interpretation. This is especially true for flight measurements using **a remotely controlled airship**. During our stationary measurements (*Section 2.4.*), a custom built airship (Airshipclub.com) was used to monitor the spatio-temporal distribution of aerosol during several days of intensive campaigns (Hovorka et al.) and also for sampling of the plumes from industrial sources for chemical analysis of specific emission sources to resolve source-apportionment within the Ostrava-Radvanice campaign in 2014, the same campaign as *Manuscript 4* (Pokorná et al., 2015). In our case, the unmanned airship has compared to the balloon a major advantage that it can carry up to 15 kg payload, and is able to perform 3D aerosol profiling. However, measurements are rather expensive and therefore limited in operational time. But even multi-day campaigns can resolve sources and spatio-temporal variations in aerosol that would not be detectable on the ground.

It is worth noting that measurement platforms can also be deployed on ships (Anders et al., 2023; Rosewig et al., 2023), cars (Vojtisek-Lom et al., 2020) and other vehicles, and even on special aircraft (Wendisch and Brenguier, 2013). Aircraft can be used to measure aerosol on a macro-scale (Heard, 2006), while the airship described above has the advantage of being able to measure within the **Planetary Boundary Layer** (**PBL**) from directly above the ground, therefore in the airshed that has the greatest contact with the areas where people live.

2.6. Emission measurements and laboratory simulations

The measurement of emissions differs in many ways from the measurement of ambient air quality. The concentrations of pollutants in the flue or exhaust are up to orders of magnitude higher than the diluted emissions in ambient air, where they are also mixed and immediately undergo a variety of atmospheric processes. Aerosol sources can be car engines and car non-exhaust emissions, such as brakes (Vojtíšek-Lom et al., 2021), marine engines (Jeong et al., 2023), aircraft jet-engines (Rohkamp et al., 2023), chimneys of industrial plants (Yang et al., 1998), but also laboratory generators of defined aerosol, such as soot generators. Prior to measurements, it is usually necessary to dilute and condition the emissions appropriately so that the concentrations are within the range of the operation of the instruments used and stable. For this purpose, for example, ejector diluters can be used, which work on the principle of mixing emissions in a fixed ratio with pure compressed-air. Especially in the case of subsequent chemical analyses, it is then necessary to ensure that this air is particle-free and VOC-free (Jeong et al., 2023; Schneider et al., 2023). Particle phase measurements are more complicated than gas phase measurements because of the particle losses and particle size discrimination that can occur with improper sampling. So-called isokinetic sampling is necessary especially for coarse particles, where the inlet velocity into the sampling tube is the same as the emission velocity in the pipe. This can be achieved by selecting a suitable flow-rate through the tube with respect to maintaining the laminarity of the flow in the tube and the velocity in the inlet nozzle can be adjusted further by changing the nozzle diameter. Since emissions are typically hot up to several hundred °C, it is necessary to keep all piping adequately heated up to the diluter to prevent condensation inside the piping, connectors and valves. Further losses can be caused by the length of the tubes, bends, constrictions, etc. and therefore it is always recommended to calculate the losses theoretically and verify them experimentally (Baron et al., 2011).

Since the behavior of aerosols in the atmosphere depends on many factors that are almost impossible to separate, and since it is an extremely complex system (Finlayson-Pitts and Pitts, 2000) in which it is often difficult to achieve repetition of the same situation and process due to constantly changing meteorology and other factors, it is useful to carry out laboratory experiments in which individual processes are simulated under defined and controlled conditions. This applies in particular to the simulation of secondary organic aerosol (SOA) formation. Large-scale atmospheric chambers with simulated atmospheres can be used, which used directly the sun to initiate photochemistry (Heard, 2006). However, these are large experimental set-ups and not the subject of this thesis.

In the *Manuscript 6*, **soot generator** (**CAST-Burner, Combustion Aerosol Standard, Jing**) was used to generate a defined aerosol concentration, **ejectors diluters** (**VKL 10 ED, Palas**, Germany), building **pumps** for the vacuum in the lines and **mass flow controllers** to control the flow rates. For the VOC and particle-free compressed air, a combination of the

compressor (**SF2, Atlas Copco, Sweden**), an air tank, a filtration system and a **zero-air generator** for VOC reduction using molecular sieves and hydrocarbon burning (**737-15, Aadco, USA**) were used.

For simulation of the aerosol aging, **potential aerosol mass reactor** (**PAM, University of Eastern Finland**) was used (Kang et al., 2007). It is an oxidation flow reactor (OFR), that simulates photo-oxidation in the atmosphere using UV lamps, ozone generation and the presence of OH radicals. In this extensive laboratory experiment, the time-of-flight **aerosol mass spectrometer** (**AMS, Aerodyne**) (Lee and Allen, 2012), **reactive oxidative species (ROS) on-line measurements** (**OPROSI, University of Basel**), and on-line instruments for toxicological analyses **Air-Liquid Interface exposure system (ALI, Vitrocell)** were used. Live cell cultures (e. g. A549 human alveolar epithelial cells) were exposed to a stream of aerosol and their viability was quantified.

2.7. Health effects and toxicology

Epidemiological studies reveal that ambient **$PM_{2.5}$** is the fifth-leading mortality risk factor globally (Cohen et al., 2015). There has been an observed increase in deaths and disability-adjusted life years (DALYs) since 1990 (Cohen et al., 2017). Short-term increments of 10 $\mu g.m^{-3}$ $PM_{2.5}$ are associated with a 1.04% increase in the risk of death, predominantly from respiratory causes (Atkinson et al., 2014). Heart failure also increases by 1.8% for a short-term increment of 10 $\mu g.m^{-3}$ $PM_{2.5}$ and 1.6% for **PM_{10}**. Even the coarse fraction of PM induces negative health effects and mortality, especially in the short term (Brunekreef and Forsberg, 2005). High-income countries generally have lower personal exposures to $PM_{2.5}$ (Lim et al., 2022).

Among gaseous compounds, exposure to **ozone, nitrogen oxides, sulfur oxides, volatile organic compounds (VOCs), dioxins**, **carbon monoxide** and some other compounds are considered harmful for humans (Jia et al., 2023; Manisalidis et al., 2020).

In general, air pollution causes **respiratory diseases** such as **chronic obstructive pulmonary disease (COPD)**, **bronchiolitis**, **asthma** and even **lung cancer** and **cardiovascular events** and diseases such as **ischemic stroke**, **central nervous system dysfunctions** (potentially even with Alzheimer's and Parkinson's disease), **cutaneous diseases**. PM exposure is also connected with dysfunctions of **reproductive and central nervous system, neuroinflammation**, with **cancer** and other diseases. The elderly, children and people with existing health conditions are particularly at risk (Block and Calderón-Garcidueñas, 2009; Manisalidis et al., 2020; Sram et al., 2013a).

Although $PM_{2.5}$ is a common metric in air pollution studies, stationary measurements may not fully reflect personal exposure, leading to potential misinterpretations (Boomhower et al., 2022). Monitoring the physico-chemical properties of particles, such as oxidative potential, is recommended over $PM_{2.5}$ mass, for a more accurate assessment of toxicological outcomes. Some higher oxidative and pro-inflammatory responses were observed at lower concentrations of PM_1 below 5 $\mu g.m^{-3}$ (Costabile et al., 2023). **Ultrafine particles (UFP)** have high surface area and high capacity for absorbing toxic organic compounds (Kwon et al., 2020). In ambient $PM_{2.5}$, it is not likely that single chemical component would be responsible for all adverse health effects (Schlesinger, 2007).

Some **Polycyclic aromatic hydrocarbons** (**PAHs**, *Section 1.4.*), often implicated in toxicity, are classified by the International Agency for Research on Cancer (IARC) as carcinogens. **Benzo[a]pyrene** is in the Group 1 as *carcinogenic to humans*, is commonly used as a marker for quantifying the equivalent carcinogenicity of other PAHs. **Dibenz[ah]anthracene (DB[ah]A)** is according to IARC *probably carcinogenic* (Group 2A), **benz[a]anthracene (B[a]A)**, **benzo[b]fluoranthene (B[b]F)**, **benzo[k]fluoranthene (B[k]F)**, **chrysene (CHRY)**, **ideno[1,2,3-cd]pyrene (I[cd]P)**, and others are *possibly carcinogenic to humas* (Group 2B) due to insufficient toxicological evidence (Russell et al, 2010). Although the US EPA recommends monitoring **16 priority PAHs**, there are many other harmful compounds like **oxygenated PAHs** (oxy-PAHs or OPAHs), **nitrated PAHs** (n-PAHs or NPAHs), **heterocyclic PAHs**, which are often not considered and therefore it could lead to underestimations (Aquilina and Harrison, 2023; Lammel et al., 2020; Li et al., 2019). Hence, toxicological studies with various assays to address genotoxicity, mutagenicity, carcinogenity and teratogenity are of interest (Idowu et al., 2019). However, quantification of the carcinogenicity and toxicity of single PAHs and mixtures of PAHs with large quantities of compounds is very complex and requires advanced methods, such as *in vitro* toxicity studies with mixtures of PAHs (Aquilina and Harrison, 2023).

In *Manuscript 5*, genotoxic assays were applied to investigate **DNA adduct** formation and **DNA strand breaks** during PAHs metabolism, revealing **oxidative DNA damage** and **aryl hydrocarbon receptor (AhR) mediated gene expressions** (**"dioxin-like activity").** These assays were linked with the concentrations of carcinogenic PAHs in size-segregated aerosol (Topinka et al., 2015). Although not all toxicological mechanisms are fully understood, metabolic routes leading to cancer, especially for **B[a]P** are well described (US EPA, ORD, Integrated Risk Information System, 2017; Xue and Warshawsky, 2005).

In the **Ostrava region**, recognized as a European hot-spot for B[a]P and PM, epidemiological studies have shown an increased incidence of bronchial asthma and acute respiratory diseases even for children (Sram et al., 2013b), an increased morbidity of pre-school children (Dostal et al., 2011) and other evidences (Jiřík et al., 2016). *Manuscript 5* focuses on what are the genotoxic effects within various particle size fraction in Ostrava, which is one of the key questions with respect to health effects.

Other both acutely and chronically hazardous substances in aerosol are **heavy metals**. For example copper and other metals can produce **reactive oxygen species (ROS)** in the body, which includes **hydrogen, peroxides (HOOH) and hydroxyl radical** which can cause adverse effects in lungs (Charrier et al., 2014) and have high pro-inflammatory and oxidative responses (Costabile et al., 2023). ROS can damage macromolecules, such as nucleic acids and cause mutations. This can lead to the development of cancer. ROS can also affect expression of genes (Klaunig, 2018; Rossner et al., 2021). An exposure route via **olfactometry bulb** has been demonstrated for **iron-soot nanoparticles**, where these nanoparticles can reach the brain directly and could possibly cause neural inflammation (Hopkins et al., 2018).

In general, toxicological studies can be carried out ***in vivo*** involving living organisms, or ***in vitro*** using isolated live cell cultures or tissues. In *Manuscript 5*, **submerged exposures** of cell lines from the size-segregated aerosol collected by high-volume cascade impactor (*Section 2.2.1.*) were performed, retrospectively in toxicology labs using particles dissolved from the polyurethane foam (PUF) and filters. While the approach used in *Manuscript 5* offers advantages like using size-segregated aerosol in four fractions and being cost-effective, it lacks consideration for pulmonary physiology, and particle physio-chemical properties are altered in solution. In contrast, *Manuscript 6* employed an **air-liquid interface (ALI)**, simulating real exposure by depositing aerosol directly on cells. ALI has advantages for this realistic approach but it is a large and expensive system, suitable for controlled laboratory experiments with high and stable aerosol concentrations. It shows potential to replace *in vivo* studies and allows the use of various cell co-cultures (Upadhyay and Palmberg, 2018).

Currently, studies focused on toxicological effects of photochemically aged aerosol are gaining more attention (Shao et al., 2022), however, the health effects of SOA have not yet been fully elucidated. Therefore, the main topic of *Manuscript 6* was to compare toxicological effects of SOA from typical biogenic and anthropogenic precursors.

3. Summary

The spatio-temporal distribution of aerosols is crucial for a comprehensive understanding of air quality. It plays a key role in assessing the real personal exposure of citizens, estimating potential health effects, identifying pollution sources, and unraveling fundamental atmospheric processes. The significance of investigating the spatio-temporal variability of aerosols is particularly pronounced in urban and rural areas, given the high diversity of sources and their inhomogeneous distributions at the micro-scale.

The complex factors influencing aerosol distribution, including atmospheric conditions, weather, variations in natural aerosol backgrounds, and chemical reactions, pose challenges. Despite these challenges, advances in instrumentation facilitate detailed analyses enabling the identification of individual pollutants and their attribution to pollution sources, even in complex urban airsheds. Comprehensive physio-chemical analyses of aerosols are essential for characterizing spatio-temporal variability of aerosol in both urban and rural air. In such approaches, stationary measurements focus on parameters like particle mass and number size distributions with sufficient temporal resolution to match with concentration changes and processes at a given location. Chemical analyses, emphasizing hazardous compounds like PAHs, along with markers and tracers for source-apportionment, are highly beneficial. Advanced statistical methods, such as PMF factor analysis, enable or enhance identification of sources. Instrumental analyses, such electron microscopy allows particle visualization and analysis. Mobile measurements using on-line instruments and samplers prove effective in exploring aerosol spatio-temporal variability. The health effects of specific substances in aerosol can be most precisely estimated and quantified by toxicological analyses.

The specific objectives of each study usually determine the planned analysis and the appropriate instrumentation.

There is no universal methodology or solution which could be possible to apply and the studies usually require a scientific approach due to the high complexity of the problem. However, both regular routine monitoring and short-term measurement campaigns are important to characterize the air quality. Then it is possible to implement appropriate measures to improve it and thus the quality of life of the population and the environment. It is necessary to reduce the long-term health issues and mortality associated with air pollution, which is a global problem.

This thesis focuses on investigating the spatio-temporal distribution of atmospheric aerosols in inhabited environments. Within this thesis, innovative mobile measurement systems were developed and utilized to explore a range of environments, including rural, urban, and suburban areas. The research includes source-apportionment experiments and an examination of the toxicological effects associated with these diverse environments.

4. Research activity

4.1. Aims of the study

Manuscript 1

The primary objective of this manuscript was to develop an innovative mobile measurements system capable of simultaneous sampling and measurements of particulate matter (PM), particle number concentration (PNC), black carbon (BC) and other air quality parameters. This system was designed to be used in both outdoor and indoor urban environments, enabling the identification of spatio-temporal variability and PM hot-spots.

The study aimed to utilize this system to investigate the personal exposure of citizens to PM during routine subway commutes, identifying hot-spots, monitoring the spatio-temporal variability of PM and PNC, and understanding the aerosol dynamics during the subway journey and on the station platforms. Furthermore, it aimed to uncover the factors contributing to this variability and compare concentrations with those found in the surrounding ambient air.

A particular focus was placed on performing elemental analysis of PM samples, primarily due to the expected metal emissions resulting from the rail and brake abrasion. To clarify this hypothesis, particle analysis using an electron microscope equipped with an EDX probe was planned, with the aim of precisely determining the elemental composition of single particles.

Manuscript 2

In this study, similarly to *Manuscript 1*, two self-made mobile systems were employed to investigate the spatio-temporal variability of emissions originating from local heating sources during the winter season within rural areas located at the Czech-German border. Specifically, the study focused on two villages located several kilometers apart on the Czech and German sides of the Bohemian Forest. The methodology involved repeating, simultaneously, two equally long walks multiple times a day, in order to assess and compare the spatio-temporal variability of aerosol on the two rural sites. Our hypothesis was that on the Czech side PM concentrations would be higher than on the German side due to a presumed lower quality of local heating and that there would be a noticeable spatio-temporal distribution of aerosol due to various domestic heating sources.

Manuscript 3

This manuscript aligns with prior studies within this thesis, focusing on using an innovative mobile measurements approach to assess air quality in suburban locations.

Employing a novel tethered helium-filled balloon, we added an additional dimension and we aimed to evaluate the impact of atmospheric temperature inversion on the overall PM concentrations within the Kladno-Švermov district, which is constantly monitored by the Czech Hydrometeorological Institute (CHMI) due to the high concentrations of benzo[a]pyrene and PM in this area.

Throughout a month-long measurement campaign, the primary aim was to track the altitudes where inversion layers occurred. Additionally, our investigation aimed to identify scenarios where the inversion layer descended below the valley's top, potentially inducing the so called 'pot lid effect.' Such a phenomenon might prevent the dispersion of emissions from local heating sites within the valley, thereby influencing the overall air quality in the area.

Manuscript 4

This study highlights the critical role of spatio-temporal distribution data in conducting source-apportionment analyses within urban and suburban areas in a critical European air pollution hot spot —the Ostrava region. This study specifically targeted this region due to the extremely complex ambient aerosol composition, influenced by many local and regional sources, including the presence of a significant metallurgical industrial complex near Ostrava-Radvanice, long-range transport, alongside observed issues with local heating and other sources, affected by meteorology. Distinguishing between these sources was a primary focus.

Specifically, by employing the Positive Matrix Factorization (PMF) method utilizing both aerosol elemental composition and particle number size distributions, this research successfully identified primary pollution sources and their respective impacts on urban (Ostrava-Radvanice) and suburban (Ostrava-Plesná) air quality within the Ostrava region.

The detailed air quality monitoring and sources identification carried out in this area hold valuable significance for implementing mitigation strategies.

Manuscript 5

This study, which complements *Manuscript 4*, investigates the temporal variability of carcinogenic polycyclic aromatic hydrocarbons (c-PAHs) concentrations in PM and their genotoxicity. The sampling of aerosol for PAHs analysis, gravimetry and genotoxic study occurred in Ostrava-Radvanice as part of a winter measurement campaign. The primary focus of this study was to examine the temporal variability of c-PAH concentrations and their genotoxicity within an aerosol segregated into four particle size fractions. By assessing which size fractions these carcinogenic PAHs primarily bound to and elucidating their genotoxic effects, this research aimed to provide crucial insights into potential health implications and aid in source mitigation strategies.

Manuscript 6

Due to the complexity of the composition and behavior of aerosols in the atmosphere and all the ongoing chemical processes, it is almost impossible to study and compare some of the individual fundamental phenomena in the atmosphere. For this reason, the final manuscript of this thesis is a laboratory experiment where individual factors can be reduced to the minimum. The focus was on investigating the toxicological effects of anthropogenic and biogenic secondary organic aerosol (SOA) typical for urban areas and remote locations. The primary aim was to investigate how atmospheric aging influences particle toxicity and whether there is a difference between biogenic SOA precursors (β-pinene) or anthropogenic precursors (naphthalene).

To achieve this, laboratory experiments were designed using a source of soot particles, an oxidation flow reactor chamber to simulate aerosol aging by photochemical reactions, measurement systems for physical and chemical characterization of the aerosol, and Air-Liquid Interface (ALI) cell exposure systems for studying toxicity using living cell cultures.

4.2. Major results and findings

4.2.1. Manuscript 1

In *Manuscript 1*, a self-made experimental system for mobile measurements was developed (*Figure 4*). The system comprises of a water-proof 71-liter aluminum box with external dimensions of L 59.5 × D 39.0 × H 38.0 cm, which is used sideways with opening to the left side. For an active ventilation, two computer fans, with a 25 cm diameter, were installed at the rear, covered by a rain-proof grids. The upper fan has been designed to vent out hot air, while the lower fan ensures air circulation by operating in the opposite direction. The design enables temperature regulation inside the box, maintaining the optimal operational temperature for the instruments. The temperature monitoring also prevents condensations (as operational instruments naturally generate heat) and minimizes losses of volatile and semi-volatile compounds during sampling. The box is equipped with three shelves, two of which are adjustable to accommodate varying equipment sizes. These shelves are interconnected through short conductive tubes leading to **omni-directional inlets (801565, TSI, USA)** strategically positioned at the breathing zone level.

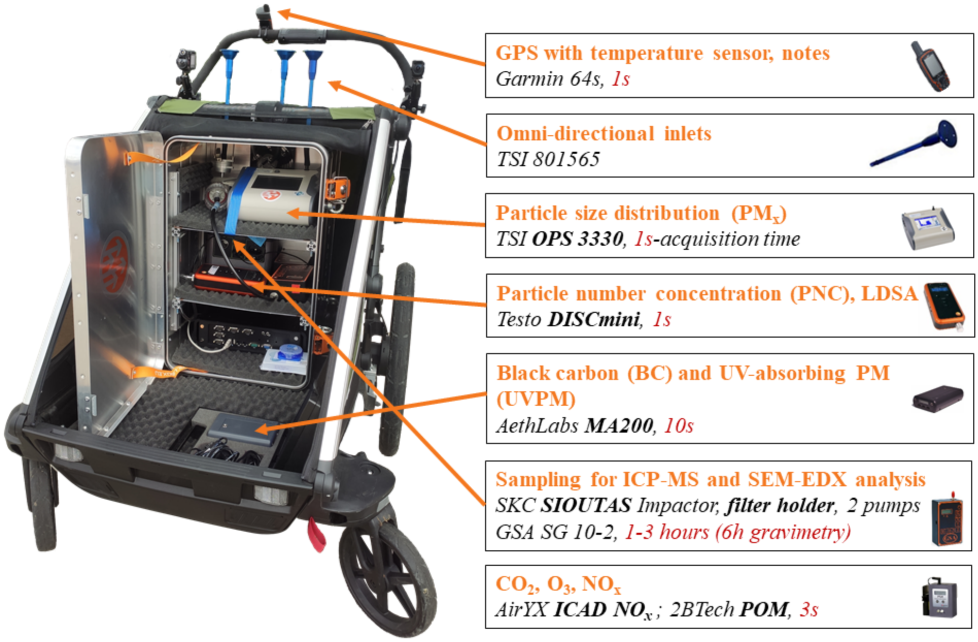

Figure 4: Self-made experimental system for mobile measurements (Bendl et al., 2023).

The **OPS 3330** (*Section 2.1.1.*), the **Sioutas cascade impactor** and/or the **filter holder** (*Section 2.2.2.*) were placed directly under the inlets to prevent particle losses. **DISCmini** (*Section 2.1.2.*) and **MA200** (*Section 2.1.3.*) were situated on the shelf below, as nanoparticles and sub-micrometer particles are not so sensitive to losses in tubing. The **GPS unit** (*Section 2.5.*) mounted on the handlebar was used to link the concentrations with GPS coordinates and served also as navigation and monitored various parameters including speed, distance and outside temperature. Throughout the study, all the data were acquired at 1-second resolution, except for the MA200, which captured data at a 10-second resolution and conducted cumulative sampling lasting 1-6 h.

The experimental aluminum box demonstrates its adaptability through the diverse configurations investigated within this thesis. It can be mounted in a modified **child carrier** (**Cab 2, Thule, Sweden**), which is cushioned and equipped with foam to absorb vibrations and used either as a stroller (*Figure 4*) or as a bicycle trailer when attached to a bicycle. While the stroller configuration offers enhanced clearance, the bicycle trailer configuration provides a faster speed and therefore higher measurements efficiency and a larger mapping area. However, the potential effect of dust resuspension behind the bicycle must be taken into account. Alternatively, the entire box can also be placed in a frame rucksack and carried on the back. This arrangement was also used during the subway rides. This is a third version of the experimental trolley. The first version was designed in Prague to measure children's exposure to PM in a bicycle trailer (*manuscript in preparation*, *part of a bachelor thesis* (Nechvátalová, 2019)). Subsequently, a slightly less compact second version, was used in studies conducted in Augsburg (Liu et al., 2023) and in Železná Ruda and Bayerisch Eisenstein (*Manuscript 2*).

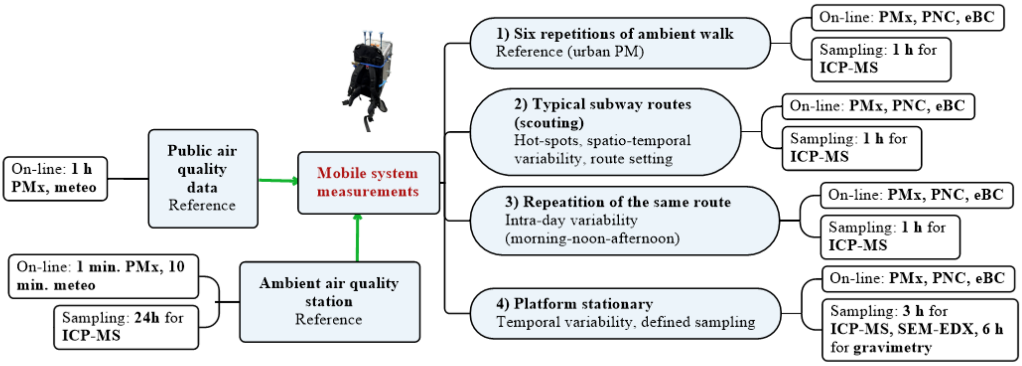

Figure 5: Strategy of measurements and sampling of the subway micro-environment using the mobile measuring system; PNC particle number concentration; PM particulate matter; eBC equivalent black carbon; ICP-MS inductively coupled plasma mass spectrometry (Bendl et al., 2023).

In *Manuscript 1*, a proposed methodology for mobile air quality monitoring within subway systems is outlined, designed to be adaptable across various subway systems worldwide (*Figure 5*). This methodology comprises several key steps:

1. **Ambient walks**: repeating typical urban/suburban ambient walks to compare indoor and outdoor concentrations;
2. **Subway measurements and mapping**: various measurements and mapping strategies within the subway environments to identify hot-spots, spatio-temporal variability of pollutants and define a typical subway route (scouting);
3. **Intra-day variability assessment**: conductions multiple repetitions of a typical subway trip several times a day to determine intra-day variability;
4. **Stationary platform measurements**: using a mobile system for measurements on selected subway station platforms to evaluate the stability of concentrations and factors affecting them.

Sampling for gravimetric analysis is necessary to correct OPS data by accounting for the effective particle density of PM in the subway. Throughout these procedures, the inclusion of reference outdoor monitoring stations plays a crucial role in ensuring data quality and facilitating accurate interpretations.

The experimental phase of this study involved measurements in the Munich subway and ambient measurements of the suburban background as a reference. Our findings revealed a substantial exposure to PM for subway passengers in Munich. Specifically, travelling on the subway meant notable exposure to the coarse aerosol fraction of PM, with values reaching up to 200-300 $\mu g.m^{-3}$ in PM_{10} fraction and up to 80 $\mu g.m^{-3}$ in $PM_{2.5}$ respirable fraction.

During repetitions of typical rides, we observed that spatial variability held more significance than temporal variability. PM concentrations exhibited a gradual increase from the terminal station to the city center and the air exchange between the tunnel and the interior of the subway was high. The dynamics of aerosols inside the subway were so fast that changes can be observed instantaneously when the doors are opened and closed with a one-second resolution. Surprisingly, no significant difference was observed between the old train with passive window ventilation and the new train with active ventilation, suggesting no air filtration systems.

PM hot-spots were particularly prevalent in the larger transfer stations. We noted substantial differences in concentrations between stations, primarily influenced by train frequency. However, factors such as ventilation and station design also played roles in affecting these concentrations.

Stationary PM measurements performed at the station platforms showed concentrations relatively stable concentrations, but distinct peaks were evident during the arrival and departure of trains, signifying the swirling and resuspension of particles at these moments.

The off-line ICP-MS analysis (*Section 2.3.2.*) revealed that the aerosol mass was dominated by iron, ranging from that from 69% to over 90%. Subsequently, SEM-EDX analyses (*Section 2.3.3.*), employing both manual and novel automatic particle classification, enabled the visualization of particles and based on single-particle analysis they were found to be predominantly iron oxides, specifically corrosion products from abraded subway tracks and wheels in the form of micrometer-sized flakes. Interestingly, the analysis also identified round iron oxide nanoparticles, potentially posing a health risk.

Total particle number concentrations were not significantly elevated in the subway compared to ambient air, but sporadic instances of PNC from traffic entering the subway via platform entrance were observed.

The eBC measurements showed a high correlation with PM_{10}, indicating the ability of the micro-aethalometer to identify PM_{10} hot-spots. Nevertheless, the absence of major BC sources in the subway led to the conclusion that the observed correlation was likely an artifact due to light-absorbing iron oxide containing PM. Measurements of ozone, CO_2 and NO_x were performed beyond the scope of this study and not specifically addressed in this context.

Notably, certain stations exceeded WHO guideline values for $PM_{2.5}$, indicating a potential health-risk associated with these aerosols, especially in the case of prolonged exposure. Consequently, several measures were proposed to mitigate these risks: installation or improvement of filters in the ventilation system of new subway cars; installation of portable air purifiers in driver's cabins; improvement of metro ventilation to prevent the intrusion of particles from traffic and mapping of the metro according to the proposed methodology for effective pollution control and mitigation.

4.2.2. Manuscript 2

This study focuses on evaluating the spatio-temporal distribution of aerosol in a rural environment using novel mobile systems developed within the framework of this thesis. Two identical mobile measurement systems were designed and built (described in the *Section 4.2.1.*) and used to perform simultaneous daily walking measurements from 5 am to 10 pm in two neighboring villages of Železná Ruda (ŽR) on the Czech site of the border and Bayerisch Eisenstein (BE) on the German site in a four days intensive measuring campaign. In contrast to *Manuscript 1*, a pair of identical **DustTrak DRX 8532** and **PTrak 8525** (*Sections 2.1.1. and 2.1.2.*) instruments were used to measure PM_{10}, $PM_{2.5}$ and PM_1 and PNC, respectively. The BC monitor was an identical **MA200** (*Section 2.1.3.*), as well as the GPS unit. In addition to notes, point-of view **cameras Tough TG Tracker (Olympus, Japan)** were used to optically identify sources. To ensure comparability, the instruments were collocated with each other and a portable weather station **WMR300** (**Oregon Scientific, USA**) was strategically placed between the villages. This was a novel approach of comparison of two villages.

During the entire campaign, the average concentrations of PM_1, $PM_{2.5}$ and PM_{10} were consistently higher in ŽR on the Czech side, aligning with our initial hypothesis, in contrast to German BE. For example, the average PM_{10} concentration was 37 ± 108 $\mu g.m^{-3}$ in ŽR, while in BE it was 16 ± 27 $\mu g.m^{-3}$ which is more than twice higher. The observed average PNC were 5024 ± 2346 $pt.cm^{-3}$ in ŽR, while in BE it was 4190 ± 1340 $pt.cm^{-3}$. However, despite these average differences between the sites, both locations exhibited substantial spatio-temporal variability in PM, PNC, and BC concentrations throughout the study period. The variability was both between and within days. Higher concentrations were particularly notable during late afternoon and evening periods, coinciding with the initiation of domestic heating, especially biomass burning. During these periods, the primary sources of air pollution were localized, stemming primarily from domestic heating activities and local traffic. Elevated concentrations of PNC and PM from traffic were then observed, notably in the proximity of the main road when mainly cross-border transit traffic was increased. In general, aerosol particles were predominantly submicron, with 90% of $PM_{2.5}$ consisting of PM_1 particles. The highest concentrations were recorded during period characterized by low wind speeds and high humidity, indicating stable atmosphere with low dispersion capacity. Consequently, meteorological conditions notably influenced the observed variations in pollutant concentrations.

Our results align with the assumption that there are multiple sources of emissions originating from local heating plants in Železná Ruda, potentially indicative of poorer quality boilers, fuel, or service. At the same time, these findings might suggest that in the Czech Republic there is a higher reliance on domestic heating stoves for primary heating, whereas on the German side, these may be predominantly used for leisure, for example in the form of fireplaces. However, a detailed investigation of the reasons why air quality is worse on the Czech side would require further research.

The approach of employing mobile systems for air quality measurements in villages demonstrated its effectiveness by covering a majority of areas and capturing spatial-temporal variability in aerosol concentrations. Such measurements are particularly valuable during the heating season, when adverse meteorological situations occur along with increased pollution sources. Although significant numbers of people live in villages, there are few permanent air quality monitoring stations. Yet, especially in the winter months during the heating season, PM concentrations above the limit can be measured at some locations or in a micro-scale, mainly due to domestic heating sources, which is difficult to regulate and control, together with the unsuitable geomorphology with the frequent temperature inversion situations. Risk areas could be identified using GIS and plot in maps. These are mainly mountainous areas and valley sites. Due to the high spatial variability, citizens living close to a significant source of emissions from a local heating may be exposed to high aerosol concentrations over a long period of time, although the average concentrations in the village may be below the limit.

4.2.3. Manuscript 3

According to official measurements and modelling by the Czech Hydrometeorological Institute (CHMI), the highest concentrations of benzo[a]pyrene (B[a]P, a carcinogenic PAH) in Bohemia in the Czech Republic are regularly measured in the district of Kladno-Švermov, about 30 km NW of Prague. The CHMI monitoring station is situated in the residential area in the middle of the square so the classification of the station is urban background. Between 2008-2018, annual B[a]P average concentrations were always exceeding the EU target value 1 ng.m^{-3} and were among the highest in the Czech Republic (Schreiberová et al., 2020). For these reasons, we carried out a comprehensive measurement campaign near this station in winter 2016 to investigate air quality and the sources of pollution. The monitoring station of the Laboratory for Air Quality Research was located near the football field, from which we also carried out several days of unique flight measurements using a remote-controlled airship. At the same time, we conducted walking measurements with mobile devices within this district. During this campaign, we observed locally elevated concentrations of PM and other pollutants with peak concentrations of PM$_{2.5}$ up to hundreds of micrograms per m^3 (unpublished data). Concurrent measurements during the campaign showed average concentrations of PAHs 25.5 ng.m^{-3} in the PM$_1$ fraction, with PM$_1$ average concentrations of 34.2 µg.m^{-3} (Křůmal and Mikuška, 2020). As part of this campaign, the innovative study (*Manuscript 3*) was conducted to test our hypothesis regarding the significant contribution of local temperature inversions to the overall elevated concentrations of particulate matter (PM). A special 2.3 m^3 helium-filled tethered balloon was constructed for this study. It was made of lightweight materials for parachuting and 300 m long Dyneema rope. This design facilitated the carriage of professional weather probe, POV camera and other lightweight instruments, while at the same time it was storable thus minimizing helium consumption. For this reason, the balloon remained continuously inflated throughout the campaign. We measured temperature, pressure and relative humidity at a resolution of 4 Hz using a **professional radiosonde** (**Vaisala, Finland**) designed for weather balloons due to the need for extremely fast sensor response. However, we have adapted it to allow recording on an SD card, enabling repetitive measurements. The exact height assignment for the measured values were calculated according to the Wallace and Hobbs equation for the dependence of height on atmospheric pressure difference (Wallace and Hobbs, 2006).

A total of 53 temperature and humidity profiles were made up to an altitude of 150-300 m. We confirmed the occurrence of frequent temperature inversions in the planetary boundary layer (PBL), primarily observed during early morning and evening hours. Additionally, recurrent inversions occurred at heights up to 50 m, coinciding with the height of the valley where the urban area is located. Correspondingly, PM$_{10}$ and PM$_{2.5}$ concentrations were above the health limits during these occurrences, with local heating identified as the primary source. In this situation, limit air movement prevent locally generated pollutants from dispersing, and at the same time nearby sources such as industry can be almost excluded. Repeated vertical profiles revealed the considerable dynamics of PBL and the importance and significance of meteorological conditions, especially in valley or otherwise closed areas where the lid over pot effect may occur. Using a simplified calculation method based on estimated valley volume and boiler emission factors, we calculated (out of the scope of this paper) that only a few outstanding emitters can raise average PM_{10} concentrations to above the limit in a single day. Several extreme emitters were documented during the measurement campaign, thus the spatio-temporal variability of aerosol in the area was significant. From this, possible different health effects according to different exposure of the population can be deduced. According to these findings, it can be assumed that some of the highest measured values in the Czech Republic are attributed to the city of Kladno mainly because of the location of the CHMI station. Thus, it is not that the concentrations are exceptional, but rather that similar common locations are not captured by the network measurements of the CHMI stations. Therefore, even models based on station measurements may underestimate concentrations in similar, predominantly rural locations. It would therefore be advisable to focus more attention on similar locations and micro-environments where a significant number of people live.

PBL measurements of temperature-humidity profiles have proven to be a suitable complement to stationary air quality measurements, allowing better interpretation of the measured data.

This manuscript gained a notable attention, evident from its 2282 reads on the ResearchGate on-line portal as of 17 December 2023 (Bendl and Hovorka, 2017), indicating increased interest in the topic.

4.2.4. Manuscript 4

The most polluted area in the Czech Republic in terms of PM and benzo[a]pyrene (B[a]P) emissions is the Moravian-Silesian region. According to long-term monitoring, it is a European hot-spot for PM. The highest concentrations of B[a]P in the Czech Republic are regularly measured in the Ostrava-Radvanice district (GPS 49°48'39.666"N, 18°20'16.300"E). Annual average B[a]P concentrations are often exceeding the annual limits of 1 $ng.m^{-3}$, e.g. in 2021 it was by more than 6 times (CHMI, 2023). For these reasons, in 2012 and 2014 we conducted intensive monthly winter measurement campaigns in the Ostrava-Radvanice urban area using the monitoring station of the Laboratory for Air Quality Studies (Institute for Environmental Studies, Charles University) to investigate spatio-temporal variability of aerosol and to identify key pollution sources. In 2012, smog and post-smog periods were recorded. During the smog, the median of $PM_{2.5}$ concentrations was 106 $\mu g.m^{-3}$ and PM_{10} reached up to 400 $\mu g.m^{-3}$ (Hovorka et al., 2012) and the 24-h average of B[a]P was up to 32 $ng.m^{-3}$ (Bendl, 2014).

In the 2014 campaign, we did not experience such a smog situation, so the median PM concentrations were relatively lower, but still concerning. In Radvanice, we measured an average concentration of PM_{10} of 61.5 ± 8.7 $\mu g.m^{-3}$, which exceeded health limits. In addition, we conducted simultaneous measurements in the suburban area of Ostrava-Plesná, 16 km far away from Ostrava-Radvanice and the industrial sources, in order to compare their influence. At this location, the average PM_{10} concentrations at the same time were 29.2 ± 4.5 $\mu g.m^{-3}$, i.e. about twice lower. This study complements previously published results from these locations (Kozáková et al., 2019; Leoni et al., 2018; Pokorná et al., 2015).

In this study, the Positive Matrix Factorization (PMF) was performed firstly on the basis of the hourly elemental composition of the aerosol obtained with the rotating drum impactor (RDI) followed by the S-XRF analysis (*Sections 2.2.1., 2.3.2.*) and secondly using the particle number size distribution (PNSD) measured by the SMPS (*Section 2.1.2.*), in 15 min. integrates. Essential parameters such as meteorological data, organic and inorganic markers were incorporated. Levoglucosan, mannosan and galactosan, and cations and anions in PM_1 fraction were sampled on quartz fiber filters (Whatman QMA) using an LVS-3 sampler in Ostrava-Plesná and in Ostrava-Radvanice by a high-volume sampler DHA-80 (Digitel, Switzerland; *Section 2.2.*) and subsequently analyzed using the system Dionex ICS-5000+ (*Section 2.3.2.*). Elemental and organic carbon were measured semi-online using the OC/EC analyzer (Sunset Laboratory, USA). Simultaneously, meteorological data were recorder at both sampling sites. Through repetitive PMF analyses with varying settings, factors were iteratively established to achieve an optimal fit with the measured data.

Generally, the PMF revealed predominant sources in the $PM_{0.15\text{-}1.15}$ fraction. In Ostrava-Radvanice, the major contributors were identified as domestic heating and the metallurgical industry. Conversely, in Ostrava-Plesná, residential heating, industry and traffic contributed to the majority of the particle number concentration.

PMF based on chemical composition had uncertainties of 17.9% and 13,5% for Ostrava-Radvanice and Ostrava-Plesná, respectively. In Ostrava-Plesná, six distinct factors were identified: 1) coal combustion, 2) mixed factor - secondary organic aerosol (SOA) and biomass burning, 3) re-suspended dust, 4) raw iron production. In Ostrava-Radvanice, four PMF factors were assigned: 1) mixed factor - SIA and coal combustion, 2) residential heating, 3) raw iron production and 4) sinter/steel production.

This manuscript provides in-depth description of each identified factor at both locations and discuss their elemental compositions, origins and correlations with meteorological data. Subsequently, a comparative analysis between the two locations was conducted using Pearson correlation coefficients for the identified factors. Since the correlations were weak, it was concluded that these were different sources and that meteorology and local orography played a significant role.

PMF based on PNSD assigned six factors in Ostrava-Plesná: 1) residential combustion, 2) urban background, 3) traffic/metallurgical industry, 4) regional pollution, 5) residential heating/re-suspended dust. In this PMF model, the PNSD were not normalized for calculations, while the output was provided in normalized particle number distribution (NSD) $dN/DlogD_p$ and volume size distributions (VSD) $dV/DlogD_p$. Contributions of each factor to NSD and VSD were discussed, as well as correlations to factors assigned by elemental analysis and the influence of meteorology and other factors was evaluated. In Ostrava-Radvanice, six factors were identified and discussed within the previous study (Leoni et al., 2018). It was 1) industrial ultrafine particles 2) mixed source industrial and fresh road traffic nanoparticles, 3) urban background, 4) coal burning, 5) regional pollution and 6) industrial coarse particles/road dust. Data were used for correlation with the PMF based on the chemical analysis. Similar to the first PMF approach, two sites were compared and moderate correlation was observed between the coal combustion factor in Ostrava-Radvanice with the local residential combustion (r=0.68) in Ostrava-Plesná and with the regional pollution (r=0.52) in Ostrava-Plesná. Regional pollution factors at both sites moderately correlated with each other (r=0.53).

This manuscript investigated the spatio-temporal variability of winter aerosol in an urban and suburban location with an extremely complex ambient aerosol composition, influenced by many local and regional sources, including heavy metallurgical industry, long-range transport, meteorology and the unfavorable orography of the Ostrava Basin. The PMF method proved to be suitable for source-apportionment of these sites, especially the presented combination of PMF based on PNSD and elemental composition of $PM_{0.15-1.15}$. The moderate-strong correlation between them was observed in Ostrava-Radvanice but in Ostrava-Plesná the correlation was weak. This indicates a different source contribution to the number and mass of particles. Meteorology and orography were found as an important factor.

4.2.5. Manuscript 5

Polycyclic aromatic hydrocarbons (PAHs) pose significant health-risk in both urban and rural air. While benzo[a]pyrene (B[a]P) is extensively monitored due to its high carcinogenicity, other concerning carcinogenic PAHs (c-PAHs) exist, including: benz[a]anthracene (B[a]A), chrysene (CHRY), benzo[b]fluoranthene (B[b]F), benzo[k]fluoranthene (B[k]F), B[a]P, dibenz[ah]anthracene (DB[ah]A), ideno[1,2,3-cd]pyrene (I[cd]P). These c-PAHs have the ability to bind to aerosol particles across various size fractions. However, routine analysis and monitoring protocols for PAHs primarily focus on cumulative PM_{10} or $PM_{2.5}$ fraction without knowing their distribution and often limiting solely to the analyses of B[a]P.

This study, as a complementary to *Manuscript 4*, focuses on exploring the temporal variability of these seven c-PAHs and their distribution among four distinct aerosol size fractions. Additionally, brief consideration is given to the sampling and sample preparation methodologies pertinent to the subsequent chemical and instrumental analysis and genotoxicity assessment.

Atmospheric aerosol sampling for gravimetric, chemical analyses, and genotoxicity studies were conducted within a winter measurement campaign in 2012 in Ostrava-Radvanice. The 26 days-long 24-h sampling was performed using a High-Volume Cascade Impactor BGI 900 (*Section 2.2.1.*) into 4 size fractions: coarse (1 – 10 μm), upper accumulation (0.5 – 1 μm), lower accumulation (0.17 – 0.5 μm), which were sampled on the polyurethane foam (PUF), and the last quazi-ultrafine fraction (qUF; <0.17 μm) sampled on a Teflon backup filter.

Preparation of PUF substrates for sampling was a meticulous process (due to the porosity of the material) involving several steps to ensure purity for chemical and toxicological analyses, accuracy and consistency in the gravimetric measurements. This included sequential leaching in deionized water, methanol (MeOH), and dichloromethane (DCM) in an ultrasonic bath. Prior to each weighing, PUF substrates and samples were conditioned to 50% humidity and 21°C in desiccators in a conditioned weighing room (*Section 2.3.4.*). Afterwards, both PUFs and filters were extracted in DCM, and the extractable organic matter (EOM) underwent HPLC analysis with fluorescence detection for c-PAHs, with concentration calculated in both ng.m^{-3} of sampled air, as well as ng.mg^{-1} of aerosol for each fraction.

For toxicological studies focusing on genotoxicity, dioxin-like activity, and oxidative DNA damage, the EOM was evaporated under a stream of N_2 and dissolved in dimethyl sulfoxide (DMSO). Please note, specific details of the genotoxicity study exceed the thesis scope and will not be further addressed here.

During the sampling, PM_{10} mean was around 90 μg.m^{-3} and the health limit of 50 μg.m^{-3} was exceeded in 21 out of 26 days. Over the whole period, we observed a variability between the aerosol mass distribution among the sampled fractions. However, on average, the majority of aerosol mass (36.3 μg.m^{-3}) were in the upper accumulation fraction, while 15.6 μg.m^{-3} were in lower accumulation fraction, 12.8 μg.m^{-3} in q-UF fraction and 27.3 μg.m^{-3} in the coarse fraction. At the same time, concentrations of c-PAHs in the upper accumulation fraction were 45.5 ng.m^{-3}, 20.6 ng.m^{-3} in the lower accumulation fraction, 11.9 ng.m^{-3} in the fine fraction and 26.3 ng.m^{-3} in the coarse fraction. Therefore, c-PAHs concentrations per sampled aerosol mass were similar for upper and lower accumulation fractions (1278 and 1322 ng.mg^{-1}, respectively), which could suggest the same origin of c-PAHs in these fractions, while for the qUF fraction the concentration per aerosol mass was lower (957 ng.mg^{-1}), as well as in the coarse fraction (885 ng.mg^{-1}). A high correlation between PM and c-PAHs was observed, especially in the coarse fraction (R=0.83). The weakest correlation (R=0.51) was in the ultrafine fraction. During the smog period, the highest concentrations of PM were recorded on 12 February 2012 and during this day, the percentage of the qUF fraction in PM_{10} increased significantly up to 31%.

Regarding the genotoxic potential analysis, the lower accumulation fraction had the highest efficiency in binding compounds forming DNA-adducts. However, there was rather uniform distribution of the genotoxic activity per aerosol mass among different size fractions. The oxidative DNA damage was interestingly highest during the sampling day, when the PM concentrations were the lowest. High dioxin-like activity was observed during the campaign, mainly in the upper accumulation fraction. The variability between days was high.

This study showed a high day-to-day variability of 7 c-PAHs within the measurement campaign and its distribution to different aerosol size-fractions. The upper accumulation fraction (0.5 – 1 μm) was the largest carrier of PM and c-PAHs, with about 40% of c-PAHs in PM_{10}. It is notable that particles smaller than 1 micrometer can easily penetrate the lung chambers (*Section 1.2.*). The qUF fraction of the aerosol carried about 30% less c-PAHs per aerosol mass. The upper accumulation fraction was also the major carrier of genotoxicity and dioxin-like activity. Oxidative DNA damage did not show clear dependance on the PM size fraction and c-PAHs and a possible reason of antioxidants in EOM was discussed. This study also confirmed that simple monitoring of $PM_{2.5}$ and PM_{10} fractions are not sufficient to estimate aerosol toxicity.

4.2.6. Manuscript 6

This Manuscript contains a solely laboratory aerosol experiment (*Section 2.6.*). The aim was to compare the toxicological effects of a secondary organic aerosol (SOA, *Sections 1.4., 1.5.*) with typical biogenic (β-pinene) and anthropogenic (naphthalene) gaseous precursors using the Air-Liquid Interface (ALI, *Section 2.7.*). β-pinene is a monoterpene often released by coniferous forests and other vegetation as a biogenic VOC, while naphthalene is a two-ring volatile PAH generated mainly in combustion processes (engines, biomass burning, industry), often present in urban and rural areas.

The experimental setup included a CAST soot-particle (SP) propane generator, producing EC-rich particles (*Section 1.4.*) of 100 nm mode. The diluted particles were subsequently mixed with vapors of naphthalene or β-pinene produced in a diffusion source located in a hot water bath. This system could be regulated to obtain a stable desired concentration of these gaseous precursors, which concentrations have been verified by FID on-line measurements (*Section 2.3.1.*). Subsequently, the mixture was humidified, D9-butanol was added as a tracer, and a final concentration of 1 $mg.m^{-3}$ soot particles, 4 $mg.m^{-3}$ VOCs, and 80 ppb D9-butanol at 40% moisture entered the potential aerosol mass reactor (PAM). We used an oxidation flow reactor (OFR) that simulates photo-oxidative aging of aerosol using OH radicals. Hydroxyl radicals were generated in situ from O_3 reactions. O_3 was produced from irradiation of wet aerosol by UV lamps (185 and 254 nm). The lamps were set so that photochemical aging corresponding to 3 days in the real atmosphere and the aerosol residence time was 113 seconds in the reactor. O_3 produced inside the reactor was then removed to a level <10 ppb using a ceramic honeycomb denuder, impregnated by $NaNO_3$. The aerosol was diluted with ejector diluters so that it was at optimal concentrations for the instrumentation and for the ALI systems. To avoid contamination, dilution was performed using VOC- and particle-free compressed air. This was done using a particle-free compressor with filters, a pressurized air tank and a system for VOC removal (Aadco, *Section 2.6.*). For physicochemical characterization of aerosol, SMPS, aethalometer, TEOM, experimental instrument for ROS measurement, AMS were used (*Sections 2.1.2.-4.*). PTR-MS (*Section 2.3.1.*) was used to measure D-9 butanol to calculate equivalent of photochemical age. Ozone was monitored using APOA 350E (Horiba) analyzer. Aerosol was also sampled in $PM_{2.5}$ fraction on quartz filters for further analysis of OC/EC analyzer (2001A, Desert Research Institute) and for chemical SOA characterization using advanced analytical platforms such as DIP-HR TOF MS (Pegasus GC-HRT 4D, Leco) and comprehensive two-dimensional GC analysis GC×GC-TOF MS (Pegasus BT 4D GC×GC, Leco) combined with direct thermal desorption (DTD). Special samples were taken also for the TEM analysis (*Section 2.3.3.*).

SOA-containing aerosol was also guided towards two ALI exposure systems (*Section 2.7.*). Each contained 3 Vitrocell modules with 6 inserts for aerosol exposure of cell cultures. Two modules were used as replicates, while the third was blown with pure air as a control. Above each insert was a so-called trumpet to allow uniform distribution of humidified aerosol/air (100 $mL.min^{-1}$), which was deposited on living cells in a 37 °C medium mainly by diffusion and sedimentation. Two live cell lines that were pre-cultured in an incubator were used for this study: 1) A549 human alveolar epithelial cells, 2) EA.hy926 hybrid human endothelial cells for mono- and co-culture experiments. After necessary preparation and care, the cells were exposed to aerosol for 4 hours. The first ALI system used undiluted aerosol and the second 1:30 diluted to cover real atmospheric conditions. After exposure, several assays were then performed to determine the condition of the cells (*Section 2.7.*).

SOA from both precursors had similar BC and OC concentrations, for naphthalene SOA SP (SOA_{NAP}-SP), the total OC was 1.1 $mg.m^{-3}$, while β-pinene SOA SP ($SOA_{\beta pin}$-SP) 1.0 $mg.m^{-3}$ from the original SP OC content of 0.3 $mg.m^{-3}$. Geometric mean of particle size was also similar for both aged SOA and was not significantly changed from original soot particles (SP). TEM showed soot agglomerates coated by organic material, while both SOA agglomerates were less fractal in shape than SP. Particle number concentration for SOA_{NAP}-SP was slightly increased compared to $SOA_{\beta pin}$-SP and only for $SOA_{\beta pin}$-SP, a nucleation of small number of around 50 nm particles was observed. Chemical analysis based on the use of GC×GC and DIP-HR-TOF MS methods revealed significantly higher amount of aromatic and heterocyclic structures for SOA_{NAP}-SP than for $SOA_{\beta pin}$-SP, which had higher amount of unsaturated cyclic and saturated cyclic and non-cyclic compounds. This was in line with the observation of lower H/C ratio for SOA_{NAP}-SP.

Cells exposures showed that the viability of cells was not significantly affected by the biogenic $SOA_{\beta pin}$-SP, as well as the pure SPs and controls. However, the anthropogenic SOA_{NAP}-SP caused 40% cell viability for the undiluted aerosol and 70% viability for 1:30 diluted aerosol. The higher concentration of H_2O_2 indicating the oxidative stress were measured in the SOA_{NAP}-SP aerosol (14.1 $\mu mol.m^{-3}$ in undiluted aerosol vs. 3.6 $\mu mol.m^{-3}$ in undiluted $SOA_{\beta pin}$-SP) with a possibility of secondary genotoxic effects.

We found out, that the atmospheric aging of soot particles can cause significant increase in aerosol toxicity. Moreover, SOA coated by condensed naphthalene as anthropogenic SOA precursor decreased cell viability, increased oxidative stress, genotoxicity and induced angiogenic and inflammatory responses, compared to biogenic SOA precursor β-pinene. The responsible compounds for the toxicity of SOA_{NAP}-SP might be the oxidation products of aromatic compounds, namely hydroxyhexadienyl-type radicals from naphthalene and the products 2-formylcinamaldehyde, 1-naphthol, 2-naphthol and naphthoquinones. Aromatic structures itself are also known for its toxicity, but degree of oxidation might increase the toxicity. We also observed that toxicological studies with co-cultures might be more realistic. This study highlights the importance of a comprehensive chemical analysis of aerosol and consideration of the atmospheric effects of aerosol aging on its health effects.

A follow-up study published in *Environment International*, which is not included in the thesis, focused on the cytotoxicity of human bronchial cells (BEAS-2B) in the same experiment (Pardo et al., 2022).

4.3. Conclusions

In this thesis, spatio-temporal variability of atmospheric aerosols in inhabited areas have been in-depth investigated, covering methodology, physical-chemical composition and implications for human health.

The mobile measurement systems developed and validated within this study (*Manuscript 1 and 2*) have emerged as valuable tools capable of capturing these dynamics, identifying pollution sources and hot-spots. Furthermore, the study demonstrated that mobile measurements can complement stationary monitoring by adding a spatio-temporal dimension to datasets, ensuring the representativeness of monitored sites, especially important when capturing long-term trends.

The proposed approaches mark a significant starting point for implementing targeted mitigation strategies, crucial for overall air quality improvements.

The research focused also on the application of such methods in inhabited areas with complex geomorphology, such as often-neglected rural and suburban locations with decreased air quality. In these areas, the vertical profiling of temperature and relative humidity using tethered-balloon facilitated data interpretation and highlighted the impact of temperature inversions on the local air quality (*Manuscript 3*).

Within *Manuscript 4*, the PMF analysis identified air pollution sources in complex urban air. Simultaneous winter-time measurements at two urban and rural locations in the Ostrava region, highlighted significant dynamics of aerosol and its variability, identified the metallurgical industry and residential combustion as key pollution contributors in the studied area and importance of the local meteorology and orography. Furthermore, the comparison between different PMF analysis based on elemental composition and on aerosol number size distributions provided critical insights.

Manuscript 5 focused on the diurnal variability and distribution of particle-bound carcinogenic PAHs and their toxicity in 4 different aerosol size fractions in Ostrava, which has been shown to be substantial information for assessing its potential health effects.

In the last *Manuscript 6*, the impact of secondary organic aerosol (SOA) on toxicity was examined. This involved comparing SOA produced by urban air's typical combustion-related precursor, naphthalene, with rural/natural background air's β-pinene from coniferous trees. Notably, anthropogenic SOA exhibited significantly higher toxicity than biogenic SOA.

In conclusion, both long-term air quality monitoring and intensive comprehensive measurement campaigns with high temporal resolution for source identification are necessary to understand the air quality in a given location, to identify sources and finally for effective mitigations. As the spatio-temporal variability of aerosol is significant at all urban and rural locations, mobile measurements are useful tools for detecting personal exposure and identifying specific sources, even in indoor locations that are often underestimated.

The future outlook in aerosol spatio-temporal variability research includes advancements such as miniaturization, automation, and enhanced accessibility of mobile instrumentation. There is a concurrent need for additional progress in real-time analytical platforms and the improvement of low-cost sensors for extensive deployment in both ambient and indoor air environments. Furthermore, the implementation of automation, machine learning, and advanced modeling techniques to enhance data processing.

5. References

Abdalmogith SS, Harrison RM. The use of trajectory cluster analysis to examine the long-range transport of secondary inorganic aerosol in the UK. Atmospheric Environment 2005;39(35):6686–95.

Aldabe J, Santamaría C, Elustondo D, Lasheras E, Santamaría JM. Application of microwave digestion and ICP-MS to simultaneous analysis of major and trace elements in aerosol samples collected on quartz filters. Anal. Methods 2013;5(2):554–9.

Anders L, Schade J, Rosewig EI, Kröger-Badge T, Irsig R, Jeong S et al. Detection of ship emissions from distillate fuel operation via single-particle profiling of polycyclic aromatic hydrocarbons. Environ. Sci.: Atmos. 2023;3(8):1134–44.

Aquilina NJ, Harrison RM. Evaluation of the cancer risk from PAHs by inhalation: Are current methods fit for purpose? Environment international 2023;177:107991.

Atkinson RW, Kang S, Anderson HR, Mills IC, Walton HA. Epidemiological time series studies of PM2.5 and daily mortality and hospital admissions: a systematic review and meta-analysis. Thorax 2014;69(7):660–5.

Bai H, Qian X, Fan J, Shi Y, Duo Y, Guo C et al. Theoretical Model of Single Fiber Efficiency and the Effect of Microstructure on Fibrous Filtration Performance: A Review. Ind. Eng. Chem. Res. 2021;60(1):3–36.

Baron PA, Kulkarni P, Willeke K. Aerosol measurement: Principles, techniques, and applications. 3rd ed. Hoboken N.J.: Wiley; 2011.

Bendl J. Aerosol Size Distribution of PAHs in the Urban Atmosphere. diploma thesis. Prague; 2014.

Bendl J, Hovorka J. Temperature and Relative Humidity Vertical Profiles within Planetary Boundary Layer in Winter Urban Airshed, 2017. https://www.researchgate.net/publication/321991310_Temperature_and_Relative_Humidity_Vertical_Profiles_within_Planetary_Boundary_Layer_in_Winter_Urban_Airshed (accessed December 17, 2023).

Bendl J, Neukirchen C, Mudan A, Padoan S, Zimmermann R, Adam T. Personal measurements and sampling of particulate matter in a subway – Identification of hot-spots, spatio-temporal variability and sources of pollutants. Atmospheric Environment 2023;308:119883.

Block ML, Calderón-Garcidueñas L. Air pollution: mechanisms of neuroinflammation and CNS disease. Trends in neurosciences 2009;32(9):506–16.

Boomhower SR, Long CM, Li W, Manidis TD, Bhatia A, Goodman JE. A review and analysis of personal and ambient PM2.5 measurements: Implications for epidemiology studies. Environmental research 2022;204(Pt B):112019.

Brunekreef B, Forsberg B. Epidemiological evidence of effects of coarse airborne particles on health. The European respiratory journal 2005;26(2):309–18.

Bukowiecki N, Lienemann P, Zwicky CN, Furger M, Richard A, Falkenberg G et al. X-ray fluorescence spectrometry for high throughput analysis of atmospheric aerosol samples: The benefits of synchrotron X-rays. Spectrochimica Acta Part B: Atomic Spectroscopy 2008;63(9):929–38.

Cepeda M, Schoufour J, Freak-Poli R, Koolhaas CM, Dhana K, Bramer WM et al. Levels of ambient air pollution according to mode of transport: a systematic review. The Lancet Public Health 2017;2(1):e23-e34.

Chamberlain RC, Fecht D, Davies B, Laverty AA. Health effects of low emission and congestion charging zones: a systematic review. The Lancet. Public health 2023;8(7):e559-e574.

Charrier JG, McFall AS, Richards-Henderson NK, Anastasio C. Hydrogen peroxide formation in a surrogate lung fluid by transition metals and quinones present in particulate matter. Environmental science & technology 2014;48(12):7010–7.

CHMI. Znečištění ovzduší na území České republiky v roce 2022. Prague: Czech Hydrometeorological Institute; 2023.

Cohen AJ, Brauer M, Burnett R, Anderson HR, Frostad J, Estep K et al. Estimates and 25-year trends of the global burden of disease attributable to ambient air pollution: an analysis of data from the Global Burden of Diseases Study 2015. Lancet (London, England) 2017;389(10082):1907–18.

Colbeck I. Environmental chemistry of aerosols. Oxford, Ames Iowa: Blackwell Pub; 2008.

Colbeck I, Lazaridis M, editors. Aerosol science: Technology and applications. Chichester West Sussex United Kingdom: Wiley; 2014.

Costabile F, Gualtieri M, Rinaldi M, Canepari S, Vecchi R, Massimi L et al. Exposure to urban nanoparticles at low PMFormula: see text concentrations as a source of oxidative stress and inflammation. Scientific reports 2023;13(1):18616.

Cusack M, Talbot N, Ondráček J, Minguillón MC, Martins V, Klouda K et al. Variability of aerosols and chemical composition of PM 10 PM 2.5 and PM 1 on a platform of the Prague underground metro. Atmospheric Environment 2015;118:176–83.

Dat N-D, Chang MB. Review on characteristics of PAHs in atmosphere, anthropogenic sources and control technologies. The Science of the total environment 2017;609:682–93.

Dilamian M, Joghataei M, Ashrafi Z, Bohr C, Mathur S, Maleki H. From 1D electrospun nanofibers to advanced multifunctional fibrous 3D aerogels. Applied Materials Today 2021;22:100964.

Dostal M, Schallerova E, Sram RJ. A High Morbidity of Preschool Children in Ostrava Hot Spot of PM10 Pollution. Epidemiology 2011;22:S276.

Ensor D. Aerosol Science and Technology: History and Reviews: RTI Press; 2011.

European Environment Agency. Europe’s air quality status 2021: Publications Office; 2022.

European Environment Agency. Europe's air quality status 2023: Publications Office; 2023.

European Parliament. Directive 2008/50/EC, 2015. http://data.europa.eu/eli/dir/2008/50/2015-09-18 (accessed December 03, 2023).

Fan W, Chen T, Zhu Z, Zhang H, Qiu Y, Yin D. A review of secondary organic aerosols formation focusing on organosulfates and organic nitrates. Journal of hazardous materials 2022;430:128406.

Finlayson-Pitts BJ, Pitts JN. Chemistry of the upper and lower atmosphere: Theory, experiments, and applications. San Diego: Academic Press; 2000.

Font O, Moreno T, Querol X, Martins V, Sánchez Rodas D, Miguel E de et al. Origin and speciation of major and trace PM elements in the Barcelona subway system. Transportation Research Part D: Transport and Environment 2019;72:17–35.

Fowler D, Brimblecombe P, Burrows J, Heal MR, Grennfelt P, Stevenson DS et al. A chronology of global air quality. Philosophical transactions. Series A, Mathematical, physical, and engineering sciences 2020;378(2183):20190314.

Fussell JC, Franklin M, Green DC, Gustafsson M, Harrison RM, Hicks W et al. A Review of Road Traffic-Derived Non-Exhaust Particles: Emissions, Physicochemical Characteristics, Health Risks, and Mitigation Measures. Environmental science & technology 2022;56(11):6813–35.

Grigoratos T, Martini G. Brake wear particle emissions: a review. Environmental science and pollution research international 2015;22(4):2491–504.

Heard DE. Analytical techniques for atmospheric measurement. Oxford, Ames Iowa: Blackwell Pub; 2006.

Hinds WC, Zhu Y, Hinds WCAtSe. Aerosol technology: Properties, behaviour, and measurement of airborne particles. Hoboken: John Wiley & Sons; 2022.

Hock N, Schneider J, Borrmann S, Römpp A, Moortgat G, Franze T et al. Rural continental aerosol properties and processes observed during the Hohenpeissenberg Aerosol Characterization Experiment (HAZE2002). Atmos. Chem. Phys. 2008;8(3):603–23.

Hooftman N, Messagie M, van Mierlo J, Coosemans T. A review of the European passenger car regulations – Real driving emissions vs local air quality. Renewable and Sustainable Energy Reviews 2018;86:1–21.

Hopke PK, Dai Q, Li L, Feng Y. Global review of recent source apportionments for airborne particulate matter. The Science of the total environment 2020;740:140091.

Hopke PK, Feng Y, Dai Q. Source apportionment of particle number concentrations: A global review. The Science of the total environment 2022;819:153104.

Hopkins LE, Laing EA, Peake JL, Uyeminami D, Mack SM, Li X et al. Repeated Iron-Soot Exposure and Nose-to-brain Transport of Inhaled Ultrafine Particles. Toxicologic pathology 2018;46(1):75–84.

Hovorka J, Kuzelova N, Bendl J, Klan M, Leoni C, Pokorna P et al. Effects of local emissions on urban visibility measured with a mobile airship monitoring platform. In: International Conference on Atmospheric Optics: Aerosols, Visibility, and the Radiative Balance. p. 448–457.

Hovorka J, Pokorná P, Bendl J, Baranová A, Grégr M, Braniš M. Podrobná charakterizace atmosférického aerosolu v lokalitě Ostrava-Radvanice v zimě 2012: Prostorová variabilita PM2,5. Ochrana ovzduší 2012;2:3.

Hovorka J, Pokorná P, Hopke PK, Křůmal K, Mikuška P, Píšová M. Wood combustion, a dominant source of winter aerosol in residential district in proximity to a large automobile factory in Central Europe. Atmospheric Environment 2015;113:98–107.

Hůnová I. Ambient Air Quality in the Czech Republic: Past and Present. Atmosphere 2020;11(2):214.

Idowu O, Semple KT, Ramadass K, O'Connor W, Hansbro P, Thavamani P. Beyond the obvious: Environmental health implications of polar polycyclic aromatic hydrocarbons. Environment international 2019;123:543–57.

Järlskog I, Jaramillo-Vogel D, Rausch J, Gustafsson M, Strömvall A-M, Andersson-Sköld Y. Concentrations of tire wear microplastics and other traffic-derived non-exhaust particles in the road environment. Environment international 2022;170:107618.

Jeong C-H, Wang JM, Hilker N, Debosz J, Sofowote U, Su Y et al. Temporal and spatial variability of traffic-related PM2.5 sources: Comparison of exhaust and non-exhaust emissions. Atmospheric Environment 2019;198:55–69.

Jeong S, Bendl J, Saraji-Bozorgzad M, Käfer U, Etzien U, Schade J et al. Aerosol emissions from a marine diesel engine running on different fuels and effects of exhaust gas cleaning measures. Environmental pollution (Barking, Essex 1987) 2023;316(Pt 1):120526.

Jia Y, Lin Z, He Z, Li C, Zhang Y, Wang J et al. Effect of Air Pollution on Heart Failure: Systematic Review and Meta-Analysis. Environmental health perspectives 2023;131(7):76001.

Jiřík V, Machaczka O, Miturová H, Tomášek I, Šlachtová H, Janoutová J et al. Air Pollution and Potential Health Risk in Ostrava Region - a Review. Cent Eur J Public Health 2016;24 Suppl(Supplement):S4-S17.

Jorga SD, Florou K, Patoulias D, Pandis SN. New particle formation and growth during summer in an urban environment: a dual chamber study. Atmos. Chem. Phys. 2023;23(1):85–97.

Kang E, Root MJ, Toohey DW, Brune WH. Introducing the concept of Potential Aerosol Mass (PAM). Atmos. Chem. Phys. 2007;7(22):5727–44.

Kangasluoma J, Cai R, Jiang J, Deng C, Stolzenburg D, Ahonen LR et al. Overview of measurements and current instrumentation for 1–10 nm aerosol particle number size distributions. Journal of Aerosol Science 2020;148:105584.

Kim K-H, Jahan SA, Kabir E, Brown RJC. A review of airborne polycyclic aromatic hydrocarbons (PAHs) and their human health effects. Environment international 2013;60:71–80.

Klán M, Pokorná P, Havlíček D, Vik O, Racek M, Plocek J et al. New comprehensive approach for airborne asbestos characterisation and monitoring. Environmental science and pollution research international 2018;25(30):30488–96.

Klaunig JE. Oxidative Stress and Cancer. Current pharmaceutical design 2018;24(40):4771–8.

Koppmann R. Volatile organic compounds in the atmosphere. 1st ed. Oxford: Blackwell; 2007.

Kousoulidou M, Fontaras G, Ntziachristos L, Bonnel P, Samaras Z, Dilara P. Use of portable emissions measurement system (PEMS) for the development and validation of passenger car emission factors. Atmospheric Environment 2013;64:329–38.

Kozáková J, Pokorná P, Cerníková A, Hovorka J, Braniš M, Moravec P et al. The Association between Intermodal (PM1-2.5) and PM1, PM2.5, Coarse Fraction and Meteorological Parameters in Various Environments in Central Europe. Aerosol Air Qual. Res. 2017;17(5):1234–43.

Kozáková J, Pokorná P, Vodička P, Ondráčková L, Ondráček J, Křůmal K et al. The influence of local emissions and regional air pollution transport on a European air pollution hot spot. Environmental science and pollution research international 2019;26(2):1675–92.

Křůmal K, Mikuška P. Mass concentrations and lung cancer risk assessment of PAHs bound to PM1 aerosol in six industrial, urban and rural areas in the Czech Republic, Central Europe. Atmospheric Pollution Research 2020;11(2):401–8.

Křůmal K, Mikuška P, Večeřa Z. Characterization of organic compounds in winter PM1 aerosols in a small industrial town. Atmospheric Pollution Research 2017;8(5):930–9.

Kumar P, Gupta NC. Commuter exposure to inhalable, thoracic and alveolic particles in various transportation modes in Delhi. The Science of the total environment 2016;541:535–41.

Kwon H-S, Ryu MH, Carlsten C. Ultrafine particles: unique physicochemical properties relevant to health and disease. Experimental & molecular medicine 2020;52(3):318–28.

Lammel G, Kitanovski Z, Kukučka P, Novák J, Arangio AM, Codling GP et al. Oxygenated and Nitrated Polycyclic Aromatic Hydrocarbons in Ambient Air-Levels, Phase Partitioning, Mass Size Distributions, and Inhalation Bioaccessibility. Environmental science & technology 2020;54(5):2615–25.

Lee S-H, Allen HC. Analytical measurements of atmospheric urban aerosol. Analytical chemistry 2012;84(3):1196–201.

Leoni C, Pokorná P, Hovorka J, Masiol M, Topinka J, Zhao Y et al. Source apportionment of aerosol particles at a European air pollution hot spot using particle number size distributions and chemical composition. Environmental pollution (Barking, Essex 1987) 2018;234:145–54.

Lepistö T, Lintusaari H, Oudin A, Barreira LM, Niemi JV, Karjalainen P et al. Particle lung deposited surface area (LDSAal) size distributions in different urban environments and geographical regions: Towards understanding of the PM2.5 dose–response. Environment international 2023;180:108224.

Li D, Yun Y, Gao R. Oxygenated Polycyclic aromatic hydrocarbons (Oxy-PAHs) facilitate lung cancer metastasis by epigenetically regulating the epithelial-to-mesenchymal transition (EMT). Environmental pollution (Barking, Essex 1987) 2019;255(Pt 2):113261.

Li J, Li H, Ma Y, Wang Y, Abokifa AA, Lu C et al. Spatiotemporal distribution of indoor particulate matter concentration with a low-cost sensor network. Building and Environment 2018;127:138–47.

Lim S, Bassey E, Bos B, Makacha L, Varaden D, Arku RE et al. Comparing human exposure to fine particulate matter in low and high-income countries: A systematic review of studies measuring personal PM2.5 exposure. The Science of the total environment 2022;833:155207.

Liu X, Hadiatullah H, Schnelle-Kreis J, Xu Y, Yue M, Zhang X et al. Levels and drivers of urban black carbon and health risk assessment during pre- and COVID19 lockdown in Augsburg, Germany. Environmental pollution (Barking, Essex 1987) 2023;316(Pt 1):120529.

Liu X, Hadiatullah H, Zhang X, Hill LD, White AHA, Schnelle-Kreis J et al. Analysis of mobile monitoring data from the microAeth® MA200 for measuring changes in black carbon on the roadside in Augsburg; 2021.

Liu X, Jayaratne R, Thai P, Kuhn T, Zing I, Christensen B et al. Low-cost sensors as an alternative for long-term air quality monitoring. Environmental research 2020;185:109438.

Lv Y, Li X, Xu TT, Cheng TT, Yang X, Chen JM et al. Size distributions of polycyclic aromatic hydrocarbons in urban atmosphere: sorption mechanism and source contributions to respiratory deposition. Atmos. Chem. Phys. 2016;16(5):2971–83.

M Figueiredo D, Nijssen R, J M Krop E, Buijtenhuijs D, Gooijer Y, Lageschaar L et al. Pesticides in doormat and floor dust from homes close to treated fields: Spatio-temporal variance and determinants of occurrence and concentrations. Environmental pollution (Barking, Essex 1987) 2022;301:119024.

Manisalidis I, Stavropoulou E, Stavropoulos A, Bezirtzoglou E. Environmental and Health Impacts of Air Pollution: A Review. Frontiers in public health 2020;8:14.

Marco G, Bo X. Air Quality Legislation and Standards in the European Union: Background, Status and Public Participation. Advances in Climate Change Research 2013;4(1):50–9.

Marjamäki M, Keskinen J, Chen D-R, Pui DY. Performance Evaluation of the Electrical Low-Pressure Impactor (ELPI). Journal of Aerosol Science 2000;31(2):249–61.

Martins LD, Hallak R, Alves RC, Almeida DS de, Squizzato R, Moreira CA et al. Long-range Transport of Aerosols from Biomass Burning over Southeastern South America and their Implications on Air Quality. Aerosol Air Qual. Res. 2018;18(7):1734–45.

Martins V, Moreno T, Minguillón MC, Amato F, Miguel E de, Capdevila M et al. Exposure to airborne particulate matter in the subway system. The Science of the total environment 2015;511:711–22.

Marvanová S, Kulich P, Skoupý R, Hubatka F, Ciganek M, Bendl J et al. Size-segregated urban aerosol characterization by electron microscopy and dynamic light scattering and influence of sample preparation. Atmospheric Environment 2018;178:181–90.

Mikuška P, Křůmal K, Večeřa Z. Characterization of organic compounds in the PM2.5 aerosols in winter in an industrial urban area. Atmospheric Environment 2015;105:97–108.

Morawska L, Afshari A, Bae GN, Buonanno G, Chao CYH, Hänninen O et al. Indoor aerosols: from personal exposure to risk assessment. Indoor air 2013;23(6):462–87.

Morawska L, Salthammer T. Indoor environment: Airborne particles and settled dust / edited by Lidia Morawska and Tunga Salthammer. Weinheim, Great Britain: Wiley-VCH; 2003.

Nechvátalová K. Expozice dětí aerosolovými částicemi v přívěsných vozících za jízdním kolem. bachelor thesis. Prague; 2019.

Ogrizek M, Kroflič A, Šala M. Critical review on the development of analytical techniques for the elemental analysis of airborne particulate matter. Trends in Environmental Analytical Chemistry 2022;33:e00155.

Pardo M, Offer S, Hartner E, Di Bucchianico S, Bisig C, Bauer S et al. Exposure to naphthalene and β-pinene-derived secondary organic aerosol induced divergent changes in transcript levels of BEAS-2B cells. Environment international 2022;166:107366.

Petzold A, Ogren JA, Fiebig M, Laj P, Li S-M, Baltensperger U et al. Recommendations for reporting "black carbon" measurements. Atmos. Chem. Phys. 2013;13(16):8365–79.

Pokorná P, Hovorka J, Klán M, Hopke PK. Source apportionment of size resolved particulate matter at a European air pollution hot spot. The Science of the total environment 2015;502:172–83.

Pokorná P, Leoni C, Schwarz J, Ondráček J, Ondráčková L, Vodička P et al. Spatial-temporal variability of aerosol sources based on chemical composition and particle number size distributions in an urban settlement influenced by metallurgical industry. Environmental science and pollution research international 2020;27(31):38631–43.

Riemer N, Ault AP, West M, Craig RL, Curtis JH. Aerosol Mixing State: Measurements, Modeling, and Impacts. Reviews of Geophysics 2019;57(2):187–249.

Rissanen M. Anthropogenic Volatile Organic Compound (AVOC) Autoxidation as a Source of Highly Oxygenated Organic Molecules (HOM). The journal of physical chemistry. A 2021;125(41):9027–39.

Rohkamp M, Rabl A, Gündling B, Saraji-Bozorgzad M, Mull C, Bendl J et al. Detailed Gaseous and Particulate Emissions of an Allison 250-C20B Turboshaft Engine. Journal of Engineering for Gas Turbines and Power 2023:1–13.

Rönkkö T, Saarikoski S, Kuittinen N, Karjalainen P, Keskinen H, Järvinen A et al. Review of black carbon emission factors from different anthropogenic sources. Environ. Res. Lett. 2023;18(3):33004.

Rosewig EI, Schade J, Passig J, Osterholz H, Irsig R, Smok D et al. Remote Detection of Different Marine Fuels in Exhaust Plumes by Onboard Measurements in the Baltic Sea Using Single-Particle Mass Spectrometry. Atmosphere 2023;14(5):849.

Rossner P, Cervena T, Vojtisek-Lom M. In vitro exposure to complete engine emissions - a mini-review. Toxicology 2021;462:152953.

Russell et al. IARC monographs on the evaluation of carcinogenic risks to humans, volume 92, some non-heterocyclic polycyclic aromatic hydrocarbons and some related exposures: This publication represents the views and expert opinions of an IARC Working Group on the Evaluation of Carcinogenic Risks to Humans, which met in Lyon, 11 - 18 October 2005. Lyon: WHO; 2010.

Sadanaga Y, Matsumoto J, Kajii Y. Photochemical reactions in the urban air: Recent understandings of radical chemistry. Journal of Photochemistry and Photobiology C: Photochemistry Reviews 2003;4(1):85–104.

Salo L, Rönkkö T, Saarikoski S, Teinilä K, Kuula J, Alanen J et al. Concentrations and Size Distributions of Particle Lung-deposited Surface Area (LDSA) in an Underground Mine. Aerosol Air Qual. Res. 2021;21(8):200660.

Schlesinger RB. The health impact of common inorganic components of fine particulate matter (PM2.5) in ambient air: a critical review. Inhalation toxicology 2007;19(10):811–32.

Schneider E, Czech H, Hansen HJ, Jeong S, Bendl J, Saraji-Bozorgzad M et al. Humic-like Substances (HULIS) in Ship Engine Emissions: Molecular Composition Effected by Fuel Type, Engine Mode, and Wet Scrubber Usage. Environmental science & technology 2023.

Schreiberová M, Vlasáková L, Vlček O, Šmejdířová J, Horálek J, Bieser J. Benzo[a]pyrene in the Ambient Air in the Czech Republic: Emission Sources, Current and Long-Term Monitoring Analysis and Human Exposure. Atmosphere 2020;11(9):955.

Seinfeld JH, Pandis SN. Atmospheric chemistry and physics: From air pollution to climate change / John H. Seinfeld and Spyros N. Pandis. Hoboken, New Jersey: John Wiley & Sons; 2016.

Shao Y, Voliotis A, Du M, Wang Y, Pereira K, Hamilton J et al. Chemical composition of secondary organic aerosol particles formed from mixtures of anthropogenic and biogenic precursors. Atmos. Chem. Phys. 2022;22(15):9799–826.

Sierra-Vargas MP, Teran LM. Air pollution: impact and prevention. Respirology (Carlton, Vic.) 2012;17(7):1031–8.

Siouti E, Kilafis K, Kioutsioukis I, Pandis SN. Simulation of the influence of residential biomass burning on air quality in an urban area. Atmospheric Environment 2023;309:119897.

Sram RJ, Binkova B, Dostal M, Merkerova-Dostalova M, Libalova H, Milcova A et al. Health impact of air pollution to children. International journal of hygiene and environmental health 2013a;216(5):533–40.

Sram RJ, Dostal M, Libalova H, Rossner P, Rossnerova A, Svecova V et al. The European Hot Spot of B[a]P and PM 2.5 Exposure—The Ostrava Region, Czech Republic: Health Research Results. ISRN Public Health 2013b;2013:1–12.

Sullivan RC, Pryor SC. Quantifying spatiotemporal variability of fine particles in an urban environment using combined fixed and mobile measurements. Atmospheric Environment 2014;89:664–71.

Talbot N, Kubelova L, Makes O, Cusack M, Ondracek J, Vodička P et al. Outdoor and indoor aerosol size, number, mass and compositional dynamics at an urban background site during warm season. Atmospheric Environment 2016;131:171–84.

Tian Y, Duan M, Cui X, Zhao Q, Tian S, Lin Y et al. Advancing application of satellite remote sensing technologies for linking atmospheric and built environment to health. Frontiers in public health 2023;11:1270033.

Topinka J, Rossner P, Milcová A, Schmuczerová J, Pěnčíková K, Rossnerová A et al. Day-to-day variability of toxic events induced by organic compounds bound to size segregated atmospheric aerosol. Environmental pollution 2015;202:135–45.

Tranchida PQ, Giocastro B, Mondello L. Multidimensional gas chromatography: Hyphenation with mass spectrometry. In: Characterization of Odorant Patterns by Comprehensive Two-Dimensional Gas Chromatography: Elsevier; 2022. p. 93–118.

Trechera P, Garcia-Marlès M, Liu X, Reche C, Pérez N, Savadkoohi M et al. Phenomenology of ultrafine particle concentrations and size distribution across urban Europe. Environment international 2023;172:107744.

Upadhyay S, Palmberg L. Air-Liquid Interface: Relevant In Vitro Models for Investigating Air Pollutant-Induced Pulmonary Toxicity. Toxicological sciences an official journal of the Society of Toxicology 2018;164(1):21–30.

US EPA. Quality Assurance Guidance Document 2.12: Monitoring PM2.5 in Ambient Air Using Designated Reference Or Class I Equivalent Methods: Air Quality Assessment Division, Office of Air Quality Planning and Standards, U.S. Environmental Protection Agency; 2016.

US EPA, ORD, Integrated Risk Information System. Toxicological Review of Benzo[a]pyrene (Final Report): EPA/635/R-17/003Fa; 2017.

van Nunen E, Vermeulen R, Tsai M-Y, Probst-Hensch N, Ineichen A, Imboden M et al. Associations between modeled residential outdoor and measured personal exposure to ultrafine particles in four European study areas. Atmospheric Environment 2020;226:117353.

van Poppel M, Peters J, Bleux N. Methodology for setup and data processing of mobile air quality measurements to assess the spatial variability of concentrations in urban environments. Environmental pollution (Barking, Essex 1987) 2013;183:224–33.

Vincent JH. Aerosol sampling: Science, standards, instrumentation and applications. Chichester England, Hoboken NJ: John Wiley & Sons; 2007.

Vojtisek-Lom M, Arul Raj AF, Jindra P, Macoun D, Pechout M. On-road detection of trucks with high NOx emissions from a patrol vehicle with on-board FTIR analyzer. The Science of the total environment 2020;738:139753.

Vojtíšek-Lom M, Beránek V, Klír V, Jindra P, Pechout M, Voříšek T. On-road and laboratory emissions of NO, NO2, NH3, N2O and CH4 from late-model EU light utility vehicles: Comparison of diesel and CNG. The Science of the total environment 2018;616-617:774–84.

Vojtíšek-Lom M, Vaculík M, Pechout M, Hopan F, Arul Raj AF, Penumarti S et al. Effects of braking conditions on nanoparticle emissions from passenger car friction brakes. The Science of the total environment 2021;788:147779.

Wallace JM, Hobbs PV. Atmospheric science: An introductory survey. 2nd ed. Amsterdam, Boston: Elsevier Academic Press; 2006.

Wang S, Zhou K, Lu X, Chen H, Yang F, Li Q et al. Online shape and density measurement of single aerosol particles. Journal of Aerosol Science 2022;159:105880.

Wendisch M, Brenguier J-L. Airborne measurements for environmental research: Methods and instruments / edited by Manfred Wendisch and Jean-Louis Brenguier. Weinheim: Wiley-VCH; 2013.

WHO. WHO global air quality guidelines: Particulate matter (PM2.5 and PM10), ozone, nitrogen dioxide, sulfur dioxide and carbon monoxide. Bonn, Germany: WHO European Centre for Environment and Health; 2021.

Wise SA, Sander LC, Schantz MM. Analytical Methods for Determination of Polycyclic Aromatic Hydrocarbons (PAHs) — A Historical Perspective on the 16 U.S. EPA Priority Pollutant PAHs. Polycyclic Aromatic Compounds 2015;35(2-4):187–247.

WMO. Guide to Instruments and Methods of Observation: Measurements of Meteorological Variables. 8th ed. Geneva: World Meteorological Organization (WMO); 2021.

Wu T, Boor BE. Urban aerosol size distributions: a global perspective. Atmos. Chem. Phys. 2021;21(11):8883–914.

Xie W, Li Y, Bai W, Hou J, Ma T, Zeng X et al. The source and transport of bioaerosols in the air: A review. Frontiers of environmental science & engineering 2021;15(3):44.

Xu B, Hao J. Air quality inside subway metro indoor environment worldwide: A review. Environment international 2017;107:33–46.

Xue W, Warshawsky D. Metabolic activation of polycyclic and heterocyclic aromatic hydrocarbons and DNA damage: a review. Toxicology and applied pharmacology 2005;206(1):73–93.

Yang H-H, Lee W-J, Chen S-J, Lai S-O. PAH emission from various industrial stacks. Journal of hazardous materials 1998;60(2):159–74.

Yu W, Ye T, Zhang Y, Xu R, Lei Y, Chen Z et al. Global estimates of daily ambient fine particulate matter concentrations and unequal spatiotemporal distribution of population exposure: a machine learning modelling study. The Lancet. Planetary health 2023;7(3):e209-e218.

Zikova N, Masiol M, Chalupa D, Rich D, Ferro A, Hopke P. Estimating Hourly Concentrations of PM2.5 across a Metropolitan Area Using Low-Cost Particle Monitors. Sensors 2017;17(8):1922.

6. APPENDIXES: Manuscripts

6.1. APPENDIX A: Manuscript 1

Bendl, J.; Neukirchen, C.; Mudan, A.; Padoan, S.; Zimmermann, R.; Adam, T. Personal measurements and sampling of particulate matter in a subway – Identification of hot-spots, spatio-temporal variability and sources of pollutants. *Atmospheric Environment* **2023,** *308*, 119883; DOI 10.1016/j.atmosenv.2023.119883.

Atmospheric Environment 308 (2023) 119883

Contents lists available at ScienceDirect

Atmospheric Environment

journal homepage: www.elsevier.com/locate/atmosenv

Personal measurements and sampling of particulate matter in a subway – Identification of hot-spots, spatio-temporal variability and sources of pollutants

Jan Bendl[a,d,*], Carsten Neukirchen[a,c], Ajit Mudan[a], Sara Padoan[a,b], Ralf Zimmermann[b,c], Thomas Adam[a,b]

[a] University of the Bundeswehr Munich, Faculty for Mechanical Engineering, Institute of Chemical and Environmental Engineering, Werner-Heisenberg-Weg 39, 85577, Neubiberg, Germany
[b] Joint Mass Spectrometry Center (JMSC) at Comprehensive Molecular Analytics (CMA), Helmholtz Zentrum München, Ingolstädter Landstr. 1, 85764, Neuherberg, Germany
[c] Joint Mass Spectrometry Center (JMSC) at Chair of Analytical Chemistry, Institute of Chemistry, University of Rostock, Albert-Einstein-Strasse 27, 18059, Rostock, Germany
[d] Institute for Environmental Studies, Faculty of Science, Charles University, Benátská 2, 128 01, Prague 2, Czech Republic

HIGHLIGHTS

- Higher spatial than temporal variability of PM in the Munich subway system was observed.
- Significant differences in PM concentrations between platforms were found, with train frequency being a key factor.
- Iron oxide particles as products of rails and wheels abrasion dominated PM mass.
- Mobile measurements of subway systems effectively identify hot-spots and air quality.
- With the proposed methodology, subway systems can be comparably mapped for site-specific PM reduction measures.

GRAPHICAL ABSTRACT

New system for mobile comprehensive air quality monitoring, Munich subway

ARTICLE INFO

Keywords:
Metro
Public transport
Indoor air quality
Personal exposure
Particulate matter
Elemental composition

ABSTRACT

A mobile measurement system for complex characterization of particulate matter (PM) was developed together with the proposed methodology and applied in the subway system of Munich, Germany. The main objectives were to observe the spatio-temporal variability of PM, personal exposure, identify hot-spots and pollution sources. Particle mass (PM_x) and number (PNC) concentrations, and equivalent black carbon (eBC) were measured at 0.1–1 Hz. On the *U5* subway line, PM_{10}, $PM_{2.5}$ and PM_1 concentrations at platforms ranged from 59 to 220, 27–80, and 9–21 μg m^{-3}, respectively. During rides towards downtown, average PM_{10}, $PM_{2.5}$ and PM_1 levels gradually increased from 8 to 220, 2 to 71 and 2–20 μg m^{-3}, respectively, with a similar dynamic of decrease on the return journey. Spatial variability of PM was generally more important than temporal, and

---

Abbreviations: PM, Particulate matter.

* Corresponding author. University of the Bundeswehr Munich, Faculty for Mechanical Engineering, Institute of Chemical and Environmental Engineering, Werner-Heisenberg-Weg 39, 85577, Neubiberg, Germany.

E-mail address: jan.bendl@unibw.de (J. Bendl).

https://doi.org/10.1016/j.atmosenv.2023.119883
Received 25 February 2023; Received in revised form 18 May 2023; Accepted 31 May 2023

significant differences were observed between platforms. During the rides, air exchange between train and tunnel was high in both air-conditioned and old passively ventilated trains. Peak PM concentrations on platforms were associated with arriving/departing trains. Subway PNC were not significantly elevated, but a few cases of intake of traffic-related particles from outside were observed, otherwise air exchange was considered low. Generally, most of the aerosol mass was composed of iron corrosion products from rails and wheels (Fe up to 66 μg m^{-3} in $PM_{2.5}$). The effective density of $PM_{2.5}$ was 2.1 g cm^{-3}. Particles were classified as 75.4% iron oxides, 5.35% metallic Fe, 1.23% aluminosilicates and 17% carbon and oxygen rich particles. The iron oxide particles consisted predominantly of Fe (63.4 ± 8.7 wt%) and O (36.2 ± 8.2 wt%). To effectively monitor subway PM and reduce overall PM exposure, we propose to identify hot-spots using our methodology and focus on improving their ventilation, as well as installing filters in air-conditioned wagons.

1. Introduction

People in urban areas around the world spend a considerable amount of time commuting and often choose subway as the most sustainable and time-efficient environmentally friendly transport mode. However, personal exposure to harmful compounds within the transport micro-environment can pose a health risk (Cepeda et al., 2017). Even low concentrations of pollutants, such as ultrafine particles (UFP), can cause long-term adverse health effects (Schraufnagel, 2020). In general, the health effects of PM exposure ranging from respiratory diseases to cancer, result in significant impairment of quality of life, premature deaths and non-negligible economic impacts (World Health Organization, 2021). Minimizing exposure to PM in public transport is, therefore, necessary and in line with the objective of the United Nation's Sustainable Development Goal #11 (Huck, 2022) and the Guidelines for Developing and Implementing a Sustainable Urban Mobility Plan (Rupprecht Consult, 2019).

Subway stations and tunnels are a specific micro-environment dominated by non-exhaust emissions (NEE) from electric trains in relatively closed space. NEE are not yet regulated and systematically monitored like vehicle exhaust emissions. Nevertheless, PM_{10} and $PM_{2.5}$ concentrations in subways have been often found to exceed WHO ambient air quality guidelines (Xu and Hao, 2017; Chang et al., 2021). The negative health effects of subway PM have been proven in various studies. These include DNA damage caused most likely by the redox-active surfaces of metal-rich particles leading to oxidative stress (Karlsson et al., 2006, 2008), as well as inflammatory, toxicity and transient biological effects (Bachoual et al., 2007). Recent research has also revealed cancer risks associated with exposure to subway PM (Roy et al., 2022). However, not all mechanisms are fully understood yet.

The main sources of subway PM described in literature are abrasion from brakes (steel alloys containing chromium and nickel), rails and wheels (mostly iron) as well as rail catenary and pantographs (copper) with iron being dominant in $PM_{2.5}$ (Minguillón et al., 2018). Due to subway systems being enclosed environments, the effects of ventilation on air quality have been observed as well as other phenomena such as piston effects of trains, which resuspend settled dust (Martins et al., 2016; Cartenì et al., 2020).

Various studies focusing on personal exposure in the subway have been conducted (Querol et al., 2012; Yang et al., 2015; Xu et al., 2016; Shakya et al., 2020; Targino et al., 2021), however, the aim of this study is to present the most comprehensive approach to characterize subway PM exclusively using a custom-built mobile measurement system (followed by laboratory analysis). One of the aims was to propose a methodology to effectively identify hot-spots, measure the spatial and temporal dynamics of the aerosol, provide an indoor/outdoor PM comparison with respect to size distribution, elemental composition and morphology of the particles. In addition, personal exposure during typical rides and specific questions such as differences between old and new trains have been addressed.

Measurements were conducted in the Munich subway system, where there has been no published study to date. In our pilot study, on-line PM measurements were focused on PM_1, $PM_{2.5}$, PM_{10}, particle number concentration (PNC), equivalent black carbon (eBC) and lung deposited surface area (LDSA), which is a relatively new health-relevant metric combining alveolar deposition efficiency of particles with their surface area (Salo et al., 2021). Filter sampling for metal contents of PM analyzed by inductively coupled plasma mass spectrometry (ICP-MS) was performed either stationary at selected platforms or during typical journeys to assess citizen exposure. The morphology and elemental composition of individual particles were analyzed using scanning electron microscopy with energy dispersive X-ray spectroscopy (SEM-EDX).

2. Materials and methods

2.1. Study area

Mobile measurements were conducted in the area of Munich with 1.5 mio. inhabitants and an area of 311 km^2. Its subway system called *U-Bahn* consists of 8 lines (*U1-U8*), the first of which was completed in 1971. The total length of the rail network is about 95 km with 100 station platforms, tunnels with a maximum depth of 25 m and around 530 trains. In 2019, 429 million passengers used the subway for transportation, however, the numbers decreased due to the Covid-19 pandemic in 2020 (251 mio.) and 2021 (254 mio.; https://www.mvg.de/). Normally, the frequency of trains is 10 min, which shortens to 5 min during rush hours (7-9 am and 3-7 pm) and extends up to 30 min at the beginning (4 a.m.) and end (2 a.m.) of the service. Currently, three train types (A, B, C) with usually 6 cars are present, while only trains A (built 1967-1983) and C (build 2000 and later) were investigated. The "old" trains (A) have no ventilation system except for windows and the interior is separated into individual wagons while "new" trains (C) have ventilation, permanently closed windows and the interiors of three wagons are connected into one large volume. Focus of this study was on the line *U5* (Fig. S3 in SI), where "new" and "old" trains are randomly in operation. Trains are powered by a 750 V third rail made of low carbon steel (in the locations sampled) or aluminium. Outside of operating hours, the Munich Transport Service (MVG) occasionally uses a *Speno* train for grinding the rails and a special vacuum locomotive (VakTrak, New International Railways & SOCOFER) to clean the tracks from trash and sedimented particles using a blower and filtration system (*https://www.u-bahn-muenchen.de/*).

In Munich, the regional overground trains *S-Bahn* (*S1-S8*) often run in tunnels that are separated from the *U-Bahn* system with few exceptions. *S-Bahn* trains are ventilated with the possibility of opening the windows. The *S7* line was partially investigated in this study.

Hauptbahnhof (Munich Central Station) and *Ostbahnhof* are transfer stations to normal long-distance and regional trains.

Table 1 lists all stations included in this study along with abbreviations indicating *U-Bahn* (*U*), *S-Bahn* (*S*), or *railway* (*R*) stations. For example, the abbreviation *CS-R* stands for Munich central railway station and *CS-S* for Munich central station of *S-Bahn* trains. As there are two *U-Bahn* station platforms at the *Munich central station*, they are additionally numbered with the higher number indicating the deeper station (e.g. *CS-U2*). *NS-U/S* indicates the station *Neuperlach Süd* with a shared platform for *U-Bahn* and *S-Bahn.* The highlighted public transport map is in SI (Fig. S3) and all routes are shown in detail in Tables S2–S5.

2.2. Measurement strategy (proposed methodology)

The starting point of all personal measurements was at the Bundeswehr University Munich (GPS: 48°04′54.5″N 11°38′20.1″E) 1 km away from the terminal station *Neuperlach Süd* (*NS-U/S*, line *U5*), which is exceptionally above-ground. The ambient air quality station for reference measurements (section 2.6.) was located on the university campus.

The strategy of measurements and sampling is schematically reported in Fig. 1. As a first step, reference measurements in the surrounding area and different scouting rides within the subway were performed to identify hot-spots and to select typical routes for repetitions at different times of the day for the spatio-temporal variability of PM. Finally, stationary measurements were conducted with the mobile system at the center of the selected platforms to obtain information on the effects of arriving trains on the variability of PM. Therefore, the study was divided into the following experiments:

1) Mobile measurements of PM, PNC, and personal sampling for metals analysis (ICP-MS) on the university campus and surrounding urban micro-environments for reference (map of route in SI Fig. S2). A 1-h typical walking route **A** (Tables 2 and 3) was repeated 6 times and the new customized measurement system was tested
2) Scouting subway rides for PM, PNC observation, and identification of hot-spots (randomly selected routes **B, C, D, E**)
3) Repetition of the same ~1h long subway routes in the morning, noon and afternoon (selected based on previous results) to estimate daily variability (route **F**)
4) Stationary measurements and sampling (~3 h) at a platform identified as a hot-spot and considered to be a representative busy transfer station in the Munich city center for detailed characterization of particles using SEM/EDX and ICP/MS (**G**: platform *U5/U4* of Munich main train station *Hauptbahnhof CS-U1*). The dynamics of the particle emissions were linked to arriving trains
5) Another extended stationary sampling (6 h) for gravimetric analysis to calculate the specific density of PM used for the optical particle sizer (OPS) correction
6) Tracking of the differences in the dynamics of PM concentration between an old and a new type of subway train during the ride on the same track (line *U5*)

At the beginning and the end of each subway experiment, a minimum 20 min measurement walk (2 km) was taken between the university campus and the *NS-U/S* subway station to allow comparison with actual ambient urban PM levels. The mobile subway measurement routes (experiment 2 & 3) included train mid-section rides, stationary measurements simulating exposure of people waiting at selected platforms, and elevator rides. Platform measurements (experiment 4 & 5) were taken in the middle of the selected platform on designated passenger seats for the time necessary to obtain a sufficient number of data points. The operator documented the time at which trains entered and exited the station, and trains were categorized as old (o) and new (n), respectively. The *S-Bahn* platforms were measured similarly to *U-Bahn*. The investigation of the regional/long-distance train platform at the main station was conducted where most people gather and where small cafés and shops are also located. Sampling was done either cumulatively during the ride or at the selected platform (experiment 4).

Table 1
List of subway/train stations with abbreviations used in this study with average platform particulate matter (PMx), particle number concentration (PNC), equivalent black carbon (eBC) and UV-absorbing PM (UVPM) concentrations where the SD represents variability among measurements. For interpretation, design of the platform cross-section is indicated, where "P" is platform, "T" is track, "-" is direct transition and "|" indicate the separation of tracks/platform by a wall. Averages from ID 10-16 were not shown due to short measuring time.

ID	Name of the station	Abbr.	Lines	Type	Number of tracks (platform design)	PM_{10} (μg m^{-3})	$PM_{2.5}$ (μg m^{-3})	PM_1 (μg m^{-3})	PNC (pt cm^{-3})	eBC (ng m^{-3})	UVPM (ng m^{-3})	Size mode (nm)	No. of measurements
1	Neuperlach Süd	NS-U	U5, S7	overgr. (open w/ roof)	3 (T-P-T-T-P)	9 ± 5	3 ± 2	2 ± 2	7300 ± 7582	111 ± 117	620 ± 486	37 ± 19	7
2	Michaelibad	MC-U	U5	undergr.	2 (T-P-T)	59 ± 26	27 ± 14	9 ± 4	6547 ± 2419	4043 ± 1964	3236 ± 1353	40 ± 4	4
3	Ostbahnhof	OB-U	U5	undergr., transfer	2 (T-P-T)	205 ± 72	80 ± 18	21 ± 5	7470 ± 2773	9416 ± 3299	6840 ± 1694	43 ± 3	4
4	Odeonsplatz	OU-U	U4, U5	undergr., transfer	2 (T-P|P-T)	179 ± 52	70 ± 20	20 ± 6	6985 ± 1597	10540 ± 2628	6622 ± 1188	43 ± 2	4
5	Hauptbahnhof (over)	CS-U1	U4, U5	undergr., transfer	2 (T-P-T)	174 ± 40	66 ± 13	18 ± 4	8817 ± 2442	8648 ± 1469	6204 ± 562	40 ± 3	4
6	Hauptbahnhof (under)	CS-U2	U1, U2, U7, U8	undergr., transfer	4 (T-P-T-T-P-T)	220 ± 32	72 ± 7	20 ± 0.3	7175 ± 754	7845 ± 2560	6052 ± 723	46 ± 10	2
7	Hauptbahnhof Nord	CS-S	S1-4, S6-8	undergr., transfer	2 (P-T-P-T-P)	126 ± 89	42 ± 30	11 ± 7	6942 ± 1749	4616 ± 3053	3385 ± 2294	42 ± 7	4
8	Hauptbahnhof	CS-R	Railway	overgr. (semi-open), transfer	15 (large hall)	26 ± 9	11 ± 1	9 ± 1	7425 ± 4543	827 ± 401	1126 ± 707	48 ± 4	2
9	Innsbrucker Ring	IR-U	U2, U5	undergr., transfer	4 (T-P-T-T-P-T)	114 ± NA	48 ± NA	14 ± NA	5817 ± NA	7345 ± NA	5118 ± NA	46 ± NA	1
10	Therese-Giehse-Allee	TG-U	U5	undergr.	2 (T-P-T)	-	-	-	-	-	-	-	short
11	Neuperlach Zentrum	NZ-U	U5	undergr.	2 (T-P-T)	-	-	-	-	-	-	-	short
12	Quiddestrasse	QI-U	U5	undergr.	2 (T-P-T)	-	-	-	-	-	-	-	short
13	Max-Weber-Platz	MW-U	U4, U5	undergr.	2 (T-P-T-T-P-T)	-	-	-	-	-	-	-	short
14	Lehel	LH-U	U4, U5	undergr.	2 (T-P|P-T)	-	-	-	-	-	-	-	short
15	Karlsplatz (Stachus)	KA-U	U4, U5	undergr.	2 (T-P|P-T)	-	-	-	-	-	-	-	short
16	Theresienwiese	TW-U	U5	undergr.	2 (T-P-T)	-	-	-	-	-	-	-	short

2.3. Custom-built mobile measuring system

We developed a new mobile measurement system (Fig. S1 and full description in the SI) consisting of an actively ventilated, water-proof aluminum box with adjustable internal shelves, which serves as a housing for all online instruments and samplers. These are connected to omni-directional inlets (801565, TSI) by short conductive tubes. For underground measurements, the experimental box was attached to a frame rucksack, which was carried by the operator. While carried, the inlets in the breathing zone were at a distance of at least 20 cm from the operator to minimize personal cloud artifacts due to particles from clothing and hair (Licina et al., 2017). While riding the subway, the backpack was placed on a passenger seat, resulting in a measurement of the breathing zone of a seated person, similar to measurements on platforms. During reference ambient measurements, the box was secured in a modified stroller (Cab 2, Thule) to absorb vibrations. The temperature inside the box was kept within the operating range of the instruments to avoid discrepancies and extensive losses of volatile components from the samples.

2.4. On-line mobile measurements

PM size-distributions (OPS 3330, TSI) and PNC, the lung deposited surface area (LDSA) and size modes (DISCmini, Testo) were measured at 1 Hz resolution (0.2 Hz for OPS during platform measurements in one case), eBC and UVPM (MA200, Aethlabs; 150 mL min^{-1}, dual-spot) were measured at 0.1 Hz resolution. GPS coordinates were acquired at 1 Hz (64s, Garmin). Since GPS signal was not available in the subway, the time of door opening and closing was documented at each station with an accuracy of 1 s. All relevant events were noted or recorded with a cell

Table 2

Summary of on-line measurements (mean ± SD) of particle number concertation (PNC), particulate matter (PMx), lung deposited surface area (LDSA), equivalent black carbon (eBC), UV-absorbing PM (UVPM) and selected ratios during the sampling time for the metal analysis by ICP-MS for comparison. Routes B-F are described also in specific tables for each measurement based on the transects of the route (suppl. Tables S4–S10) to see the exact contribution of different environment.

Measurement	ID	Date	Duration	Start	Stop	PM_{10}	$PM_{2.5}$	PM_1	PNC	Size mode	LDSA	eBC	UVPM	$PM_{2.5}$/ PM_{10}	PM_1/ $PM_{2.5}$	eBC/ UVPM
		DD-MM-YY	min.	hh:mm	hh:mm	μg m^{-3}	μg m^{-3}	μg m^{-3}	pt cm^{-3}	nm	$μm^2$ cm^{-3}	ng m^{-3}	ng m^{-3}			
Ambient walk 1	**A1**	19-10-21	91	15:35	17:06	16 ± 33	1.6 ± 1.0	0.9 ± 0.4	10352 ± 17752	37 ± 5	18 ± 10	371 ± 313	836 ± 325	0.1	0.5	0.4
Ambient walk 2	**A2**	26-10-21	74	14:21	15:35	8 ± 1	2.6 ± 0.8	1.2 ± 0.1	3262 ± 1373	47 ± 7	8 ± 3	401 ± 411	661 ± 443	0.3	0.5	0.6
Ambient walk 3	**A3**	26-10-21	67	15:46	16:53	9 ± 29	2.5 ± 0.7	1.1 ± 0.1	5963 ± 20012	53 ± 9	13 ± 11	31 ± 15	497 ± 266	0.3	0.4	0.1
Ambient walk 4	**A4**	27-10-21	81	7:50	9:11	15 ± 55	1.6 ± 1.7	0.7 ± 0.2	39615 ± 12525	22 ± 5	42 ± 10	1125 ± 751	1610 ± 755	0.1	0.4	0.7
Ambient walk 5	**A5**	27-10-21	77	9:25	10:42	15 ± 70	1.8 ± 1.9	0.7 ± 0.4	21653 ± 15180	29 ± 5	30 ± 11	NA ± NA	NA ± NA	0.1	0.4	NA
Ambient walk 6	**A6**	27-10-21	74	13:13	14:27	8 ± 17	1.8 ± 0.8	0.8 ± 0.1	5049 ± 1452	49 ± 3	14 ± 2	625 ± 437	709 ± 416	0.2	0.5	0.9
Subway scouting 1	**B**	04-11-21	97	7:17	8:54	137 ± 102	57 ± 39	17 ± 11	5550 ± 1922	41 ± 10	13 ± 5	7359 ± 5730	4659 ± 5015	0.4	0.3	1.6
Subway scouting 2	**C**	05-11-21	72	7:48	9:00	147 ± 119	51 ± 33	15 ± 8	12237 ± 5851	38 ± 6	24 ± 5	6906 ± 4445	4946 ± 2668	0.3	0.3	1.4
Subway scouting 3	**D**	17-11-21	101	8:47	10:28	109 ± 105	41 ± 32	14 ± 7	6998 ± 4236	44 ± 8	16 ± 7	4267 ± 4299	3369 ± 3074	0.4	0.3	1.3
Subway scouting 4	**E**	24-11-21	51	9:31	10:22	170 ± 71	59 ± 16	19 ± 4	6068 ± 2308	55 ± 5	19 ± 5	8423 ± 3624	5773 ± 2005	0.3	0.3	1.5
Subway route morning	**F1**	07-12-21	118	7:54	9:53	104 ± 89	41 ± 34	12 ± 9	6528 ± 3042	41 ± 7	14 ± 6	4560 ± 4313	3458 ± 2835	0.4	0.3	1.3
Subway route noon	**F2**	07-12-21	119	12:28	14:27	73 ± 58	29 ± 21	8 ± 6	5486 ± 2166	42 ± 8	13 ± 6	3707 ± 2913	3294 ± 2451	0.4	0.3	1.1
Subway route afternoon	**F3**	07-12-21	98	16:32	18:10	121 ± 82	45 ± 30	14 ± 8	13138 ± 6454	39 ± 5	27 ± 10	6022 ± 4402	4632 ± 2388	0.4	0.3	1.3
Platform sampling 1	**G1**	17-05-22	181	14:08	17:08	231 ± 52	96 ± 10	25 ± 3	6099 ± 630	56 ± 3	20 ± 1	8998 ± 2860	6919 ± 1499	0.4	0.3	1.3
Platform sampling 2	**G2**	19-07-22	164	20:36	23:20	218 ± 50	85 ± 8	26 ± 2	7857 ± 713	54 ± 3	25 ± 1	9967 ± 1153	7142 ± 772	0.4	0.3	1.4
Platform sampling 3	**G3**	28-08-22	360	14:06	20:06	181 ± 32	105 ± 24	29 ± 5	5074 ± 1111	64 ± 7	19 ± 2	5030 ± 608	4421 ± 478	0.6	0.3	1.1

phone camera for further data analysis. Temperature and relative humidity were measured sporadically by a data-logger with sensors (Almemo, Ahlborn or BiVOC2V2, Holbach).

The OPS was factory calibrated (TSI) with Polystyrene Latex (PSL) according to ISO 12501-1/4 and the dead time correction was used. As the density of the subway particles can differ significantly from the ambient air (Cha and Olofsson, 2018), corrections to the OPS were used for all measurements performed in the subway interiors and trains using gravimetric analysis by the external filter sampling (Section 2.5.1.). To avoid particle losses and minimize the time delay, the OPS was placed directly under the inlet.

Prior to each measurement, the instruments' flowrates were checked/calibrated using a mass flow meter (4043 H, TSI) as well as zero-filter checks (OPS), and automatic zero adjustments (DISCmini) were performed. The time was synchronized based on the GPS satellites.

2.5. Off-line measurements

For ICP-MS analysis, PM samples were collected on 47 mm quartz filters (preconditioned at 500 °C for 5 h) using the SG10-2 personal sampler (GSA) with a constant flowrate of 9 lpm and a filter holder with or without $PM_{2.5}$ pre-impactor (Sioutas, SKC; $PM_{2.5}$ or PM_{total}). The same filters were utilized for gravimetry prior to ICP-MS analysis. For quality assurance, two additional samples were taken simultaneously on 47 mm polycarbonate (PC) and 37 mm Teflon filters by additional SG10-2 samplers. For SEM-EDX analysis, BiVOC2V2 sampler (Holbach) with a constant flowrate of 2 lpm was used with a filter-holder and 47 mm PC filter, which also served as a support for 5 silica wafers (P-type boron dotted 5 × 5 mm). The samplers were calibrated using a mass flow meter (4043 H, TSI). Information on the filter material is given in Table S1 in SI. Time and duration of sampling are given in Table 3. Both blanks and field blanks were collected from each filter type.

2.5.1. Gravimetric analysis for correction of OPS data

Simultaneous 6h long sampling of $PM_{2.5}$ and PM_{total} for gravimetric analysis on three filter types (Section 2.5.) was performed on August 28, 2022 from 14:06 to 20:06 on the central part of the *U-Bahn* platform of the main train station *CS-U1* (line *U5/U4* with a 10 min interval on both lines). Filters were weighed prior and after sampling using a microbalance (Cubis MCA2.7S-2S00-F, Sartorius) and pre-conditioned (45% RH, 22 °C) for 24 h in a weighing chamber (pureGMC 18-EPA1065) with a corona discharge for filter deionization. All filters were weighed five times and the aerosol mass on the filter was calculated as the weight difference of the averages before and after the exposure. Then, the average 6-h PM mass concentration ($\mu g\ m^{-3}$) was calculated. For quality control, blank filters were weighed twice before and after exposure.

The OPS was measuring simultaneously at 0.2 Hz. The $PM_{2.5}$ mode from the entire sampling period was compared to the mode of gravimetric mass concentration from the PC, PTFE and quartz filter. The entire size range of the OPS from 0.3 to 10 μm (for underground measurements only) was then corrected by the correction factor:

$$OPS\ correction\ factor = \frac{c\ (g)}{c\ (OPS)} \tag{1}$$

where c (g) is the mass concentration of $PM_{2.5}$ from gravimetry and c (OPS) is the mode of $PM_{2.5}$ mass concentration from OPS.

2.5.2. Metal analysis using ICP-MS

Samples have been digested according to DIN 14902 (VDI 2267-part 15) by a Microwave speedwave ENTRY (Berghof) with a mixture of nitric acid (HNO_3, ultrapure grade, 69%) and hydrogen peroxide (H_2O_2, ultrapure grade 30%). Subsequently, samples have been diluted to a final volume of 50 mL with a final concentration of 5% of HNO_3. All the samples have been filtered utilizing a 0.2 μm syringe filter (Whatman Puradisc, 25 mm, 0.2 μm) and analyzed by Inductively Coupled Plasma

Table 3
Metal analysis by ICP-MS from mobile (A-G) and stationary (Ref) samples. Tables describing each transect and contribution of subway mobile measurements (B-F) are in the Supporting Information.

Measurement type	Reference ambient $PM_{2.5}$	Repetitions of the same ambient walk				Subway and railway scouting				Repetitions of a subway route at the same day			Subway platform stationary		Subway/ ambient
Route type/ stations	Station at UniBW	Urban PM background				NS-U, IR-U, OP-U, NS-U/S	OB-U, MC-U, NS-U/S	CS-U1, CS-U2, CS-R, OU-U	CS-U2, CS-U1, NS-U/S	NS-U/S, OB-U, OU-U, CS-R, CS-S, NS-U/S			CS-U1		Indoor/ outdoor ratio
ID	**Ref**	**A3**	**A4**	**A5**	**A6**	**B**	**C**	**D**	**E**	**F1**	**F2**	**F3**	**G1**	**G2**	**G1/Ref**
Sampling date	17-05-22	26-10-21	27-10-21	27-10-21	27-10-21	04-11-21	05-11-21	17-11-21	24-11-21	07-12-21	07-12-21	07-12-21	17-05-22	19-07-22	
Start sampling (hh:mm)	9:00	15:46	7:50	9:25	13:13	7:17	7:48	8:47	9:31	7:54	12:28	16:32	14:08	20:33	
Stop sampling (hh:mm)	9:00	16:53	9:11	10:42	14:27	8:54	9:00	10:28	10:22	9:53	14:27	18:10	17:08	23:21	
Sampling time (min.)	1440	67	82	78	74	97	72	102	51	118	119	97	180	168	
Sampled air (m^3)	641	0.60	0.74	0.70	0.67	0.88	0.65	0.91	0.46	1.07	1.07	0.88	1.53	1.43	
PM fraction	$PM_{2.5}$	PM_{tot}	PM_{tot}	PM_{tot}	PM_{tot}	PM_{tot}	PM_{tot}	PM_{tot}	PM_{tot}	PM_{tot}	PM_{tot}	PM_{tot}	$PM_{2.5}$	PM_{tot}	$PM_{2.5}$
Fe ($\mu g\ m^{-3}$)	**0.073**	**2.6**	**1.6**	<LOQ	<LOQ	**115**	**123**	**20**	**122**	**56**	**49**	**91**	**67**	**171**	**911**
Mn ($ng\ m^{-3}$)	**12.6**	**35**	**28**	**28**	<LOQ	**1045**	**1123**	**177**	**1113**	**523**	**503**	**804**	**617**	**1560**	**49**
Cr ($ng\ m^{-3}$)	**1.2**	**205**	**159**	**154**	**180**	**420**	**448**	**151**	**786**	**306**	**215**	**384**	**197**	**484**	**163**
Cu ($ng\ m^{-3}$)	**2.8**	**250**	**143**	**113**	**117**	**641**	**577**	**120**	**651**	**439**	**357**	**635**	**262**	**534**	**95**
Ni ($ng\ m^{-3}$)	**0.51**	**232**	**73**	**57**	**109**	**317**	**308**	**76**	**683**	**206**	**141**	**245**	**146**	**344**	**286**
V ($ng\ m^{-3}$)	**0.10**	<LOQ	<LOQ	<LOQ	<LOQ	<LOQ	<LOQ	<LOQ	<LOQ	<LOQ	<LOQ	<LOQ	<LOQ	**31**	NA
Pb ($ng\ m^{-3}$)	**0.90**	**24**	**25**	**22**	<LOQ	<LOQ	<LOQ	<LOQ	**44**	**16**	<LOQ	**16**	<LOQ	**9**	NA
Mn to Fe (%)	17	1.3	1.8	NA	NA	0.91	0.91	0.89	0.91	0.93	1.03	0.88	0.92	0.91	
Cr to Fe (%)	1.7	7.9	9.9	NA	NA	0.37	0.36	0.76	0.64	0.55	0.44	0.42	0.30	0.28	
Cu to Fe (%)	3.8	9.6	8.9	NA	NA	0.56	0.47	0.60	0.53	0.78	0.73	0.70	0.39	0.31	
Ni to Fe (%)	0.7	8.9	4.5	NA	NA	0.28	0.25	0.39	0.56	0.37	0.29	0.27	0.22	0.20	

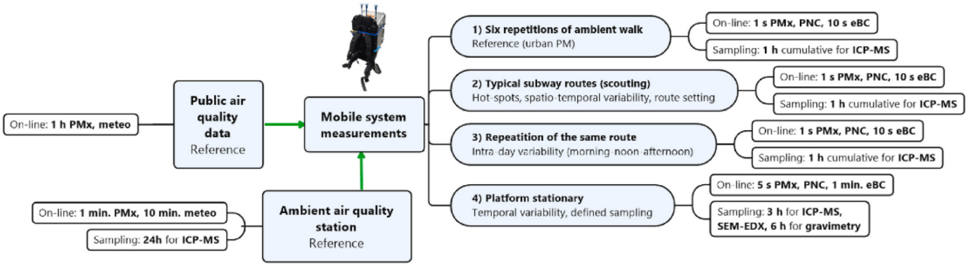

Fig. 1. Strategy of measurements and sampling of the subway micro-environment using the mobile measuring system; PNC, particle number concentration; PM, particulate matter; eBC, equivalent black carbon; ICP-MS, inductively coupled plasma mass spectrometry.

Mass Spectrometry (ICP-MS, Agilent Technologies 8900). Calibration standard curves for all measured elements were used for the quantification, as well as for the calculation of limits of detection (LOD) and quantification (LOQ). Three technical replicates have been performed for each sample, field and method blank. To check the extraction efficiency on each sample, prior to the digestion, a spike with a concentration of 20 μg L^{-1} of internal standard mix for ICP-MS systems was added. The constancy and the correctness of the analytical values of the used internal standard (ISTD) were checked in time through a control chart that documents the trend of the ISTD values.

2.5.3. *Imaging and single particle elemental analysis using SEM-EDX*

Samples used for analysis via SEM-EDX were stored in a desiccator under vacuum for 24 h to ensure removal of volatile components. Afterwards, 12 mm circular punches were cut from 47 mm PC filters, which were then transferred to 12 mm SEM pin stub sample holders with EDX suitable adhesive carbon pads in between. To minimize charging effects, the surface of the filters was coated in a Q150T ES Plus sputter device (Quorum technologies) with a thin carbon layer utilizing a woven carbon fiber string in pulsed cord evaporation mode.

Particles collected from subway stations were imaged with the built in Inlens and SE2 detectors of a Gemini Sem 360 (Carl Zeiss). EDX analysis was conducted with an Ultim Max 40 detector (Oxford instruments) at the optimum detector working distance of 8.5 mm. Usage of a silicon drift detector with a thin detector window ensured suitability for analysis of low-Z elements ($Z > 6$) such as C and O. The EHT was set to 5 kV for particles smaller than 0.5 μm to reduce the interaction volume of the beam, thus minimizing total passage of the beam through the particles with subsequent excitement of underlying materials such as the PC filter. Larger particles were measured with either 12 kV (particle sizes from 0.5 to 2.5 μm) or 20 kV acceleration voltage (particles >2.5 μm). Semi-quantitative EDX data was recorded for over 180 000 particles, followed by automated classification based on their main contributing elemental concentrations.

2.6. *Reference stationary PM sampling and measurements*

An air quality station on the university campus (GPS: 48°04′37.5″N 11°38′21.2″E) served as a reference for the subway measurements. A high-volume sampler (DHA-80, Digitel) with a $PM_{2.5}$ sampling head and a flowrate of 500 lpm was used to compare elemental composition between ambient air and in the subway. Daily 24-h samples starting at 9 a. m. were collected on 150 mm filters (Whatman QM-A, pre-conditioned for 5 h at 500 °C). PM size-distribution with 1 min time-resolution (APDA-372, Horiba with the Sigma-2 sampling head complying with VDI 2119-4, $PM_{2.5}$ according to EN14907 and PM_{10} EN 12341) and a weather station with 10 min data acquisition (Vantage 2 Pro, Davis) supported the interpretations.

2.7. *Data analysis*

On-line raw data were manually checked for potential errors caused by mobile use of instruments and processed in the manufacturer's software. PNC data from DISCmini were corrected for induction effects and cross-checked against a CPC (5416, Grimm) prior to the campaign. OPS data were corrected (see chapter 3.5.1.). BC and UVPM data (MA200, AethLabs) were smoothed using the Optimized Noise-reduction Averaging (ONA) algorithm with a smoothing factor of 0.01 (Hagler et al., 2011; Liu et al., 2021; Ji et al., 2022). When GPS signal was available, PNC and PM data were merged together with the GPS coordinates and plotted on maps using ArcGIS Pro software (ESRI). ICP-MS and SEM-EDX data were processed with the manufacturer's software.

3. Results and discussion

3.1. *Reference ambient PM measurement (stationary and mobile)*

For comparison with subway measurements, the average ambient concentrations of PM_1, $PM_{2.5}$ and PM_{10} on the university campus in May 2022 were 6 ± 4, 7 ± 4, 11 ± 5 μg m^{-3}, in July 2022 5 ± 3, 6 ± 4, 12 ± 7 μg m^{-3}, and in August 2022 5 ± 2, 7 ± 3, 11 ± 6 μg m^{-3}, respectively. At the same time, $PM_{2.5}$ values measured at the background station of the Bavarian Monitoring System for Air Quality (LÜB) in *Johanneskirchen* (Munich; *https://www.lfu.bayern.de/luft/immissionsmessungen/*), were 8 ± 4, 9 ± 4 and 9 ± 4 μg m^{-3} in May, July and August 2022, respectively. In October, November and December 2021, the $PM_{2.5}$ concentration in *Johanneskirchen* were 7 ± 4, 6 ± 5, 5 ± 5 μg m^{-3}, respectively. In summary, $PM_{2.5}$ levels on the campus were slightly lower than in the city. This confirms our reference site and its classification as an urban background station.

Six repetitions of the identical 1-h route in the vicinity of the station *Neuperlach Süd* (*NS-U/S*, see Fig. S2 with a detailed description in the SI) were used as comparison with the subway measurements (Fig. 4). They showed relatively high ambient spatio-temporal variability in PNC (Table 2) with the main road as the dominant source. Traffic strongly contributed to PNC values at the above-ground *U5* terminus *NS-U/S*. PNC were highest during the morning rush-hour (Ambient walk A4 and A5) and lowest in the early afternoon when traffic was reduced (A2, A6). According to DISCmini, the size mode ranged between 22 and 53 nm. PM_1 dynamics did not follow the PNC trend because ultrafine particles contribute little to the total mass concentration due to their low mass per particle. Furthermore, the OPS size range started at 300 nm. The PM_1/$PM_{2.5}$ ratio was similar for all 6 routes (0.4–0.5), which could indicate the same/similar dominant source of fine particles. PM_{10} had high SD (noise) due to the 1 Hz acquisition time and greater dynamics. Average eBC value between walks was 511 ± 417 ng m^{-3} and average ultraviolet absorbing PM (UVPM) was 863 ± 525 ng m^{-3} with the highest value of 1.6 μg m^{-3} on October 27, when PNC was also highest. Since UVPM is an indicator of wood smoke and the measurements were taken during the heating season, domestic heating could contribute to the elevated background concentrations. The eBC/UVPM ratio was 0.7 on this day, otherwise, it varied from 0.1 to 0.9 between walks. The results of metal analysis by ICP-MS from the cumulative sampling can be found in Section 3.5.

3.2. Corrections of on-line subway measurements using gravimetry

The average $PM_{2.5}$ mass concentrations at the *CS-U1* platform (August 28, 2022, 14:06-20:06) calculated from PC, PTFE and quartz filters (simultaneous sampling) were 100.2 ± 4.13, 103.2 ± 1.65 and 102.9 ± 5.66 μg m^{-3}, respectively, with a median of 102.9 μg m^{-3}, whereas the $PM_{2.5}$ median measured on-line by the OPS was 48.8 μg m^{-3} (with a preset density 1 g cm^{-3} and default refractive index). Therefore, the correction factor of 2.11 from both medians was determined. This should roughly correspond to the average effective density of $PM_{2.5}$ in g cm^{-3}. However, as aerosol composition and particle structure vary over time, place and particle size, a more detailed measurement of effective density would be beneficial for precise correction. This aspect should be considered while comparing absolute values from on-line optical PM instruments among different studies but also within the same subway system due to different micro-environments. In Stockholm, precisely measured subway particle effective density was 1.87 ± 0.22 g cm^{-3}, which is in a similar range (Cha and Olofsson, 2018), however, the correction factors in Athens, Barcelona and Oporto suggest that there is high variability among subway systems (Martins et al., 2016), probably also in effective densities. One of the reasons could be different relative contributions of subway generated particles to PM e.g., due to different air exchange rates with the ambient environment and/or different emission patterns. During the same time, the PM_{total} concentration was 209.0 ± 7.79 μg m^{-3} (gravimetry) resulting in $PM_{total}/PM_{2.5}$ ratio of 2.1 (assuming zero sampling losses). Based on the corrected OPS, the PM_{10} concentration was 181 μg m^{-3} implying that particles larger than 10 μm in size should contribute about 28 μg m^{-3} to the PM_{total}. As a result, $PM_{2.5}/PM_{10}$ ratio was 0.6, PM_1/PM_{10} was 0.2, and $PM_1/PM_{2.5}$ was 0.3. The sampling was done on Sunday, however, the number of persons on the platform was comparable to weekdays (not quantified).

3.3. On-line PM subway measurements – general overview

Table 1 summarizes the average concentrations of PM, PNC, eBC and UVPM at selected underground and overground platforms of the *U-Bahn, S-Bahn* and railway main train station from all our measurements and lists the station abbreviations used in the figures.

The lowest PM mass concentrations were measured at *Michaelibad* (*MC-U*) with PM_{10}, $PM_{2.5}$, PM_1 = 59 ± 26, 27 ± 14, 9 ± 4 μg m^{-3}, respectively. The highest average concentrations were at the deeper *U-Bahn* platform of the *Hauptbahnhof* transfer station (*CS-U2*) with PM_{10}, $PM_{2.5}$, PM_1 = 220 ± 32, 72 ± 7 and 20 ± 0.3 μg m^{-3}, respectively. These values are concerning when compared to the WHO Air Quality Guidelines values of daily PM_{10} and $PM_{2.5}$ for outdoor air.

Table 2 shows the comparison between the different mobile and platform measurements, where **A1-A6** are repetitions of ambient walks, **B-E** are subway scouting trips, **F1-F3** are repetitions of the same ride in the morning, midday and afternoon, and **G1-G3** are several hours long stationary measurements on the *CS-U1* platform. The highest concentrations of PM_{10}, $PM_{2.5}$, PM_1 = 231 ± 52, 96 ± 10, 25 ± 3 μg m^{-3}, respectively, were recorded during the 3h long stationary measurement on May 17. This was in a similar range as at the Prague transfer station *Muzeum* with 214.8, 93.9 and 44.8 μg m^{-3} of PM_{10}, $PM_{2.5}$, PM_1, respectively (Cusack et al., 2015), however, the PM_1 in Munich was 2.3 times lower. The reason could be a lower contribution of ambient traffic-related particles to PM_1, which could be caused by both the reduced nearby traffic sources in Munich and/or lower air exchange with outside air (ventilation). This hypothesis is supported by the PNC values (Table 2, Fig. 4), which are, on average, at a similar level to the ambient urban background. This is also valid for LDSA and size-mode, both measured in the range of 10–300 nm and associated with PNC. $PM_{2.5}/PM_{10}$ ratio in the subway ranged from 0.4 to 0.6 and is higher than for ambient air (see Section 4.2.). Based on reviews of Carteni (Carteni et al., 2020) and Chang (Chang et al., 2021) on subway PM in other cities, the highest average PM_{10} and $PM_{2.5}$ concentrations of 470 μg m^{-3} and 260 μg m^{-3}, respectively, were recorded on the platform in Stockholm in 2000 (Johansson and Johansson, 2003). In Rome in 2005, PM_{10} was 409 ± 22 μg m^{-3} (Perrino et al., 2015). High PM_{10} values were also observed in Seoul, Barcelona, Paris, Beijing, Milan, Budapest, Athens and other cities, while relatively low concentrations were determined in Naples, Sydney, and Turin (Carteni et al., 2020).

The mean eBC concentration at the *CS-U1* platform was 8.0 ± 2.6 μg m^{-3} (**G1-G3**) and mean UVPM 6.2 ± 1.5 μg m^{-3}, which was significantly higher than in ambient air (during ambient walks **A1-A6** the mean eBC was 0.5 ± 0.4 μg m^{-3} and the highest values 2.5 ± 1.5 μg m^{-3} were recorded on December 7. 2021). Both eBC and UVPM correlated with PM measured by OPS. For comparison, in subway in Sao Paolo eBC were 11.33 ± 12.98 μg m^{-3} (Targino et al., 2021), in Helsinki 6.3 ± 1.8 μg m^{-3} (Aarnio et al., 2005), and in Montreal 4.6 ± 2.3 μg m^{-3} (van Ryswyk et al., 2017). Sources of BC are typically linked to combustion processes (e.g. diesel emissions), however, since we observed only minor amounts of soot-agglomerates via SEM in the Munich subway, we hypothesize that most of the eBC readings is caused by the interference of light absorbing iron oxide particles, which we identified as the major source of aerosol mass based on results from ICP-MS (Section 3.5.) and SEM-EDX (Section 3.6.). Moreover, PNC levels in the subway also suggested low intake of traffic related particles. Other sources of carbonaceous particles in the subway could be disc brake abrasion, as graphite is added to brake discs as a lubricant (Lyu and Olofsson, 2020), and carbon from electric motor brushes (Font et al., 2019). However, based on our SEM-EDX and ICP-MS analysis of trace elements typical for brake emissions, this cannot explain all eBC readings. Nevertheless, as the micro-aethalometer values correlated with the subway-PM measured by OPS, it was a good indicator of PM hot-spots. The possibility of micro-aethalometer artifacts in the subway has already been discussed (Midander et al., 2012; Targino et al., 2021) and we expect that interferences might affect published results from other subway studies. Therefore, this topic should be the subject of further investigation.

3.3.1. Subway scouting: hot-spots identification, effect of platform design on PM

Scouting rides (Table 2, **B-E**) represent various common trips of about 1h in the Munich subway system in November 2021 (same season as the reference ambient walks). As each of these routes was different, the exact routes are listed in SI (Tables S2–S8) with mean values of PM_{10}, $PM_{2.5}$, PM_1, PNC, eBC and UVPM for each transect (where the ambient walk is *aw*, the indoor walk *iw*, the subway ride *r*, and the platform stationary is *s*). The time of cumulative personal sampling for ICP-MS (section 3.5.) is marked in bold.

Based on these data, hot-spots were identified as transfer stations with higher train frequencies. The highest PM_{10} average values from repeated measurements (Table 1) were measured at *CS-U2*, the deepest of the *U-Bahn* platforms with values of 220 ± 32 μg m^{-3}, while the *U-Bahn* station *CS-U1* located above this platform, had an average concentration of 174 ± 40 μg m^{-3}. The depth of the station may play a role (Carteni et al., 2015) but number of trains, station design (Table 1) and eventually ventilation seem to be responsible for the differences. *CS-U2*, with its four tracks not-separated by a wall, allows for a greater volume of mixing air compared to *CS-U1* with two tracks. The total train frequency is similar, but the peak-hour frequency at *CS-U2* is nearly twice as high. However, even with the same actual train frequency, PM_{10} concentrations at the *CS-U2* station were higher than at *CS-U1*

(Table S4). An interesting comparison is between the *U-Bahn* transfer station *Innsbrucker Ring* (*IR-U*, Table S2) with the lowest observed PM_{10} (114 μg m^{-3}, only one measurement) and *CS-U2* with the highest PM, which has almost the same platform design. Given that the difference in PM_{10} was approximately a factor of two when measured with similar actual train frequencies (Table S2, Table S4), it appears that *IR-U* is better ventilated. To investigate the difference in PM between two-track platforms, we compared *U-Bahn* station *Odeonsplatz* (*OU-U*, 179 ± 52 μg m^{-3}) with two tracks separated by a wall and *U-Bahn* station *CS-U1* with the shared platform mentioned above. As seen in Table 1, no significant difference in PM was observed. The measurements for these comparisons were not done simultaneously, but based on the standard deviations of repeated measurements at different times and even seasons, the concentrations were relatively stable. However, more measurements would be needed to accurately quantify the differences. Additional CO_2 measurements would help to investigate the effect of ventilation on PM. Another important hot-spot among the investigated routes was the *U-Bahn* transfer station *Ostbahnhof* (*OB-U*, 205 ± 72 μg m^{-3}), where $PM_{2.5}$ and PM_1 reached 80 ± 18 μg m^{-3} and 21 ± 5 μg m^{-3}, respectively. The busy *S-Bahn* underground station *Hauptbahnhof (CS-S*, a two-track platform with extended platforms on both sides of the tracks) yielded PM_{10} 236 ± 52 μg m^{-3} in the scouting measurement on November 24, 2021, but the mean value of the other investigations was 126 ± 89 μg m^{-3} and the lowest measured PM_{10} of 34 ± 21 μg m^{-3} on December 7, 2021 (Table S6). The neighboring *U-Bahn* stations *CS-U1* and *CS-U2* showed higher PM concentrations even at lower train frequencies. Because *S-Bahn* trains exit the tunnel to the surface 200 m beyond the *CS-S* station, it is probably better ventilated. More measurements would be needed to compare, which train emits/resuspends more particles.

In summary, the recommended PM levels for ambient air by the WHO (World Health Organization, 2021) were exceeded at almost all measurement sites and are, therefore, high for long-term exposure.

3.3.2. Repetition of the same route: intra-day variability, indoor/outdoor comparison

Based on the subway scouting rides (section 3.3.1.), a route was defined for repeated measurements. The heat-map (Fig. 4) summarizes the on-line measurements of the repetitions of the same route in the morning (*m*), noon (*n*) and afternoon (*a*) and shows how many times the concentrations of PM_1, $PM_{2.5}$, PM_{10}, PNC, eBC and UVPM were elevated on the specific transect of the route (x-axis) compared to the average concentrations of the reference ambient routes (section 3.1.). Ambient walking measurements (*aw*) at the beginning and end of each route show the deviation from the reference ambient measurement at a given time. Stationary measurements at selected platforms (*s*) and subway rides (*r*) are located between the dashed vertical lines indicating train boarding and exiting.

Generally, PM concentrations were highest during the morning and afternoon rush-hours and lowest during midday. Train frequency was a key factor, as it was 5 min in the morning (7-9 am) and afternoon (3-7 pm) rush-hours and 10 min during noon, which corresponds with measured PM (the morning measurement period occurred between 7:54-9:53 and the afternoon period between 16:32-18:10). Other factors may contribute to intra-day variability, such as the number of people moving on the platform, as discussed e.g. in the Shanghai study (Zhao et al., 2017).

At the stations (*s*) measured, the highest PM concentrations were generally at transfer stations with more lines and thus higher overall train and passenger frequencies. $PM_{2.5}$ concentrations at *OB-U* station were 44 times higher than ambient urban background levels. During the ride, the PM concentrations were usually greater in the tunnel than on the platforms. This was observed also in Prague (Braniš, 2006), but not in Barcelona (Martins et al., 2015). The tunnel was found to be a dominant source of PM and the quality/lack of train ventilation influenced how much PM entered the trains. Similar findings have been reported in Athens (Martins et al., 2016) and Naples (Cartenì et al., 2015). At *S-Bahn* platforms the PM concentrations were lower than at *U-Bahn* platforms as well as during *S-Bahn* trips. As discussed in Section 3.3., PNC inside trains and on platforms were generally at ambient levels. On elevators, all PM concentration decreased to the half while PNC values increased suggesting that there is a sufficient air exchange with the outside, which is more polluted by traffic in the city center.

To compare personal exposure, average time periods spent at the platforms and in the trains as well as average human breathing rates would need to be considered. In Barcelona, concentrations were higher at platforms, however, based on their calculations, the dose was double in trains due to the longer exposure time (Martins et al., 2016).

From the heat-map in Fig. 4, it is visible that spatial variability of PM is more important than temporal and the PM concentrations are raising when travelling from open-space terminus *NS* to the city.

Because no emissions from combustion processes have been observed at the majority of platforms, eBC and UVPM readings are most likely FePM interferences, as discussed in Section 3.3. However, the MA-200 instrument can explain the PM spatio-temporal variability similar to OPS. As the MA-200 has a suitable size for mobile measurements, its use for identifying hot-spots might be interesting and more detailed analysis of eBC and UVPM might be part of a future study.

3.3.3. Micro-scale PM spatio-temporal variability during the specific rides, old vs. new trains

Exemplarily, Fig. 2 shows the detailed variability of PM and PNC in 1 Hz resolution with a 10 s moving average (line). It represents the typical ride from the terminus *NS-U/S*, which is over-ground so ambient urban PM and PNC concentrations were present at the station and inside the train. This represents an ideal start for investigating the dynamics of concentrations inside the train and the behavior of PM in the tunnel system.

PM_{10} concentrations started to raise when the train entered the tunnel and reached about four times higher values within only 1 min until the next stop. The rapid exchange was accelerated by open windows in the wagon of the “old” train, which was empty. PM concentrations increased relatively uniformly throughout the entire ride to downtown. In less than 20 min, PM_{10} reached up to one order of magnitude higher levels at *U-Bahn* station *CS-U1* (city center). Opening the doors at the stations (indicated by vertical lines) typically caused an immediate slight decrease in PM_{10} concentrations as the air was exchanged and diluted. The largest decrease occurred at the *U-Bahn* station *IR*, which has an exceptionally large size and relative low concentration levels, as discussed in Section 3.3.1. The station itself did not serve as a significant sink for PM_{10} from the tunnel since concentrations rose sharply up- and downstream of the *IR* platform.

$PM_{2.5}$ and PM_1 were increasing gradually (slightly step-wise) with a similar trend, but the overall dynamics were lower with concentrations up to about 100 and 25 μg m^{-3}, respectively. PM_1 remained stable and the effects of the stations were negligible.

PNC did not follow the trend of PM and remained mostly at urban background levels, as shown previously (Table 2, Fig. 4). At the *U-Bahn* station *Neuperlach Zentrum* (*NZ-U*), PNC were around 11 500 pt cm^{-3}, which is appr. twice as high as the usual values in the *U-Bahn*. Most likely, traffic related particles were introduced into the subway system, since there is a large bus station, a shopping mall, and a relatively busy street above the *NZ-U* station. Interestingly, PNC were already rising at the previous subway stop. A similar situation on a smaller scale occurred at the next stop *U-Bahn* station *Quiddestrasse* (*QI-U*), and thereafter, the PNC decreased to “normal” levels within 2 min of travelling, while $PM_{2.5}$ continued to increase. The lower PNC in tunnels and stations in the city center might be caused by the lack of ventilation rather than absence of traffic-related particles above the subway.

The same experimental route was repeated with a new train (*n*) with air conditioning and closed windows (Fig. S6). First, on the way from *CS-U1* to the terminal station *NS-U/S* and then, after a short brake, back to the *CS-U1* platform with exactly the same train. The average

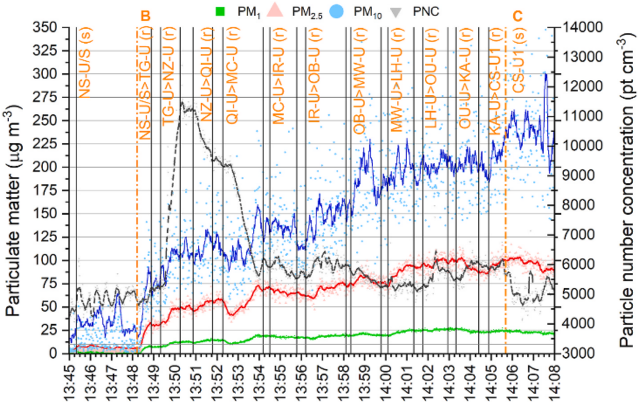

Fig. 2. PM$_1$, PM$_{2.5}$, PM$_{10}$ and particle number concentration (PNC) dynamics during the ride (B) from the over-ground subway terminal station NS-U/S towards CS-U1 station by the old train (U5 line) on 17. 5. 2022. First vertical black line represents entering the train, which was waiting in the station (s), orange dashed line entering the tunnel and following black lines indicate door opening/closing at the stations (stations' abbreviations are above with indication of the direction of the ride (r), list of abbreviation is in the Table 1). Scatter represents 1s dynamics of concentrations and color lines are 10s moving averages. PM$_x$ data of the part B and C were corrected based on the effective density of PM$_{2.5}$ (2.106 g cm^{-3}) measured at CS-U1 on 28. 8. 2022.

concentrations of PM$_1$, PM$_{2.5}$, PM$_{10}$ were only 8-10% higher on the way from *CS-U1*, PNC were 2% higher. After the 40 min measurement at *CS-U1*, the same route to *NS-U/S* was repeated by an old train (o). Surprisingly, the difference in dynamics between old and new train in the same direction was only 7-12% for PM$_1$, PM$_{2.5}$, PM$_{10}$ and 13% for PNC. The air conditioning systems seemed to be not efficient enough or were not equipped with air filters, which would clean the indoor air. Therefore, the air conditioning systems should be improved to achieve higher filtration efficiencies, such as in Barcelona (Querol et al., 2012).

3.4. PM dynamics on subway platforms during stationary measurements

As described in Section 4.2. and 4.3., PM concentrations measured stationary at the *U-Bahn* platform *CS-U1* were relatively stable in the range of 10^2 µg m^{-3}of PM$_{10}$ (Table 2, Fig. 4). PM and PNC were illustrated in Fig. 3, which shows a 42-min representative section in order to investigate the source and what might influence the microdynamics. The columns indicate the time the train was in the station (*U5* in brown, *U4* in green), the arrow indicates the direction of travel (left: *Laimer Platz to Theresenwiese*, right: direction *NS-U/S to Arabellapark*).

Significant signals of PNC were associated with high numbers of people exiting the train (e.g. at 14:13-14:14), but the exact number was not noted. The signal decrease occurred relatively fast after departure of the train due to the wind caused by train movement (piston effect). The movement of the train is also affecting PM, probably due to the entering of polluted air from the tunnel. A similar behavior was described e.g. in Barcelona (Moreno et al., 2014). In some cases, when two trains left at the same time but in opposite directions (e.g. time 14:42-14:43 and 14:35), the PM$_{10}$ concentration raised rapidly for a short time. In this

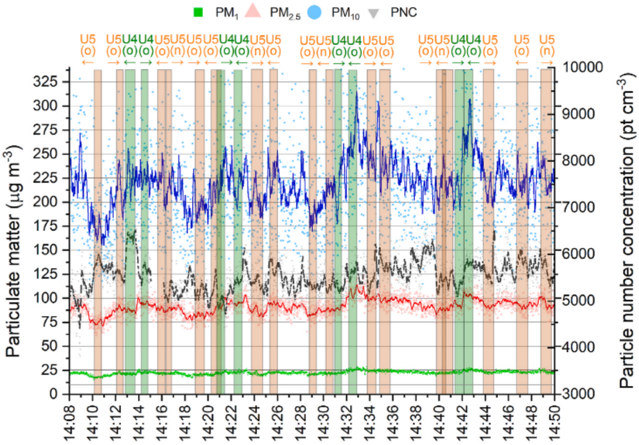

Fig. 3. Dynamics of PM$_1$, PM$_{2.5}$, PM$_{10}$ and particle number concentration PNC (1s scatter) with 10s moving averages (color lines) at the Munich U4/U5 subway station CS1-U on 17. 5. 2022. Columns indicate trains in the station (arrival-departure), the line U4 (green) and U5 (brown) and the direction is indicated above (right arrow is towards NS U5/Arabelespark U4 station), "o" indicates the old train and "n" the new train.

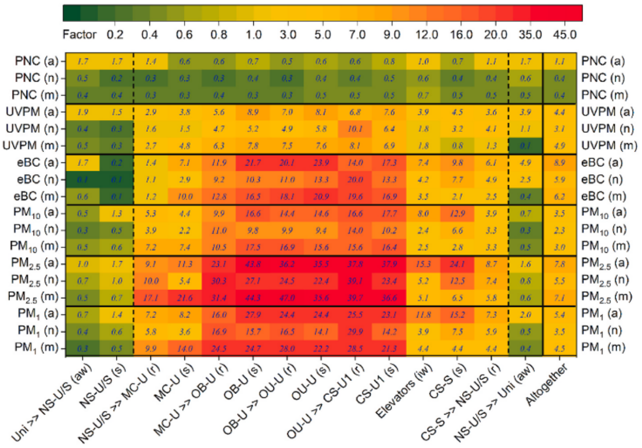

	Uni >> NS-U/S (aw)	NS-U/S (s)	NS-U/S >> MC-U (r)	MC-U (s)	MC-U >> OB-U (r)	OB-U (s)	OB-U >> OU-U (r)	OU-U (s)	OU-U >> CS-U1 (r)	CS-U1 (s)	Elevators (iw)	CS-S (s)	CS-S >> NS-U/S (r)	NS-U/S >> Uni (aw)	Altogether	
PNC (a)	1.7	1.7	1.4	0.6	0.6	0.7	0.5	0.6	0.6	0.8	1.0	0.7	1.1	1.7	1.1	PNC (a)
PNC (n)	0.5	0.2	0.3	0.3	0.3	0.4	0.3	0.4	0.4	0.5	0.6	0.4	0.4	0.6	0.4	PNC (n)
PNC (m)	0.4	0.4	0.3	0.3	0.4	0.3	0.3	0.5	0.5	0.5	0.7	0.5	0.5	0.5	0.4	PNC (m)
UVPM (a)	1.9	1.5	2.9	3.8	5.6	8.9	7.0	8.1	6.8	7.6	3.9	4.5	3.6	3.9	4.4	UVPM (a)
UVPM (n)	0.4	0.3	1.6	1.5	4.7	5.2	4.9	5.8	10.1	6.4	1.8	3.2	4.1	1.1	3.1	UVPM (n)
UVPM (m)	0.5	0.3	2.7	4.8	6.3	7.8	7.5	7.6	8.1	6.9	1.8	0.8	1.3	0.1	4.9	UVPM (m)
eBC (a)	1.7	0.2	1.4	7.1	11.9	21.7	20.1	23.9	14.0	17.3	7.4	9.8	6.1	4.9	8.9	eBC (a)
eBC (n)	0.1	0.1	1.1	2.9	9.2	10.3	11.0	13.3	20.0	13.3	4.2	7.7	4.9	2.5	5.9	eBC (n)
eBC (m)	0.6	0.1	1.2	10.0	12.8	16.5	18.1	20.9	19.6	16.9	3.5	2.1	2.5	0.4	6.2	eBC (m)
PM_{10} (a)	0.5	1.3	5.3	4.4	9.9	16.6	14.4	14.6	16.6	17.7	8.0	12.9	3.9	0.7	3.5	PM_{10} (a)
PM_{10} (n)	0.3	0.5	3.9	2.2	11.0	9.8	9.9	9.4	14.0	10.2	2.4	6.6	3.3	0.3	2.3	PM_{10} (n)
PM_{10} (m)	0.5	0.6	7.2	7.4	10.5	17.5	16.9	15.6	15.6	16.4	2.5	2.8	3.3	0.5	3.0	PM_{10} (m)
$PM_{2.5}$ (a)	1.0	1.7	9.1	11.3	23.1	43.8	36.2	35.5	37.8	37.9	15.3	24.1	8.7	1.6	7.8	$PM_{2.5}$ (a)
$PM_{2.5}$ (n)	0.7	1.0	10.0	5.4	30.3	27.1	24.5	22.4	39.1	23.4	5.2	12.5	7.4	0.8	5.5	$PM_{2.5}$ (n)
$PM_{2.5}$ (m)	0.5	0.7	17.1	21.6	31.4	44.3	47.0	35.6	39.7	36.6	5.1	6.5	5.8	0.6	7.1	$PM_{2.5}$ (m)
PM_1 (a)	0.7	1.4	7.2	8.2	16.0	27.9	24.4	24.4	25.5	23.1	11.8	15.2	7.3	2.0	5.4	PM_1 (a)
PM_1 (n)	0.4	0.6	5.8	3.6	16.9	15.7	16.5	14.1	29.9	14.2	3.9	7.5	5.9	0.5	3.5	PM_1 (n)
PM_1 (m)	0.3	0.5	9.9	14.0	24.5	24.7	28.0	22.2	28.5	21.3	4.4	4.4	4.4	0.4	4.5	PM_1 (m)

Fig. 4. Spatio-temporal variability of PM_1, $PM_{2.5}$, PM_{10}, equivalent black carbon (eBC), UV-absorbing PM (UVPM), particle number concentration (PNC) during the repetition of the same route in the morning (m), noon (n) and afternoon (a) on 12. 7. 2021. Each route is divided into ambient walk (aw), indoor walk (iw), stationary measurements at platforms (s) and rides by the train (r). Dashed line indicates entering and exiting the train. Heatmap represents the ratio of the average absolute concentrations of each part of the route to the overall average of 6 repetitions of a typical ambient walk (urban PM background) around the NS-U/S station. Last column "Altogether" represents the average from the whole route. Route starts and finishes at the campus of the Bundeswehr University (Uni) and consist of underground (U) and overground (S) stations listed in Table 1.

experiment, there was no significant difference in PM concentrations between new and old trains. Most likely, both trains resuspended PM similarly and any possible difference in emissions did not appear on the platform.

3.5. ICP-MS metal analysis

Table 3 shows the results of ICP-MS analysis for personal samples from 4 typical ambient walks (**A3-A6**) and 24-h reference stationary ambient air sampling using a high-volume sampler for comparison (**Ref**), 4 scouting subway routes (**B-E**), 3 repetitions of the same route (**F1-F3**), and two stationary platform measurements (**G1, G2**). All samples contain the PM_{total} fraction except **G1** and **Ref**, where it is $PM_{2.5}$. All routes are described in the previous chapters (Table 2 contains corresponding averages from on-line instruments) and additional parameters are available for comparison (Table 1, Tables S2–S8). In addition to Fe, Mn, Cr, Cu, Ni, V and Pb listed in Table 3, other elements were analyzed of which Na, Al, K, Zn and Ba were excluded from the dataset due to high blank concentrations. The reason for this could be the short sampling time, contamination and/or use of quartz filters. For other elements (Be, Mg, V, Co, As, Se, Ag, Cd, Sb and Th), both blanks and all samples were below the limit of detection (LOQ). This may be due to short sampling times and/or low concentrations in the air.

During the subway scouting rides, the highest concentrations of iron (Fe) in the PM_{total} fraction of 123 μg m^{-3} was recorded on November 5, 2021, while the highest concentration during the ambient walks was 2.6 μg m^{-3} on October 26. 2021. Fe was the dominating metal in the subway, as in other subway systems (Font et al., 2019; Chang et al., 2021; Ji et al., 2021). Subway scouting routes **B-E** yielded similar values with the exception of route **D**, which contained 48-min. measurements at the railway main train station (*CS-R*, Table S4). PM concentrations on the *CS-R* platform were close to ambient levels probably due to good ventilation. The Fe content per average aerosol mass followed a similar trend in all subway samples (on average about 1.7 compared to 0.2 in the ambient air). Further abundant metals were manganese (Mn), chromium (Cr), and copper (Cu). A significant increase in the subway was also observed for vanadium (V), however, most of the filters were below the LOQ.

Stationary measurements on the U-Bahn platform *CS-U1* revealed an Fe concentration of 67 μg m^{-3} in the $PM_{2.5}$ fraction on May 17, 2022 accounting for about 69% of $PM_{2.5}$ (Table 2). On July 19, 2022, the Fe concentration in PM_{total} was 171 μg m^{-3} while PM_{10} and $PM_{2.5}$ fractions were 218 ± 50 μg m^{-3} and 85 ± 8 μg m^{-3}, respectively. Therefore, most of the PM mass was formed by ferruginous particles (FePM).

The ratio of iron to other metals could provide information on the origin of the particles if compared to the corresponding ratios in materials subject to abrasion. The Mn/Fe ratio was 0.01 as in the Barcelona subway, where it was considered as a typical ratio for the origin of steel from wheels, rails and brakes (Moreno et al., 2015). The average ratios of different metals compared to Fe at *CS-U1* platform were 0.91% (Mn), 0.39% (Cr), 0.45% (Cu), 0.30% (Ni), 0.018% (V), respectively, while the usual composition of one of the most common rail steel R260 is: 0.92–1.07% (Mn), 0.03–0.12% (Cr), 0.01–0.12% (Cu), 0.01–0.08% (Ni), 0.002–0.011% (V), respectively. The variation for some elements may be due to the contribution of other sources or slightly different steel types used. Cu, Mn, Cr, and Ni are present in brake pads (with high variance), which are subject to wear (Font et al., 2019).

3.6. SEM-EDX imaging and single particle elemental analysis

The majority of subway particles analyzed via SEM exhibited a rough, splintery surface, oftentimes present as flakes (exemplary micrographs of characteristic particles are shown in Fig. 5a and Figs. S8-11Figs. S7–10 in the SI), which is in agreement with results of studies all over the world (Jung et al., 2012; Loxham et al., 2013; Moreno et al., 2015; Perrino et al., 2015; Wang et al., 2016; Grana et al., 2017; Chang et al., 2021; Guseva Canu et al., 2021). The uneven and rough edges found for most particles suggest that they are mainly derived from abrasion processes, most likely at the rail-wheel-brake interface (Kang et al., 2008; Byeon et al., 2015; Moreno et al., 2015; Perrino et al., 2015; Wang et al., 2016).

EDX analysis revealed that these particles consist predominantly of Fe (63.4 ± 8.67 wt%) and O (36.2 ± 8.2 wt%), with lower contents of Si (0.1 ± 0.9 wt%). Since filter samples used for EDX analysis were sputtered with a layer of carbon, no information on the concentration of carbon could be obtained. Moreno et al. (2015) reported element concentrations for iron-rich particles of 40.0–65.0 wt% for Fe, 9.0–32.5 wt % for O, 2.0–19.5 wt% for C, and 1.0–8.5 wt% for Si. While our findings are in agreement with their Fe and O ranges, the amounts of Si vary, which might be explained by the usage of different steel types for train

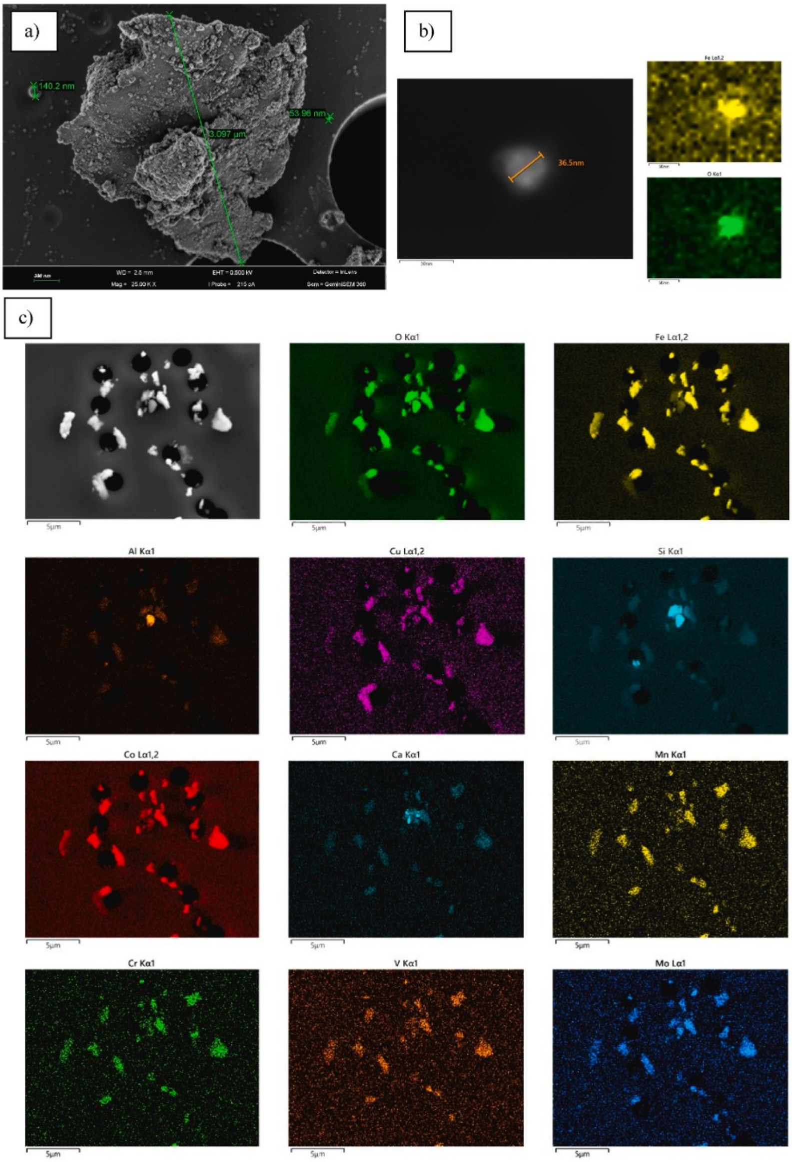

Fig. 5. a) SEM-micrograph of flake-like subway particle consisting predominantly of Fe and O with attached clusters of 20–30 nm sized spherical iron oxide and carbon containing particles, b) EDX mapping of 37 nm subway particle at 5 kV, c) EDX mapping of subway particles on a polycarbonate filter at 20 kV (size range of particles 200 nm–2.5 µm) Print in color.

rails and wheels in the Barcelona subway system, as well as differences in the composition of front and lateral brake pads between Munich and Barcelona.

Automated classification of EDX data showed that 75.43% of the >180 000 analyzed particles were made of iron oxides, while 5.35% consisted of metallic Fe and 1.23% belonged to geological, soil-derived particles. A total of 16.89% of all particles was not classified, however, large peaks for carbon and oxygen were observed in the spectra of these particles. This led to the assumption that these particles were mainly carbonaceous. Byeon et al. (2015) who used passive sampling reported values of 66 ± 9% for $PM_{2.5\text{-}1}$ in the Seoul subway system, while Jung et al. (2010) stated that 71 - 79% of all particles at stations without platform protection doors in Seoul consisted of iron-rich particles. These values are in accordance with our data highlighting the similarities in sampled subway aerosols around the globe.

The elemental distribution of Munich subway aerosol was similar for iron-rich particles of all analyzed sizes (250 nm - 5 μm) suggesting that the particles are originating from the same source. However, we observed that with decreasing particle size the ratio of iron to oxygen also decreased from Fe/O = 2.19 for particles of 5 μm to a ratio of Fe/O = 1.37 for particles of 250 nm. This can be explained by the increased ratio of surface area to volume of smaller particles, which facilitates oxidation processes at the surface of the particles.

Furthermore, clusters of nanoparticles adhering to larger ferruginous particles could be observed (Fig. 5), which were either iron-rich or of carbonaceous nature, and were also described by other research groups (Kang et al., 2008; Jung et al., 2010, 2012; Moreno et al., 2015). Iron oxide bearing nanoparticles were also found in an isolated form with their size ranging from 20 to 150 nm. An exemplary EDX mapping of a 37 nm iron oxide particle is given in Fig. 5b. Spherical Fe particles could originate from condensation of gaseous iron formed from sparking (Kang et al., 2008; Jung et al., 2010) while carbonaceous nanoparticles could be formed from oxidation of volatile organic compounds on the active metal surface of host particles (Kang et al., 2008; Moreno et al., 2015) or adhesion of soot particles from the outside air (Moreno et al., 2015; Grana et al., 2017). Graphite can also be found in brake pads and carbon particles can originate from electromotor brushes as discussed in Section 3.3. Literature suggests that iron oxides in the subway environment are present as hematite (Fe_2O_3), magnetite (Fe_3O_4) and maghemite ($\gamma\text{-}Fe_2O_3$) (Jung et al., 2012; Lu et al., 2015; Moreno et al., 2015), which we were not able to distinguish via EDX measurements.

Apart from the main elements Fe, O, and C the majority of particles in the subway aerosol was accompanied by trace elements such as Cu, Co, Mn, Cr, V, and Mo. These elements were also discovered by research groups world-wide (Kang et al., 2008; Jung et al., 2010; Midander et al., 2012; Moreno et al., 2015). Particles containing $BaSO_4$ or Sb that are attributed to brake wear and which were previously found in different subway systems (Kang et al., 2008; Moreno et al., 2015; Chang et al., 2021; Guseva Canu et al., 2021) were rare in the samples. In total, only 25 of >180 000 particles could be related to braking events via these metals. Fig. 5c shows an elemental mapping of subway particles on a PC filter.

While Munich subway aerosol (line *U5*) is similar in composition to subway systems in other cities, the often-reported Cu-rich particles, which are believed to originate from sparking and abrasion processes at the pantograph-catenary interface (Mugica-Álvarez et al., 2012; Moreno et al., 2015; Wang et al., 2016; Guseva Canu et al., 2021), were only scarcely observed in this study. In fact, only 220 of the total 182 020 particles analyzed were classified as Cu-rich and the reason might be that subway trains in Munich are powered by the third rail, which is made of low-carbon stainless steel at the sampled location (*https://www.u-bahn-muenchen.de/*).

Apart from iron-rich PM, several particles of supposedly geological origin were present in the samples. Particles attributed to this class consisted mainly of aluminium-magnesium silicates and quartz with occasional calcium carbonates, which is also described in the literature (Kang et al., 2008; Mugica-Álvarez et al., 2012; Byeon et al., 2015; Moreno et al., 2015; Perrino et al., 2015). These particles, as well as soot particles that were found in the samples, might entered the subway system by commuters or by mixing of in the subway generated aerosol with air from outside the system via ventilation (Kang et al., 2008; Mugica-Álvarez et al., 2012).

During the manual SEM-EDX analysis, we found several Fe-rich particles with layered structures interconnected by grooves. The structure and genesis of this particle type is unknown and has not been discussed in literature to our knowledge. A SEM micrograph and EDX spectra of one of the unknown particles, which consisted mainly of Fe, O, and C but also traces of Mn and Cr is given in Fig. S12 in the SI. The concentrations of Mn and Cr might indicate that the particle originated from some type of steel, however, its texture is not common for abrasion or evaporation derived particles but resembles more a crystalline structure. An additional EDX mapping of the particle class is given in Fig. S13 in the SI.

3.7. *Summary*

In the selected part of the *U-Bahn* subway line *U5*, PM_{10}, $PM_{2.5}$ and PM_1 concentrations at platforms ranged from 59 to 220, 27–80 and 9–21 μg m^{-3}, respectively. During typical trips, the average values ranged from 73 to 170, 29–59, 8 - 19 μg m^{-3}, respectively. The highest PM_{10} levels on the *CS-U2* platform were 231 ± 52 μg m^{-3}. Compared to WHO air quality recommendations, PM levels were generally high for long-term or repeated exposure, and mitigation measures for PM should be of great interest. The measured hot-spots could be classified as *very poor/extremely poor* compared to other subway systems (Cartenì et al., 2020). Most of the particle mass consisted of ferrous particles (FePM) from wheel and rail abrasion. Inadequate ventilation of platforms and tunnels is likely to be the cause of high PM levels. Probably for the same reason, subway PNC levels were not elevated even in the city center (10^3 - 10^4 pt cm^{-3}). Only a few cases of outdoor traffic-related particles with high PNC entering the subway platform were observed so ambient air was not the dominant source of PM.

Using mobile measurements, we observed a high spatial variability of PM among platforms and tunnel sections, which increased from the above-ground terminus *NS-U/S* towards downtown. The highest concentrations were measured at transfer stations with an overall high train frequency. The intra-day variability was mainly influenced by train frequency, so that PM concentrations were highest during the morning and afternoon rush-hour. Otherwise, concentrations at specific platforms were relatively stable over time (day of week, season). The same trend was observed from the eBC readings, but it is likely to be due to light-absorbing metal artifacts so further investigation of BC is needed.

The design of the station affected the concentrations – platforms with larger volumes tended to have lower PM concentrations than smaller with the same train frequency but the PM_{10} variability between these platforms was higher than on the double-track platforms. PM dynamics inside the train were high during rides due to the high air exchange with the outside tunnel. Old trains without air conditioning and with opened windows had slightly higher PM concentrations than new trains with air conditioning but the difference was less than 12% indicating poor or no filtration.

ICP-MS analysis quantified elevated levels of metals in the subway, particularly iron and metals present in the steel of the rails and wheels. Ferrous particles formed the majority of the aerosol mass. SEM-EDX analysis revealed the shape and size distribution of the metal particles. Trace elements typical for subways have been detected. The copper content in the Munich subway appeared to be lower than in other cities probably due to the absence of copper catenaries. Our results show that iron-rich particles and other metals are present even in the inhalable fraction of the aerosol, which could cause negative health effects. One of the described toxicological effects is the formation of reactive oxidative species (ROS) through the Fenton reaction, which can induce oxidative stress (Kanti Das et al., 2014). However, most of the mass of these particles is formed by larger particles and not UFP, which can be deduced from the fact that PNC and LDSA in metro stations are not significantly elevated compared to ambient air values. Nevertheless, iron oxides nanoparticles around 30 nm were found. Given the potential association between iron nanoparticles and neurodegenerative diseases via the olfactory nerve entry route (Hopkins et al., 2018; Liu et al., 2018), toxicological investigations with real subway aerosol on this topic would be of interest.

To effectively mitigate air pollution, individual comprehensive measurements need to be made as subway systems can vary widely. While platform screen doors (PSD), air conditioning and other measures can reduce PM concentrations in the subway, they usually do not mitigate them completely (Chang et al., 2021; van Ryswyk et al., 2021). Measurements at selected platforms, as presented in other studies (Johansson and Johansson, 2003; Colombi et al., 2013; Moreno et al., 2014; Cusack et al., 2015; Chang et al., 2021), provide a comprehensive characterization of PM variability at one or several sites but often do not account for spatio-temporal variability in the wide variety of micro-environments during typical commuter rides. In addition, such campaigns can have high requirements on organization and equipment installation, which may be one reason why only a limited number of metro systems around the world have been characterized.

Based on our results, we propose to improve the air conditioning system of the new trains (ideally equipped with HEPA filters) and improve the ventilation of the platforms, but in such a way that there are no subway exhausts near busy streets or other sources of aerosol. More frequent dusting of the tracks and the best available brake system technology could also be beneficial. Wearing face-masks in subway could help to decrease the personal exposure from coarse particles as suggested by Ji et al. (2021), however, protection from nanoparticles is limited. Drivers and subway operators might be the most exposed to PM concentrations, so we propose to install air purifiers in the driver's cab.

The presented methodology for comprehensive air quality characterization in subways using a mobile measurement system has proven to be a fast and thorough way to determine the aerosol composition to which a subway passenger is exposed to. It can be used to map PM and PNC concentrations in different cities in a comparable manner by taking into account the high spatio-temporal variability of PM. Furthermore, realistic doses of specific pollutants can be calculated. This relatively low-cost approach typically requires no special preparations and measurements can be made rather effectively. Repeated trips can identify hot-spots and estimate personal exposure. Sampling for chemical analysis and particle imaging can reveal sources and potential health risks. In the future, it can be used to monitor potential air quality limits and the effectiveness of measures. The same system can also be used to compare different modes of transportation. Moreover, gas phase measurements and bioaerosol sampling can be added.

Funding sources

This research is funded by dtec.bw – Digitalization and Technology Research Center of the Bundeswehr [project LUKAS and MORE]. Dtec.bw is funded by the European Union – NextGenerationEU. This research was also supported by the project ULTRHAS – ULtrafine particles from TRansportation – Health Assessment of Sources, a project funded under the EU's Research and Innovation programme Horizon 2020, Grant Agreement No. 955390. We acknowledge financial support by Universität der Bundeswehr München.

CRediT authorship contribution statement

Jan Bendl: Conceptualization, Data curation, Formal analysis, Investigation, Methodology, Supervision, Visualization, Writing – original draft. **Carsten Neukirchen:** Formal analysis, Investigation, Methodology, Writing – original draft, Writing – review & editing. **Ajit Mudan:** Investigation. **Sara Padoan:** Investigation, Methodology, Writing – original draft. **Ralf Zimmermann:** Writing – review & editing. **Thomas Adam:** Conceptualization, Funding acquisition, Investigation, Methodology, Project administration, Resources, Supervision, Writing – review & editing.

Declaration of competing interest

The authors declare that they have no known competing financial interests or personal relationships that could have appeared to influence the work reported in this paper.

Data availability

Data will be made available on request.

Acknowledgement

Measurements were supported by students from the University of the Bundeswehr Munich M.Eng course Computer Aided Engineering (CAE): Ferdinand Lindenpütz, Moritz Tenckhoff, Rene Pfeiffer, Gregor Franke, Erik Milde. Construction of the measuring system was supported by the CAE master student Sören Möhrs.

Abbreviations

CPC	condensation particle counter
eBC	Equivalent Black Carbon
EC	Elemental Carbon
EDX	energy-dispersive X-ray spectroscopy
GPS	Global positioning system
ICP-MS	Inductively coupled plasma mass spectrometry
LDSA	lung deposited surface area
NEE	non-exhaust emissions
OC	Organic Carbon
ONA	Optimized Noise-Reduction Averaging
OPS	Optical particle sizer
PC	Polycarbonate
PAHs	Polycyclic Aromatic Hydrocarbons
PM	Particulate Matter
PM_x	particulate matter smaller than X μm in the aerodynamic diameter
PNC	particle number concentration
PSD	platform screed doors
SEM-EDX	Scanning electron microscopy with energy dispersive X-ray spectroscopy
SIA	secondary inorganic aerosols
UFP	ultrafine particles
UVPM	ultraviolet absorbing particulate matter

Appendix A. Supplementary data

Supplementary data to this article can be found online at https://doi.org/10.1016/j.atmosenv.2023.119883.

References

Aarnio, P., Yli-Tuomi, T., Kousa, A., Mäkelä, T., Hirsikko, A., Hämeri, K., Räisänen, M., Hillamo, R., Koskentalo, T., Jantunen, M., 2005. The concentrations and composition of and exposure to fine particles (PM2.5) in the Helsinki subway system. Atmos. Environ. 39, 5059–5066.

Bachoual, R., Boczkowski, J., Goven, D., Amara, N., Tabet, L., On, D., Leçon-Malas, V., Aubier, M., Lanone, S., 2007. Biological effects of particles from the paris subway system. Chem. Res. Toxicol. 20, 1426–1433.

Braniš, M., 2006. The contribution of ambient sources to particulate pollution in spaces and trains of the Prague underground transport system. Atmos. Environ. 40, 348–356.

Byeon, S.-H., Willis, R., Peters, T.M., 2015. Chemical characterization of outdoor and subway fine (PM(2.5-1.0)) and coarse (PM(10-2.5)) particulate matter in Seoul (Korea) by computer-controlled scanning electron microscopy (CCSEM). Int. J. Environ. Res. Publ. Health 12, 2090–2104.

Cartenì, A., Cascetta, F., Campana, S., 2015. Underground and ground-level particulate matter concentrations in an Italian metro system. Atmos. Environ. 101, 328–337.

Cartenì, A., Cascetta, F., Henke, I., Molitierno, C., 2020. The role of particle resuspension within PM concentrations in underground subway systems. Int. J. Environ. Sci. Technol. 17, 4075–4094.

Cepeda, M., Schoufour, J., Freak-Poli, R., Koolhaas, C.M., Dhana, K., Bramer, W.M., Franco, O.H., 2017. Levels of ambient air pollution according to mode of transport: a systematic review. Lancet Public Health 2, e23–e34.

Cha, Y., Olofsson, U., 2018. Effective density of airborne particles in a railway tunnel from field measurements of mobility and aerodynamic size distributions. Aerosol. Sci. Technol. 52, 886–899.

Chang, L., Chong, W.T., Wang, X., Pei, F., Zhang, X., Wang, T., Wang, C., Pan, S., 2021. Recent progress in research on PM2.5 in subways. Environmental science. Processes & impacts 23, 642–663.

Colombi, C., Angius, S., Gianelle, V., Lazzarini, M., 2013. Particulate matter concentrations, physical characteristics and elemental composition in the Milan underground transport system. Atmos. Environ. 70, 166–178.

Cusack, M., Talbot, N., Ondráček, J., Minguillón, M.C., Martins, V., Klouda, K., Schwarz, J., Ždímal, V., 2015. Variability of aerosols and chemical composition of PM 10 , PM 2.5 and PM 1 on a platform of the Prague underground metro. Atmos. Environ. 118, 176–183.

Font, O., Moreno, T., Querol, X., Martins, V., Sánchez Rodas, D., Miguel, E. de, Capdevila, M., 2019. Origin and speciation of major and trace PM elements in the Barcelona subway system. Transport. Res. Transport Environ. 72, 17–35.

Grana, M., Toschi, N., Vicentini, L., Pietroiusti, A., Magrini, A., 2017. Exposure to ultrafine particles in different transport modes in the city of Rome. Environmental pollution (Barking, Essex : 1987 228, 201–210.

Guseva Canu, I., Crézé, C., Hemmendinger, M., Ben Rayana, T., Besançon, S., Jouannique, V., Debatisse, A., Wild, P., Sauvain, J.J., Suárez, G., Hopf, N.B., 2021. Particle and metal exposure in Parisian subway: relationship between exposure biomarkers in air, exhaled breath condensate, and urine. Int. J. Hyg Environ. Health 237, 113837.

Hagler, G.S., Yelverton, T.L., Vedantham, R., Hansen, A.D., Turner, J.R., 2011. Post-processing method to reduce noise while preserving high time resolution in aethalometer real-time black carbon data. Aerosol Air Qual. Res. 11, 539–546.

Hopkins, L.E., Laing, E.A., Peake, J.L., Uyeminami, D., Mack, S.M., Li, X., Smiley-Jewell, S., Pinkerton, K.E., 2018. Repeated iron-soot exposure and nose-to-brain transport of inhaled ultrafine particles. Toxicol. Pathol. 46, 75–84.

Huck, W. (Ed.), 2022. Sustainable Development Goals. Nomos Verlagsgesellschaft mbH & Co. KG.

Ji, W., Li, X., Wang, C., 2021. Composition and exposure characteristics of PM2.5 on subway platforms and estimates of exposure reduction by protective masks. Environ. Res. 197, 111042.

Ji, W., Zhao, K., Liu, C., Li, X., 2022. Spatial characteristics of fine particulate matter in subway stations: source apportionment and health risks. Environmental pollution (Barking, Essex : 1987 305, 119279.

Johansson, C., Johansson, P.-Å., 2003. Particulate matter in the underground of Stockholm. Atmos. Environ. 37, 3–9.

Jung, H.-J., Kim, B., Malek, M.A., Koo, Y.S., Jung, J.H., Son, Y.-S., Kim, J.-C., Kim, H., Ro, C.-U., 2012. Chemical speciation of size-segregated floor dusts and airborne magnetic particles collected at underground subway stations in Seoul, Korea. J. Hazard Mater. 213–214, 331–340.

Jung, H.-J., Kim, B., Ryu, J., Maskey, S., Kim, J.-C., Sohn, J., Ro, C.-U., 2010. Source identification of particulate matter collected at underground subway stations in Seoul, Korea using quantitative single-particle analysis. Atmos. Environ. 44, 2287–2293.

Kang, S., Hwang, H., Park, Y., Kim, H., Ro, C.-U., 2008. Chemical compositions of subway particles in Seoul, Korea determined by a quantitative single particle analysis. Environ. Sci. Technol. 42, 9051–9057.

Kanti Das, T., Wati, M.R., Fatima-Shad, K., 2014. Oxidative stress gated by Fenton and haber weiss reactions and its association with alzheimer's disease. Arch Neurosci 2.

Karlsson, H.L., Holgersson, A., Möller, L., 2008. Mechanisms related to the genotoxicity of particles in the subway and from other sources. Chem. Res. Toxicol. 21, 726–731.

Karlsson, H.L., Ljungman, A.G., Lindbom, J., Möller, L., 2006. Comparison of genotoxic and inflammatory effects of particles generated by wood combustion, a road simulator and collected from street and subway. Toxicol. Lett. 165, 203–211.

Licina, D., Tian, Y., Nazaroff, W.W., 2017. Emission rates and the personal cloud effect associated with particle release from the perihuman environment. Indoor Air 27, 791–802.

Liu, J.-L., Fan, Y.-G., Yang, Z.-S., Wang, Z.-Y., Guo, C., 2018. Iron and alzheimer's disease: from pathogenesis to therapeutic implications. Front. Neurosci. 12, 632.

Liu, X., Hadiatullah, H., Zhang, X., Hill, L.D., White, A.H.A., Schnelle-Kreis, J., Bendl, J., Jakobi, G., Schloter-Hai, B., Zimmermann, R., 2021. Analysis of Mobile Monitoring Data from the microAeth® MA200 for Measuring Changes in Black Carbon on the Roadside in Augsburg, p. 13.

Loxham, M., Cooper, M.J., Gerlofs-Nijland, M.E., Cassee, F.R., Davies, D.E., Palmer, M.R., Teagle, D.A.H., 2013. Physicochemical characterization of airborne particulate matter at a mainline underground railway station. Environ. Sci. Technol. 47, 3614–3622.

Lu, S., Liu, D., Zhang, W., Liu, P., Fei, Y., Gu, Y., Wu, M., Yu, S., Yonemochi, S., Wang, X., Wang, Q., 2015. Physico-chemical characterization of PM2.5 in the microenvironment of Shanghai subway. Atmos. Res. 153, 543–552.

Lyu, Y., Olofsson, U., 2020. On black carbon emission from automotive disc brakes. J. Aerosol Sci. 148, 105610.

Martins, V., Cruz Minguillón, M., Moreno, T., Querol, X., Miguel, E. de, Capdevila, M., Centelles, S., Lazaridis, M., 2015. Deposition of aerosol particles from a subway microenvironment in the human respiratory tract. J. Aerosol Sci. 90, 103–113.

Martins, V., Moreno, T., Mendes, L., Eleftheriadis, K., Diapouli, E., Alves, C.A., Duarte, M., Miguel, E. de, Capdevila, M., Querol, X., Minguillón, M.C., 2016. Factors controlling air quality in different European subway systems. Environ. Res. 146, 35–46.

Midander, K., Elihn, K., Wallén, A., Belova, L., Karlsson, A.-K.B., Wallinder, I.O., 2012. Characterisation of nano- and micron-sized airborne and collected subway particles, a multi-analytical approach. Sci. Total Environ. 427–428, 390–400.

Minguillón, M.C., Reche, C., Martins, V., Amato, F., Miguel, E. de, Capdevila, M., Centelles, S., Querol, X., Moreno, T., 2018. Aerosol sources in subway environments. Environ. Res. 167, 314–328.

Moreno, T., Martins, V., Querol, X., Jones, T., BéruBé, K., Minguillón, M.C., Amato, F., Capdevila, M., Miguel, E. de, Centelles, S., Gibbons, W., 2015. A new look at inhalable metalliferous airborne particles on rail subway platforms. Sci. Total Environ. 505, 367–375.

Moreno, T., Pérez, N., Reche, C., Martins, V., Miguel, E. de, Capdevila, M., Centelles, S., Minguillón, M.C., Amato, F., Alastuey, A., Querol, X., Gibbons, W., 2014. Subway platform air quality: assessing the influences of tunnel ventilation, train piston effect and station design. Atmos. Environ. 92, 461–468.

Mugica-Álvarez, V., Figueroa-Lara, J., Romero-Romo, M., Sepúlveda-Sánchez, J., López-Moreno, T., 2012. Concentrations and properties of airborne particles in the Mexico City subway system. Atmos. Environ. 49, 284–293.

Perrino, C., Marcovecchio, F., Tofful, L., Canepari, S., 2015. Particulate matter concentration and chemical composition in the metro system of Rome, Italy. Environ. Sci. Pollut. Res. 22, 9204–9214.

Querol, X., Moreno, T., Karanasiou, A., Reche, C., Alastuey, A., Viana, M., Font, O., Gil, J., Miguel, E., de, Capdevila, M., 2012. Variability of levels and composition of PM_{10} and $PM_{2.5}$ in the Barcelona metro system. Atmos. Chem. Phys. 12, 5055–5076.

Roy, D., Lyou, E.S., Kim, J., Lee, T.K., Park, J., 2022. Commuters health risk associated with particulate matter exposures in subway system – globally. Build. Environ. 216, 109036.

Rupprecht Consult, 2019. Guidelines for Developing and Implementing a Sustainable Urban Mobility Plan, second ed., p. 168

Salo, L., Rönkkö, T., Saarikoski, S., Teinilä, K., Kuula, J., Alanen, J., Arffman, A., Timonen, H., Keskinen, J., 2021. Concentrations and size distributions of particle lung-deposited surface area (LDSA) in an underground mine. Aerosol Air Qual. Res. 21, 200660.

Schraufnagel, D.E., 2020. The health effects of ultrafine particles. Exp. Mol. Med. 52, 311–317.

Shakya, K.M., Saad, A., Aharonian, A., 2020. Commuter exposure to particulate matter at underground subway stations in Philadelphia. Build. Environ. 186, 107322.

Targino, A.C., Krecl, P., Brimblecombe, P., Oukawa, G.Y., Danziger Filho, J.E., Moreno, F.L., 2021. Spatio-temporal variability of airborne particulate matter in the São Paulo subway. Build. Environ. 189, 107526.

van Ryswyk, K., Anastasopolos, A.T., Evans, G., Sun, L., Sabaliauskas, K., Kulka, R., Wallace, L., Weichenthal, S., 2017. Metro commuter exposures to particulate air pollution and PM2.5-associated elements in three Canadian cities: the urban transportation exposure study. Environ. Sci. Technol. 51, 5713–5720.

van Ryswyk, K., Kulka, R., Marro, L., Yang, D., Toma, E., Mehta, L., McNeil-Taboika, L., Evans, G.J., 2021. Impacts of Subway System Modifications on Air Quality in Subway Platforms and Trains. Environmental science & technology. https://doi.org/10.1021/acs.est.1c00703.

Wang, B.-Q., Liu, J.-F., Ren, Z.-H., Chen, R.-H., 2016. Concentrations, properties, and health risk of PM2.5 in the Tianjin City subway system. Environ. Sci. Pollut. Res. Int. 23, 22647–22657.

World Health Organization, 2021. WHO Global Air Quality Guidelines: Particulate Matter (PM2.5 and PM10), Ozone, Nitrogen Dioxide, Sulfur Dioxide and Carbon Monoxide. WHO European Centre for Environment and Health, Bonn, Germany, p. 285.

Xu, B., Hao, J., 2017. Air quality inside subway metro indoor environment worldwide: a review. Environ. Int. 107, 33–46.

Xu, B., Yu, X., Gu, H., Miao, B., Wang, M., Huang, H., 2016. Commuters' exposure to PM2.5 and CO2 in metro carriages of Shanghai metro system. Transport. Res. Transport Environ. 47, 162–170.

Yang, F., Kaul, D., Wong, K.C., Westerdahl, D., Sun, L., Ho, K., Tian, L., Brimblecombe, P., Ning, Z., 2015. Heterogeneity of passenger exposure to air pollutants in public transport microenvironments. Atmos. Environ. 109, 42–51.

Zhao, L., Wang, J., Gao, H.O., Xie, Y., Jiang, R., Hu, Q., Sun, Y., 2017. Evaluation of particulate matter concentration in Shanghai's metro system and strategy for improvement. Transport. Res. Transport Environ. 53, 115–127.

Supporting Information for:

Personal Measurements and Sampling of Particulate Matter in a Subway – Identification of Hot-spots, Spatio-temporal Variability and Sources of Pollutants

Jan Bendl[a,d,*], Carsten Neukirchen[a,c], Ajit Mudan [a], Sara Padoan[a, b], Ralf Zimmermann[b, c], Thomas Adam[a,b]

[a] University of the Bundeswehr Munich, Faculty for Mechanical Engineering, Institute of Chemical and Environmental Engineering, Werner-Heisenberg-Weg 39, 85577, Neubiberg, Germany

[b] Joint Mass Spectrometry Center (JMSC) at Comprehensive Molecular Analytics (CMA), Helmholtz Zentrum München, Ingolstädter Landstr. 1, 85764 Neuherberg, Germany

[c] Joint Mass Spectrometry Center (JMSC) at Chair of Analytical Chemistry, Institute of Chemistry, University of Rostock, Albert-Einstein-Strasse 27, 18059 Rostock, Germany

[d] Institute for Environmental Studies, Faculty of Science, Charles University, Benátská 2, 128 01 Prague, Czech Republic

*Corresponding author: jan.bendl@unibw.de (Jan Bendl)

Phone number: +49 89 6004 2473

Number of pages – 16

Number of figures – 15

Number of tables – 9

1.1 Development of the system for ambient/indoor spatio-temporal PM characterization

The measuring system was designed for mobile aerosol measurements and sampling, but can also be used for gas phase measurement and sampling. It can be placed inside the stroller/trailer for walking and cycling measurements, or attached to a frame-rucksack for walking measurement when a stroller cannot be used. The box can also be attached to a car or other carriers, or even used as a stationary environmental enclosure.

It has a water-proof 71-liter, 4.4 kg aluminum box with external dimensions of L 59.5 x D 39.0 x H 38.0 cm, quality proved by the German Technical Inspection Association (TÜV), which is used sideways with door-like opening to the left side. Active ventilation is provided by two USB ventilators (diameter 25cm) on the backside, while one is in the bottom and the second one is in the top of the box. They are covered by a special grid preventing rain from entering the system. The upper ventilator is pushing out hot air while the lower ventilator is installed in the opposite direction (fig. S1). Ventilators are powered by a power bank and can be set to various speeds based on ambient temperatures. The aim is to keep inside the optimal temperature for instruments and samples to prevent malfunctions and losses of samples, especially volatile and semi-volatile compounds. The temperature in the box should always be slightly above outside temperature to prevent condensation in tubes/instruments, which is provided by natural heating of the instruments in operation. In some cases, heated inlet tubes can be additionally installed.

On the top of the box are 4 drilled holes with water-tide grommets for inlet installations. Omni-directional inlets (TSI) and the DISCmini (Testo) inlet are connected, but various other inlets can be used and further holes can be drilled/covered easily. When used in the stroller arrangement (in our case Thule Cab2 with brakes) the inlets are located exactly 100 cm above ground, which is in the breathing zone of a child. When used in a frame backpack, the inlets are in the breathing zone of an adult. Omnidirectional inlets should be used with a cap that prevents water from entering the hose.

Inside the box there are four rails made of ITEM profiles (profile 5, 20x10 mm) connected to the sides of the box (Fig. S1), with two adjustable shelves made of metal sheet (2 mm thickness), while the bottom is used as a third shelf. For optimal vibration damping, the foam originally intended for sound damping was used on the bottom of each shelf and on the sides. The instruments are optimally secured with a strap with a small ratchet. It was tested for the instruments used to avoid an undesirable increase in the amplitude of shaking, but effectively absorbed the vibrations.

In our case, the optical particle counter (OPS 3330, TSI) had to be placed at the top because larger particles are much more sensitive to losses, so the inlet is directly connected to the flexible conductive hose without having to bend it. In contrast, the DISCmini particle counter (Testo) can be placed on the bottom floor and the inlet tubing can be bent, since most particles are nanoparticles, which are not that sensitive to losses. The second floor is also used for filter holders and personal impactors (SIOUTAS, SKC). Pumps and computer are located on the bottom.

The GPS device and the instruments with the GPS sensor (Micro-Aethalometer MA200, AethLabs) must be located outside the box if they do not have an external antenna due to signal loss. Point-of-view cameras can be used for data analysis. The devices can be connected to a laptop/industrial computer with power supply to transmit the data directly and potentially display it in real time to the operator, or can even be remotely controlled via remote desktop using a GSM internet connection.

The basic requirements for setting up the device are the correct time according to GPS satellites, sufficient batteries/external power supply and data acquisition time set according to the measurement speed, where 1 Hz data is needed for cycling measurements, 1 or 5 Hz data for walking measurements. The GPS must always provide 1 Hz data in order to merge the data with all systems.

Attachment to the stroller is using a Velcro strap to its construction, while attachment to the backpack is by straps with ratchets and 4 eyelets on each side of the box.

Fig. S1: *Photo of the stroller (left) and the frame-rucksack (right) arrangement for walking measurements in the subway and used for other mobile aerosol measurements*

1.2 Stroller measurements of ambient air as a reference

The route for the ambient aerosol measurements as a reference to the subway mobile measurements was selected based on the following requirements:

1) The route must be around 1h long to observe enough micro-environments and have enough sample material on filter but, at the same time, the ambient PM background should not change significantly over the measuring time
2) The route should start and end at the same location to observe the change of background concentrations.
3) The route should be close to the long-term air quality monitoring station to allow data comparison.
4) Typical urban microenvironments should be included, e.g., busy and non-busy streets, highways, parks, residential areas, sports facilities, restaurants or kiosks (cooking emissions), schools, kindergartens, public buildings, et cetera.
5) It should be possible to repeat the same route for spatio-temporal variability, ideally also several times a day

In our case, these points were fulfilled by the route that mostly crosses the campus of the Bundeswehr University Munich (UniBW, Fig. S2), starting near the north gate to the west through administrative buildings towards the main gate with light traffic, then along the storage and sports facilities towards the Faculty of Mechanical Engineering with industrial machinery and in close proximity to the highway (southwest corner). Then back along the swimming pool, large parking lots with light traffic along the measuring station in the area of the University test circuit. The route continues through the student dorms (residential area) off campus where the cemetery is located. On the east side of the route is the end of the road tunnel, a busy intersection, and a road with heavy traffic and a 50 km/h speed limit where public transportation also operates. Buses also operate on the northern part of the roadway, but traffic there is milder and the speed limit is reduced to 30 km/h in the middle of the roadway.

The particle number concentration (PNC) best illustrates the variability due to traffic sources.

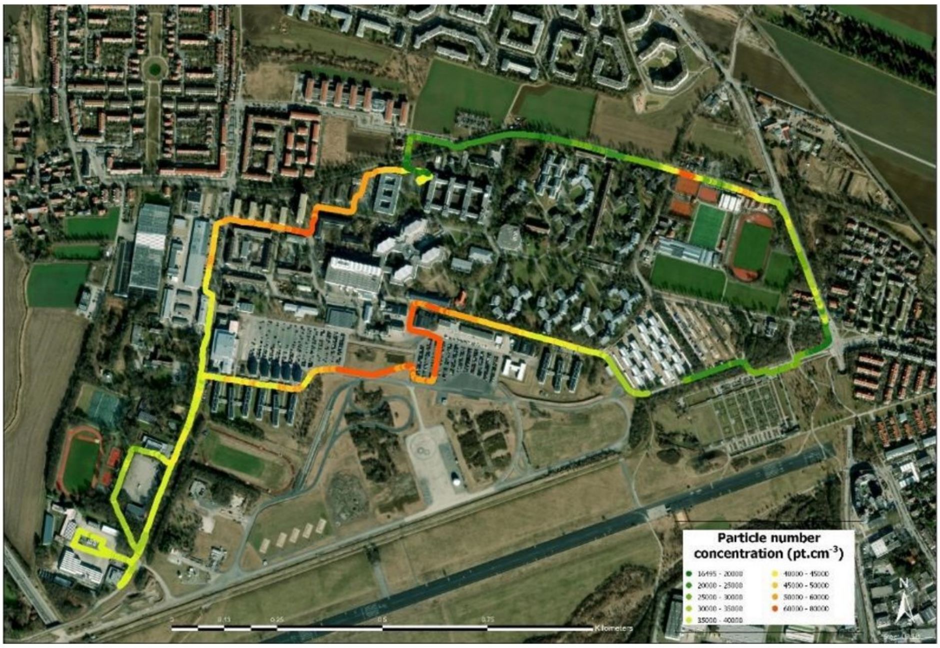

Fig. S2: *Spatio-temporal variability of particle number concentration during stroller measurement at Bundeswehr University Campus in Neubiberg, 27. 11. 2022 (7:50 – 9:11), samples for ICP-MS analysis were taken over the whole period of the walk (beginning is towards West)*

1.3 Subway mobile PM measurements

The stations included in this study are highlighted in the official public transport plan of the city of Munich (Fig. S3). For practical reasons, the study focused on the southern lines, but the city center was also included, so the selection of platforms and routes should be representative for the other lines, but further research is needed to confirm this assumption.

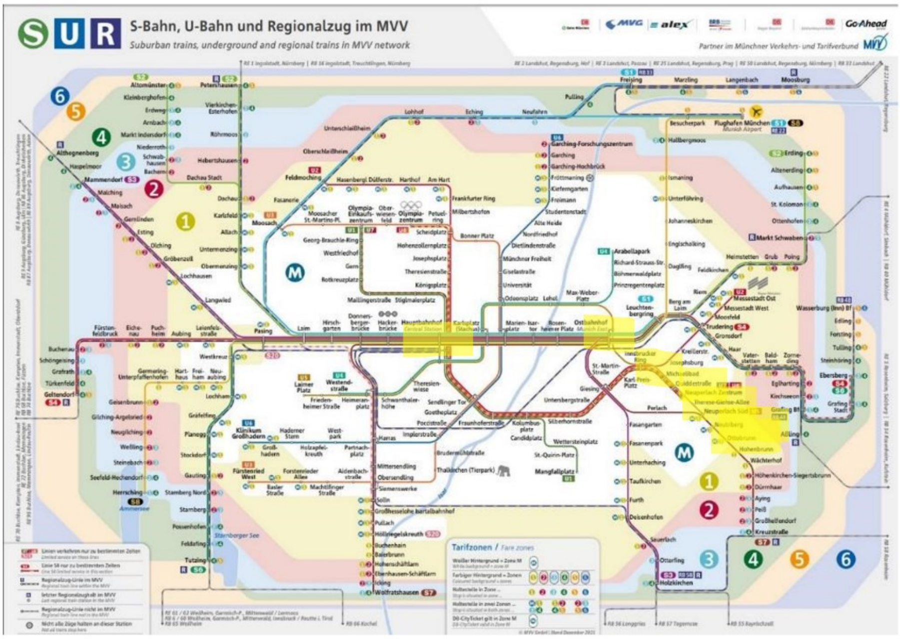

Fig. S3: Plan of the Munich public transport system including the subway (U-Bahn), overground trains (S-Bahn) and trains (observed areas are highlighted), source: https://www.mvv-muenchen.de/

Since concentrations change during the mobile measurements, each walk was divided into transects and the average values of selected parameters were recorded with standard deviations (Tab. S4-S10). In these tables, ambient walking measurements are listed at the beginning and end of each table to give an overview of the urban background. Then, the averages of stationary measurements (for at least several minutes to have enough data points), trips in the tunnel (*r*), and walks in the environment (*aw*) or indoors (*iw*) were recorded. The main purpose of these tables is to show the context of cumulative sampling (in bold) and other measured parameters for specific comparisons. The frequency of trains is calculated from the sum of all trains arriving at the station during the measurement period, therefore it does not correspond to the actual number of trains in a given hour. If the measurement time was too short for the information to be reliable, the number is preceded by a "~". This is also indicated before the measurement at the train station, where the number of arriving trains corresponds only to the adjacent platforms.

To illustrate the behavior of the aerosol and the transition from the ambient to the metro environment, see Fig. S2 on 17. 5. 2022 showing the PM_x and PNC dynamics during the walk from the university campus to the *NS* aboveground platform (A), where the PM_x concentration was similar to typical urban background levels and the PNC concentration was about 6000 pt cm^{-3}, with high short-term peaks due to traffic, the food kiosk, and a diesel engine at the construction site (around 1:40 pm). The black vertical line shows the approach to the old train with the windows open, since it was previously in the depot. The rate of increase in the 1-min. average is visible for PM_x particles, while PNC remains at a similar level. The dynamics of PM_{10} during the ride (B) is shown in greater detail in the Fig. 2 in the article. C represents 3-h long sampling periods and measurements at the main station, where concentrations are relatively stable. Some similarities in PNC and $PM_{2.5}$ variations were observed during this period; however, they do not overlap. In other cases, the opposite seems to be the case, such as at 15:40. A more detailed look at the steady-state measurements is discussed in Section 4.5. Part D is the return trip to *NS-U/S* on the same train.

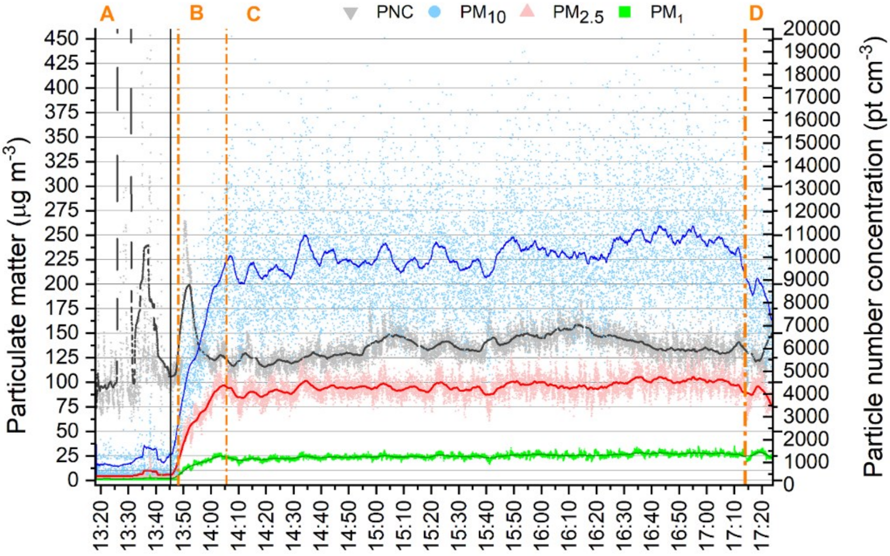

Fig. S4*: Dynamics of PM_1, $PM_{2.5}$ and PM_{10} and particle number concentration PNC (1s scatter) with 5 min. moving average (bold line) during the walk from the UniBW campus to the subway station Neuperlach Süd NS-U/S (A), entering the train (black vertical line); ride by the old train with open windows (line U5) to the main train station CS-U1 (B); stationary measurements during 3-h long sampling at the CS-U1 platform (C), ride back to NS-U/S (D). 17. 5. 2022*

Fig. S5*: PM_{10} variability (1 Hz) during the walk from the University campus to the subway station NS-U/S along the main street with higher traffic (A), waiting on the over-ground platform open to the ambient air and a ride into the tunnel by the old train (U5 line) with opened windows (B), 17. 5. 2022, 13:18 – 13:49*

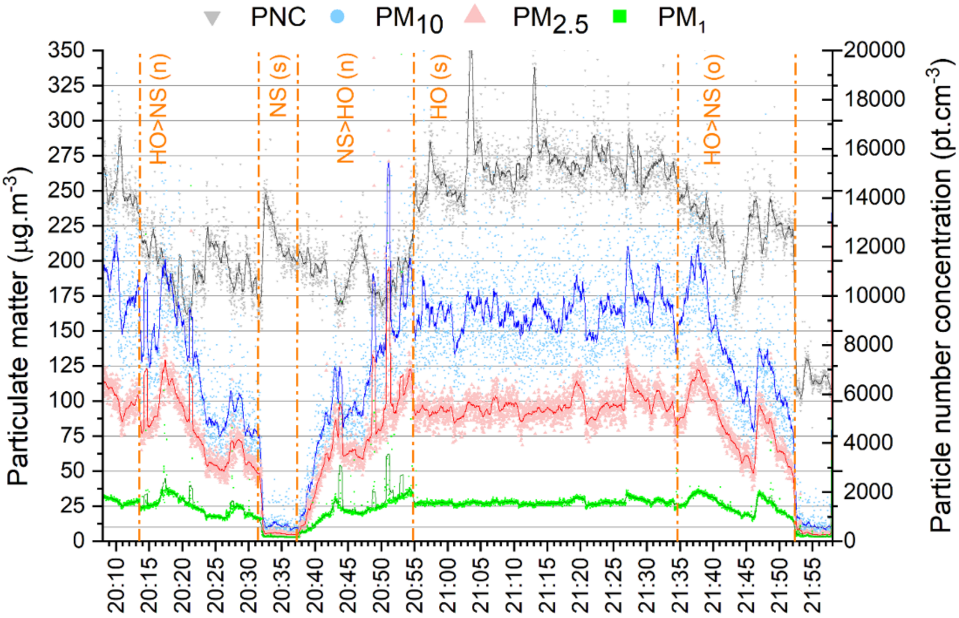

Fig. S6: *Comparison of the dynamics of PMx and particle number concentration (PNC) in 1s (scatter) and 30s moving average (color lines) during the way from underground station CS-U1 to over-ground terminal station NS-*U/S *by a new train (n) with air conditioning and back with exactly the same train. Stationary measurements (s) on the CS-U1 platform followed by the same way using the old train (o) with open windows to the tunnel on 28. 8. 2022.*

Tab. S1: *Sampling overview with the filter-material used*

Experiment	Purpose	Location	Fraction	Sampling	Flowrate (lpm)	Filter type	Filter vendor	LOT	Preconditioning
1	ICP-MS, gravimetry	Mobile/platform	PM_{total}	filter-holder with omni-directional inlet (TSI), SG10-2 (GSA) pump	9	Quartz 47 mm	Munktell ZEFA	3646	5h at 500°C
2	ICP-MS, gravimetry	Platform	$PM_{2.5}$	filter-holder with SKC pre-impactor and omni-directional inlet (TSI), SG10-2 (GSA) pump	9	Quartz 47 mm	Munktell ZEFA	3646	5h at 500°C
3	gravimetry	Platform	$PM_{2.5}$ and $PM_{>2.5}$	Sioutas impcator (SKC), two stages, SG10-2 (GSA) pump	9	PTFE 37 mm and 25 mm	SKC 225-1709 ($PM_{10-2.5}$) and Mitex ($PM_{2.5}$)	2153-7E5-306 and R8JA94705	without
4	SEM-EDX	Platform	PM_{total}	filter-holder with omni-directional inlet (TSI), Holbach BiVoc2 or SG10-2 (GSA) pump	2	Polycarbonate 47 mm	Whatman Nuclepore + silica wafers (p-type boron dotted)	A29752339	without

Tab. S2: *First scouting route (B) on 4. 11. 2021 segmented into units, where ">>" indicates movement from place to place and the abbreviations are the names of stations (university campus is Uni), which are listed in Table 1 in the article. In brackets, aw is ambient walk, s stationary, r ride. Average values and SD of particulate matter (PM$_x$), particle number concentration (PNC), equivalent black carbon (eBC) and UV absorbing PM (UVPM) are in the table. Concentration which are not reasonable due to the short acquisition time and low concentration are red. Sampling period for ICP-MS analysis is marked bold (7:17:02-8:54:25).*

ID	Location	Duration	Start	Stop	Train frequency	PM$_{10}$	PM$_{2.5}$	PM$_1$	PNC	eBC	UVPM
		min.	h:mm:ss	h:mm:ss	no. of trains (trains/hour)	µg m^{-3}	µg m^{-3}	µg m^{-3}	pt cm^{-3}	ng m^{-3}	ng m^{-3}
1	Uni >> NS-U/S (aw)	17	6:59:50	7:17:01		1 ± 7	0.3 ± 2	0.1 ± 0.1	3493 ± 8240	200 ± 347	182 ± 219
2	**NS-U/S (s)**	19	**7:17:02**	**7:36:15**	13 (41)	2 ± 5	0.6 ± 1	0.4 ± 0.9	5020 ± 3286	37 ± 0	146 ± 281
3	NS-U/S >> IR-U (r)	9	**7:36:16**	**7:45:20**		101 ± 62	44 ± 29	12 ± 8	4943 ± 1167	3330 ± 4223	3326 ± 2596
4	**IR-U (s)**	20	**7:45:21**	**8:05:15**	16 (48)	114 ± 45	48 ± 14	14 ± 4	5817 ± 1453	7345 ± 2350	5118 ± 1231
5	IR-U >> OU-U (r)	7	**8:05:16**	**8:12:20**		221 ± 62	102 ± 18	32 ± 5	4105 ± 542	13726 ± 3130	4980 ± 14684
6	**OU-U (s)**	25	**8:12:21**	**8:37:37**	11 (26)	240 ± 74	95 ± 18	27 ± 4	5820 ± 573	12507 ± 4304	7882 ± 2206
7	OU-U >> NS-U/S (r)	17	**8:37:38**	**8:54:25**		141 ± 77	60 ± 27	17 ± 8	6421 ± 1640	7502 ± 3833	4993 ± 2114
8	NS-U/S >> Uni (aw)	19	8:54:26	9:13:20		1 ± 3	0.2 ± 0.2	0.1 ± 0.0	4380 ± 11198	-136 ± 1176	172 ± 606

Tab. S3: *Second scouting route (C) on 5. 11. 2021 segmented into units, where ">>" indicates movement from place to place and the abbreviations are the names of stations (university campus is Uni), which are explained in Table 1 in the article. In brackets, aw is ambient walk, s stationary, r ride. Average values and SD of particulate matter (PM$_x$), particle number concentration (PNC), equivalent black carbon (eBC) and UV absorbing PM (UVPM) are in the table. Sampling period for ICP-MS analysis is marked bold (7:48:15-9:00:35).*

ID	Location	Duration	Start	Stop	Train frequency	PM$_{10}$	PM$_{2.5}$	PM$_1$	PNC	eBC	UVPM
		min.	h:mm:ss	h:mm:ss	no. of trains (trains/hour)	µg m^{-3}	µg m^{-3}	µg m^{-3}	pt cm^{-3}	ng m^{-3}	ng m^{-3}
1	Uni >> NS-U/S (aw)	21	6:56:00	7:17:00		10 ± 19	1 ± 3	0.4 ± 0.2	27630 ± 51683	117 ± 308	761 ± 782
2	**NS-U/S (s)**	7	7:17:01	7:23:45	2 (~17)	10 ± 11	1 ± 1	0.6 ± 0.1	11534 ± 1733	322 ± 153	1098 ± 356
3	NS-U/S >> OB-U (r)	24	7:23:46	7:48:15		66 ± 55	30 ± 16	12 ± 5	10033 ± 3272	5496 ± 2717	4207 ± 1677
4	**OB-U (s)**	20	**7:48:16**	**8:08:30**	8 (24)	293 ± 92	91 ± 16	24 ± 3	9625 ± 1020	12853 ± 2927	8411 ± 1656
5	Elevators (iw)	14	**8:08:31**	**8:22:45**		101 ± 91	32 ± 32	9 ± 9	21258 ± 7340	4929 ± 3596	3856 ± 2196
6	OB-U >> MC-U (r)	5	**8:22:46**	**8:27:35**		180 ± 57	72 ± 9	21 ± 2	10190 ± 1208	8866 ± 3559	6501 ± 1898
7	**MC-U (s)**	21	**8:27:36**	**8:48:50**	6 (17)	68 ± 28	31 ± 7	11 ± 2	9135 ± 736	5977 ± 2221	4214 ± 1596
8	MC-U >> NS-U/S (r)	7	**8:48:51**	**8:55:59**		100 ± 40	43 ± 11	14 ± 3	10601 ± 2153	7236 ± 2435	5046 ± 1794
9	NS-U/S >> Uni (aw)	32	**8:56:00**	9:27:30		10 ± 16	1 ± 2	1 ± 0.4	13251 ± 9145	1890 ± 1192	1647 ± 794

Tab. S4: *Third scouting route (D) on 17. 11. 2021 segmented into units, where ">>" indicates movement from place to place and the abbreviations are the names of stations (university campus is Uni), which are explained in Table 1 in the article. In brackets, aw is ambient walk, s stationary, r ride. Average values and SD of particulate matter (PM$_x$), particle number concentration (PNC), equivalent black carbon (eBC) and UV absorbing PM (UVPM) are in the table. Sampling period for ICP-MS analysis is marked bold (8:47:00-10:28:30)*

ID	**Location**	**Duration**	**Start**	**Stop**	**Train frequency**	**PM$_{10}$**	**PM$_{2.5}$**	**PM$_1$**	**PNC**	**eBC**	**UVPM**
		min.	h:mm:ss	h:mm:ss	no. of trains (trains/hour)	µg m^{-3}	µg m^{-3}	µg m^{-3}	pt cm^{-3}	ng m^{-3}	ng m^{-3}
1	Uni >> NS-U/S (aw)	18	7:59:55	8:17:45		7 ± 6	4 ± 3	4 ± 2	8551 ± 11656	682 ± 517	945 ± 512
2	**NS-U/S (s)**	5	8:17:46	8:22:30		9 ± 5	6 ± 1	5 ± 1	7064 ± 1218	95 ± 0	1138 ± 275
3	NS-U/S >> CS-U1 (r)	22	8:22:31	8:44:20		115 ± 58	57 ± 25	18 ± 6	5123 ± 1657	5248 ± 3506	4732 ± 2328
4	**CS-U1 (s)**	23	8:44:21	**9:07:20**	18 (47)	165 ± 46	67 ± 9	20 ± 2	10496 ± 2823	10355 ± 2015	6781 ± 1841
5	Elevators (iw)	4	**9:07:21**	**9:11:15**		180 ± 91	57 ± 20	16 ± 4	13520 ± 5973	5489 ± 3011	4889 ± 2348
6	**CS-U2 (s)**	19	**9:11:16**	**9:29:50**	16 (51)	243 ± 84	77 ± 13	20 ± 2	7709 ± 770	6035 ± 2303	5540 ± 1783
7	Elevators (iw)	6	**9:29:51**	**9:36:00**		163 ± 101	57 ± 28	17 ± 6	10947 ± 6473	6358 ± 3480	5380 ± 2594
8	**CS-R (s)**	48	**9:36:01**	**10:23:50**	~2	20 ± 24	10 ± 7	8 ± 3	4212 ± 2538	544 ± 749	626 ± 745
9	CS-U1 >> NS-U/S (r)	19	**10:23:51**	10:42:47		120 ± 48	53 ± 15	17 ± 4	6024 ± 1866	5095 ± 2308	4533 ± 1557
10	NS-U/S >> Uni (aw)	19	10:42:48	11:02:00		7 ± 9	3 ± 2	3 ± 2	17156 ± 81964	1189 ± 1247	1080 ± 969

Tab. S5: *Fourth scouting route (E) on 24. 11. 2021 segmented into units, where ">>" indicates movement from place to place and the abbreviations are the names of stations (university campus is Uni), which are explained in Table 1 in the article. In brackets, aw is ambient walk, s stationary, r ride. Average values and SD of particulate matter (PM$_x$), particle number concentration (PNC), equivalent black carbon (eBC) and UV absorbing PM (UVPM) are in the table. Sampling period for ICP-MS analysis is marked bold (9:31:21-10:22:39).*

ID	**Location**	**Duration**	**Start**	**Stop**	**Train frequency**	**PM$_{10}$**	**PM$_{2.5}$**	**PM$_1$**	**PNC**	**eBC**	**UVPM**
		min.	h:mm:ss	h:mm:ss	no. of trains (trains/hour)	µg m^{-3}	µg m^{-3}	µg m^{-3}	pt cm^{-3}	ng m^{-3}	ng m^{-3}
1	Uni >> NS-U/S (aw)	13	7:55:35	8:08:06		11 ± 20	4 ± 2	4 ± 1	22411 ± 82839	643 ± 305	928 ± 429
2	**NS-U/S (s)**	4	8:08:07	8:11:56	2 (~30)	14 ± 49	5 ± 3	4 ± 0	2154 ± 300	264 ± 81	813 ± 330
3	NS-U/S >> CS-U1 (r)	19	8:11:57	8:31:12		139 ± 78	58 ± 28	22 ± 8	4229 ± 1114	8372 ± 5356	5790 ± 3219
4	Elevators (iw)	3	**8:31:13**	**8:34:25**		191 ± 66	67 ± 17	23 ± 4	11775 ± 5901	12739 ± 2905	8689 ± 2096
5	**CS-R (s)**	31	**8:34:26**	**9:05:11**	~8	33 ± 24	12 ± 2	10 ± 1	10637 ± 4882	1111 ± 559	1626 ± 793
6	Elevators (iw)	3	**9:05:12**	**9:07:55**		104 ± 89	37 ± 29	14 ± 4	8107 ± 1849	2724 ± 2838	2301 ± 2404
7	**CS-S (s)**	20	**9:07:56**	**9:27:57**	16 (48)	236 ± 56	82 ± 9	21 ± 2	6205 ± 571	8446 ± 2753	6211 ± 1849
8	Elevators (iw)	9	**9:27:58**	**9:36:44**		131 ± 111	39 ± 30	12 ± 5	7666 ± 4751	4168 ± 2143	3473 ± 1519
9	**CS-U2 (s)**	2	**9:36:45**	**9:38:00**	3	228 ± 64	67 ± 7	16 ± 1	6570 ± 248	3982 ± 1050	3831 ± 757
10	**CS-U1 (s)**	26	**9:38:10**	**10:04:33**	13 (30)	196 ± 56	66 ± 10	20 ± 2	6646 ± 939	9941 ± 3313	6700 ± 1853
11	CS-U1 >> NS-U/S (r)	18	**10:04:34**	**10:22:22**		130 ± 47	53 ± 9	18 ± 3	4565 ± 582	7963 ± 3097	5444 ± 1549
12	NS-U/S >> Uni (aw)	12	10:22:23	10:34:46		7 ± 17	3 ± 1	3 ± 0.2	3635 ± 2258	1642 ± 1471	1628 ± 992

1.4 Repetition of the same subway route

The tables below are in the same style as in the previous chapter, here exactly the same route is repeated, however, some of the times spent at different locations vary due to train arrivals and departures.

Tab. S6: *First repetition of the same route (F1) on 7. 12. 2021 (7:27:50-10:14:00) segmented into units, where ">>" indicates movement from place to place and the abbreviations are the names of stations (university campus is Uni), which are explained in Table 1 in the article. In brackets, aw is ambient walk, s stationary, r ride. Average values and SD of particulate matter (PM_x), particle number concentration (PNC), equivalent black carbon (eBC) and UV absorbing PM (UVPM) are in the table. Sampling period for ICP-MS analysis is marked bold (7:54:45-9:53:10).*

ID	Location	Duration	Start	Stop	Train frequency	PM_{10}	$PM_{2.5}$	PM_1	PNC	eBC	UVPM
		min.	h:mm:ss	h:mm:ss	no. of trains (trains/hour)	µg m^{-3}	µg m^{-3}	µg m^{-3}	pt cm^{-3}	ng m^{-3}	ng m^{-3}
1	Uni >> NS-U/S (aw)	25	7:27:50	7:52:50		6 ± 11	1 ± 1	0.3 ± 0.1	5530 ± 3902	284 ± 392	389 ± 378
2	**NS-U/S (s)**	6	7:52:51	**7:58:50**	1	8 ± 10	1 ± 2	0.4 ± 0.4	5109 ± 1249	55 ± 230	270 ± 0
3	NS-U/S >> MC-U (r)	6	**7:58:51**	**8:04:30**		87 ± 39	34 ± 12	9 ± 3	4911 ± 436	632 ± 1615	2327 ± 973
4	**MC-U (s)**	6	**8:04:31**	**8:10:13**	4 (40)	89 ± 44	43 ± 19	13 ± 5	4670 ± 554	5098 ± 2102	4156 ± 1446
5	MC-U >> OB-U (r)	4	**8:10:14**	**8:13:50**		126 ± 36	63 ± 7	22 ± 2	5202 ± 308	6546 ± 771	5465 ± 711
6	**OB-U (s)**	14	**8:13:51**	**8:28:00**	5 (21)	211 ± 58	88 ± 16	22 ± 4	4984 ± 439	8436 ± 1688	6718 ± 1315
7	OB-U >> OD-U (r)	5	**8:28:01**	**8:32:40**		203 ± 52	94 ± 8	25 ± 1	4755 ± 788	9253 ± 1566	6436 ± 1464
8	**OD-U (s)**	10	**8:32:41**	**8:43:00**	4 (24)	188 ± 52	71 ± 9	20 ± 2	6779 ± 860	10675 ± 1566	6574 ± 1916
9	OD-U >> CS-U1 (r)	3	**8:43:01**	**8:46:20**		188 ± 53	79 ± 11	26 ± 4	6779 ± 478	10014 ± 3101	6961 ± 1619
10	**CS-U1 (s)**	12	**8:46:20**	**8:58:15**	9 (45)	197 ± 55	73 ± 12	19 ± 3	6482 ± 570	8629 ± 4105	5978 ± 1628
11	Elevators (iw)	19	**8:58:16**	**9:17:00**		30 ± 38	10 ± 13	4 ± 4	9758 ± 4870	1779 ± 2275	1545 ± 1576
12	**CS-S (s)**	10	**9:17:01**	**9:27:00**	7 (42)	33 ± 21	13 ± 4	4 ± 1	6532 ± 1439	1052 ± 1087	711 ± 837
13	CS-S >> NS-U/S (r)	26	**9:27:01**	**9:53:10**		39 ± 37	12 ± 6	4 ± 2	6597 ± 3318	1280 ± 702	1150 ± 689
14	NS-U/S >> Uni (aw)	21	9:53:11	10:14:00		6 ± 11	1 ± 1	0.4 ± 0.2	6475 ± 13906	187 ± 3067	126 ± 2963

Tab. S7: *Second repetition of the same route (F2) on 7. 12. 2021 (12:10:20-14:45:15) segmented into units, where ">>" indicates movement from place to place and the abbreviations are the names of stations (university campus is Uni), which are explained in Table 1 in the article. In brackets, aw is ambient walk, s stationary, r ride. Average values and SD of particulate matter (PM_x), particle number concentration (PNC), equivalent black carbon (eBC) and UV absorbing PM (UVPM) are in the table. Sampling period for ICP-MS analysis is marked bold (7:54:45-9:53:10).*

ID	Location	Duration	Start	Stop	Train frequency	PM_{10}	$PM_{2.5}$	PM_1	PNC	eBC	UVPM
		min.	h:mm:ss	h:mm:ss	no. of trains (trains/hour)	µg m^{-3}	µg m^{-3}	µg m^{-3}	pt cm^{-3}	ng m^{-3}	ng m^{-3}
1	Uni >> NS-U/S (aw)	18	12:10:20	12:28:38		4 ± 5	1 ± 0.6	0.4 ± 0.1	6865 ± 31489	32 ± 0	310 ± 148
2	**NS-U/S (s)**	10	**12:28:39**	**12:38:39**	2 (~40)	6 ± 7	2 ± 1	0.6 ± 0.3	3401 ± 765	32 ± 0	221 ± 111
3	NS-U/S >> MC-U (r)	11	**12:38:40**	**12:49:27**		46 ± 53	20 ± 10	5 ± 2	4219 ± 1123	558 ± 1009	1401 ± 729
4	**MC-U (s)**	10	**12:49:28**	**12:59:26**	3 (18)	26 ± 22	11 ± 6	3 ± 1	4309 ± 763	1488 ± 626	1316 ± 496
5	MC-U >> OB-U (r)	4	**12:59:27**	**13:02:59**		132 ± 52	60 ± 17	15 ± 5	3794 ± 368	4697 ± 2077	4075 ± 1511
6	**OB-U (s)**	10	**13:03:00**	**13:12:35**	5 (33)	118 ± 38	54 ± 10	14 ± 2	5166 ± 930	5283 ± 1185	4522 ± 882
7	OB-U >> OD-U (r)	5	**13:12:36**	**13:17:46**		118 ± 37	49 ± 6	15 ± 1	3780 ± 631	5607 ± 1428	4232 ± 756
8	**OD-U (s)**	15	**13:17:47**	**13:33:05**	5 (20)	113 ± 41	45 ± 11	13 ± 3	6041 ± 987	6786 ± 1800	5040 ± 1776
9	OD-U >> CS-U1 (r)	3	**13:33:06**	**13:35:37**		168 ± 50	78 ± 8	27 ± 1	5319 ± 357	10196 ± 1871	8717 ± 1238
10	**CS-U1 (s)**	13	**13:35:38**	**13:48:20**	6 (28)	122 ± 42	47 ± 10	13 ± 2	6976 ± 998	6770 ± 2293	5527 ± 1856
11	Elevators (iw)	8	**13:48:21**	**13:56:46**		28 ± 32	10 ± 9	3 ± 3	8535 ± 4535	2140 ± 1239	1578 ± 888
12	**CS-S (s)**	10	**13:56:47**	**14:07:04**	7 (42)	80 ± 34	25 ± 4	7 ± 1	5541 ± 583	3953 ± 1268	2745 ± 968
13	CS-S >> NS-U/S (r)	20	**14:07:05**	**14:27:27**		39 ± 32	15 ± 8	5 ± 3	6043 ± 2173	2494 ± 1529	3550 ± 2914
14	NS-U/S >> Uni (aw)	17	14:27:28	14:44:15		4 ± 5	2 ± 0.5	0.5 ± 0.1	8709 ± 19712	1272 ± 1013	984 ± 982

Tab. S8: *Third repetition of the same route (F3) on 7. 12. 2021 (16:10:05-18:25:50) segmented into units, where ">>" indicates movement from place to place and the abbreviations are the names of stations (university campus is Uni), which are explained in Table 1 in the article. In brackets, aw is ambient walk, s stationary, r ride. Average values and SD of particulate matter (PM_x), particle number concentration (PNC), equivalent black carbon (eBC) and UV absorbing PM (UVPM) are in the table. Sampling period for ICP-MS analysis is marked bold (16:32:40-18:10:00).*

ID	**Location**	**Duration** min.	**Start**	**Stop**	**Train frequency** no. of trains (trains/hour)	**PM_{10}** $\mu g\ m^{-3}$	**$PM_{2.5}$** $\mu g\ m^{-3}$	**PM_1** $\mu g\ m^{-3}$	**PNC** pt cm^{-3}	**eBC** ng m^{-3}	**UVPM** ng m^{-3}
1	Uni >> NS-U/S (aw)	20	16:10:05	16:30:00		6 ± 7	2 ± 1	0.6 ± 0.2	24765 ± 29486	864 ± 886	1605 ± 1140
2	**NS-U/S (s)**	7	16:30:01	**16:37:10**	2 (17)	15 ± 13	3 ± 1	1 ± 1	24119 ± 6727	82 ± 0	1275 ± 903
3	NS-U/S >> MC-U (r)	7	**16:37:11**	**16:44:20**		63 ± 36	18 ± 7	7 ± 2	19411 ± 2232	714 ± 1466	2478 ± 533
4	**MC-U (s)**	5	**16:44:21**	**16:49:30**	3 (24)	53 ± 25	23 ± 5	7 ± 1	8073 ± 1063	3611 ± 1122	3256 ± 940
5	MC-U >> OB-U (r)	4	**16:49:31**	**16:53:20**		119 ± 45	46 ± 11	14 ± 3	8543 ± 717	6094 ± 1716	4870 ± 1045
6	**OB-U (s)**	10	**16:53:21**	**17:03:07**	5 (30)	199 ± 48	87 ± 7	25 ± 2	10105 ± 848	11090 ± 1928	7708 ± 1504
7	OB-U >> OD-U (r)	5	**17:03:08**	**17:08:30**		172 ± 47	72 ± 6	22 ± 1	7844 ± 598	10253 ± 1467	6028 ± 1796
8	**OD-U (s)**	10	**17:08:31**	**17:18:30**	5 (30)	175 ± 48	71 ± 7	22 ± 1	9301 ± 732	12194 ± 2383	6992 ± 1644
9	OD-U >> CS-U1 (r)	3	**17:18:31**	**17:21:45**		199 ± 52	75 ± 9	23 ± 2	7896 ± 602	7153 ± 2763	5850 ± 1605
10	**CS-U1 (s)**	12	**17:21:46**	**17:33:50**	12 (60)	212 ± 59	75 ± 9	21 ± 2	11313 ± 1144	8837 ± 2983	6530 ± 1586
11	Elevators (iw)	11	**17:33:51**	**17:44:50**		96 ± 62	30 ± 16	11 ± 4	14729 ± 6640	3758 ± 2528	3373 ± 1682
12	**CS-S (s)**	4	**17:44:51**	**17:48:50**	6 (90)	155 ± 53	48 ± 7	14 ± 1	9491 ± 597	5013 ± 2480	3875 ± 1172
13	CS-S >> NS-U/S (r)	20	**17:48:51**	**18:09:00**		47 ± 39	17 ± 12	7 ± 3	15647 ± 7250	3139 ± 1464	3065 ± 1119
14	NS-U/S >> Uni (aw)	17	**18:09:01**	18:25:50		9 ± 8	3 ± 1	2 ± 1	24923 ± 23754	2479 ± 1531	3342 ± 1667

1.5 Differences between the travelling in new and old trains

Tab. S9: *Difference between concentration of particulate matter (PM) in µg m^{-3} and particle number concentration (PNC) in pt cm^{-3} inside old (type B) and new (type C) train during the repetition of the same route between Neuperlach Süd NS-U/S and Hauptbahnhof Oben CS-U1, while the direction of 1 and 3 are from CS-U1 to NS-U/S and 2 in the opposite direction, 28. 8. 2022 between 20:15-21:50.*

Median	**PM_1**	**$PM_{2.5}$**	**PM_{10}**	**PNC**
1 New >	24.0	74.6	112.7	11120
2 New <	22.1	67.0	101.0	10884
3 Old >	25.9	81.7	127.8	12750

1.6 SEM-EDX analysis

Based on the mapping of 180 000 particles described in the Materials and methods of this paper (Section 3.5.3: Imaging and single particle elemental analysis using SEM-EDX), the particle size distribution is illustrated (Fig. S7).

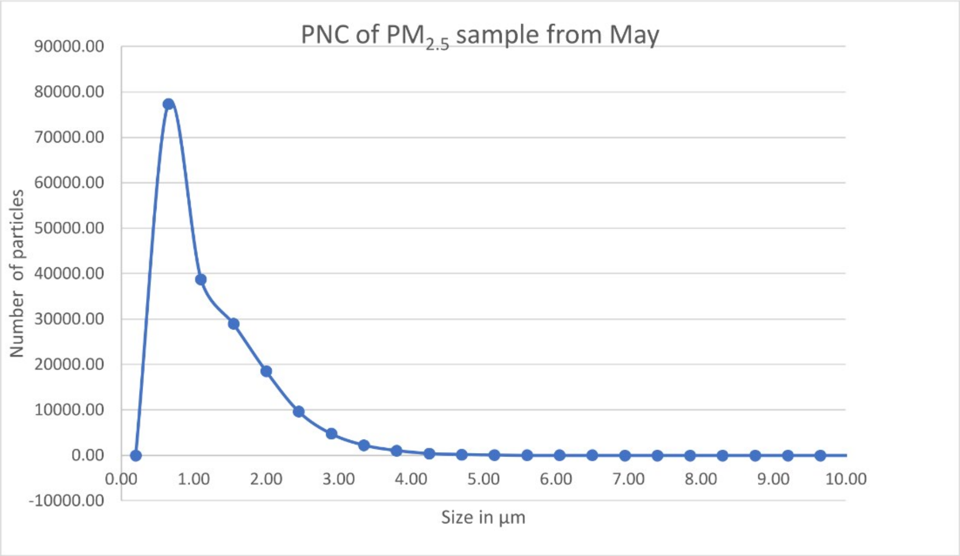

Fig. S7: *Particle size distribution based on the mapping of 180 000 particles by the EDX sensor, bin size 0.25*

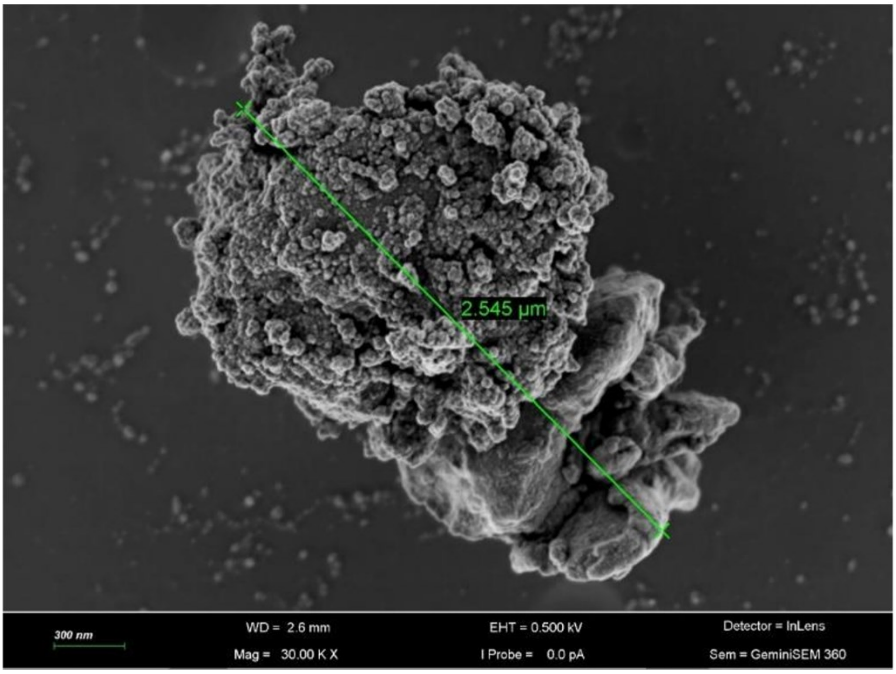

***Fig. S8**: SEM micrograph of an iron oxide particle from the Munich subway*

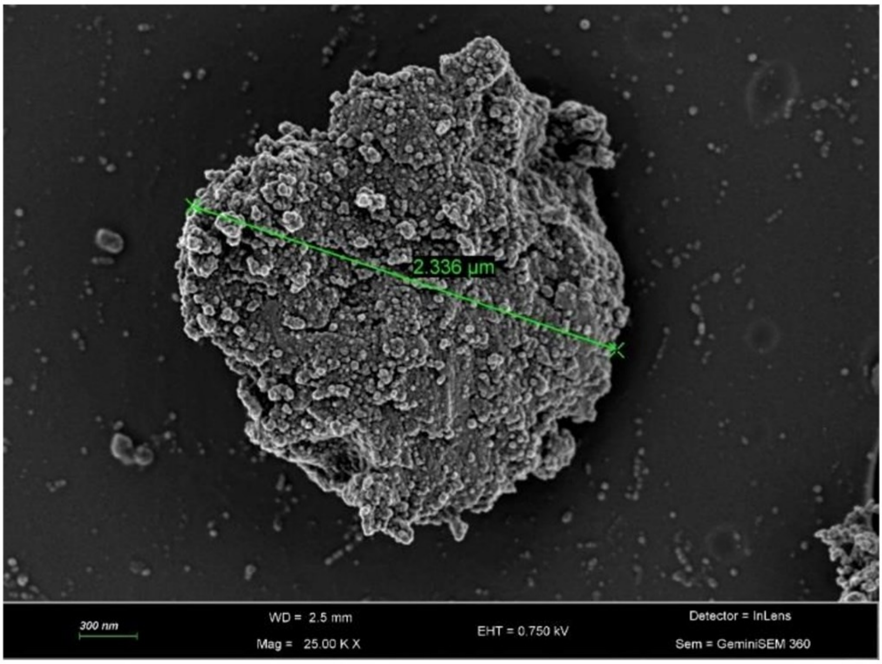

Fig. S9: *SEM micrograph of an iron oxide particle from the Munich subway*

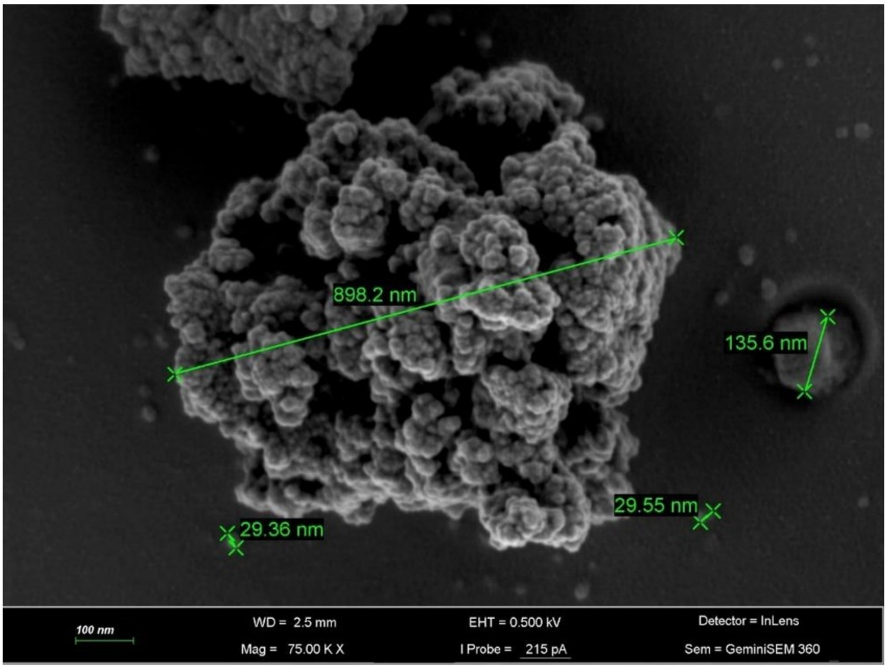

Fig. S10: *SEM micrograph of an iron oxide particle from the Munich subway*

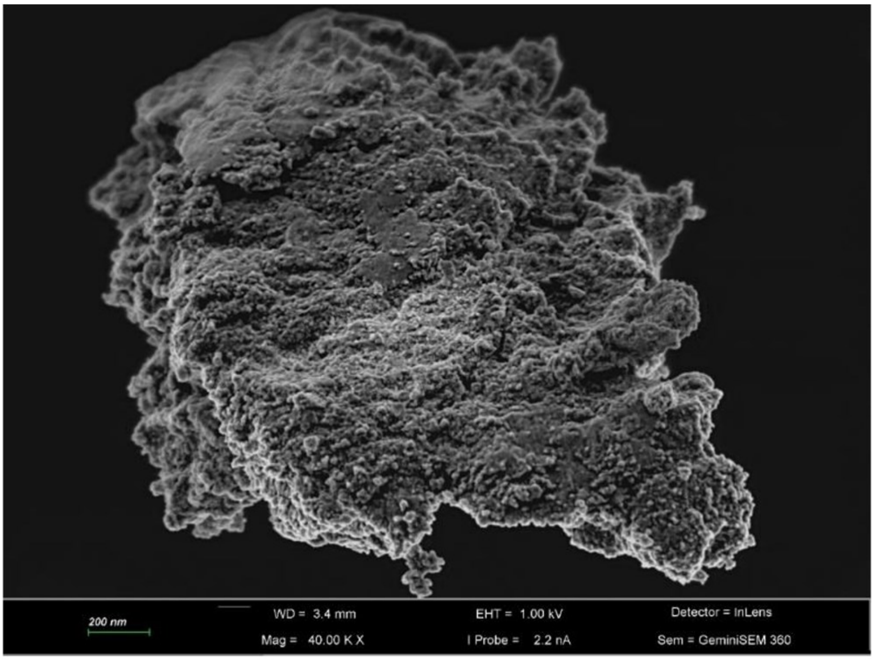

Fig. S11: SEM micrograph of an iron oxide particle from the Munich subway

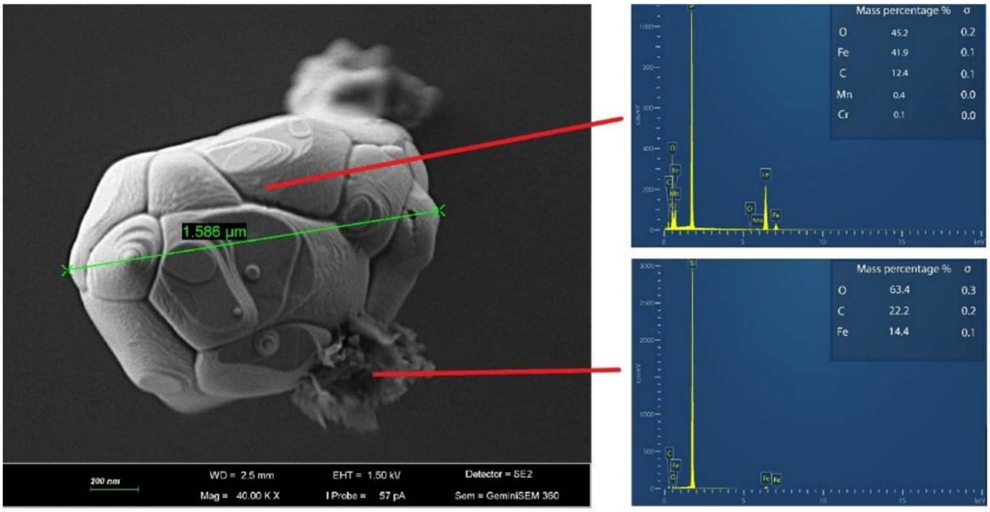

	Mass percentage %	σ
O	45.2	0.2
Fe	41.9	0.1
C	12.4	0.1
Mn	0.4	0.0
Cr	0.1	0.0

	Mass percentage %	σ
O	63.4	0.3
C	22.2	0.2
Fe	14.4	0.1

***Fig. S12:** SEM micrograph + EDX spectra of a layered iron oxide particle of unknown origin from the Munich subway*

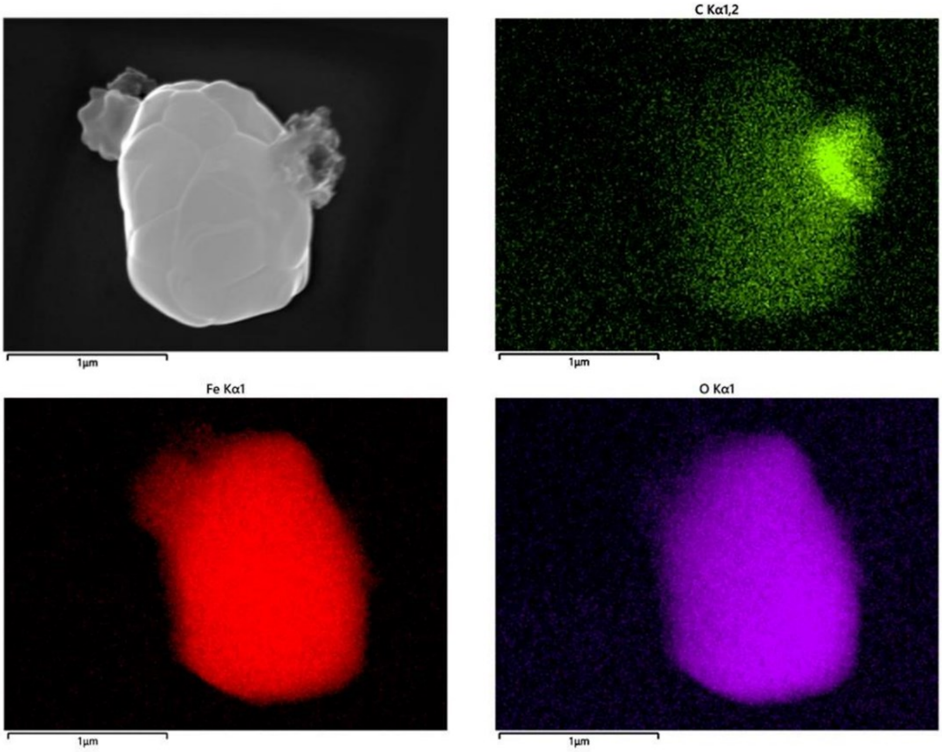

Fig. S13: EDX mapping of a layered iron oxide particle of unknown origin from the Munich subway

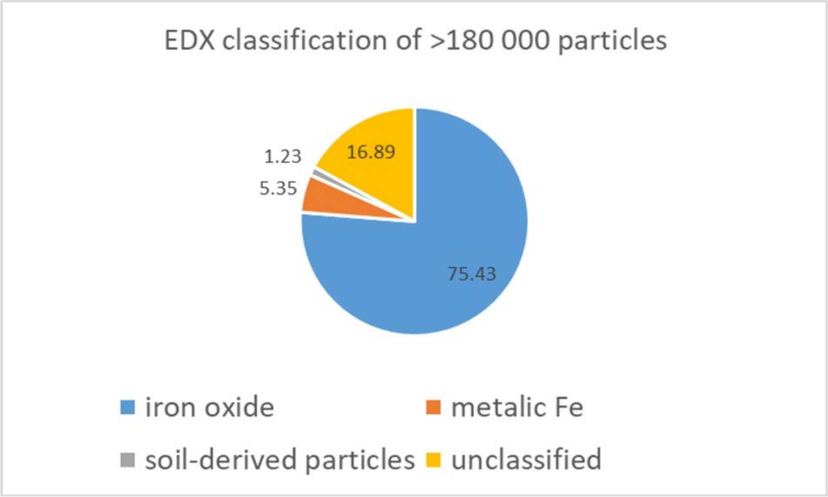

***Fig. S14**: EDX classification of more than 180 000 particles, sampled at U-Bahn station CS-U1 platform on 28. 8. 2022 (14:06–20:06)*

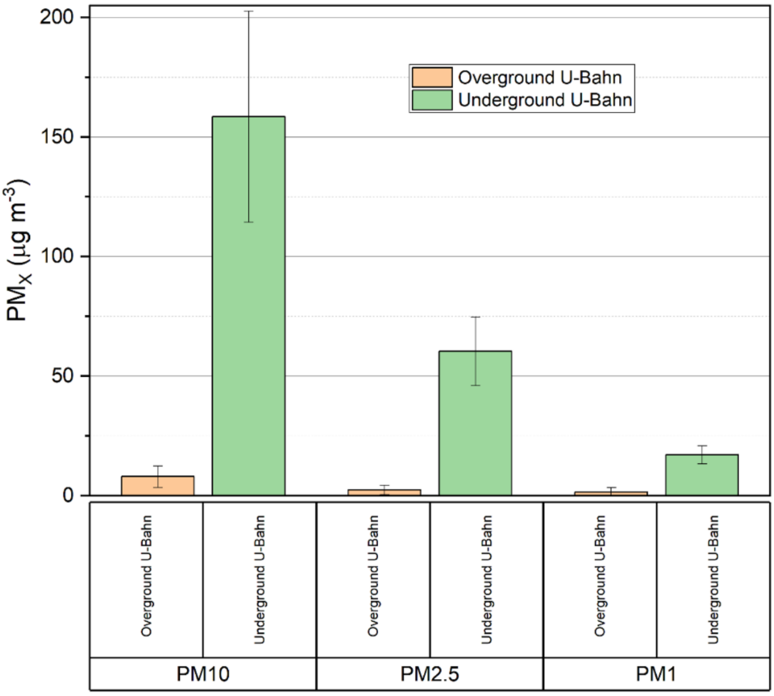

Fig. S15*: Comparison of underground and overground stations: Underground stations: Michaelibad U5, Ostbahnhof U5, Odeonsplatz U4/U5, Hauptbahnhof U4/U5, Hauptbahnhof U1-U8, Innsbrucker ring U2/U5, Overground: Neuperlach Süd. Data for each station are available in the Table 1*

1.7. ICP-MS analysis

Standard calibration mix used for this study with the ICP-MS Agilent 8900:

- ICV-Standard calibration line: Agilent Technology Co., Part number: 5183-4682; Ca, Fe, K, Mg, Na, Sr, Ag, Al, As, Ba, Be, Cd, Co, Cr, Cu, Mn, Mo, Ni, Pb, Sb, Se, Th, TI, U, V, Zn
- Internal standard mix for ICP-MS systems: Agilent Technology Co., Part number: 5188-8525, 100 µg mL Bi, Ge, In, Li, Lu, Rh, Sc, Tb in 10% HNO_3)

6.2. APPENDIX B: Manuscript 2

Liu, X.; Schnelle-Kreis, J.; Zhang, X.; **Bendl, J.**; Khedr, M.; Jakobi, G.; Schloter-Hai, B.; Hovorka, J.; Zimmermann, R. Integration of air pollution data collected by mobile measurement to derive a preliminary spatiotemporal air pollution profile from two neighboring German-Czech border villages. *The Science of the Total Environment* **2020,** *722*, 137632; DOI 10.1016/j.scitotenv.2020.137632.

Science of the Total Environment 722 (2020) 137632

Contents lists available at ScienceDirect

Science of the Total Environment

journal homepage: www.elsevier.com/locate/scitotenv

Integration of air pollution data collected by mobile measurement to derive a preliminary spatiotemporal air pollution profile from two neighboring German-Czech border villages

Xiansheng Liu [a,b], Jürgen Schnelle-Kreis [a,*], Xun Zhang [c,*], Jan Bendl [a,d], Mohamed Khedr [a,b], Gert Jakobi [a], Brigitte Schloter-Hai [a], Jan Hovorka [d], Ralf Zimmermann [a,b]

[a] *Joint Mass Spectrometry Center, Cooperation Group Comprehensive Molecular Analytics, Helmholtz Zentrum München, German Research Center for Environmental Health, Ingolstädter Landstr. 1, 85764 Neuherberg, Germany*
[b] *Joint Mass Spectrometry Center, Chair of Analytical Chemistry, University of Rostock, Rostock, Germany*
[c] *Beijing Key Laboratory of Big Data Technology for Food Safety, School of Computer and Information Engineering, Beijing Technology and Business University, Beijing 100048, China,*
[d] *Institute for Environment Studies, Faculty of Science, Charles University, Prague, Czech Republic*

HIGHLIGHTS

- A novel mobile monitoring approach was used to capture variation in small-scale air.
- The study illustrates the potential of mobile measurement methods in small-scale.
- As an example case study, small-scale air pollution hotspots could be located.

GRAPHICAL ABSTRACT

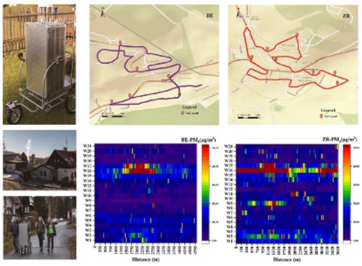

ARTICLE INFO

Article history:
Received 14 December 2019
Received in revised form 11 February 2020
Accepted 28 February 2020
Available online 11 March 2020

Editor: Jianmin Chen

Keywords:
PM_X
PNC
BC
Mobile monitoring
Small-scale air-pollution

ABSTRACT

Generally, there are only a few fixed air quality monitoring stations installed in villages or rural areas and only a few studies on small-scale variations in air pollution have been described in detail, which make it difficult to estimate human exposure in such environments and related adverse health effects. Moreover, biomass combustion can be an important source of air pollution in rural areas, comparable to vehicle and industrial emissions in urban planning. And their air pollutants are mainly affected by local sources. For this reason, a survey on rural air pollution was carried out in this study. Therefore, portable, battery-powered monitoring devices were used to measure particulate matter (PM_{10}, $PM_{2.5}$, PM_1, particle number concentration, and black carbon) in order to study air quality in rural communities. The focus of the investigations was to explore the application of mobile monitoring equipment in small-scale environments, compare the differences in rural air pollutants between two neighboring villages in two countries, and the identification of pollution hotspots. The measurements were carried out in November 2018 in two villages on the German-Czech border. Over a period of four days, 21 mobile measurements along fixed routes were carried out simultaneously at both locations. The analysis of the data revealed significant differences in PN and PM concentrations in rural air pollutants between the two countries. The spatial and

---

* Corresponding authors.
E-mail addresses: juergen.schnelle@helmholtz-muenchen.de (J. Schnelle-Kreis), zhangxun@btbu.edu.cn (X. Zhang).

https://doi.org/10.1016/j.scitotenv.2020.137632

temporal distribution of air pollution hotspots in the Czech village was higher than that in the German village. The relationships between the measurement parameters were weak but highly significant and the meteorological parameters can effect air pollution. Overall, the results of this study show that mobile measurements are suitable for effectively recording and distinguishing spatial and temporal characteristics of air quality.

1. Introduction

In recent years, air pollution research has involved different spatial scales, focusing on different research subjects, including global scales (Van Donkelaar et al., 2010), regional scales (Kutzner et al., 2018), and urban scales (Gong et al., 2015). The research topic is gradually analyzing the characteristics of concentration changes based on observation data, and is gradually investigating optical characteristics and radiation forcing. Accordingly, various European countries have adopted a series of monitoring and control measures in response to the air pollution problem in Europe, and achieved relatively significant phased results. A multi-layered sensor-based monitoring device and a gridded air pollution monitoring system were deployed to monitor the air pollution status of the target area. Air pollution grid monitoring greatly improves the ability to detect small (100 m) hotspots in the target area. So far, many studies have focused on urban air pollution in cities, e.g. Vienna (Dons et al., 2012), Barcelona, Lugano (Reche et al., 2011), Paris (Reche et al., 2011), Chicago (Babich et al., 2000), Augsburg (Wolf et al., 2017), Manila (Alas et al., 2018), Shanghai (Liu et al., 2019), etc. Although the urban air pollution poses a serious health problem for people, the rural air pollution also higher ($PM_{10} \geq 20\ \mu g/m^3$ annual mean, $PM_{2.5} \geq 10\ \mu g/m^3$ annual mean). Braniš and Domasová (2003) found that when comparing PM_{10} data from villages and Prague, the average particle concentration in rural areas was higher in all three seasons (two winter and one summer) studied. Hovorka et al. (2015) also claimed the influence of wood combustion in villages on the air quality near the city. However, there are only a few fixed stations installed in rural areas and only a few studies on small-scale variations of air pollution have been published. PM_1 was studied in rural site of Austria by Gomiščcek et al. (2004); BC in a rural areas of India by Rehman et al., 2011, and $PM_{2.5}$ in a rural site in Chongqing, southwest China and PM_{10} in Mol, Belgium by Peng and Peters et al. (Peng et al., 2019; Peters et al., 2013).

More importantly, the number of villages is generally much larger than the number of cities. Although the population density in cities is much higher, the number of people living in rural areas has gradually increased during the five-year period from 2010 to 2015 across the EU-28 by 1.7 percentage points (EUROSTAT, 2017).

While in most European cities little solid fuel is used for heating, the use of wood for heating is widespread in rural communities. Therefore, biomass combustion can be an important source of air pollution in rural areas, comparable to vehicle and industrial emissions in urban planning (Begam et al., 2016). Moreover, their air pollutants are mainly affected by local sources. Therefore, field studies on air pollution in villages can help to understand the impact of solid fuel combustion on local air quality and exposure of the rural population to it. For this reason, a survey of rural air pollutants was carried out in this study. In addition, in the Czech countryside firewood is mainly used for home heating, while in Germany it is more frequently used for leisure. To compare differences in rural air pollutants between two countries, two neighboring German-Czech border villages with similar population and structure were selected for this study.

In addition, current gridded air pollution monitoring systems use fixed deployment methods. The monitoring area is usually divided into 500 m to 3 km long grids with each grid containing at least one fixed installation monitoring node (fixed monitoring station). However, based on the fixed sample observation of the atmospheric pollutant concentration, the spatial representation is limited due to the number of sampling points, and the spatial analysis and spatial simulation on the area are relatively few. In order to avoid this case, nowadays, mobile monitoring (Gong et al., 2015) has conducted a collection of real-time air quality measurements to assess in situ emissions, local air quality trends, and air pollutant exposures. This measurement strategy uses the complex, one-second multi-pollution data over time and for each location to drive the limits of traditional data analysis (Brantley et al., 2014). It can solve the central monitoring problem of insufficient description of air pollution exposure. Mobile measurements are used in human exposure studies to quantify individual exposures and demonstrate the importance of exposure differences in different microenvironments (Dons et al., 2012).

Based on the above reasons, this small-scale air pollution monitoring manuscript used a portable instrument-based micro air pollution monitoring devices to investigate the exposure of PM (PM_1, $PM_{2.5}$ and PM_{10}), black carbon (BC) concentration and particulate number concentration (PNC) at two different villages, one in Germany and one in the Czech Republic. The measurements were carried out during November 22–25, 2018. The collected data were used to identify air pollution hotspots, analyze the average concentration and variation of each region and to discuss the influencing factors.

2. Methods

2.1. Study area and monitoring protocol

The mobile measurements were carried out in two neighboring villages at the German-Czech border, Bayerisch Eisenstein (49.12N, 13.20E), Germany and Zelezna Ruda (49.14N, 13.24E), Czech Republic. Both villages are climatic health resorts, which have comparable number of residents (BE: 1045, ZR: 1745), residential houses and geographical structure with one main road following the valley and one main road on the uphill slope northwest. Residential areas are mainly located on the slopes of the valley (Fig. 1). There are no factories in or close to the villages.

In both villages fixed routes were defined using sidewalks or the right hand side of the road which were repeatedly walked in the course of the investigations. The route in Bayerisch Eisenstein was approximately 5 km long, the route in Zelezna Ruda 4 km (Fig. 1). The average walking time for the entire route was approximately 60 min at both sites. Most parts of the routes were located in residential areas with little traffic. From 5 am to 10 pm, parallel walks were carried out at both sites every 2–3 h to compare air pollution in the two villages. 20 and 21 walks were successfully performed on 4 days between November 22 and 25, 2018 in Bayerisch Eisenstein and Zelezna Ruda, respectively (Table 1).

Short-term stationary and mobile monitoring significantly reduces the total measurement time and allows the measurement of a larger number of sites (Begam et al., 2016). Therefore, the mobile platform was placed at the endpoint after every walk, and measurements were continued for 1 h. The results of these measurements were used as short-term stationary measurements and were compared with the mobile monitoring results.

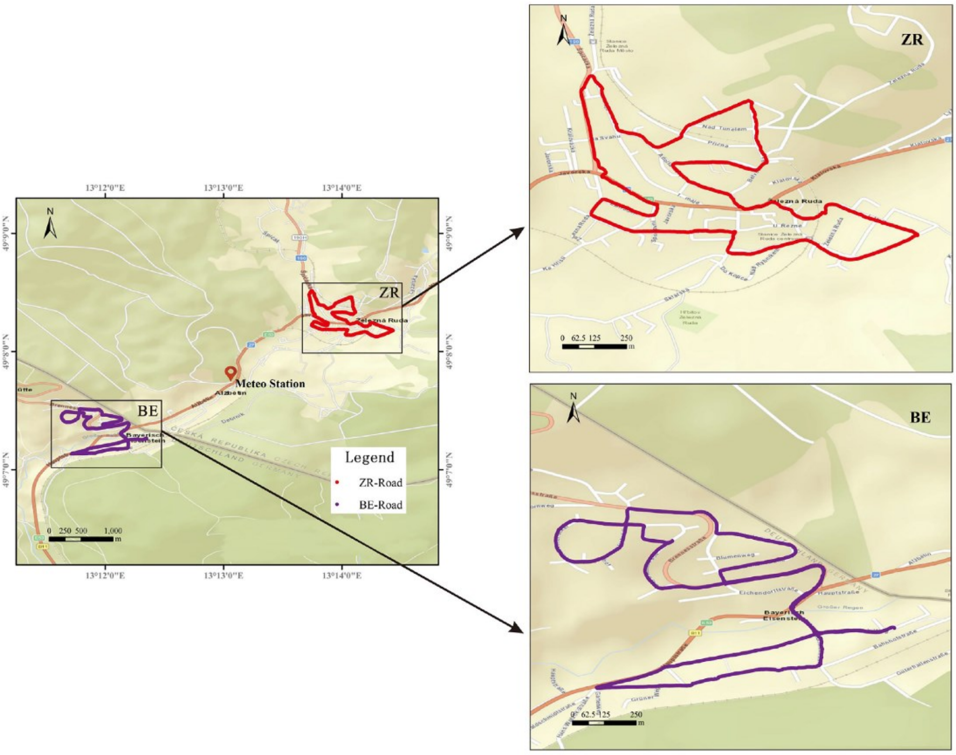

Fig. 1. The monitoring routes in Bayerisch Eisenstein (BE) and Zelezna Ruda (ZR) and Meteo station.

Meteorological data were measured at a fixed site, Meteo Station (49.13N, 13.23E), between the two villages (Fig. 1).

Table 1
Overview of the measurement walks.

Walk	Date	Start time BE	End time BE	Start time ZR	End time ZR
1	2018/11/22	16:20	17:13	17:08	18:27
2		19:00	19:47	19:04	20:03
3		21:00	21:55	21:02	22:07
4	2018/11/23	05:05	06:05	05:13	06:18
5		07:00	07:57	07:02	07:56
6		09:00	09:54	09:09	10:07
7		11:00	11:54	11:02	12:08
8		14:00	14:50	14:04	14:55
9		16:15	17:09	15:59	17:03
10		18:05	19:04	18:03	19:16
11		20:00	21:07	20:02	20:55
12	2018/11/24	Skip	Skip	07:10	08:08
13		09:03	09:58	08:59	10:12
14		13:56	15:04	14:08	15:08
15		16:00	17:04	16:08	17:01
16		18:00	19:07	17:58	18:48
17		20:05	21:11	20:10	21:08
18	2018/11/25	05:00	06:00	05:03	06:07
19		07:00	07:59	06:59	07:53
20		09:07	10:11	09:03	10:01
21		11:00	11:59	11:04	11:58

2.2. Mobile platform

Mobile measurements for PM_X, PNC, and BC, in parallel at both locations, were conducted by two identical mobile platforms. The platform consists of a trolley and a large aluminum box, which protects the instruments and positions the inlets at breathing height (approx. 1.5 m above ground). The detection frequency for PMx and PNC was 1 Hz. Data on PM_X (PM_1, $PM_{2.5}$, PM_{10}) mass were recorded by a laser nephelometer - DustTrak DT (DRX 8532, TSI Inc., USA). Particle number concentrations (PNC), within the size range of 20–1000 nm, were measured by condensation particle counters (P-Trak 8525, TSI Inc., USA). BC concentration was measured by aethalometers (microAethalometer, MA200, AethLabs, USA) with a time resolution of 10 s to avoid too much noise of the BC signal. The aethalometer measures the light attenuation through a filter tape at 5 wavelengths while the filter is continuously collecting the aerosol (Begam et al., 2016). The measurement at 880 nm is defined as the concentration of Black Carbon (BC) (Petzold et al., 2013; Olson et al., 2015). Because there is a lot of noise in other wavelengths, the research is mainly concentrating on BC.

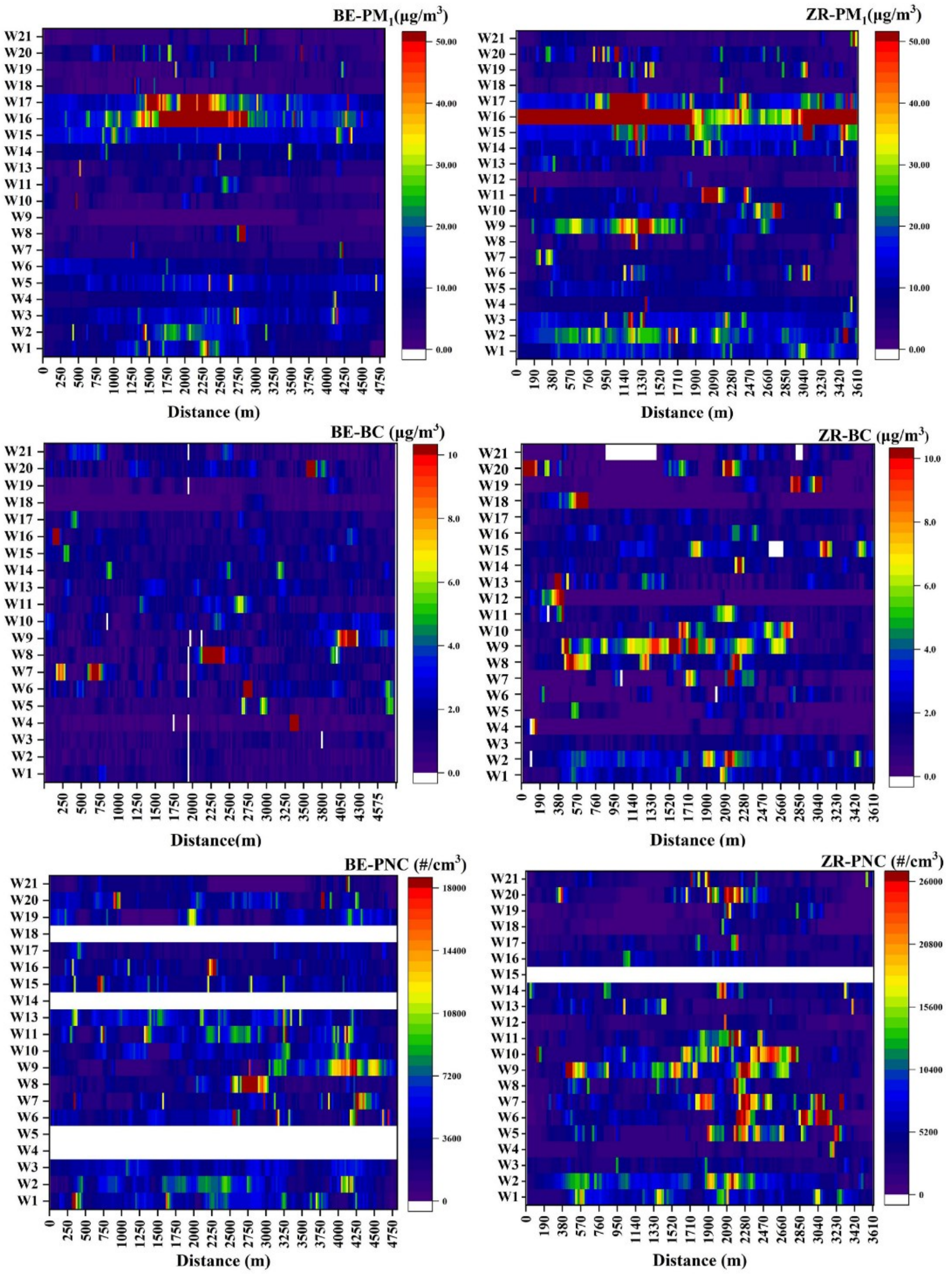
BE-PM$_1$(μg/m^3)
W21 W20 W19 W18 W17 W16 W15 W14 W13 W11 W10 W9 W8 W7 W6 W5 W4 W3 W2 W1
0 250 500 750 1000 1250 1500 1750 2000 2250 2500 2750 3000 3250 3500 3750 4000 4250 4500 4750
Distance (m)
0.00 10.00 20.00 30.00 40.00 50.00
ZR-PM$_1$(μg/m^3)
W21 W20 W19 W18 W17 W16 W15 W14 W13 W12 W11 W10 W9 W8 W7 W6 W5 W4 W3 W2 W1
0 190 380 570 760 950 1140 1330 1520 1710 1900 2090 2280 2470 2660 2850 3040 3230 3420 3610
Distance (m)
0.00 10.00 20.00 30.00 40.00 50.00
BE-BC (μg/m^3)
W21 W20 W19 W18 W17 W16 W15 W14 W13 W11 W10 W9 W8 W7 W6 W5 W4 W3 W2 W1
250 500 750 1000 1250 1500 1750 2000 2250 2500 2750 3000 3250 3500 3800 4050 4300 4575
Distance(m)
0.0 2.0 4.0 6.0 8.0 10
ZR-BC (μg/m^3)
W21 W20 W19 W18 W17 W16 W15 W14 W13 W12 W11 W10 W9 W8 W7 W6 W5 W4 W3 W2 W1
0 190 380 570 760 950 1140 1330 1520 1710 1900 2090 2280 2470 2660 2850 3040 3230 3420 3610
Distance (m)
0.0 2.0 4.0 6.0 8.0 10.0
BE-PNC (#/cm^3)
W21 W20 W19 W18 W17 W16 W15 W14 W13 W11 W10 W9 W8 W7 W6 W5 W4 W3 W2 W1
0 250 500 750 1000 1250 1500 1750 2000 2250 2500 2750 3000 3250 3500 3750 4000 4250 4500 4750
Distance (m)
0 3600 7200 10800 14400 18000
ZR-PNC (#/cm^3)
W21 W20 W19 W18 W17 W16 W15 W14 W13 W12 W11 W10 W9 W8 W7 W6 W5 W4 W3 W2 W1
0 190 380 570 760 950 1140 1330 1520 1710 1900 2090 2280 2470 2660 2850 3040 3230 3420 3610
Distance (m)
0 5200 10400 15600 20800 26000

Besides the PMx and BC measurements the platforms were equipped with a GPS (Garmin GPSMAP 64s, recording resolution 1s) to register measurement location and a POV camera (Olympus Tough TG Tracker, 5s) to capture local and mobile pollution sources such as smoking chimneys, trucks or smokers.

At the fixed site, air temperature, relative humidity, wind direction WD, wind speed WS, with 1 min integration time, were monitored by the "Ultra-Precision Professional Weather Station System WMR300" from Oregon Scientific.

2.3. Instrumentation preparation and data validation

Instrument preparation took place in our laboratory before each walk and consisted of zero calibration checks, cleaning and greasing of the DustTrak impactor, cleaning of the DustTrak chamber, replacement of the MA200 filter strip, battery and memory checks, and clock synchronization. Flow measurements were performed with a factory calibrated flow meter.

2.4. Data analysis and processing protocols

2.4.1. Kruskal-Wallis test

Firstly, a total data inspection of mobile and stationary measurements was made from Bayerisch Eisenstein and Zelezna Ruda. Pollutant concentrations were statistically compared using a non-parametric Kruskal-Wallis test at a critical value (α) of 0.05 (Kruskal and Wallis, 1952). This is a non-parametric alternative to a one-way ANOVA. The Kruskal-Wallis test investigates whether the sampled populations have the same median. Furthermore, an analysis of the mobile and stationary variability of the air quality measurements was performed by one-way ANOVA. Data analysis was performed using the Data Processing System 9.5 (DPS) (Tang and Zhang, 2013).

2.4.2. Post-processing of BC data

If the aethalometer measures in environments with low BC concentrations and/or at high time resolution negative values can occur. This is caused by using delta ATN to calculate the BC values. Since the aethalometer relies on this delta ATN when calculating eBC values, it does make sense to ensure that delta ATN is above a certain value before doing any calculations. Negative values often contain valid information that is required to post-process or smooth the data over a longer interval, so arbitrary removal of negative values may be detrimental to a dataset.

Data preprocessing must be performed to eliminate these negative values using the BC concentration data measured by the aethalometer. microAeth users can upload their data file to AethLabs and use the post-processing tools to smooth their data (http://www.aethlabs.com). Various different algorithms are available for data smoothing. This study uses a commonly applied time-adaptive noise reduction method centered moving average. The centered moving average is a smoothing technique that is used to make the long term trends of a time series clearer (Easton and McColl, 1997). There is no shift or group delay in the data using the centered moving average, unlike a simple moving average. The comparison between original BC measurements and corrections treated by centered moving average (the averaging period is 70s) is illustrated in Fig. S1 (ZR-Walk monitored on November 24 14:08–14:55 (Walk 14)). The denoising results show that the centered moving average can remove negative anomalies that occur in the original BC.

Table 2
Non-parametric Kruskal-Wallis test of PM_1, BC concentrations and PNCs measured along the routes in BE and ZR.

	BE-PM_1	BE-BC	BE-PNC	ZR-PM_1	ZR-BC	ZR-PNC
Chi-sq.	866.558	366.123	188.448	754.549	413.879	360.662
df	19	19	15	20	20	19
Sig.	0	0	0	0	0	0

3. Results and discussion

3.1. Summary of the mobile measurements

For mobile measurements, the observed average PM_1, $PM_{2.5}$, and PM_{10} concentrations in BE and ZR during the study period were 10 ± 11, 11 ± 11, 16 ± 27 $\mu g/m^3$ and 19 ± 34, 21 ± 39, 37 ± 108 $\mu g/m^3$, respectively, being similar to those sampled in the suburban of Bologna, Italy (Sarti et al., 2015), the urban area in Milan, Italy (Vecchi et al., 2004), the urban centre in Austria (Gomiščček et al., 2004), Chicago, USA (Babich et al., 2000), and the suburban routes in Northampton, UK, during the winter of 1999/2000 (Gulliver and Briggs, 2004). However, for PM_{10}, they are much higher than the urban background in Barcelona, Spain and Lugano, Switzerland (Reche et al., 2011) and for $PM_{2.5}$, they are higher than the urban road way in Newark, US (Yu et al., 2016).

The observed average BC concentrations were 1.30 ± 1.35 $\mu g/m^3$ and 1.70 ± 2.45 $\mu g/m^3$, which are similar to those reported and at urban background sites in Baden-Württemberg, Barcelona and Lugano (Gidhagen et al., 2005), and Paris (Healy et al., 2012), and the urban center of Augsburg as reported by Gu (2013). However, the observed average BC concentrations were higher than those of the urban industrial area in Huelva (0.7 ± 0.4 $\mu g/m^3$) and the urban center in Chicago reported by Reche et al. (2011) and Babich et al. (2000). Nevertheless, these values are much lower when compared to those noticed during the urban traffic investigated in Baden-Württemberg by Reche (Reche et al., 2011). The observed average PNC measured in BE and ZR during the study period were 4190 ± 1340 $\#/cm^3$ and 5024 ± 2346 $\#/cm^3$, being similar to those reported from the rural forest and the 100 m high urban tower in Stockholm (Gidhagen et al., 2005).

When comparing the air pollution in two villages, it can be found that the concentration of air pollution in ZR is generally higher than that in BE villages, and for PM, the concentrations in ZR are twice or more than that of BE.

3.2. Spatio-temporal variation of air pollution across two villages

3.2.1. Spatio-temporal variation

A significant difference between temporal dynamics of PM, PN and BC was observed ($p < 0.05$) by plotting the 25 m average PM, PN and BC concentrations for a selection of roads (Fig. 2).

The temporal variability showed significant differences between walks carried out within the same measurement day as well as between different measurement days comparing data for the same time of day, both in Bayerisch Eisenstein and Zelezna Ruda.

A statistical analysis of the temporal pattern of the factors revealed significant concentrations differences between the measurement walks (Table 2) for both in Bayerisch Eisenstein and Zelezna Ruda, but also between some of the mobile walks on the different days. In Bayerisch Eisenstein, for example, PM_1 concentrations were significantly higher at 18 o'clock (W16 (18:00–19:07)) and 20 o'clock (W17 (20:05–21:11)) on November 24 than in other hours. In Zelezna Ruda, PM_1 concentrations were higher on November 24, 2018, during the fifth (18:00–19:00) walk (W16 (17:58–18:48)) in contrast to the

Fig. 2. PM_1, BC and PN concentrations for the different walks (y-axis) at a selection of road (x-axis) in BE and ZR. The colors are scaled between the extremes and differ between the plots. White pixels represent no data due to instrument failures.

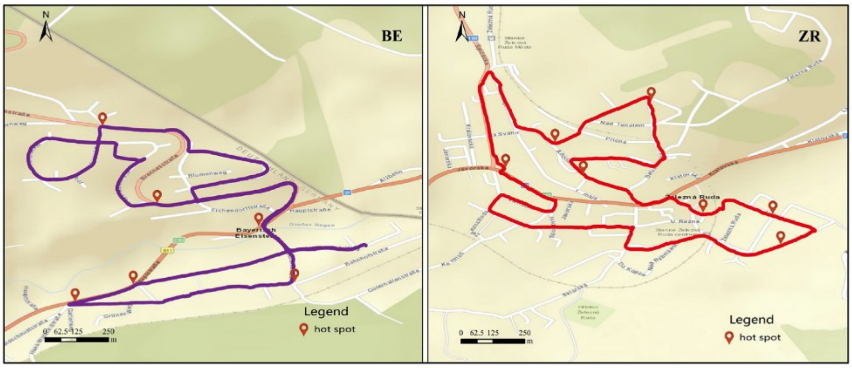

Fig. 3. Schematic diagram of a highly-concentrated contaminated hotspot with high suspicion on the sampling route.

remaining five walks; the same is true for the BC concentrations during the fourth (16:00–17:00) walk (W9 (15:59–17:03)).

The spatial variability of air pollution was lower, but overall significant for PNC in BE ($p < 0.01$) and for BC and PNC in ZR ($p < 0.05$). In BE, measured PM and PN concentrations were significantly higher on roads from 2250 m to 3250 m from the starting point. The differences in BC and PN concentrations between 25 m selected road in ZR were overall significant, especially from 1000 m to 2000 m from the starting

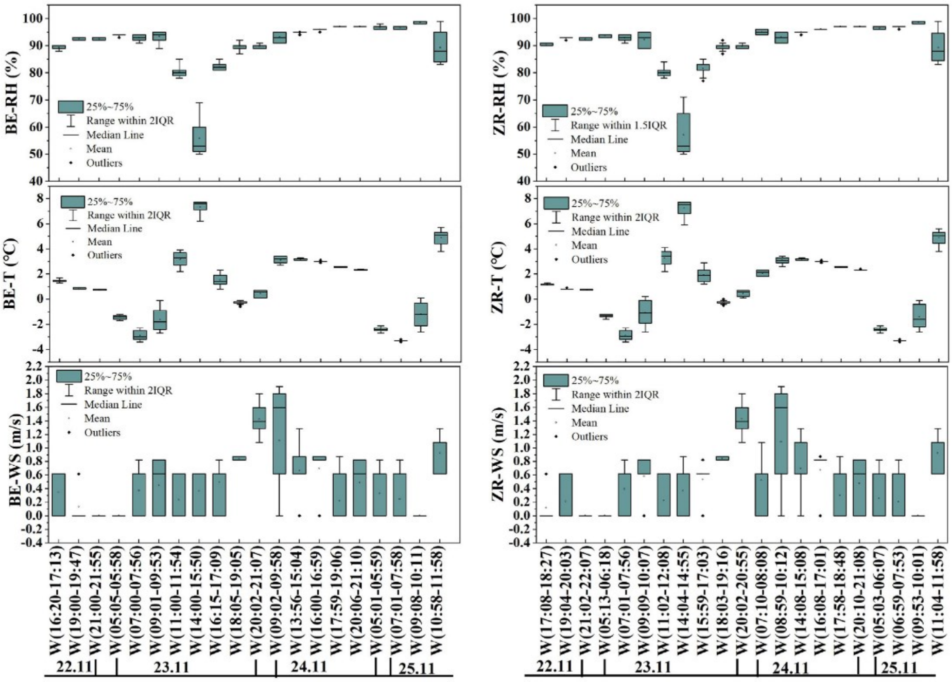

Fig. 4. Meteorology box plots from each mobile sample collection in two villages on November 22–24, 2018 (The meteorological data were monitored at the same place between the two villages and the data were divided according to their respective walking sampling times).

point. The main causes of this spatial difference identified using the photos taken during the sampling period are the smoke emitted from homes during heating and the emissions from the vehicles passing by.

When comparing differences in PM (PM_1, $PM_{2.5}$, PM_{10}) concentrations and PN concentrations measured in two villages, these were generally significant ($p < 0.05$), based on all the sampling data from the two villages over four days and using the ANOVA method. From Fig. 2, it is also clear that the spatial and temporal distribution of air pollution hotspots in ZR was higher than that in BE. In the time distribution, after 16 o'clock, the hotspot area of ZR is obviously more than that of BE. After analyzing the photos during the sampling period, it was found that in ZR, smoke from homes due to heating or cooking increased. Similarly, in terms of spatial distribution, most of the abnormally high value points in the two villages have become hotspots due to the increase in traffic flow. When comparing the concentration of the hotspot area with the background concentration of the city, it was found that the value of the hotspot area was 5–10 times that of the background area (Gomiščeк et al., 2004; Kutzner et al., 2018; Peters et al., 2013).

However, when comparing differences between black carbon concentrations measured in two villages, they are generally less pronounced than for PM_1 concentration and differences in PNC and were often non-significant.

3.2.2. Hotspots parsing of PM_1 and BC in BE and ZR

Starting from the mobile monitoring, the collected data is subjected to peak extraction, position marking, and hotspot area summary. According to the aggregated results, the detected hotspots are combined with on-site photos to verify and analyze the reasons, forming a logical closed loop of the entire mobile monitoring.

Therefore, to capture the fine spatio-temporal patterns required to pinpoint hotspots and periods of the day that are detrimental to human health, multi-angle data display is also important. Based on mobile monitoring data, and combined the Fig. 2, the moving data continuously monitored in different time periods is superimposed and drawn, which can visually display the measured data of the mobile monitoring over a certain period of time. As shown in Fig. S2, the data collected by all the mobile monitoring devices in a period of time is summarized and counted, and the average value is calculated on the walking path segment length and then projected onto the corresponding road segment on the map. By using discrete points of different colors to indicate the concentration of pollutants, the average level of air pollution in the road sections involved can be assessed visually. At same time, PM_1 and black carbon concentration can significantly extract peaks from the environmental background. In addition to feedback of the measured pollution concentration, the data of the mobile monitoring also records the corresponding spatial latitude and longitude coordinates. The location of the extracted peaks is marked on the map (Fig. 3), and this study has also shown that the peak aggregation of multiple mobile patrol periods occurs in relatively concentrated regions. It can roughly depict a high concentration of contaminated hotspots with high suspicion in the target area. According to the summary of the hotspot areas, there are no pollution sources such as factories around the two villages. Combine field-specific photos identified during sampling for field verification. Its pollution mainly comes from local pollution. Therefore, the pollution in this area, was divided into the two following categories.

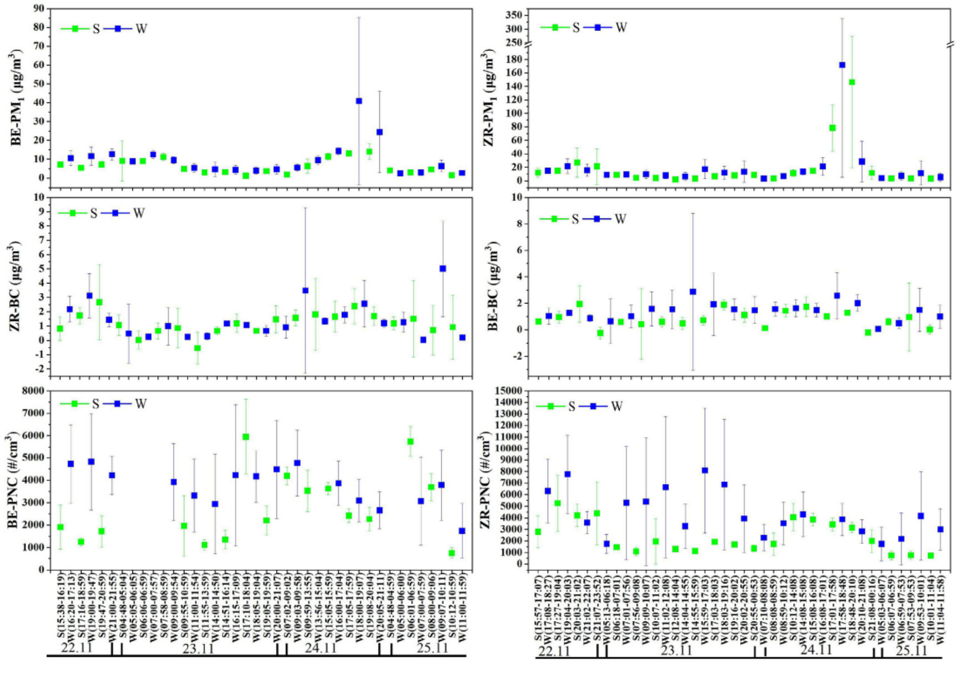

Fig. 5. Temporal fluctuations of PM_1, black carbon concentrations and PNCs from mobile and stationary measurements in BE and ZR (S, stationary measurement; W, mobile measurement).

(1) Traffic peaks: Peaks of traffic in some sections of the walking path during peak hours due to the surge in traffic volume.
(2) Biomass burning: Some villagers use wood mainly in the evening for heating.

3.3. Characteristics of meteorology

Studies have shown that elevated temperatures, reduced frequency of precipitation, and low wind speed may adversely affect regional atmospheric conditions (Dawson et al., 2007; Correia et al., 2013). Fig. 4 shows the pattern of the average relative humidity (RH), temperature (T) and wind speed (WS) in the 20 and 21 walks of BE and ZR, respectively. It can be seen, that the RH values are between 75% and 100% except on the 23rd November from 2 pm to 3 pm, where T is between −4 and 8 °C and wind speed is <2 m/s. Tai et al. (2010) used the method of correlation analysis to study the meteorological parameters (such as temperature, relative humidity and wind direction) that affect the concentration of $PM_{2.5}$, and obtained a relationship between the concentration distribution of pollutants and meteorological factors. So the relationship between the pollutants and meteorological factors will be discussed later.

3.4. Characteristics of air pollution concentrations in BE and ZR

3.4.1. Characteristics of PM concentrations in BE and ZR

Fig. S3 represents the pattern of the average PM_1 concentrations in the 20 and 21 walks of BE and ZR (since PM_1, $PM_{2.5}$ and PM_{10} show the same pattern, only the pattern graph of PM_1 was drawn here), respectively. In principle, the PM concentration follows the same pattern in both villages. PM_1 concentrations in BE and ZR are lower all day from 5 to 7 h local time (LT), which may be due to this period of time, there is less road traffic and people have not started house heating. Therefore, the pollutant emissions are less, and the air quality is improved. At around 18:00–19:00 h LT in the evening, however, the PM_1 concentrations are increasing probably due to the heating. At the same time, the traffic flows during this period, which can aggravate local air pollution.

In order to examine the concentration of atmospheric particulate matter in two villages in a more comprehensive way, the frequency distribution of the particles in the two villages is shown in Fig. S4, which used a frequency step size of 1 μg/m³. PM_1 and $PM_{2.5}$ are approximately normally distributed in monitoring period. It can be seen in Fig. S4 that PM_1 accounts for the vast majority. The ratios of $PM_1/PM_{2.5}$ are generally >90%, which indicates that air pollution mainly comes from submicron particles in the villages. The PM_1 concentration in the two

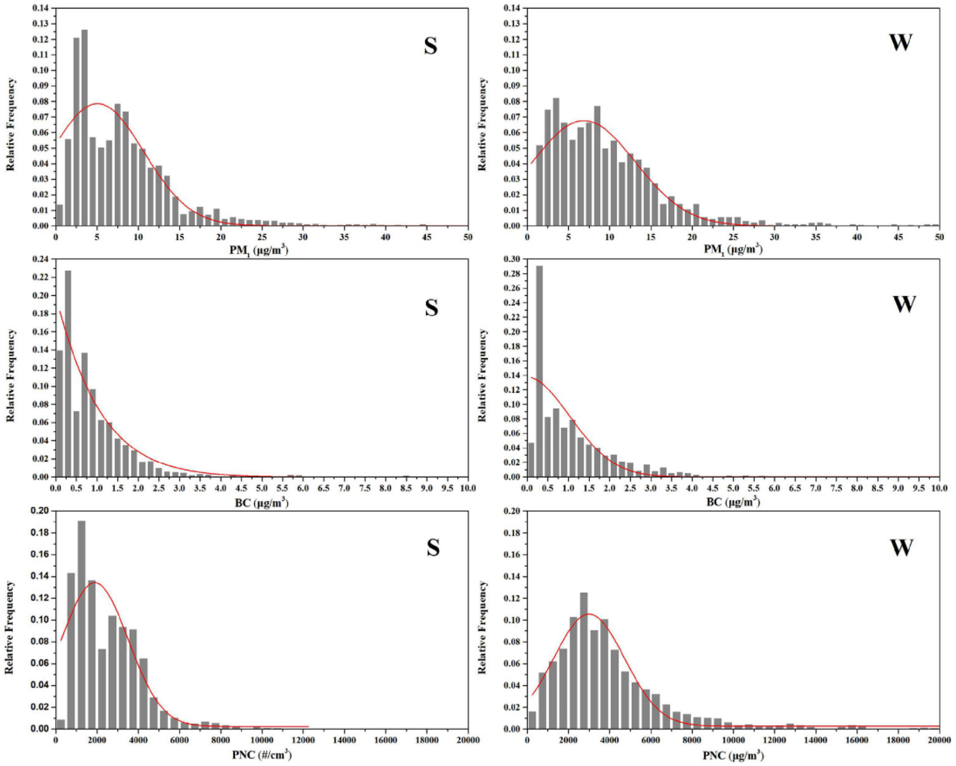

Fig. 6. Comparison of frequency distribution of PM1, BC and PNC for the stationary and mobile monitoring in Bayerisch Eisenstein (BE) and Zelezna Ruda (ZR) (x-axis, PM_1, BC concentrations and PNCs; y-axis, frequency of pollutants concentration, S, stationary measurement, W, mobile measurement).

villages of BE and ZR is concentrated between 0 and 30 μg/m^3 and the probability of exceeding 30 μg/m^3 is low for both villages. Comparing the PM$_1$ of the two villages, the median value of the PM$_1$ concentration in ZR is close to or even above 9 μg/m^3, which is twice that the value in BE (4 μg/m^3), indicating that the probability of high concentrations of fine particles is higher in the ZR atmosphere. This also determines the characteristic that the total particulate matter concentration in ZR is higher than in BE. This indicates that in the village of ZR more primary pollutants of particulate matter and secondary particulate matter are released.

3.4.2. Characteristics of black carbon concentration in BE and ZR

Fig. S5 is showing the pattern of the average black carbon concentration in the 20 and 21 walks of BE and ZR, respectively. It can be seen that the BC concentrations of BE and ZR are lower all day from 5 to 7 o'clock, and their variation is similar with PM$_1$. The frequency distribution of the BC concentration was made using a frequency step size of 0.1 μg/m^3 (Fig. S6). The median average concentration of BC was 1.05 μg/m^3 in BE and 1.16 μg/m^3 in ZR, showing that the atmospheric concentration of BC in ZR is slightly higher than that in BE. According to our survey, there is mostly wood combustion in the two villages.

3.4.3. Characteristics of particle number concentration in BE and ZR

Fig. S7 shows the pattern of the average particle number concentration in the 20 and 21 walks of BE and ZR, respectively (a few of sampled PNC data were missing due to an instrument failure). It can be seen that the peak PNC generally occurs in the afternoon, which may be due to the rise of the traffic. Similarly, the PNCs follow the same pattern with PM$_1$ in both villages. Furthermore, as can be seen from PNC in ZR, they are lower all day from 5 to 7 h local time (LT), showing the same characteristics with PM$_1$ and BC.

The frequency distribution of the fine mode particles in the mobile monitoring of the two villages is shown in Fig. S8. In general, the frequency distribution of the particulate number concentration in all mobile monitoring periods is approximately normally distributed. The particulate number concentration in the two villages is concentrated between 500 and 10,000 #/cm, and the probability of exceeding 10,000 #/cm^3 is low. Comparing the PNCs of the two villages, both distributions are very similar and in the known background range. The median values of the PNC in two villages are 1154 and 2631 #/cm^3, indicating that there are greater chances of high concentration of ultrafine particles in ZR atmosphere.

3.5. Mobile vs. stationary measurements

The average PM$_1$, BC concentrations, and PNCs of each walk were compared with the hourly averaged stationary measurements. The stationary measurements followed similar patterns as the average PM$_1$, BC, and PNC from mobile measurements in the two villages (Fig. 5). However, the stationary measured absolute values were generally below the measured concentrations at the previous walks, except for some walks in ZR. This was the case because the stationary sites were located in the background while the walks partly took place near the sources. Combined with on-site sampling photos, the concentrations became higher during stationary monitoring due to the passing of vehicles.

The frequency distribution of PM, BC, and PN between the mobile and the stationary monitoring of the two villages is shown in Fig. 6. The concentrations from the stationary measurements are concentrated between 0 and 20 μg/m^3 for PM$_1$, between 0 and 2.5 μg/m^3 for BC, and between 0 and 6000 #/cm^3 for PNC. The mobile measurements revealed concentrations between 0 and 25 μg/m^3 for PM$_1$, between 0 and 3.5 μg/m^3 for BC, and between 0 and 8000 #/cm^3 for PNC. Obviously, the concentrations range, mode and median of the air pollutants monitored by mobile monitoring are higher than the stationary monitoring. This is due to the fact that the mobile monitoring process will be closer to the source of pollution, which further demonstrates the superiority of mobile monitoring. However, for all mobile and stationary monitored data, the frequency distribution of the BC concentration mean values show a non-normal distribution, while PM$_1$ and PNC values are nearly normal-distributed.

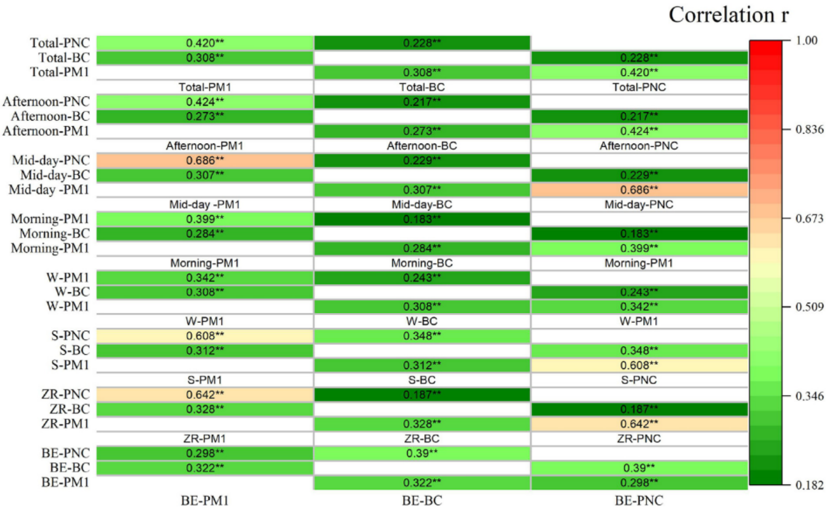

Fig. 7. Spearman correlation coefficient between the three air pollutants ($^{**}p < 0.01$).

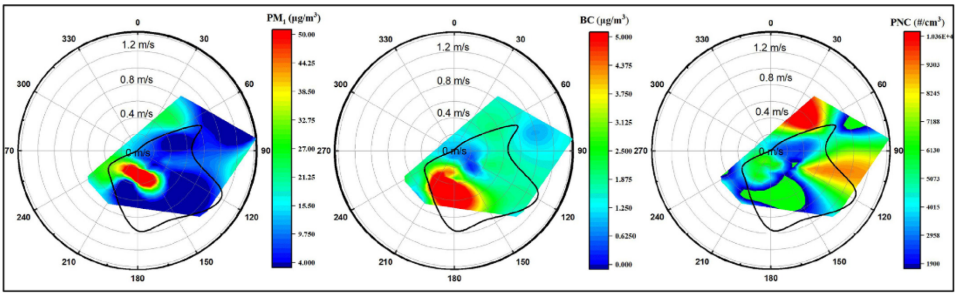

Fig. 8. Relationship of PM$_1$, BC and PNC with wind direction and speed.

3.6. Relationships between PM$_1$, BC and PNC

Fig. 7 presents the spearman correlation coefficient between PM$_1$, BC, and PNC. There were weak but highly significant ($p < 0.01$)correlations between them, which has been also found by Yu et al. (2016). They also found the inter-pollutant correlations varied by the sampling area and sampling time (Yu et al., 2016). Among the three possible pairs (i.e., PM$_1$-BC, BC-PNC, and PNC-PM$_1$), the pair of PM$_1$ and PNC was the strongest, except in BE area. The correlation coefficients of PM$_1$-BC and PM$_1$-PNC were stronger in the area of ZR than in BE. Additionally, the three pairs were stronger in the stationary measurement than that in the mobile measurement, which may be due to the stable environment conditions of the air monitoring equipment during fixed monitoring. Authors also reported diurnal correlations being higher during mid-day (10:00–14:00) than in the morning (5:00–10:00) or in the afternoon (14:00–22:00), which is due to the traffic flow, which was higher during mid-day. Patton et al. (2014) reported different correlation coefficients that were higher in neighborhoods near highways and lower in urban background neighborhoods. This strong correlation also suggests that PM$_1$, BC and PNC have similar sources. However, it is not possible to quantify the contribution rate of pollutants representing different source to black carbon aerosols.

3.7. Meteorological effects on PM$_1$, BC concentrations, and PNCs

The analysis revealed that the temperature correlated positively with the black carbon concentration ($r = 0.352$, $p < 0.05$) and the relative humidity was negatively correlated with PNC ($r = -0.428$, $p < 0.05$). Moreover, Zhu et al. (2002) found that wind speed and direction are the determining factors for the concentration of air pollutants. Fig. 8 shows the distributions of PM$_1$, BC, and PNC with wind speed and direction. The radius in Fig. 8 represents the wind speed (m/s), the color represents mass or number concentrations of contaminants, and the solid black lines show the frequencies of wind from different directions. The figure shows that the wind speed and wind direction are closely related to the pollutant concentration. High PM$_1$ concentrations rose from the southeast to southwest (150°–210°) and high BC concentrations and PNCs rose from the east (90°–120°). The BC concentrations from the southeast were generally above 5 μg/m^3. It was likely that the pollution in the region of ZR areas was relatively high. Kumar et al. (2011) found that increase in wind speed decreases BC and vice-versa. During the sampling period, the maximum wind speed is <1.6 m/s, which represents the Class 1 wind. Studies have shown that pollution accumulates under low and calm winds (Begam et al., 2016) indicating that the pollution in the study area was highly impacted by local emissions (Shen et al., 2015). Liu et al. (2018) found that the average ratio of PM$_{2.5}$ to PM$_{10}$ significantly increased with the increase of RH during their observation period, which indicated that high RH aggravated the pollution caused by fine particles. During our sampling period, the relative humidity was 91% on average, so high humidity and low wind speed were typical static weather conditions, which aggravated the pollution. In addition, it has been reported that the lifetimes of BC range from 40 h to over 1 week (Ogren and Charlson, 1983). Therefore, BC is also a type of pollutant with long-distance transport. However, the two villages are located in the shallow valley, which has the characteristics of basin topography, small wind speed, high static wind frequency, and the pollutants in the air are not easy to spread, especially in winter. So in this environment case, the extent of regional air pollution influence is mainly limited to the downwind region near the source (Sadiq et al., 2015).

4. Conclusions

In this study, a mobile monitoring approach was used to capture spatial/temporal characteristics at small-scale air pollution. Mobile real-time measurement of ambient particle matter (PM$_1$, PM$_{2.5}$, PM$_{10}$), black carbon and particle number concentrations have been carried out using mobile platforms in two neighboring villages.

This study illustrates the potential of mobile measurement methods to map short-term (e.g. winter), small-scale air pollution both for comparison purposes and estimation of absolute aerosol levels. As an example case study, we have completed locating and verifying the pathways of two villages, serving as small-scale PM$_1$, BC, and PNC hotspots, by several vehicular devices within about 20–21 walks. There are significant differences in PN and PM concentrations in rural air pollutants between the two villages. And the spatial and temporal distribution of air pollution hotspots in ZR was higher than that in BE. The relationships between the measurement parameters were weak but highly significant and the meteorological parameters can effect on the air pollution.

The novel aspect of this mobile monitoring approach was the simultaneous measurement along two pathways at same time to assess and compare spatial gradients at a small-scale air pollution while controlling temporal variations. We also displayed the mobile monitoring data from multiple views and verified the feasibility and values of mobile monitoring for small-scale air pollution.

In the future, this monitoring method can be used for research work. We plan to use this method to study the changes in the four seasons in the countryside to accurately estimate the extent of air pollution exposure and pollution changes on roadsides in rural areas.

CRediT authorship contribution statement

Xiansheng Liu: Resources, Investigation, Data curation, Writing - original draft.**Jürgen Schnelle-Kreis:**Methodology, Supervision.**Xun Zhang:** Data curation.**Jan Bendl:**Resources, Investigation.**Mohamed Khedr:**

Resources, Investigation.**Gert Jakobi:**Resources.**Brigitte Schloter-Hai:** Writing - review & editing.**Jan Hovorka:**Conceptualization.**Ralf Zimmermann:**Writing - review & editing.

Acknowledgements

Xiansheng Liu's PhD work is funded by the China Scholarship Council (CSC) under the State Scholarship Fund (File No. 201706860028), and partially by the Germany Federal Ministry of Transport and Digital Infrastructure (BMVI) as part of SmartAQnet (grant No. 19F2003B), and Support Project of High-level Teachers in Beijing Municipal Universities in the Period of 13th Five–year Plan (CIT&TCD201904037). We also thank Pengfei Tai, Xiuxiu Lin and Yanling Xu for providing assistance in data preprocessing and Aethlabs (especially Jeff Blair) for providing assistance with troubleshooting the MA200.

Declaration of competing interest

The authors declare that they have no known competing financial interests or personal relationships that could have appeared to influence the work reported in this paper.

Appendix A. Supplementary data

Supplementary data to this article can be found online at https://doi.org/10.1016/j.scitotenv.2020.137632.

References

Alas, H.D., Müller, T., Birmili, W., Kecorius, S., Cambaliza, M.O., Simpas, J.B.B., ... Wiedensohler, A., 2018. Spatial characterization of black carbon mass concentration in the atmosphere of a Southeast Asian megacity: an air quality case study for Metro Manila, Philippines. Aerosol Air Qual. Res 18, 2301–2317. https://doi.org/10.4209/aaqr.2017.08.0281.

Babich, P., Davey, M., Allen, G., Koutrakis, P., 2000. Method comparisons for particulate nitrate, elemental carbon, and PM2.5 mass in seven US cities. J. Air Waste Manage. Assoc. 50 (7), 1095–1105. https://doi.org/10.1080/10473289.2000.10464152.

Begam, G.R., Vachaspati, C.V., Ahammed, Y.N., Kumar, K.R., Babu, S.S., Reddy, R.R., 2016. Measurement and analysis of black carbon aerosols over a tropical semi-arid station in Kadapa, India. Atmos. Res. 171, 77–91. https://doi.org/10.1016/j.atmosres.2015.12.014.

Braniš, M., Domasová, M., 2003. PM10 and black smoke in a small settlement: case study from the Czech Republic. Atmos. Environ. 37 (1), 83–92. https://doi.org/10.1016/S1352-2310(02)00700-8.

Brantley, H.L., Hagler, G.S.W., Kimbrough, E.S., Williams, R.W., Mukerjee, S., Neas, L.M., 2014. Mobile air monitoring data-processing strategies and effects on spatial air pollution trends. Atmos. Meas. Tech. 7 (7), 2169–2183.

Correia, A.W., Pope III, C.A., Dockery, D.W., Wang, Y., Ezzati, M., Dominici, F., 2013. The effect of air pollution control on life expectancy in the United States: an analysis of 545 US counties for the period 2000 to 2007. Epidimiology 24 (1), 23. https://doi.org/10.1097/EDE.0b013e3182770237.

Dawson, J.P., Adams, P.J., Pandis, S.N., 2007. Sensitivity of PM 2.5 to climate in the Eastern US: a modeling case study. https://hal.archives-ouvertes.fr/hal-00302769.

Dons, E., Panis, L.I., Van Poppel, M., Theunis, J., Wets, G., 2012. Personal exposure to black carbon in transport microenvironments. Atmos. Environ. 55, 392–398. https://doi.org/10.1016/j.atmosenv.2012.03.020.

Easton, V.J., McColl, J.H., 1997. Statistics glossary, time series data. Statistics Glossary-Time Series Data 12, 12. http://www.stats.gla.ac.uk/steps/glossary/.

EUROSTAT, 2017. Statistics on Rural Areas in the EU. https://ec.europa.eu/eurostat/statistics-explained/index.php/Statistics_on_rural_areas_in_the_EU.

Gidhagen, L., Johansson, C., Langner, J., Foltescu, V.L., 2005. Urban scale modeling of particle number concentration in Stockholm. Atmos. Environ. 39 (9), 1711–1725. https://doi.org/10.1016/j.atmosenv.2004.11.042.

Gomiščček, B., Hauck, H., Stopper, S., Preining, O., 2004. Spatial and temporal variations of PM1, PM2.5, PM10 and particle number concentration during the AUPHEP—project. Atmos. Environ. 38 (24), 3917–3934. https://doi.org/10.1016/j.atmosenv.2004.03.056.

Gong, W., Zhang, T., Zhu, Z., Ma, Y., Ma, X., Wang, W., 2015. Characteristics of PM1.0, PM2.5, and PM10, and their relation to black carbon in Wuhan, Central China. Atmosphere 6 (9), 1377–1387. https://doi.org/10.3390/atmos6091377.

Gu, J., 2013. Characterizations and Sources of Ambient Particles in Augsburg, Germany. https://opus.bibliothek.uni-augsburg.de/.

Gulliver, J., Briggs, D.J., 2004. Personal exposure to particulate air pollution in transport microenvironments. Atmos. Environ. 38 (1), 1–8. https://doi.org/10.1016/j.atmosenv.2003.09.036.

Healy, R.M., Sciare, J., Poulain, L., Kamili, K., Merkel, M., Müller, T., ... McGillicuddy, E., 2012. Sources and mixing state of size-resolved elemental carbon particles in a European megacity: Paris. Atmospheric Chemistry and Physics 12, 1681–1700. https://doi.org/10.5194/acp-12-1681-2012.

Hovorka, J., Pokorná, P., Hopke, P.K., Křůmal, K., Mikuška, P., Píšová, M., 2015. Wood combustion, a dominant source of winter aerosol in residential district in proximity to a large automobile factory in Central Europe. Atmos. Environ. 113, 98–107. https://doi.org/10.1016/j.atmosenv.2015.04.068.

Kruskal, W.H., Wallis, W.A., 1952. Use of ranks in one-criterion variance analysis. J. Am. Stat. Assoc. 47 (260), 583–621. https://doi.org/10.2307/2280779.

Kumar, K.R., Narasimhulu, K., Balakrishnaiah, G., Reddy, B.S.K., Gopal, K.R., Reddy, R.R., ... Babu, S.S., 2011. Characterization of aerosol black carbon over a tropical semi-arid region of Anantapur, India. Atmospheric Research 100 (1), 12–27. https://doi.org/10.1016/j.atmosres.2010.12.009.

Kutzner, R.D., von Schneidemesser, E., Kuik, F., Quedenau, J., Weatherhead, E.C., Schmale, J., 2018. Long-term monitoring of black carbon across Germany. Atmos. Environ. 185, 41–52. https://doi.org/10.1016/j.atmosenv.2018.04.039.

Liu, F., Tan, Q.W., Jiang, X., Jiang, W.J., Song, D.L., 2018. Effect of relative humidity on particulate matter concentration and visibility during winter in Chengdu. Huan Jing Ke Xue 39 (4), 1466–1472. https://doi.org/10.13227/j.hjkx.201707112.

Liu, M., Peng, X., Meng, Z., Zhou, T., Long, L., She, Q., 2019. Spatial characteristics and determinants of in-traffic black carbon in Shanghai, China: combination of mobile monitoring and land use regression model. Sci. Total Environ. 658, 51–61. https://doi.org/10.1016/j.scitotenv.2018.12.135.

Ogren, J.A., Charlson, R.J., 1983. Elemental carbon in the atmosphere: cycle and lifetime. Tellus Ser. B Chem. Phys. Meteorol. 35 (4), 241–254. https://doi.org/10.1111/j.1600-0889.1983.tb00027.x.

Olson, M.R., Victoria Garcia, M., Robinson, M.A., Van Rooy, P., Dietenberger, M.A., Bergin, M., Schauer, J.J., 2015. Investigation of black and brown carbon multiple-wavelength-dependent light absorption from biomass and fossil fuel combustion source emissions. J. Geophys. Res.-Atmos. 120 (13), 6682–6697. https://doi.org/10.1002/2014JD022970.

Patton, A.P., Perkins, J., Zamore, W., Levy, J.I., Brugge, D., Durant, J.L., 2014. Spatial and temporal differences in traffic-related air pollution in three urban neighborhoods near an interstate highway. Atmos. Environ. 99, 309–321. https://doi.org/10.1016/j.atmosenv.2014.09.072.

Peng, C., Tian, M., Chen, Y., Wang, H., Zhang, L., Shi, G., ... Zhai, C., 2019. Characteristics, Formation Mechanisms and Potential Transport Pathways of PM2.5 at a Rural Background Site in Chongqing, Southwest China. Aerosol and Air Quality Research 19 (9). https://doi.org/10.4209/aaqr.2019.01.0010 (1980-1992+).

Peters, J., Theunis, J., Van Poppel, M., Berghmans, P., 2013. Monitoring PM10 and ultrafine particles in urban environments using mobile measurements. Aerosol Air Qual. Res. 13 (2), 509–522. https://doi.org/10.4209/aaqr.2012.06.0152.

Petzold, A., Ogren, J.A., Fiebig, M., Laj, P., Li, S., Baltensperger, U., ... Wehrli, C., 2013. Recommendations for reporting" black carbon" measurements. https://doi.org/10.5194/acp-13-8365-2013.

Reche, C., Querol, X., Alastuey, A., Viana, M., Pey, J., Moreno, T., ... Rosa, J.D.D.L., 2011. New considerations for PM, Black Carbon and particle number concentration for air quality monitoring across different European cities. https://doi.org/10.5194/acp-11-6207-2011.

Rehman, I.H., Ahmed, T., Praveen, P.S., Kar, A., Ramanathan, V., 2011. Black carbon emissions from biomass and fossil fuels in rural India. Atmos. Chem. Phys. Discuss. 11 (4). https://doi.org/10.5194/acpd-11-10845-2011.

Sadiq, M., Tao, W., Liu, J., Tao, S., 2015. Air quality and climate responses to anthropogenic black carbon emission changes from East Asia, North America and Europe. Atmos. Environ. 120, 262–276. https://doi.org/10.1016/j.atmosenv.2015.07.001.

Sarti, E., Pasti, L., Rossi, M., Ascanelli, M., Pagnoni, A., Trombini, M., Remelli, M., 2015. The composition of PM1 and PM2. 5 samples, metals and their water soluble fractions in the Bologna area (Italy). Atmos. Pollut. Res. 6 (4), 708–718. https://doi.org/10.5094/APR.2015.079.

Shen, L., Li, L., Lü, S., Zhang, X., Liu, J., An, J., Wang, F., 2015. Characteristics of black carbon aerosol in Jiaxing, China during autumn 2013. Particuology 20, 10–15. https://doi.org/10.1016/j.partic.2014.08.002.

Tai, A.P., Mickley, L.J., Jacob, D.J., 2010. Correlations between fine particulate matter (PM2.5) and meteorological variables in the United States: implications for the sensitivity of PM2.5 to climate change. Atmos. Environ. 44 (32), 3976–3984. https://doi.org/10.1016/j.atmosenv.2010.06.060.

Tang, Q.Y., Zhang, C.X., 2013. Data Processing System (DPS) software with experimental design, statistical analysis and data mining developed for use in entomological research. Insect Sci. 20 (2), 254–260. https://doi.org/10.1111/j.1744-7917.2012.01519.x.

Van Donkelaar, A., Martin, R.V., Brauer, M., Kahn, R., Levy, R., Verduzco, C., Villeneuve, P.J., 2010. Global estimates of ambient fine particulate matter concentrations from satellite-based aerosol optical depth: development and application. Environ. Health Perspect. 118 (6), 847–855. https://doi.org/10.1289/ehp.0901623.

Vecchi, R., Marcazzan, G., Valli, G., Ceriani, M., Antoniazzi, C., 2004. The role of atmospheric dispersion in the seasonal variation of PM1 and PM2.5 concentration and composition in the urban area of Milan (Italy). Atmos. Environ. 38 (27), 4437–4446. https://doi.org/10.1016/j.atmosenv.2004.05.029.

Wolf, K., Cyrys, J., Harciníková, T., Gu, J., Kusch, T., Hampel, R., ... Peters, A., 2017. Land use regression modeling of ultrafine particles, ozone, nitrogen oxides and markers of particulate matter pollution in Augsburg, Germany. Science of the Total Environment 579, 1531–1540. https://doi.org/10.1016/j.scitotenv.2016.11.160.

Yu, C.H., Fan, Z., Lioy, P.J., Baptista, A., Greenberg, M., Laumbach, R.J., 2016. A novel mobile monitoring approach to characterize spatial and temporal variation in traffic-related air pollutants in an urban community. Atmos. Environ. 141, 161–173. https://doi.org/10.1016/j.atmosenv.2016.06.044.

Zhu, Y., Hinds, W.C., Kim, S., Sioutas, C., 2002. Concentration and size distribution of ultrafine particles near a major highway. J. Air Waste Manage. Assoc. 52 (9), 1032–1042. https://doi.org/10.1080/10473289.2002.10470842.

6.3. APPENDIX C: Manuscript 3

Bendl, J.; Hovorka, J. Temperature and Relative Humidity Vertical Profiles within Planetary Boundary Layer in Winter Urban Airshed. *IOP Conf. Ser.: Earth Environ. Sci.* **2017,** *95*, 52003; DOI 10.1088/1755-1315/95/5/052003.

Temperature and Relative Humidity Vertical Profiles within Planetary Boundary Layer in Winter Urban Airshed

Jan Bendl [1], **Jan Hovorka** [1]

[1] Air Quality Laboratory, Institute for Environmental Studies, Faculty of Science, Charles University, Benatska 2, 128 01, Prague 2, Czech Republic

bendlhonza@gmail.com

Abstract. The planetary boundary layer is a dynamic system with turbulent flow where horizontal and vertical air mixing depends mainly on the weather conditions and geomorphology. Normally, air temperature from the Earth surface decreases with height but inversion situation may occur, mainly during winter. Pollutant dispersion is poor during inversions so air pollutant concentration can quickly rise, especially in urban closed valleys. Air pollution was evaluated by WHO as a human carcinogen (mostly by polycyclic aromatic hydrocarbons) and health effects are obvious. Knowledge about inversion layer height is important for estimation of the pollution impact and it can give us also information about the air pollution sources. Temperature and relative humidity vertical profiles complement ground measurements. Ground measurements were conducted to characterize comprehensively urban airshed in Svermov, residential district of the city of Kladno, about 30 km NW of Prague, from the 2nd Feb. to the 3rd of March 2016. The Svermov is an air pollution hot-spot for long time benzo[a]pyrene (B[a]P) limit exceedances, reaching the highest B[a]P annual concentration in Bohemia – west part of the Czech Republic. Since the Svermov sits in a shallow valley, frequent vertical temperature inversion in winter and low emission heights of pollution sources prevent pollutant dispersal off the valley. Such orography is common to numerous small settlements in the Czech Republic. Ground measurements at the sports field in the Svermov were complemented by temperature and humidity vertical profiles acquired by a Vaisala radiosonde positioned at tethered He-filled balloon. Total number of 53 series of vertical profiles up to the height of 300 m was conducted. Meteorology parameters were acquired with 4 Hz frequency. The measurements confirmed frequent early-morning and night formation of temperature inversion within boundary layer up to the height of 50 m. This rather shallow inversion had significant influence on air quality due to inversion cap over the valley. Nevertheless, formation of an inversion showed strong diurnal variability. For example, on the 18th Feb. early morning shallow inversion quickly disappeared within less than 2 hours. According to this study tethered balloon measurements has proved to be a good tool for completion comprehensive ground air quality measurements.

1. Introduction

In Central and Eastern Europe, local heating is often major source of winter urban air pollution, especially in small cities with family houses heated by solid fuel as the case study from the Czech Republic has shown [1]. Wood, black and low-quality brown coal is mainly burned in the Czechia. Despite law some people burn also waste, which is common alarming phenomenon mostly in poor districts. Other sources of air pollution are traffic, industry and in the microscale also cigarette smoke, cooking etc. Long-range transport and atmospheric processes also plays its role. In the process of combustion polycyclic aromatic hydrocarbons (PAHs) adsorbed on aerosol particles are produced. Some PAHs are highly carcinogenic, egg. benzo[a]pyrene (B[a]P), and with other toxic organic compounds pose the greatest risk to human health from the particulate matter (PM), which is aerosol particle size dependent [2]. Therefore, outdoor air pollution was classified by International Agency for Research on Cancer (IARC) as a carcinogenic to humans [3].

PM_x and PAHs health limits are exceeded in urban area especially in winter during inversion situations and unfavourable micro-scale geomorphology like closed valleys. The planetary boundary layer (PBL) is a dynamic system with turbulent flow where horizontal and vertical air mixing depends mainly on the weather and geomorphology. Normally, air temperature from the Earth surface decreases with height but inversion situation may occur, mainly during winter. During inversion and smog, the valleys are filled with fumes from all the low emission height sources and PM concentration are rising. Inversion layer height and time of its occurrence are the key factors, which affect air quality inside the valley. Pollutant dispersion is much higher above the inversion layer. By the inversion layer height observation, we can estimate the area for which ground air pollution monitoring inside the valley is relevant. Moreover, inversion layer over the valley minimizes long-range transport influence so we can neglect it in source apportionment studies.

Tethered balloon measurements can answer mainly these questions: What is the inversion layer height? How often these situations occur? What is the dynamics of inversion layer formation? For which area are ground air quality measurements relevant?

2. Material and methods

Comprehensive characterization of urban aerosol was conducted in residential district of the city of Kladno Svermov, about 30 km NW of Prague, from the 2nd February to the 3rd of March 2016. The Svermov is an air pollution hot-spot for long time benzo[a]pyrene limit exceedances, reaching the highest B[a]P annual concentration in Bohemia – west part of the Czech Republic. Svermov is the residential district of Kladno city and is situated in a shallow valley. The volume of the valley was estimated according to the contours of the map and approx. height of 50 m to 120 900 000 m^3.

Five minute integrates of aerosol number size distributions in the range of 14 nm – 10 000 nm (by TSI SMPS, APS), CO, NOx, SO_2, O_3, CH_4, NMHC (by HORIBA), meteorology parameters: ambient temperature (T), relative humidity (RH), atmospheric pressure, global radiation (GR), precipitation were measured at the isothermic station placed at the sports field in Svermov (GPS: 50°10'0.421" N, 14°6'41.965"E).

Simultaneously, measurements with tethered balloon were conducted in the immediate vicinity to the station. Total number of 53 series of vertical profiles for temperature (T), relative humidity (RH), pressure up to the height of 300 m within the atmospheric boundary layer was conducted by tethered, helium-filled balloon with a volume of 2.3 m^3. Balloon can carry two instruments and point-of-view camera. Meteorology parameters (temperature, relative humidity, atmospheric pressure) were acquired with 4 Hz frequency by Vaisala radiosonde. Heights were calculated from the atmospheric pressure data according to Wallace and Hobbs [4] by the equation:

$$h = \left(\frac{R}{g}\right)(T)\ln\left(\frac{p0}{p}\right) \tag{1}$$

where R is the general gas constant, g is the acceleration of gravity, p_0 is the atmospheric pressure on the ground and p atmospheric pressure at the height h, T is the average temperature in the layer p_0-p.

Balloon take-off is practically possible only when the wind speed <1.5 ms^{-1}. Higher wind speeds prevent reaching the maximum height of 300 m. Whereas strong wind indicates well-mixed boundary layer, it is not a disadvantage in the view of inversion layer observation. Unrolling of Dyneema rope was fast for capturing the whole vertical profile at the short time and only way up was plotted to graphs, similarly to practice with weather balloons.

Figure 1. Tethered helium filled balloon for T and RH vertical profiles, air quality station in the background, Kladno-Svermov, Czech Republic, 6. 2. 2016

Figure 2. The map of Kladno–Svermov district (red outline) with the tethered-balloon launching point (target), source: www.mapy.cz

3. Results and discussions

Total number of 53 vertical profiles by tethered balloon were made. Figure 3 left (7. 2. 2016) shows the normal situation where air temperature from the Earth surface decreases with height with small fluctuation near ground till 15 m. In average temperature decreased by 0.9 °C per 100 m height while relative humidity raised from 67 to 76 % (3.2 % per 100 m in average) during this profile. On February 7 was calm SW wind with median 0.6 ms^{-1}, temperature median was -0.4 °C, relative humidity median 92 %, global radiation 7 Wm^{-2} and PM_{10} daily median was 48 μgm^{-3}.

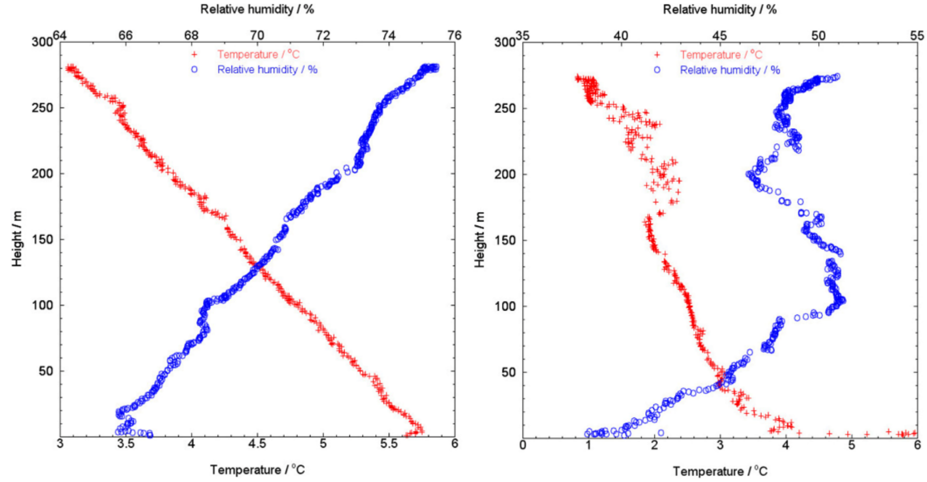

Figure 3. Temperature (T/°C) and relative humidity (RH/%) versus height (m), 7. 2. 2016 (left), 25. 2. 2016, 13:50-13:55 (right), Kladno-Svermov

During 25th January, there were similar meteorology conditions: WS median 0.5 ms^{-1}, the same SW direction, T median -4.2°C, RH median 80 %, GR median 8 Wm^{-2} but PBL up to 300 m was less stable which is evident from the figure 3 right. PM_{10} median was 25 μgm^{-3} which is almost twice a lower concentration. Ground concentration of measured gases were SO_2 1.7 ppb, O_3 34.6 ppb, NO_2 4.5 ppb, NO 0.02 ppb, CH_4 1.7 ppm.

Stronger N wind at the height of 200 – 270 m was indicated by the balloon wobbling, which was visible from the ground.

The different situation is on figure 4, which represents dynamic change during 18th January.

Left graph shows morning temperature inversion up to 30 m, the layer between 30 and 50 m is almost isothermal and second inversion follows up to 80 m. The third inversion from the ground is from 95 to 120 m height. Balloon was launched from 7:56 to 8:04 up to only 140 m due to stronger wind at this altitude. Two more vertical profiles were made before: at 7:32 and 7:46 and data looked almost the same as profile at 7:56 (figure 4 left).

Vertical profile 2 hours later (10:13-10:21) is on the right of figure 4, where the inversion is just disappearing. Ground temperature inversion lasts till 20 m height. This inversion disappeared completely 20 minutes later (10:34, not shown) and since then we didn't observe any inversion up to 300 m till 16:11, when we conducted the last flight.

During this day (January 18) medians of meteorological parameters at 4 m height were: WS 0.4 ms^{-1} (S wind prevailed), T -3.9 °C, RH 92 %, GR 7 Wm^{-2}.

Comparison between these two vertical profiles (figure 4) is shown in the table 1. PM_{10} concentration is decreasing as the temperature inversion is disappearing.

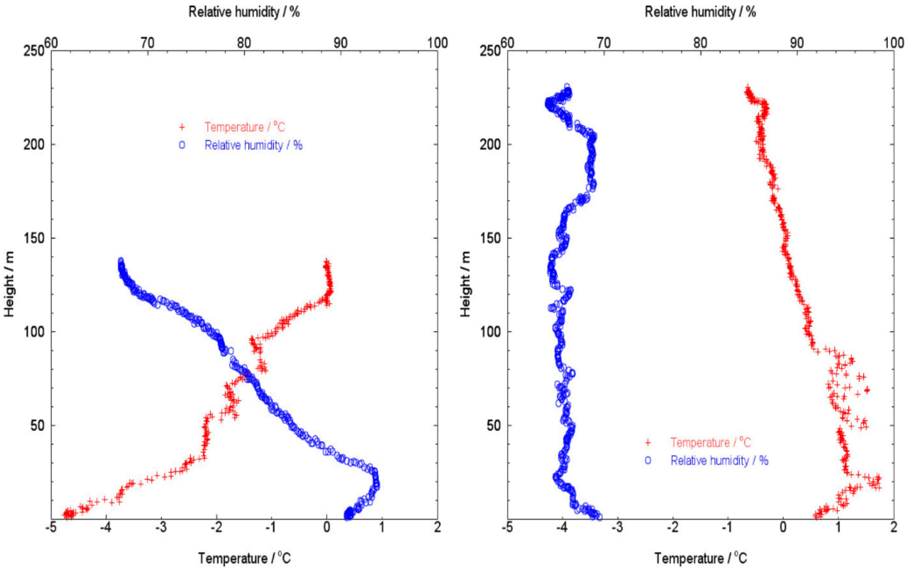

Figure 4. Temperature (T/°C) and relative humidity (RH/%) versus height (m), 18. 2. 2016, 7:56-8:04 (left), 10:13-10:21 (right), Kladno-Svermov

Table 1. Comparison of meteorological parameters measured by the ground station between two vertical profiles, Kladno-Svermov.

	18th January 2016, **7:56-8:04**	18th January 2016, **10:13-10:21**
Wind	0.3 ms^{-1}	**0.7 ms^{-1}**
Temperature	-6.2 °C	**1.4 °C**
Relative Humidity	**94 %**	77 %
Global Radiation	29 Wm^{-2}	**224 Wm^{-2}**
PM$_{10}$	**21 µgm^{-3}**	13 µgm^{-3}
Gaseous concentration	SO_2 1.22 ppb, O_3 4.34 ppb, **NO_2 17.8 ppb**, **NO 49.9 ppb**, CH_4 1.9 ppm	**SO_2 3.52 ppb**, **O_3 14.7 ppb**, NO_2 4.3 ppb, NO 3 ppb, CH_4 1.8 ppm

Evening inversion on 12th January from 22:25 to 22:30 is at figure 5. PM$_{10}$ concentration was 51 µgm^{-3} (over the health limit), T -5.4 °C, 0.9 ms^{-1} strong wind with SW direction, relative humidity 92 % and global radiation 7 Wm^{-2}. Gaseous concentration during the profile were: SO_2 0.3 ppb, O_3 6.8 ppb, NO_2 10.7 ppb, NO 1.14 ppb and CH_4 2.8 ppm.

Temperature inversion layer occurs till approx. 60 m height which means people living under the edge of the valley are under the inversion cap and PM$_{10}$ concentration measured by the station is relevant for them. Unfortunately, most of observed inversions were up to around 50 m height from the bottom of the valley.

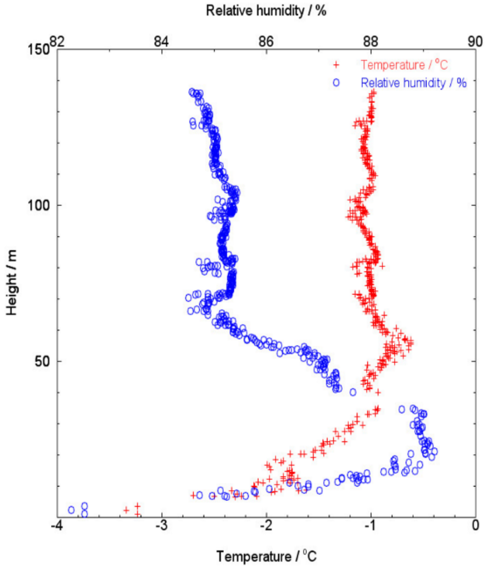

Figure 5. Temperature (T/°C) and relative humidity (RH/%) versus height (m), 12. 2. 2016, 22:25-22:30, Kladno-Svermov

4. Conclusions

Tethered balloon T&RH measurements up to 300 m confirmed frequent formation of temperature inversions within planetary boundary layer in the locality of Svermov residential district. Inversions usually reached a height of 50 m from the bottom of the closed valley and we observed them mainly during mornings and nights. Daytime vertical profiles shown fast dynamic changes. Because the valley is just around 50 m deep, the lid over pot effect can occur, which means worse air pollutant dispersion. This can lead to smog and PM health limit exceedance. Within the microscale, temperature inversion can strongly influence local air quality. According to this study tethered balloon measurements has proved to be a good low-cost tool for completion comprehensive ground air quality measurements. Limitations are spacy balloon launch area and max 1.5 ms^{-1} wind speed for balloon launch, however we can estimate well-mixed air in these situations.

Acknowledgment(s)

This work was supported by the project CENATOX under grant GAČR P503/12/G147.

References

[1] J. Hovorka, P. Pokorna, P. K. Hopke, K. Krumal, P. Mikuska. and M. Pisova, "Wood combustion, a dominant source of winter aerosol in residential district in proximity to a large automobile factory in Central Europe," *Atmospheric Environment*, vol. 113: pp. 98-107, 2015.
[2] J. Topinka, P. Rossner, A. Milcova, J. Schmuczerova, K. Pencikova, A. Rossnerova, A. Ambroz, J. Stolcpartova, J. Bendl, J. Hovorka, M. Machala, "Day-to-day variability of toxic events induced by organic compounds bound to size segregated atmospheric aerosol," *Environmental Pollution*, vol. 202, pp. 135-145, 2015.
[3] IARC: Outdoor air pollution a leading environmental cause of cancer deaths, Press release
[4] J. M. Wallace, P. V. Hobbs, "Atmospheric Science, an Introductory Survey." *Academic*, 1977.

6.4. APPENDIX D: Manuscript 4

Pokorná, P.; Leoni, C.; Schwarz, J.; Ondráček, J.; Ondráčková, L.; Vodička, P.; Zíková, N.; Moravec, P.; **Bendl, J.**; Klán, M.; Hovorka, J.; Zhao, Y.; Cliff, S. S.; Ždímal, V.; Hopke, P. K. Spatial-temporal variability of aerosol sources based on chemical composition and particle number size distributions in an urban settlement influenced by metallurgical industry. *Environmental Science and Pollution Research International* **2020,** *27* (31), 38631–38643; DOI 10.1007/s11356-020-09694-0.

Environmental Science and Pollution Research (2020) 27:38631–38643
https://doi.org/10.1007/s11356-020-09694-0

RESEARCH ARTICLE

Spatial-temporal variability of aerosol sources based on chemical composition and particle number size distributions in an urban settlement influenced by metallurgical industry

Petra Pokorná[1] · Cecilia Leoni[2] · Jaroslav Schwarz[1] · Jakub Ondráček[1] · Lucie Ondráčková[1] · Petr Vodička[1] · Naděžda Zíková[1] · Pavel Moravec[1] · Jan Bendl[3] · Miroslav Klán[3] · Jan Hovorka[3] · Yongjing Zhao[4] · Steven S. Cliff[4] · Vladimír Ždímal[1] · Philip K. Hopke[5,6]

Received: 19 January 2020 / Accepted: 11 June 2020 / Published online: 5 July 2020

Abstract

The Moravian-Silesian region of the Czech Republic with its capital city Ostrava is a European air pollution hot spot for airborne particulate matter (PM). Therefore, the spatiotemporal variability assessment of source contributions to aerosol particles is essential for the successful abatement strategies implementation. Positive Matrix Factorization (PMF) was applied to highly-time resolved $PM_{0.15-1.15}$ chemical composition (1 h resolution) and particle number size distribution (PNSD, 14 nm – 10 µm) data measured at the suburban (Ostrava-Plesná) and urban (Ostrava-Radvanice) residential receptor sites in parallel during an intensive winter campaign. Diel patterns, meteorological variables, inorganic and organic markers, and associations between the chemical composition factors and PNSD factors were used to identify the pollution sources and their origins (local, urban agglomeration and regional). The source apportionment analysis resolved six and four $PM_{0.15-1.15}$ sources in Plesná and Radvanice, respectively. In Plesná, local residential combustion sources (coal and biomass combustion) followed by regional combustion sources (residential heating, metallurgical industry) were the main contributors to $PM_{0.15-1.15}$. In Radvanice, local residential combustion and the metallurgical industry were the most important $PM_{0.15-1.15}$ sources. Aitken and accumulation mode particles emitted by local residential combustion sources along with common urban sources (residential heating, industry and traffic) were the main contributors to the particle number concentration (PNC) in Plesná. Additionally, accumulation mode particles from local residential combustion sources and regional pollution dominated the particle volume concentration (PVC). In Radvanice, local industrial sources were the major contributors to PNC and local coal combustion was the main contributor to PVC. The source apportionment results from the complementary datasets elucidated the relevance of highly time-resolved

---

Main finding
The source apportionment results using complementary datasets elucidated the relevance of highly time-resolved parallel measurements given the variable local meteorology with the possibility of replication at any receptor.

Responsible editor: Gerhard Lammel

Electronic supplementary material The online version of this article (https://doi.org/10.1007/s11356-020-09694-0) contains supplementary material, which is available to authorized users.

✉ Petra Pokorná
pokornap@icpf.cas.cz

[1] Department of Aerosol Chemistry and Physics, Institute of Chemical Process Fundamentals of the CAS, v. v. i., Rozvojová 1/135, 165 02 Prague 6, Czech Republic

[2] Rhea Group, Avenue Einstein 8, 1300 Wavre, Belgium

[3] Institute for Environmental Studies, Faculty of Science, Charles University, Benátská 2, 128 01 Prague 2, Czech Republic

[4] Air Quality Research Center, University of California, Davis, One Shields Ave, Davis, CA 95616-5270, USA

[5] Department of Public Health Sciences, University of Rochester Medical Center, 265 Crittenden Boulevard, Rochester, NY 14642-0708, USA

[6] Center for Air Resources Engineering and Science, Clarkson University, Potsdam, NY 13699-5708, USA

parallel measurements at both receptor sites given the specific meteorological conditions produced by the regional orography. These results are in agreement with our previous studies conducted at this site.

Keywords Highly time-resolved parallel measurements · Elemental composition · Regional transport · Local heating · Metallurgical industry · Nanoparticles

Introduction

Suspended particulate matter (PM) is complex with respect to its mass concentration, particle size distributions, chemical composition and its sources. Anthropogenic activities including industrial effluent, combustion emissions and physical processes such as wind-blown dust and traffic emissions are typically factors dominating the spatial and temporal PM variations (DeGaetano and Doherty 2004). With respect to small-scale spatial variations in urban areas, the largest variations occur in the ultrafine (< 0.1 μm) and the coarse mode ($PM_{2.5-10}$, re-suspended dust) (Lagudu et al. 2011; Kumar et al. 2012; Wang et al. 2012). Secondary aerosols that contribute to the accumulation mode (0.1–1 μm) show more homogenous spatial distributions (Moon 2001). Despite the limited spatial variations of fine PM within the city, understanding and controlling air pollution in highly polluted areas require multiple-site measurements. During pollution events, it is important to assess the origin of the higher PM concentrations to be able to employ measures to improve air quality (Petit et al. 2017; Waked et al. 2018). Despite the local origin of some PM, the observed PM is also influenced by medium and long-range transport processes. Therefore, for mitigation strategies to be effective, they must be scaled at regional, national and even continental levels (Guerreiro et al. 2014; Guan et al. 2017).

The Moravian-Silesian region, located in the eastern part of the Czech Republic, represents an EU air pollution hot spot. Epidemiological studies from Ostrava, the major city of the region, displayed negative health impacts for the local population, particularly for children, caused by deteriorated air quality (Dostál et al. 2013; Šram et al. 2013; Topinka et al. 2015). The area has been historically burdened with extensive industrial activity in the Upper Silesian basin. The key factors influencing the air quality in the Moravian-Silesian region are (i) exploitation and use of the high quality black coal, (ii) extensive heavy industry, (iii) high density of built-up areas with local heating by solid fuels, (iv) dense transport infrastructure on both sides of the Czech-Polish border, and (v) orography influencing the meteorological conditions with prevailing wind direction from south-west and north-east as well as long-lasting periods of stable conditions (from autumn to spring) with subsequent worsened dispersion conditions. Currently, approximately 760 facilities, large and medium stationary sources of air pollution, are registered in the region (CHMI 2018). Only several dozens of facilities—power plants and enterprise energy generation—and metallurgical production facilities have a substantial effect on overall emissions (TSP, SO_2 and NO_x); nevertheless, fugitive TSP emissions produced e.g. from landfills, handling of bulk materials and halls with dusty operations are not taken into consideration in the emission inventories. Therefore, the planning and implementation of effective abatement strategies to improve air quality in Ostrava are challenging due to the presence of miscellaneous sources, some of them situated near residential areas.

In order to analyse the spatial and temporal changes in airborne PM regarding to the effective abatement strategy implementation, the application of receptor model is highly effective. Receptor models analyse data matrices of aerosol chemical and physical characteristics of samples collected at a given locality, the receptor, to apportion their sources (Polissar et al. 2001). In the literature, a wide range of statistical models and modelling approaches is available e.g. CMB, PCA, PMF, UNMIX, ME and COPREM, and one of the main differences between the models is the degree of knowledge required about the pollution sources prior to the application of receptor models (Viana et al. 2008). PMF is a powerful tool for source resolution using highly time resolved aerosol composition data and has been used successfully in identifying the sources of airborne particles in many studies (e.g.; Ancelet et al. 2012, 2014; Pancras et al. 2013; Moreno et al. 2013; Hovorka et al. 2015; Hopke 2016). Particulate matter toxicity depends on its chemical and physical characteristics: composition, size, morphology or solubility (Heal et al. 2012). Thus, source apportionment studies focus not only on chemical composition but also on particle number size distribution data (Kim et al. 2004; Zhou et al. 2004, 2005a; Ogulei et al. 2007a, b; Kasumba et al. 2009; Pey et al. 2009; Harrison et al. 2011; Cusack et al. 2013; Beddows et al. 2015; Sowlat et al. 2016; Masiol et al. 2016; Squizzato et al. 2019). By investigating particles in various size ranges, it is possible to more clearly identify and apportion contributions from those sources that contributed more to the particle number than to the particle mass (Vu et al. 2015). The two approaches are often complementary (Zhou et al. 2005b; Beddows et al. 2015).

The aim of this study was to access the spatial and temporal variability of winter air pollution sources including nanoparticles in the districts of Ostrava-Radvanice and Ostrava-Plesná, examples of industry affected urban and suburban residential receptor sites. The source apportionment was performed using highly time-resolved elemental composition of

$PM_{0.15-1.15}$ and particle number size distributions (PNSD, 14–10 μm) measured from February 9 to March 3, 2014. The factors resolved from mass chemical compositions and the PNSDs by PMF were compared and associations were determined. The study complements previous source apportionment studies performed at the sites (Pokorná et al. 2015 and 2016; Leoni et al. 2018; Kozáková et al. 2019). The results from the parallel highly time-resolved chemical and PNSD measurements at these two different site types provided further insights into the spatial and temporal variability of the source contributions to PM at this site.

Methods

Experimental

A twin intensive sampling campaign was performed from February 6 to March 6, 2014 in Ostrava-Radvanice and Ostrava-Plesná as urban and suburban residential receptor sites, respectively (Fig. SI1). The distance between the two sites was approximately 16 km.

Five-minute integrated PNSD was measured with a Scanning Mobility Particle Sizer (14–730 nm, SMPS-3936 L25, TSI Inc. and 14.6–710.5 SMPS-3936 L75, TSI Inc.) and an Aerodynamic Particle Sizer (0.542–20 μm, APS-3321, TSI Inc.).

A standard reference sampler (LVS-3, Sven Leckel Ingenieurbüro GmbH, Berlin, Germany; flow rate of 2.3 m^3 h^{-1}) with quartz fibre filters (47 mm; Whatman QMA, GE Healthcare, Maidstone, UK) was used to measure 24-h PM_1 concentrations in Plesná. A high-volume sampler (DHA-80, Digitel, Switzerland, flow rate 30 m^3 h^{-1}) with quartz fibre filters (150 mm diameter; Whatman QMA, GE Healthcare, Maidstone, UK) was used to determine the 24-h concentrations of PM_1 in Radvanice. The samples were analysed for both cations and anions using a Dionex ICS-5000 system (Dionex, Sunnyvale, CA, USA) and for elemental carbon (EC) and organic carbon (OC) using a semi-continuous analyser (Sunset Laboratory Inc., Tigard, OR, USA) operated in an offline mode and using Eusaar2 protocol. PM_1 samples from Plesná were also analysed for monosaccharide anhydrides (levoglucosan, mannosan and galactosan) using a Dionex ICS-5000+ system (Dionex, Sunnyvale, CA, USA). Detailed descriptions of the methods and limits of detection (LODs) along with quality assurance and control for the used methods were reported by Kozáková et al. (2019).

Size segregated and time resolved PM were collected with a Davis Rotating-drum Uniform-size-cut Monitor – 3DRUM (DELTA Group UC-Davis), from February 19 to March 3 and were used to provide 1-h PM elemental compositions. The particles were collected on Mylar substrates lightly greased with Apiezon™. The 3DRUM collects particles in 3 size ranges from 150 to 10 μm. The two size range samples from 0.15 to 1.15 μm were analysed for 24 elements using synchrotron X-ray fluorescence (S-XRF) by the Air Quality Research Center, University of California (Leoni et al. 2018). For the source model, data from the two size ranges of 3DRUM were merged to obtain $PM_{0.15-1.15}$ to replicate the size range of the PNSD.

In Radvanice, 5-min meteorological data—wind speed (WS) and wind direction (WD), temperature (T), relative humidity (RH) and precipitation (P)—were recorded directly at the site during the whole sampling campaign. In Plesná, the meteorological data were available from the nearest representative automatic monitoring stations managed by the Czech Hydrometeorological Institute (Kozáková et al. 2019).

Data analysis

Descriptive statistics

Measured data (online measurement and chemical analysis of filter samples) and modelling results were statistically analysed using descriptive statistics, Pearson correlation and regression analysis to discover underlying patterns and trends regarding the monitoring campaign.

PMF Modelling

PMF (USEPA version 5.0) was applied to $PM_{0.15-1.15}$ chemical composition and PNSD data (15–10 μm). A 1-h integration time $PM_{0.15-1.15}$ chemical composition as a sum of two size fractions was used for PMF input along with missing mass (MM) for missing data for OC/EC (Pokorná et al. 2013). Hourly aerosol mass concentrations assigned as total variable were calculated from 5-min integrates of the number size distributions with a particle density of 1.5 g cm^{-3} (Shen et al. 2002) recorded by an APS and a SMPS. Due to the importance of the local meteorology given by the orography of the region (Pokorná et al. 2015; Černikovský et al. 2016; Leoni et al. 2018; Kozáková et al. 2019), the matrices of the chemical composition from the two sites were modelled separately by PMF.

For the PNSD PMF, the time resolutions from 5 min to 1 h were examined and it was determined that a 15-min resolution was optimal as the best compromise to maintain a high time resolution but avoid unwanted noise. Additionally, the input data were handled by merging three consecutive bins. Since the size segregation of SMPS is based on particle electrical mobility while the APS and 3DRUM impactor use particle aerodynamic properties, the mobility diameter was converted into aerodynamic. The uncertainties were calculated according to Vu et al. (2015). The total variable was calculated summing all the bins. The detailed information was reported in Leoni et al. (2018). PMF was also applied to PNSD from

Plesná (modelled with and without chemical composition data) to extract those factors governing particle number down to the nanometric scale.

The model was run several times using (i) different number of factors, (ii) different extra modelling uncertainties and (iii) for PNSD data different uncertainty input matrices, different C3 value (Vu et al. 2015) in order to obtain the highest S/N ratio and the Q_{true} closest to $Q_{theoretical}$, to determine the most physically meaningful result and the best diagnostics.

The polar plots and daily patterns were obtained using the Openair R Package (Carslaw and Ropinks 2012).

Schematic picture synthetizing all methods (measurement techniques, chemical analysis and data analysis) utilized in this study could be found in the Supplementary Information (Fig. SI2).

Results and discussion

Campaign overview

During the sampling campaign, the average PM_{10} concentrations calculated from the merged SMPS and APS number size distributions in Plesná and Radvanice were 29.2 ± 4.5 μg m^{-3} and 61.5 ± 8.7 μg m^{-3}, respectively. The $PM_{0.15-1.15}$ comprised 90% and 48% of PM_{10} in Plesná and Radvanice, respectively. These PM ratios indicate important differences in the PM size distribution and likely major sources at these locations. The elemental concentrations of almost all elements were lower in Plesná relative to Radvanice (Tables SI1 – 2). On average, the higher arsenic concentrations in Plesná point to the importance of coal combustion there (Tab. SI1). The average particle number concentrations were distributed in four particle modes: nanoparticles (15–30 nm), Aitken mode particles (30–80 nm), accumulation mode particles (80–1 μm) and coarse particles (1–10 μm) are presented in Table 1. The campaign was characterized by prevailing southwesterly and northeasterly winds at both sites due to the topography of the Ostrava region. Wind speed averaged 1.7 ± 0.6 m s^{-1} in Plesná and 1.2 ± 0.5 m s^{-1} in Radvanice.

Factors resolved with chemical composition

To estimate the optimal number of sources, the PMF model was run several times (units of tens for different model settings) and 3 to 8 factors were tested for each data set. The Q values, the resulting source profiles and the scaled residuals were examined. For each data set, the optimum number of factors was chosen based on an adequate fit of the model to the data as shown by the scaled residual histograms and physically interpretable results. The most stable solutions were found for 6-factor and 4-factor solutions for Plesná and Radvanice, respectively. Extra modelling uncertainties of 13.5% for Plesná and 17.9% for Radvanice were included to encompass errors not considered in the uncertainty assessment. All runs converged, the scale residuals were normally distributed, and no unmapped factors were detected with the bootstrap error estimation. No swaps were observed with the displacement error analysis, indicating that there was limited rotational ambiguity (Table SI3).

Table 1 Average particle number concentrations (# cm^{-3}) of the sampling campaign at Plesná and Radvanice site

Site [# cm^{-3}]	Nanoparticles	Aitken	Accumulation	Coarse
Plesná	0.9×10^3	2.2×10^3	3.1×10^3	2
Radvanice	3.5×10^3	6.4×10^3	6×10^3	3.7

The six factors in Plesná were assigned as *coal combustion, mixed factor secondary inorganic aerosol (SIA) and biomass burning, residential heating, biomass burning, re-suspended dust and raw iron production*. The 4 factors in Radvanice were ascribed to *mixed factor SIA and coal combustion, residential heating, raw iron production and sinter/steel production*. The factor elemental profiles and the time-series plots of the estimated contributions from each factor to the $PM_{0.15-1.15}$ mass are shown in Figs. 1 and 3.

Plesná

Factor 1. The first factor, local residential coal combustion, was associated with high concentrations of As, MM, Pb, Cu and Br (Rogula-Kozłowska et al. 2012, 2013a, b; Rogula-Kozłowska and Klejnowski 2013). This factor dominated during the monitoring period with an average contribution of 49% to $PM_{0.15-1.15.}$ The high factor contributions with WS up to 2 m s^{-1} point to local sources primarily situated from the sampling site to the NW/SE (Fig. 2) directions corresponding to the residential area. The time series show a local heating pattern, with a peak in the morning around 8 a.m. and in the evening starting from 5 p.m., with a maximum at 10 p.m. and lasting all night (Fig. SI3). This pattern can be also linked to the stable atmospheric conditions during winter nights, trapping the emissions near the ground. The regression analysis shows moderate relationship between the coal combustion factor and PM_1 OC ($R^2 = 0.40$). Surprisingly, this factor does not correspond to the coal combustion factor presented in Kozáková et al. (2019). This difference is likely due to the differences in the monitored periods (from February 6 to March 6, 2014), lack of chemical species (PM_1 water-soluble ions and OC/EC) and merged data matrix for Ostrava-Radvanice and Ostrava-Plesná sites.

Factor 2. This mixed factor represented mainly by S and K was ascribed to SIA and biomass burning (Leoni et al. 2018). This factor contributed 18% to the mean $PM_{0.15-1.15}$ mass on average. The polar plot points to the source/s of regional

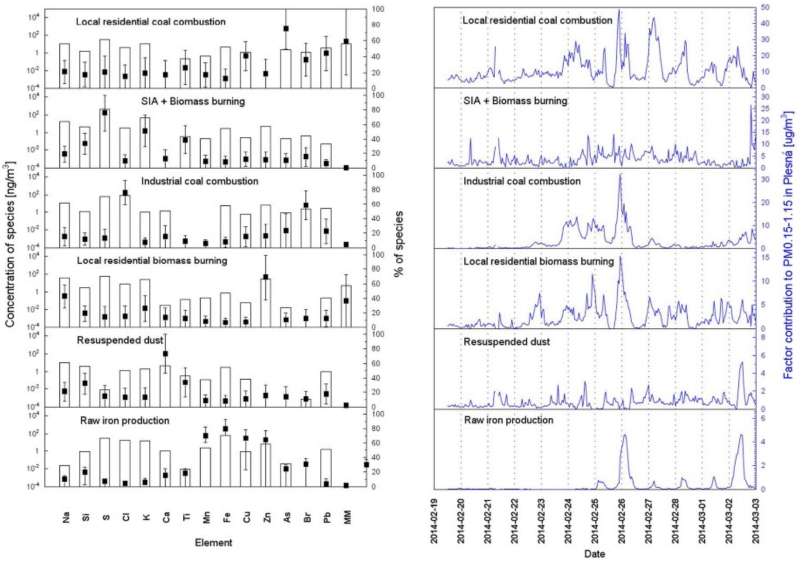

Fig. 1 Plesná factor profiles (concentration of the species, bars; percentage of the species, markers; DISP Average, box; DISP Max and DISP Min, whiskers) and time series resolved for $PM_{0.15-1.15}$ by PMF

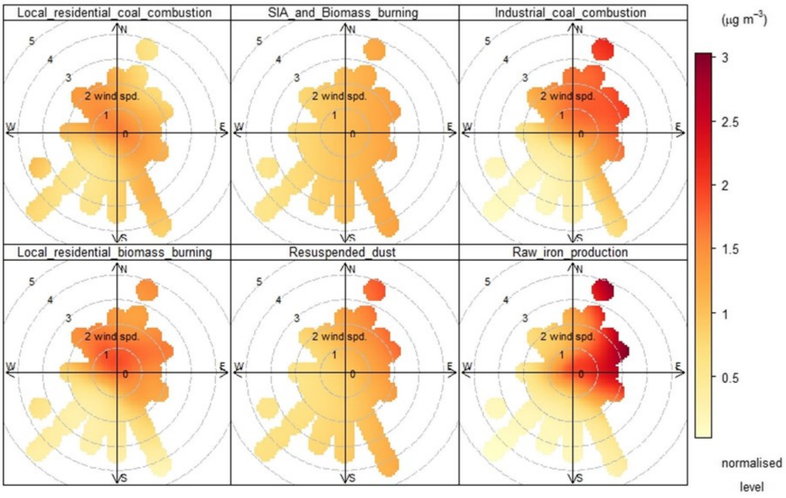

Fig. 2 Polar plots for Plesná $PM_{0.15-1.15}$ factors

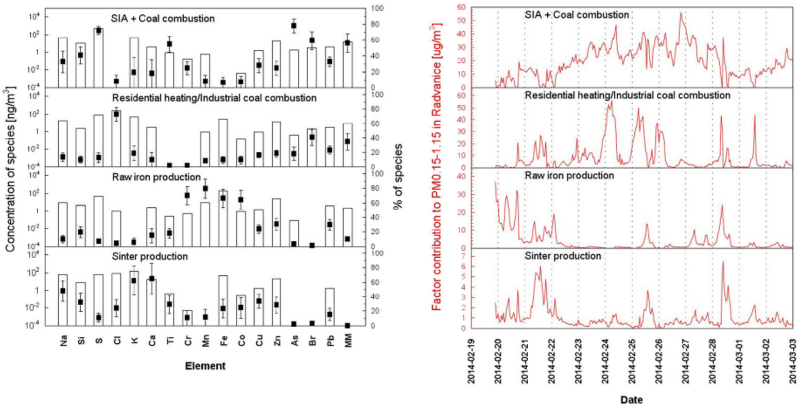

Fig. 3 Radvanice factor profiles (concentration of the species—bars, percentage of the species—markers; DISP Average—box, DISP Max and DISP Min—whiskers) and time series resolved for PM$_{0.15–1.15}$ by PMF.

origin from N over E to S (Fig. 2). The factor shows a moderate and strong relationship with PM$_1$ K$^+$, levoglucosan, NH$_4^+$ and SO$_4^{-2}$, respectively ($R^2 = 0.40$, $R^2 = 0.44$, $R^2 = 0.48$, $R^2 = 0.80$). In the source apportionment study by Kozáková et al. (2019), secondary sulphate and nitrate of regional origin and biomass burning of local origin contributed to PM$_1$ by 30%, 26% and 24%, respectively. The diverse result is the consequence of the lack of water-soluble ions in the data matrix and a different monitored period since the SIA and biomass burning peaks from 4 to March 6 are missing in the current study (3DRUM data series from February 19 to March 3).

Factor 3. The third factor was associated with high Cl and Br. There were moderate and strong correlations with the combustion factors (Factor 1 $r = 0.53$ and Factor 4 $r = 0.74$), and statistically significant correlations with PM$_1$, Cl$^-$, EC and K$^+$ ($R^2 = 0.73$, $R^2 = 0.80$, $R^2 = 0.62$). This factor was assigned as industrial coal combustion of regional origin; however, the residential combustion sources should be also considered due to good correlation with EC 24-PM$_1$, as well as with local residential combustion sources in Plesná. Cl and Br are naturally present in coal as trace elements as well as Hg, As and Se (Finkelman et al. 1993). These elements mostly evaporate during combustion and condense either homogeneously as sub-micron ash or heterogeneously onto already existing fine ash, the former one being more difficult to be captured (Clarke 1993; Vejahati et al. 2010). Zíková et al. (2016) and Li et al. (2019) show the NH$_4$Cl footprint of coal combustion in Beijing as an ageing product of HCl emissions from local combustion appliances and heating plants. The high factor contributions with WS of > 2 m s^{-1} from the NE point to sources of regional origin (Fig. 2). The three distinct midnight peaks on February 24, 25 and 26 reflect the stagnant atmospheric conditions during winter nights and points to the medium to large combustion source/s of a regional origin. This factor contributed 15% to PM$_{0.15–1.15}$ and corresponds to the coal combustion factor of regional origin apportioned in Kozáková et al. (2019) with contribution of 18% to PM$_1$.

Factor 4. This factor assigned as local biomass burning contained Zn, Na, MM and K. K also derives from other sources including waste incinerators and cooking (Duan et al. 2004; Wang et al. 2007; Caseiro et al. 2009; Mkoma et al. 2013). The campaign average contribution of this factor to the PM$_{0.15–1.15}$ mass was 12%. The high factor contributions during periods of low WS (< 2 m s^{-1}) point to local sources situated from NW over N to SE from the sampling site. The factor shows a strong relationship with PM$_1$ levoglucosan and K$^+$, respectively ($R^2 = 70$ and 0.81, respectively). The daily pattern corresponds to the daily pattern of factor coal combustion (Fig. SI3). Kozáková et al. (2019) present a biomass-burning factor with a contribution of 24% to PM$_1$.

Factor 5. This factor, re-suspended dust, was associated with the major crustal elements. (Almeida et al. 2005; Rogula-Kozłowska et al. 2012) and on average, contributed 4% to the PM$_{0.15–1.15}$ mass. The dust source was located in the NE quadrant from the sampling site and became more important when WS was of > 2 m s^{-1} (Fig. 2). The re-suspended dust factor was not resolved by Kozáková et al. (2019) due to the limited elemental analyses of the PM samples. Therefore, they lacked the tracers of dust emissions.

Factor 6. The last factor was ascribed to raw iron production. Its profile shows a high concentration of metals especially Mn, Fe and Cu (Querol et al. 2007; Zhou et al. 2004; Cohen et al. 2010). The campaign average of the raw iron factor contributions was 2%. Source/s of rather regional origin from the NE and E (Fig. 2), and therefore from across the Polish border. However, the local sources in Ostrava could not be overlooked. The regression analysis shows a weak and strong relationship between the raw iron factor and PM_1 Na^+, and K^+ ($R^2 = 0.32$ and $R^2 = 0.71$, respectively). Since the tracers for raw iron factor were missing in the Kozáková et al. (2019) study, the factor was not resolved.

The difference in the number and origin of the factors resolved by PMF based on $PM_{0.15–1.15}$ and PM_1 chemical composition reflects the different measurement period, analysed variables, sampling integration time and modelling approach (two separate matrices in this study and one common matrix for both sites due to the limited number of 24 h samples in Kozáková et al. 2019).

Radvanice

Factor 1. The first factor was associated with high concentrations of S, As, Br and MM. Thus, this factor represents secondary inorganic aerosol (SIA) and coal combustion. The polar plot points primarily to the residential area of Ostrava-Radvanice district situated to the north of the sampling site (Fig. 4). This mixed factor dominated during the measurement campaign (59%). The highest factor contributions to $PM_{0.15–1.15}$ occurred for low WS (< 2 m s^{-1}) and at a temperature lower than the campaign average. The factor shows weak and moderate relationships with PM_1 EC, SO_4^{2-}, and OC ($R^2 = 0.25$, $R^2 = 0.26$, $R^2 = 0.40$). The mixed factor secondary inorganic aerosol/coal combustion/biomass burning (SIA/CC/BB) by Leoni et al. (2018) was also resolved based on the chemical composition of $PM_{0.09–1.15}$. Although the results presented in Leoni et al. (2018) corresponded to a sampling period from February 10 to March 2, 2014, and the present study ran from February 19 to March 3, 2014, the agreement between the two analyses is good.

Factor 2. This factor characterized by Cl, Br and MM was ascribed to local residential heating. However, the industrial coal combustion source/s should be considered since the polar plot shows a high concentration from the north for a WS $<$ 2 m s^{-1} and from the southwest when the WS was between 2 and 4 m s^{-1} (Fig. 4). The chemical profile represents coal and wood combustion in residential boilers and high temperature coke combustion in the metallurgical industry (blast furnace and steel production). The three distinct peaks on February 24, 25 and 26 corresponded to the peaks of the industrial coal combustion factor identified in Plesná. The mean residential heating and industry factor contributed 29% to $PM_{0.15–1.15}$. The regression analysis shows moderate relationships with PM_1 Cl^- and OC ($R^2 = 0.46$, $R^2 = 0.47$, respectively). This factor was not resolved by Leoni et al. (2018). However, the three main peaks between February 24 and 26 correspond to high contributions of the mixed factor SIA/CC/BB of $PM_{0.09–1.15}$.

Factor 3 was identified as raw iron production since its profile was primarily associated with Cr, Mn and Fe. The campaign average of the factor contributions to $PM_{0.15–1.15}$ was 11% that is in agreement with the 10% value reported

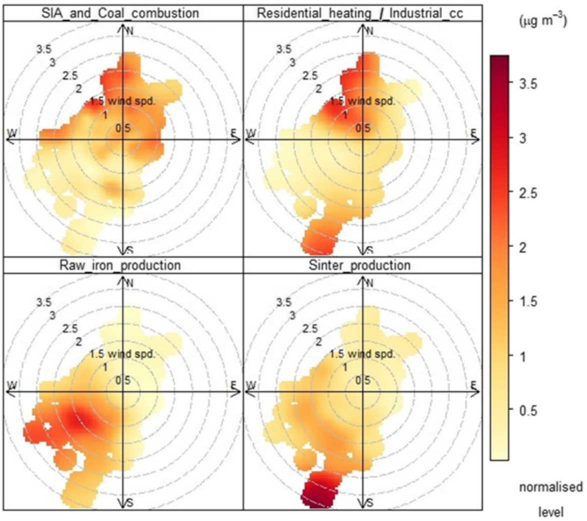

Fig. 4 Polar plots for the Radvanice $PM_{0.15–1.15}$ factors

by Leoni et al. (2018). The high factor contributions from the SW point to local metallurgical sources.

Factor 4. The fourth factor was ascribed to sinter production because of its profile shows high concentration of Na, K and Ca. According to our previous studies (Pokorná et al. 2015), the chemical profile corresponds to sinter production. It does not correspond well to the sinter/steel production factor resolved by Leoni et al. (2018). This factor contributed 1% to $PM_{0.15-1.15}$ with high contribution from SE with WS of 3 m s^{-1}, and therefore, it likely represents the nearby metallurgical complex (Fig. 4). The sinter production factor showed a significant correlation with the raw iron production factor (Factor 4, $r = 0.72$) and weak and very strong correlations with PM_1 Na^+ and K^+ ($R^2 = 0.21$ and $R^2 = 0.83$, respectively). The road dust factor identified by Leoni et al. (2018) was not resolved in this study of $PM_{0.15-1.15}$. The difference in the number of the factors

Resolved from the $PM_{0.15-1.15}$ and $PM_{0.09-1.15}$, chemical composition was probably driven by the different measurement periods. Additionally, the Pokorná et al. (2015) source apportionment presented five $PM_{0.15-1.15}$ factors at the Radvanice site; coal combustion, sinter production—hot phase, traffic, raw iron production and desulfurization slag processing. The 2012 measurement campaign was affected by a long-term smog period. Therefore, the meteorological conditions were not comparable with the present study. However, there was an overall agreement in the main sources influencing the air quality at the receptor site.

Plesná and Radvanice source comparisons

To assess the relationship between the resolved factor contributions at the two sites, the Pearson correlation coefficients (r) were computed. The mixed factor SIA and coal combustion (*Factor 1, Radvanice*) shows a low correlation with the factors of local residential biomass burning (*Factor 4, Plesná; $r = 0.16$*), local residential coal combustion (*Factor 1, Plesná; $r = 0.21$*) and industrial coal combustion (*Factor 3, Plesná; $r = 0.25$*). Additionally, the mixed factor local residential heating and industrial coal combustion (*Factor 2, Radvanice*) correlated weakly with industrial coal combustion (*Factor 3, Plesná; $r = 0.27$*). These limited pairwise correlations between the factors time series suggest that different sources were contributing to $PM_{0.15-1.15.}$ These results reflect the important effects of the local meteorology given by the region's orography.

Factors resolved with PNSD and association with chemical composition factors

Plesná

The model was run approximately 100 times to find the most physically meaningful result and the best diagnostics. Due to the low S/N ratio, four variables were set as weak (18.4 nm, 5.1 μm, 6.7 μm and 7.8 μm; midpoint of the size bins) and their uncertainty tripled. Four variables in the coarse size were excluded from the matrix given the high noise level in the data (9.7 μm, 11.9 μm, 14.9 μm, 18.5 μm, midpoint of the size bins). The model was run with different factor numbers (3–9) with 0% extra modelling uncertainty. The most stable solution was found for 6 factors. All runs converged, the scaled residuals were normally distributed, no unmapped factors were detected with bootstrap error estimation and no swaps were observed with displacement error analysis, indicating that the solution was stable (Table S1). The six factors in Plesná were assigned as *residential combustion, urban background, traffic/metallurgical industry, new particle formation (NPF)/ metallurgical industry, regional pollution and residential heating/re-suspended dust*. The non-normalized PNSD (N cm^{-3}) was analysed by the model. For the result presentation, the model outputs were converted to dN/d (log Dp) and dV/d (log Dp). The factor NSD and volume size distributions (VSD) are shown in Fig. 5.

Factor 1. This factor includes particles in the Aitken mode and accumulation mode (Aitk2) with the number mode diameter (NMD) at 75 nm and distinct volume mode diameter (VMD) at 274 nm (small VMD at 2 μm, Fig. 5). The average concentration was 2.5×10^3 particle cm^{-3} with a maximum of 1.2×10^4 particle cm^{-3}. This factor is the important contributor for PNC (34%) and a minor contributor to volume concentration (11%). The highest concentrations were under an eastern WD at a WS of 2–3 m s^{-1} (Fig. 6). The diel heating pattern and/or the stagnant atmospheric conditions during winter nights is also obvious (Fig. SI4). There is a moderate correlation with $PM_{0.15-1.15}$ factors of industrial coal combustion ($r = 0.47$), local residential biomass burning ($r = 0.46$), raw iron production ($r = 0.44$) and local residential coal combustion ($r = 0.41$). This factor represents urban background also identified in Radvanice by Leoni et al. (2018) (NMD 93 nm) and similar to the London urban background site reported by Vu et al. (2016) (NMD 93 nm). An urban background factor with morning and evening maxima (Fig. SI4), the same factor daily pattern, attributed to road traffic and residential heating, was observed in the studies by Beddows et al. (2015) and by Masiol et al. (2017).

Factor 2. This includes accumulation mode particles (Acc1) and is the major contributor to PNC (30%) and to volume concentration (38%). The size distribution has a predominant mode, with NMD at 144 nm and VMD at 379 nm (Fig. 5). The average concentration was 2.6×10^3 particle cm^{-3} and peaks up at 6.7×10^3 particle cm^{-3}. The daily variability reflects the heating pattern with morning and afternoon peaks. However, this pattern was also linked to the stagnant atmospheric conditions during winter nights (Fig. SI4). The highest concentrations were observed with a low WS (< 2 m s^{-1}) mainly from the northeast (Fig. 6). In comparison

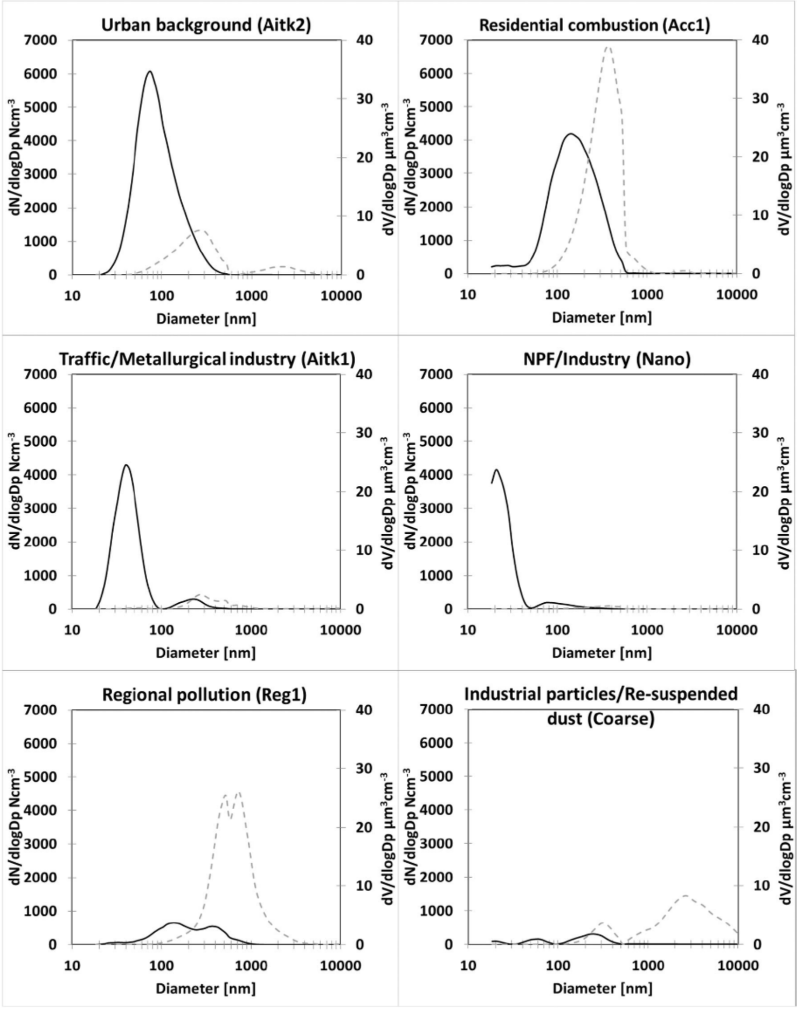

Fig. 5 PNSD PMF factors for Plesná. The volume size distribution (dashed lines) was re-calculated from the PNSD assuming spherical particles

with the factors resolved based on the $PM_{0.15-1.15}$ chemical composition in Plesná, this factor has a moderate correlation with local residential coal combustion ($r = 0.50$), local residential biomass burning ($r = 0.48$) and industrial coal combustion ($r = 0.44$). This factor represents the residential combustion sources of local origin. In Radvanice, a coal combustion factor with NMD at 160 nm and VMD at 500 nm contributed by 14% to PNC and by 42% to PVC (Leoni et al. 2018).

Factor 3 contributed 12% to PNC and 1% to PVC, having a prominent mode at 39 nm (Aitk1, Fig. 5). It shows an average concentration of 7.6×10^3 particle cm^{-3} with a peak at 9.7×10^3 particle cm^{-3}. The polar plot shows high PNC from the north-northeast to south-southeast for $W > 2$ m s^{-1} (Fig. 6). There was

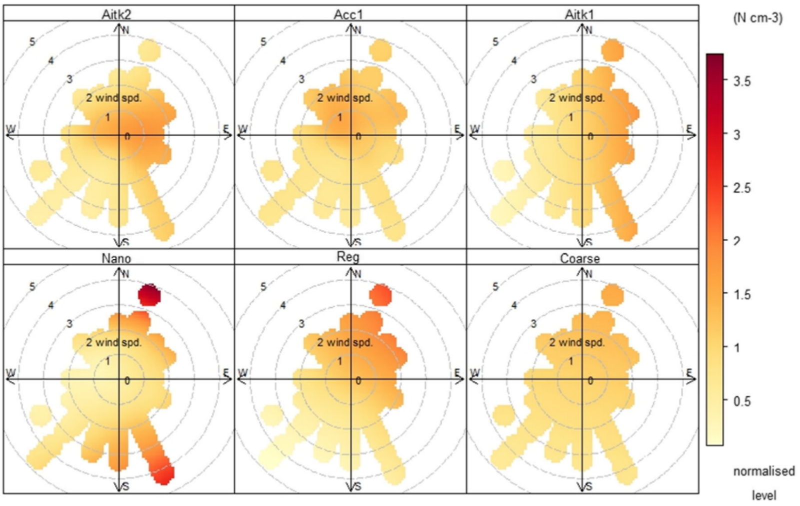

Fig. 6 Polar plots for Plesná NSD factors

no significant correlation with the factors resolved based on the PM chemical composition due to the size range of the impactor. These particles are likely to be from traffic and industrial origins given the prevailing wind direction and the industrial source identification by Leoni et al. (2018) with NMD at 45 nm in Radvanice. Other studies reported a high concentration of ultrafine particles emitted by steel and iron production (Weitkamp et al. 2005; Cheng et al. 2008; Riffault et al. 2015).

Factor 4. This factor includes particles in the nucleation mode (Nano) with a mode at 21 nm (Fig. 5) and a contribution of 8% to PNC. The average particle concentration was 6.0×10^2 particle cm^{-3} with a maximum of 3.7×10^3 particle cm^{-3}. The factor shows a diel pattern with the maxima between 1 PM and 2 PM (Fig. SI4) pointing to photochemical nucleation by the highest solar radiation and particle growth recorded on 26.2, beginning between 1 PM and 2 PM (Fig. SI5). The highest PNC was recorded with WS > 3 m s^{-1} from the north-northeast and south-southeast. According to the polar plots, new particle formation (NPF) events were most probably accompanied by industrial emissions of local and regional origin, from transboundary transport of pollution from the Polish part of Silesia (Fig. 6). The metallurgical industry has been identified as a source of nanoparticles (Dall'Osto et al. 2008; Riffault et al. 2015; Leoni et al., 2016 and 2018); however, no statistically significant correlation with the factors resolved based on the PM chemical composition was found.

Factor 5. It is characterized by accumulation mode particles (Reg) with two NMD (144 and 379 nm) and VMD (524 and 724 nm). This factor is a major contributor to volume concentrations (33%) and a minor contributor to PNC (7%) with an average concentration of 4.9×10^2 particle cm^{-3} and a maximum at 2.3×10^3 particle cm^{-3}. The factor shows the dial course linked to the heating pattern and/or the stagnant atmospheric conditions during winter nights. The highest PNC occurred for northeasterly winds with a WS of > 2 m s^{-1}. The factor correlates moderately with the $PM_{0.15–1.15}$ factors of industrial coal combustion ($r = 0.65$), local residential biomass burning ($r = 0.47$) and secondary inorganic aerosol along with biomass burning.

The last factor, *Factor 6* is characterized by supermicrometre mode particles (Coarse) with appreciable VMD at 3 μm (small VMD at 306 nm, Fig. 5). It contributes 16% to PVC and 2% to PNC. The factor average concentration was 1.4×10^2 particle cm^{-3} with a peak value of 8.8×10^2 particle cm^{-3}. The polar plots showed the highest PNC for northeasterly winds of > 2 m s^{-1} (Fig. 6). The factor does not have a clear diel pattern (Fig. SI4). The factor shows moderate correlation with raw iron production ($r = 0.53$). However, the expected correlation with the re-suspended dust factor is very weak ($r = 0.16$), probably due to the upper cut point of the impactor being 1.15 μm. In comparison with Radvanice, Leoni et al. (2018) identified a mixed industrial coarse particle and road dust factor.

Radvanice

Since the source apportionment of aerosol particles based on PNSD in Radvanice is the subject of the study by Leoni et al.

(2018), only the PNSD sources apportionment in Plesná is fully presented in this study. Briefly, Leoni identified six sources. Mixed source industrial and fresh road traffic, industrial ultrafine particles and urban background contributed most to the PNC (26%, 28%, 24%, respectively). The highest contribution to the particle volume concentration (PVC) was coal combustion along with mixed source industrial coarse particles and road dust (42% and 20%).

For the purpose of this study, the Pearson correlation coefficients (r) between the Radvanice PNSD and $\mathrm{PM}_{0.15-1.15}$ resolved factors were computed. Mixed source industrial and fresh road traffic nucleation (*Factor 1, Radvanice*; Leoni et al. 2018) shows moderate to strong correlation with sinter (*Factor 4*) and raw iron production (*Factor 3*) $r = 0.47$ and $0 = 0.74$, respectively. Industrial ultrafine particles (*Factor 2, Radvanice*; Leoni et al. 2018) strongly correlated ($r = 0.74$) with sinter production (*Factor 4*). Coal combustion (*Factor 4, Radvanice*; Leoni et al. 2018) shows moderate correlations with mixed sources residential heating and industrial coal combustion (*Factor 2*, $r = 0.64$), and secondary inorganic and coal combustion (*Factor 1*, $r = 0.57$). Regional pollution (*Factor 5, Radvanice*; Leoni et al. 2018) correlated moderately with mixed sources residential heating and industrial coal combustion (*Factor 2*, $r = 0.53$). Mixed source industrial coarse particles and road dust (*Factor 6, Radvanice*; Leoni et al. 2018) shows moderate correlations with raw iron and steel production (*Factor 3 and 4*) $r = 0.49$ and $r = 0.64$, respectively.

Plesná and Radvanice source comparisons

To assess the relationship between the resolved PNSD factors at the two sites, the Pearson correlation coefficients (r) were computed to compare the shared variance. The factor coal combustion (*Factor 4, Radvanice*; Leoni et al. 2018) shows moderate correlation with the Plesná factors of residential combustion of local origin (*Factor 2*) $r = 0.68$ and regional pollution (*Factor 5*) $r = 0.52$. Additionally, the factor regional pollution (*Factor 5*, *Radvanice*; Leoni et al. 2018) correlated moderately with the factor regional pollution in Plesná (*Factor 5*) $r = 0.53$.

Conclusions

This study accessed the spatial and temporal variability of the winter air particulate pollution sources in an urban settlement influenced by metallurgical industry using atmospheric aerosol chemical composition and PNSD. The modelling results confirmed the relevance and importance of the complementary datasets enabling the identification of sources contributing to both particle mass and particle number. While in Radvanice, the PNSD and $\mathrm{PM}_{0.15-1.15}$ sources show moderate to strong correlation, in Plesná, the two mixed PNSD sources show weak correlation (traffic and industry—Aitken mode at 39 nm and nanoparticles with a mode at 21 nm) with the $\mathrm{PM}_{0.15-1.15}$ sources.

The study results elucidated the importance of the local meteorology given by the region's orography. Similar sources according to the factor chemical profiles resulted from different physical sources. In Plesná, residential combustion sources of local origin followed by regional combustion sources primarily contributed to $\mathrm{PM}_{0.15-1.15}$ (Tab. SI4). Surprisingly, the influence of the local industrial emissions was not very important at the site. In Radvanice, local residential combustion and the metallurgical industry were the most important sources (Tab. SI5), which agrees with our previous studies (Pokorná et al. 2015, 2016). Aitken and accumulation mode particles emitted by the urban background (residential heating, industry and traffic) along with local residential combustion sources were the major contributors to PNC in Plesná (Tab. SI4). Additionally, NPF events contributing 8% to PNC were probably mixed with local industrial nanoparticles similar to what was reported in the previous study by Leoni et al. (2018). In contrast, at the Radvanice site, the local industrial sources were the major contributor to PNC (Leoni et al. 2018). However, for a NE prevailing wind with speeds of > 2 m s^{-1}, air pollution transboundary transport and regional sources were evident at both receptor sites in agreement with the results presented by Kozáková et al. (2019). Last but, not least, since the measurement campaign was conducted in winter and the sampling sites are moderately influenced by the traffic density, the contribution of road traffic sources to PM and PNSD seems to be reasonable. However, the measurement of additional road traffic tracers and/or the annual measurement will enable more precise source apportionment of road traffic at both sites.

To conclude, the presented results are representative for winter seasons by the same meteorological conditions, since the meteorology plays a crucial role in the air pollution not only in the Ostrava city, but also in the whole Moravian-Silesian region. Therefore, the long-term complex measurement (highly time- and size-resolved chemical composition and PNSD) at least at three measurement sites well distributed in the city will enable precise source apportionment, and consequent planning and implementation of effective abatement strategies to improve air quality.

The methodology presented in this study can be replicated at any receptor to elucidate the spatial and temporal variability of the air particulate pollution sources contributing to particle mass as well as particle number concentrations.

Funding information This work was supported by the Czech Science Foundation under the project P503/12/G147 and by the MEYS of the Czech Republic from the ERDF project "ACTRIS-CZ RI" (No. CZ.02.1.01/0.0/0.0/16_013/0001315). The research fellowship of one of the authors (P.P.) at the CARES, Clarkson University, was funded by the Fulbright Scholar Program. This research used resources of Beamline 10.3.1 of the Advanced Light Source, which is a DOE Office of Science User Facility under contract no. DEAC02-05CH11231.

References

Almeida AM, Pio CA, Freitas MC, Reis MA, Trancoso MA (2005) Source apportionment of fine and coarse particulate matter in sub-urban area at the Western European Coast. Atmos Environ 39:3127–3138

Ancelet T, Davy PK, Mitschell T, Trompetter WJ, Markwitz A, Weatherburn DC (2012) Source of particulate matter pollution in a small New Zealand city. Environ. Sci. Technol. 46:4767–4774

Ancelet T, Davy PK, Trompetter WJ, Markwitz A, Weatherburn DC (2014) Sources and transport of particulate matter on an hourly time-scale during the winter in a New Zealand urban valley. Urban Clim 10:644–655

Beddows DCS, Harrison RM, Green DC, Fuller GW (2015) Receptor modeling of both particle composition and size distribution. Atmos Chem Phys 15:10107–10125

Carslaw DC, Ropinks K (2012) Openair e an R package for air quality data analysis. Environ Model Soft 27-28:52–61

Caseiro A, Bauer H, Schmidl C, Pio CA, Puxbaum H (2009) Wood burning impact on PM10 in three Austrian regions. Atmos Environ 43:2186–2195

Černikovský L, Krejčí B, Blažek Z, Volná V (2016) Transboundary air pollution transport in the Czech-polish border region between the cities of Ostrava and Katovice. Cent Eur J Public Health 24:45–50

Cheng YH, Chao YC, Wu CH, Tsai CJ, Uang SN, Shih TS (2008) Measurement of ultrafine particles concentrations and size distribution in an iron foundry. J Hazard Mater 158:124–130

CHMI, Czech Hydrometeorological Institute (2018) Air pollution in the Czech Republic in:2018 http://portal.chmi.cz/files/portal/docs/uoco/isko/grafroc/18groc/gr18en/KO_rocenka_2018.pdf

Clarke LB (1993) The fate of trace elements during coal combustion and gasification: an overview. Fuel 72(6):731–736

Cohen DD, Crawford J, Stelcer E, Bac VT (2010) Characterisation and source apportionment of fine particulate matter at Hanoi 2001 to 2008. Atmos Environ 44:230–328

Cusack M, Pérez N, Pey J, Alastuey A, Querol X (2013) Source apportionment of fine PM and sub-micron particle number concentrations at a regional background site in the western Mediterranean: a 2.5 year study. Atmos Chem Phys 13:5173–5187

Dall'Osto M, Booth MJ, Smith W, Fisherb R, Harrison RM (2008) A study of the size distributions and the chemical characterization of airborne particles in the vicinity of a large integrated steelworks. Aerosol Sci Technol 42:981–991

DeGaetano AT, Doherty OM (2004) Temporal, spatial and meteorological variations in hourly PM2.5 concentration extremes in New York City. Atmos Environ 38:1547–1558

Dostál, M., Pastorková, A., Rychlík, S., Rychlíková, E., Švecová, V., Schallerová, E., Šrám, R.J., 2013. Comparison of child morbidity in regions of Ostrava, Czech Republic, with different degrees of pollution: a retrospective cohort study. Environ Health 12, 1–11

Duan M, Zhuang G, Li X, Tao H, Zhuang Y (2004) The characteristics of carbonaceous species and their sources in PM2.5 in Beijing. Atmos Environ 38:3443–3452

Finkelman R, Trace B, minor elements in coal. In Organic Geochemistry; Engel, M. H., Macko, S. A. (eds) (1993) Plenum Press: New York: 593–607

Guan Q, Cai A, Wang F, Yang L, Xu C, Liu Z (2017) Spatio-temporal variability of particulate matter in the key part of Gansu Province, Western China. Environ Pollut 230:189–198

Guerreiro CBB, Foltescu V, de Leeuw F (2014) Air quality status and trends in Europe. Atmos Environ 98:376–384

Harrison RM, Beddows DCS, Dall'Osto M (2011) PMF analysis of wide range particle size spectra collected on a major highway. Environ. Sci. Technol. 45:5522–5528

Heal MR, Kumar P, Harrison R (2012) Particles, air quality, policy and health. Chem Soc Rev 41:6606–6630

Hopke PK (2016) A review of receptor modeling methods for source apportionment. Journal of Air and Waste Management Association 66:237–259

Hovorka, J., Pokorná, P., Hopke, P.K., Křůmal, K., Mikuška, P., Píšová, M., 2015. Wood combustion, a dominant source of winter aerosol in residential district in proximity to a large

Kasumba J, Hopke PK, Chalupa DC, Utell MJ (2009) Comparison of sources of submicron particle number concentrations measured at two sites in Rochester. NY Sci of the Total Environ 407:5071–5084

Kim, E., Hopke P.K., Larson, T.V., Covert, D.S., 2004. Analysis of ambient particle size distributions using Unmix and positive matrix factorization Environ. Sci & Technol 38, 202–209

Kozáková J, Pokorná P, Vodička P, Ondráčková L, Ondráček J, Křůmal K, Mikuška P, Hovorka J, Moravec P, Schwarz J (2019) Influence of regional air pollution transport at a European air pollution hotspot. Environ Sci Pollut Res 26:1675–1692

Kumar P, Hopke PK, Raja S, Casuccio G, Lersch TL, West RR (2012) Characterization and heterogeneity of coarse particles across an urban area. Atmospheric Environ 46:339–359

Lagudu, U.R.K., Raja, S., Hopke, P.K., Chalupa, D.C., Utell, M.J., Casuccio, G.; Lersch, T. L, West, R.R., 2011. Environ. Sci Technol 45,8, 3288–3296

Leoni C, Hovorka J, Docekalova V, Cajthaml T, Marvanova S (2016) Source impact determination using airborne and ground measurements of industrial plumes. Environ. Sci. Technol. 50:9881–9888

Leoni C, Pokorná P, Hovorka J, Masiol M, Topinka J, Zhao Y, Křůmal K, Cliff S, Mikuška P, Hopke PK (2018) Source apportionment of number size distributions and mass chemical composition in a European air pollution hot spot. Environ Pollut 234:145–154

Li XH, Yang K, Han JZ, Ying Q, Hopke PK (2019) Sources of humic-like substances (HULIS) in PM2.5 in Beijing: receptor modeling approach. Sci Total Environ 671:765–775

Masiol M, Vu TV, Beddows DCS, Harrison RM (2016) Source apportionment of wide range particle size spectra and black carbon collected at the airport of Venice (Italy). Atmos Environ 139:56–74

Masiol M, Hopke PK, Felton HD, Frank BP, Rattigan OV, Wurth MJ, LaDuke GH (2017) Source apportionment of PM2.5 chemically speciated mass and particle number concentrations in New York City. Atmos Environ 148:215–229

Mkoma SL, Kawamura K, Fu PQ (2013) Contributions of biomass/biofuel burning to organic aerosols and particulate matter in Tanzania, East Africa, based on analyses of ionic species, organic and elemental carbon, levoglucosan and mannosan. Atmos Chem Phys 13:10325–10338

Moon C (2001) Exposure assessment of air pollutants: a review on spatial heterogeneity and indoor/outdoor/personal exposure to suspended particulate matter, nitrogen dioxide and ozone. Atmos Environ 35:1–32

Moreno T, Kojima T, Amato A, Lucarelli F, de la Rosa J, Calzolai G, Nava S, Chiari M, Alastuey A, Querol X, Gibbons W (2013) Daily and hourly chemical impact of springtime transboundary aerosols on Japanese air quality. Atmos Chem Phys 13:1411–1424

Ogulei D, Hopke PK, Chalupa DC, Utell MJ (2007a) Modeling source contributions to submicron particle number concentrations measured in Rochester. New York Aerosol Sci and Technol 41:179–2001

Ogulei D, Hoppke PK, Ferro AR, Jaques PA (2007b) Factor analysis of submicron particle size distributions near a major United States-Canada trade bridge. Journal of the Air & Waste Management Assoc 57:190–203

Pancras JP, Landis MS, Norris GA, Vedantham R, Dvonch JT (2013) Source apportionment of ambient fine particulate matter in Dearborn, Michigan, using hourly resolved PM chemical composition data. Sci Total Environ 448:2–13

Petit JE, Amodeo T, Meleux F, Bessagnet B, Menut L, Grenier D, Pellan Y, Ockler A, Rocq B, Gros V, Sciare J, Favez O (2017) Characterising an intense PM pollution episode in March 2015 in France from multi-site approach and near real time data: climatology, variabilities, geographical origins and model evaluation. Atmos Environ 155:68–84

Pey J, Querol X, Alastuey A, Rodríguez S, Putaud JP, Van Dingenen R (2009) Source apportionment of urban fine and ultrafine particle number concentration in a Western Mediterranean city. Atmos Environ 43:4407–4415

Pokorná P, Hovorka J, Kroužek J, Hopke PK (2013) Particulate matter source apportionment in a village situated in industrial region of Central Europe. J Air Waste Manag Assoc 63:1412–1421

Pokorná P, Hovorka J, Klán M, Hopke PK (2015) Source apportionment of size resolved particulate matter in European air pollution hot spot. Sci Total Environ 502:172–183

Pokorná P, Hovorka J, Hopke PK (2016) Elemental composition and source identification of very fine aerosol particles in a European air pollution hot-spot. Atmospheric Pollution Research 7:671–679

Polissar AV, Hopke PK, Poirot RL (2001) Atmospheric aerosol over Vermont: chemical composition and sources. Environmental Science & Technology 35:4604–4621

Querol X, Viana M, Alastuey A, Amato F, Moreno T, Castillo S, Pey J, de la Rosa J, Sánchez de la Campa A, Artíñano B, Salvador P, García Dos Santos S, Fernández-Patier R, Moreno-Grau S, Negral L, Minguillón MC, Monfort E, Gil JI, Inza A, Ortega LA, Santamaría JM, Zabalza J (2007) Source origin of trace elements in PM from regional background, urban and industrial sites of Spain. Atmos Environ 41:7219–7231

Riffault V, Arnds J, Marris H, Mbengue S, Setyan A, Alleman LY, Deboudt K, Flament P, Augustin P, Delbarre H, Wenger J (2015) Fine and ultrafine particles in the vicinity of industrial activities: a review. Environ Sci Technol 45(21):2305–2356

Rogula-Kozłowska W, Klejnowski K (2013) Submicrometer aerosol in rural and urban backgrounds in southern Poland: primary and secondary components of PM1. Bull Environ Contam Toxicol 90:103–109

Rogula-Kozłowska W, Klejnowski K, Rogula-Kopiec P, Mathews B, Szopa S (2012) A study on the seasonal mass closure of ambient fine and coarse dusts in Zabrze, Poland. Bull Environ Contam Toxicol 88:722–729

Rogula-Kozłowska W, Błaszczak B, Szopa S, Klejnowski K, Sówka I, Zwoździak A, Jabłońska M, Mathews B (2013a) PM2.5 in the central part of Upper Silesia, Poland: concentrations, elemental composition, andmobility of components. EnvironMonit Assess 185:581–601

Rogula-Kozłowska W, Kozielska B, Klejnowski K, Szopa S (2013b) Hazardous compounds in urban PM in the central part of Upper Silesia (Poland) in winter. Arch Environ Prot 39:53–65

Shen S, Jaques PA, Zhu Y, Geller MD, Sioutas C (2002) Evaluation of the SMPS–APS system as a continuous monitor for measuring PM2.5, PM10 and coarse (PM2.5–10) concentrations. Atmos Environ 36:3939–3950

Sowlat MH, Hasheminassab S, Sioutas C (2016) Source apportionment of ambient particle number concentrations in central Los Angeles using positive matrix factorization (PMF). Atmos Chem Phys 16: 4849–4866

Squizzato S, Masiol M, Emami F, Chalupa DC, Utell MJ, Rich DQ, Hopke PK (2019) Long-term changes of source apportioned particle number concentrations in a metropolitan area of the northeastern United States. Atmosphere 10(27):1–17

Šram RJ, Binková B, Dostál M, Merkerová-Dostalová M, Líbalová H, Milcová A, Rossner P, Rossernová A, Schmuczerová J, Švecová V, Topinka J, Votavová H (2013) Health impact of air pollution to children. Int J Hyg Environ Health 216:533–540

Topinka J, Rossner P, Milcová A, Schmuczerová J, Pečíková K, Rossnerová A, Ambrož A, Štolcpartová J, Bendl J, Hovorka J, Machala M (2015) Day-to-day variability of toxic events induced by organic compounds bound to size segregated atmospheric aerosol. Environ Pollut 202:135–145

Vejahati F, Xu Z, Gupta R (2010) Trace elements in coal: associations with coal and minerals and their behavior during coal utilization – a review. Fuel 89(4):904–911

Viana M, Kuhlbusch TAJ, Querol X, Alastuey A, Harrison RM, Hopke PK, Winiwarter W, Vallius M, Szidat S, Prévôt ASH, Hueglin C, Bloemen H, Wåhlin P, Vecchi R, Miranda AI, Kasper-Giebl A, Maenhaut W, Hitzenberger R (2008) Source apportionment of particulate matter in Europe: a review of methods and results. J Aerosol Sci 39:827–849

Vu T, Delgado Saborit JM, Harrison RM (2015) Review: particle number size distribution from seven major sources and implications for source apportionment studies. Atmos Environ 122:144–132

Vu, T.V., Beddows, D.C.S., Delgado-Saborit, J.M., Harrison, R.M., 2016. Source apportionment of the lung dose of ambient submicrometre particulate matter. Aerosol Air Qual. Res. 16 (7), 1548–1557

Waked A, Bourin A, Michoud V, Perdrix E, Alleman LY, Sauvage S, Delaunay T, Vermeesch S, Petit JE, Riffault V (2018) Investigation of the geographical origins of PM10 based on long, medium and short-range air mass back-trajectories impacting Northern France during the period 2009-2013. Atmos Environ 193:143–152

Wang Q, Shao M, Liu Y, William K, Paul G, Li X, Liu Y, Lu S (2007) Impact of biomass burning on urban air quality estimated by organic tracers: Guangzhou and Beijing as cases. Atmos Environ 41:8380–8390

Wang YG, Hopke PK, Utell MJ (2012) Urban-scale seasonal and spatial variability of ultrafine particle number concentrations. Water. Air and Soil Pollution 223(5):2223–2235

Weitkamp EA, Lipsky EM, Pancras PJ, Ondov JM, Polidori A, Turpin BJ, Robinson AL (2005) Fine particle emission profile for a large coke production facility based on highly time-resolved fence line measurements. Atmos Environ 39(36):6719–6733

Zhou L, Hopke PK, Paatero P, Ondov JM, Pancras JP, Pekney NJ, Davidson CI (2004) Advanced factor analysis for multiple time resolution aerosol composition data. Atmos Environ 38:4909–4920

Zhou, L., Kim, E., Hopke, PK., 2005a. Mining airborne particulate size distribution data by positive matrix factorization. J. of Geophysical Research 110, D07S19

Zhou, L., Hopke, P.K., Stanier, C.O., Pandis, S.N., Ondov, J.M., Pancras, J.P., 2005b. Investigation of the relationship between chemical composition and size distribution of airborne particles by partial least squares and positive matrix factorization J. of Geophysical Research 110, D07S18

Zíková N, Wang YG, Yang FM, Li XH, Tian M, Hopke PK (2016) On the source contribution to Beijing PM2.5 concentrations. Atmos Environ 134:84–95

6.5. APPENDIX E: Manuscript 5

Topinka, J.; Rossner, P.; Milcová, A.; Schmuczerová, J.; Pěnčíková, K.; Rossnerová, A.; Ambrož, A.; Štolcpartová, J.; **Bendl, J.**; Hovorka, J.; Machala, M. Day-to-day variability of toxic events induced by organic compounds bound to size segregated atmospheric aerosol. *Environmental Pollution* 2015, 202, 135–145; DOI 10.1016/j.envpol.2015.03.024.

Environmental Pollution 202 (2015) 135–145

Contents lists available at ScienceDirect

Environmental Pollution

journal homepage: www.elsevier.com/locate/envpol

Day-to-day variability of toxic events induced by organic compounds bound to size segregated atmospheric aerosol

Jan Topinka [a, *], Pavel Rossner Jr. [a], Alena Milcová [a], Jana Schmuczerová [a], Kateřina Pěnčíková [b], Andrea Rossnerová [a], Antonín Ambrož [a], Jitka Štolcpartová [a, c], Jan Bendl [c], Jan Hovorka [c], Miroslav Machala [b, *]

[a] *Department of Genetic Ecotoxicology, Institute of Experimental Medicine, Czech Academy of Sciences, Vídeňská 1083, 142 20 Prague 4, Czech Republic*
[b] *Department of Chemistry and Toxicology, Veterinary Research Institute, Hudcova 70, 62100 Brno, Czech Republic*
[c] *Institute for Environmental Studies, Faculty of Science, Charles University in Prague, Albertov 6, 128 43 Prague 2, Czech Republic*

ARTICLE INFO

Article history:
Received 4 January 2015
Received in revised form
11 March 2015
Accepted 13 March 2015
Available online 26 March 2015

Keywords:
Air pollution
Carcinogenic PAH
Dioxin-like activity
DNA adducts
Oxidative damage
Particulate matter

ABSTRACT

This study quantified the temporal variability of concentration of carcinogenic polycyclic aromatic hydrocarbons (c-PAHs), genotoxicity, oxidative DNA damage and dioxin-like activity of the extractable organic matter (EOM) of atmospheric aerosol particles of aerodynamic diameter ($d_{ae,}$ μm) coarse ($1 < d_{ae} < 10$), upper- ($0.5 < d_{ae} < 1$) and lower-accumulation ($0.17 < d_{ae} < 0.5$) and ultrafine (<0.17) fractions. The upper accumulation fraction formed most of the aerosol mass for 22 of the 26 study days and contained ~44% of total c-PAHs, while the ultrafine fraction contained only ~11%. DNA adduct levels suggested a crucial contribution of c-PAHs bound to the upper accumulation fraction. The dioxin-like activity was also driven primarily by c-PAH concentrations. In contrast, oxidative DNA damage was not related to c-PAHs, as a negative correlation with c-PAHs was observed. These results suggest that genotoxicity and dioxin-like activity are the major toxic effects of organic compounds bound to size segregated aerosol, while oxidative DNA damage is not induced by EOM.

1. Introduction

Complex mixtures of organic compounds, including polycyclic aromatic hydrocarbons (PAHs), are present in various size fractions in air particulate matter (PM) and have been associated with many adverse health effects in humans, such as respiratory diseases and cancer. These conclusions from experimental and epidemiological findings were the major reasons why the International Agency for Research on Cancer (IARC) in 2013 classified outdoor air pollution as carcinogenic to humans (Group 1) (IARC, 2013).

Organic aromatic compounds bound to atmospheric PM may exert their toxicity by various mechanisms including genotoxicity (formation of DNA adducts, DNA strand breaks) caused mainly by c-PAH metabolism leading to DNA-reactive metabolites such as PAH-diolepoxides (Melendez-Colon et al., 2000), oxidative DNA damage, proteins and lipids induced mostly by alternative PAH-metabolism leading to the formation of quinones (Park et al., 2006; Hanzalová et al., 2010). Moreover, non-genotoxic mechanisms of toxicity of airborne complex mixtures associated with aryl hydrocarbon receptor (AhR)-mediated gene expression ("dioxin-like activity") were observed (Andrysík et al., 2011; Líbalová et al., 2012).

Most previous studies on the toxic effects of ambient air pollution used either cumulative PM size fraction (mostly $PM_{2.5}$ or PM_{10}) (Perrone et al., 2010; Leung et al., 2014), although the deposition of PM in human lung strongly depends on PM particle size (Heyder et al., 1986). Some studies used pooled PM samples collected during long-term sampling periods (Topinka et al., 2010, 2011), which may have been a limitation particularly for short-

---

Abbreviations: 8-oxodG, 8-oxodeoxyguanosine; d_{ae}, aerodynamic diameter; B[a]P, benzo[a]pyrene; B[b]F, benzo[b]fluoranthene; B[k]F, benzo[k]fluoranthene; B[a]A, benz[a]anthracene; BPDE, benzo[a]pyrene-r-7,t-8-dihydrodiol-t-9,10-epoxide [±]; c-PAHs, carcinogenic polycyclic aromatic hydrocarbons; CHRY, chrysene; CT DNA, calf-thymus DNA; DRZ, diagonal radioactive zone; DB[al]P, dibenzo[a,l]pyrene; DB[ah]A, dibenz[a,h]anthracene; DCM, dichlormethane; 7,12-DMBA, 7,12-dimethylbenz[a]anthracene; DMSO, dimethylsulfoxide; EOM, extractable organic matter; HPLC, high performance liquid chromatography; I[cd]P, indeno[1,2,3-c,d]pyrene; PAH, polycyclic aromatic hydrocarbons; PM, particulate matter; PM_{10}, particulate matter of aerodynamic diameter <10 μm; TEQ, toxic equivalency factor; WHO, World Health Organization.

* Corresponding authors.

E-mail addresses: jtopinka@biomed.cas.cz (J. Topinka), machala@vri.cz (M. Machala).

http://dx.doi.org/10.1016/j.envpol.2015.03.024
0269-7491/

term effects. Other studies tried to use chemical characterisation of PM, mostly at the PAH-level, and then calculated total relative toxic equivalency factors (TEF) for mixtures based on the relative toxic potencies of the mixture's components relative to a standard compound, i.e. benzo[a]pyrene (B[a]P) (Halek et al., 2008; Fisher et al., 2011). However, this approach did not take into account the interactions of components leading to synergistic and antagonistic effects of PM components.

In contrast to previous studies, we used a 4-stage cascade impactor to simultaneously sample ambient air particles of different aerodynamic diameter at a sampling site representing one of the highest air pollution levels in Europe, the district of Ostrava-Radvanice and Bartovice (Czech Republic). Coal combustion, iron producing technologies, and traffic were sources of atmospheric aerosols in the district during the winter of 2012 (Pokorná et al., 2015). The c-PAHs bound to PM, namely benz[a]anthracene (B[a]A), chrysene (CHRY), benzo[b]fluoranthene (B[b]F), benzo[k]fluoranthene (B[k]F), benzo[a]pyrene (B[a]P), dibenz[a,h]anthracene DB[ah]A, and indeno[1,2,3-cd]pyrene (I[cd]P), genotoxic potential, oxidative DNA damage and dioxin activity of organic extracts from PM (EOM) were determined on a daily basis for 26 consecutive days. To our knowledge, this is the first time that c-PAHs together with the toxicity markers listed above were determined in size fractionated PM on a daily basis to assess size and time variability of all toxicity parameters. We aimed to use relatively simple methods covering major toxic events to relate PM mass in 4 size fractions and c-PAH bound to PM with 3 major toxic endpoints determined in vitro (genotoxic potential, oxidative DNA damage and dioxin-like activity). Moreover, these relationships were assessed in 26 consecutive daily PM samples, i.e. in a relatively dense time period.

2. Materials and methods

2.1. Chemicals and biochemicals

Spleen phosphodiesterase was purchased from ICN Biomedicals, Inc.; micrococcal nuclease, and calf thymus DNA (CT DNA) were from Sigma (Deisenhofen, Germany); nuclease P1 was from Wako Chemicals, Japan; polyethylene-imine cellulose TLC plates (0.1 mm) were from Macherey–Nagel (Düren, Germany); c-PAHs (99% pure) were from Supelco, Inc.; T4 polynucleotide kinase (USB); and γ-^{32}P-ATP (3000 Ci/mmol, 10 μCi/μl) were from Perkin Elmer. 2,3,7,8-Tetrachlorodibenzo-p-dioxin (TCDD) was purchased from Cambridge Isotope Laboratories (Andover, MA); All other chemicals and solvents were of HPLC or analytical grade.

2.2. PM sampling

Prior to air sampling, the PUF substrates were cleaned in accordance with the BGI manual (BGI 900 High Volume Cascade Impactor, Guidance Manual, 2008). The PUF's cleaning consisted of consecutive leaching, hourly for each solvent, in ultrapure water, hexane, methanol, and dichlormethane in an ultrasonic bath. After the sonication, the substrates were dried in a clean air hood for 48 h. For weighing, the substrates and the ultra-filters were equilibrated for 24 h in a desiccator (~50% humidity, saturated $Mg(NO_3)_2{*}6H_2O$, $T = 21$ °C) and weighed at air-conditioned weighing room, wrapped in aluminum foil, placed in double sealed plastic bags with a zipper and stored in a sealed container in a laboratory. Immediately after the air sampling, the exposed substrates were weighed under the same conditions and stored at −20 °C till the chemical analysis. Two sets of field blanks were prepared and were manipulated as real samples except air sampling. Both aerosol mass and chemical species concentrations were blank corrected; nevertheless blank values were always well below 1% of concentrations of all the parameters determined. Coarse ($1 < d_{ae} < 10$ μm), upper accumulation ($0.5 < d_{ae} < 1$ μm), lower accumulation ($0.17 < d_{ae} < 0.5$ μm) aerosol particles were collected on polyurethane foam (PUF) and the smallest aerosol particles of $d_{ae} < 0.17$ μm, in this study termed quazi-ultrafine particles (qUF), were trapped on PTFE-coated Glass Micro-Fiber Absolute filters (Pallflex 70 TX40). The aerosol was sampled at a flow rate of 900 l/min by means of a HiVol cascade impactor (BGI 900, USA), which has the smallest attainable cut-off at 0.17 μm. Aerosol samples were consecutively collected with an integrating time of 23 h from January 26th to February 21st 2012 in a residential district of Ostrava-Radvanice and Bartovice (49°48′40.4″N, 18°20′15.8″E). The impactor was positioned on the roof of a mobile station at a height of 4 m. The PUF's substrates trap in some extent also gaseous PAH, i.e. exhibit positive sampling artifact. To evaluate this artifact, an additional PUF substrate layer was placed after the ultra-filters to trap exclusively gaseous PAH. Then, the after-filter PUF substrate was analyzed for 13 PAH including c-PAH. The positive sampling artifact for specific PAH varied with an ambient air temperature and diameter of aerosol particles and due to complexity will be subject of separate report. Nevertheless, sampling artifact was found negligible for PAH of the vapor pressure below 10^{-4} Pa, which applies for all the c-PAH evaluated in this paper.

2.3. PUF and filter extraction and PAH analysis

Both the PUFs and the absolute filters were extracted by dichloromethane. The chemical analysis of PAHs was performed in the laboratories of a certified company, ALS Czech Republic s.r.o., Prague (EN ISO CSN IEC 17025), by HPLC with fluorescence detection according to the standard procedures set in ISO 11338-2. The recovery of PAH extraction is controlled by laboratory control spikes. It is permanently stable (~80%). The PAH concentrations were blank corrected. The concentrations of seven of the PAHs regarded by the IARC as carcinogenic, namely B[a]A, CHRY, B[b]F, B[k]F, B[a]P, DB[ah]A, and I[cd]P, were analyzed in each EOM sample (of these, B[a]P is classified as carcinogenic to humans). For the in vitro experiments, EOM samples were evaporated under a stream of nitrogen. The residue was redissolved in dimethyl sulfoxide (DMSO). Samples were kept in a freezer at −80 °C until analysis.

2.4. Incubation of EOMs with CT DNA (in vitro acellular assay)

The assay was performed as previously described (Binkova et al., 2007). Rat liver S9 fraction was purchased from Toxila (Pardubice, Czech Republic). B[a]P (1 μM) and DMSO treated CT DNA samples were used as positive and negative controls, respectively.

2.5. DNA adduct analysis

Calf thymus DNA (CT DNA) was isolated by phenol/chloroform/isoamylalcohol extraction and ethanol precipitation (Gupta, 1985). ^{32}P-postlabeling analysis of DNA adducts was performed as described previously (Phillips and Castegnaro, 1999; Reddy and Randerath, 1986). A BPDE-DNA adduct standard was run in triplicate in each postlabeling experiment in order to check for interassay variation.

2.6. Oxidative DNA damage

After incubation with/without the S9 fraction described in 2.4., DNA was purified as reported by Rossner (Rossner et al., 2009) omitting the RNAse and proteinase K incubation steps. Levels of 8-oxodeoxyguanosine (8-oxodG) in DNA were analyzed using the

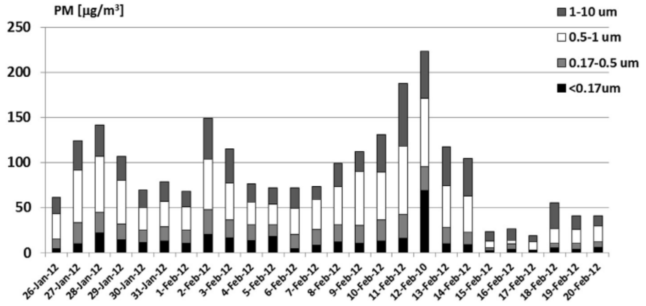

Fig. 1. PM mass distribution in 4 aerosol size fractions for individual sampling days. Samples were collected by a high volume sampler in Ostrava-Radvanice (Czech Republic) in winter 2012.

Table 1
Mean levels of PM, c-PAHs, DNA adducts and oxidative DNA damage for various aerosol size fractions for the overall sampling period of 26 consecutive days (January 26-February 20, 2012).

d_{ae} [µm]	PM mass conc. [µg/m^3]	c-PAHs[a]		DNA adducts [adducts/10^8 nucleotides]				Oxidative DNA damage			
		ng/m^3	ng/mg PM	Adducts/m^3		Adducts/mg PM		8-oxodG/m^3		8-oxodG/mg PM	
				+S9	−S9	+S9	−S9	+S9	−S9	+S9	−S9
1–10	27.3	26.3	885	22.5	4.8	905	175	1.19	1.14	60.8	58.7
0.5–1	36.3	45.5	1278	28.7	7.9	993	233	1.16	1.38	61.2	80.8
0.17–0.5	15.6	20.6	1322	17.3	3.7	1218	260	1.22	1.16	182	177
<0.17	12.8	11.9	957	9.7	2.5	798	230	1.13	1.35	161	206

[a] Carcinogenic PAHs include benz[a]anthracene, chrysene, benzo[b]fluoranthene, benzo[k]fluoranthene, benzo[a]pyrene, dibenz[a,h]anthracene, and indeno[1,2,3-cd] pyrene.

competitive ELISA performed according to a modified protocol (Rossner et al., 2009). The assay was run in three independent experiments; mean 8-oxo-dG levels per 10^5 guanosine molecules and standard deviations were calculated and used for statistical analyses.

2.7. Dioxin activity - DR-CALUX assay

Rat hepatoma H4IIE.Gud.Luc1.1 cells (BDS, Amsterdam, The Netherlands), stably transfected with a luciferase reporter gene under the control of dioxin responsive elements (Sanderson et al., 1996), were used to detect AhR-mediated activity in the DR-CALUX® assay as described in Andrysík et al. (2011). The toxic equivalents related to TCDD were calculated as picograms TCDD/m^3 of air from dose–response curves. All calculations were performed with SlideWritePlus 3.0 for Windows and Microsoft Excel.

2.8. Statistical analysis

Pearson's correlation coefficient was used to analyze the correlation of DNA adduct levels, 8-oxo-dG levels and dioxin activity with PM mass, c-PAH and B[a]P in EOMs extracted from size segregated aerosol collected for 23 h daily for 26 days. The correlation between toxicity markers was analyzed using the same approach as all variables followed a normal distribution.

3. Results

3.1. Distribution of PM mass and c-PAHs among PM size-fractions

Daily PM_{10} concentrations in Ostrava-Radvanice during the sampling period were generally very high (Fig. 1) and may represent a significant health risk. The mean level of PM_{10} for the overall sampling period was more than 90 µg PM_{10}/m^3 (Table 1). Taking into account the daily PM_{10} limit of 50 µg/m^3, it should be noted that in 21 out of 26 days this limit was exceeded, in most cases by 2- to 4-fold. The mass distribution of PM among the size fractions differed substantially among the various sampling days. The upper accumulation fraction acquired the majority of aerosol mass in most of the sampling days (22 out of 26 days). In contrast, the ultrafine fraction (<0.17 µm) showed the lowest mass in 21 sampling days. Interestingly, the day with the highest PM concentration values, a significant increase in PM in ultrafine fraction was detected, which may transiently increase the contribution of the fraction to total PM toxicity (Fig. 1). Strong changes in meteorological conditions during the period February 15–20 (temperature increased by 20 °C, snow, wind) caused ~5-fold decrease in total PM_{10} levels and a more significant contribution by the coarse fraction (~50%).

Similar to PM mass distribution among size fractions, the distribution of the sum of 7 c-PAHs bound to PM varied between individual sampling days (Fig. 2A). The upper accumulation fraction was the major carrier of c-PAHs in most sampling days (23 out of 26 days), which was further supported by the fact that for the overall sampling period mean c-PAH levels in the upper accumulation fraction accounted for ~44% of total c-PAHs in PM_{10} (Table 1). Interestingly, the ultrafine fraction was responsible for only ~11% of c-PAHs.

While c-PAH levels per m^3 of sampled air in PM fractions reflect the relative distribution of the c-PAH mass, the ability of the PM fraction to bind c-PAHs should be compared in terms of c-PAHs per mg of PM (Fig. 2B, Table 1). This comparison indicated that differences among the fractions were relatively low suggesting comparable efficiency of individual fractions to bind c-

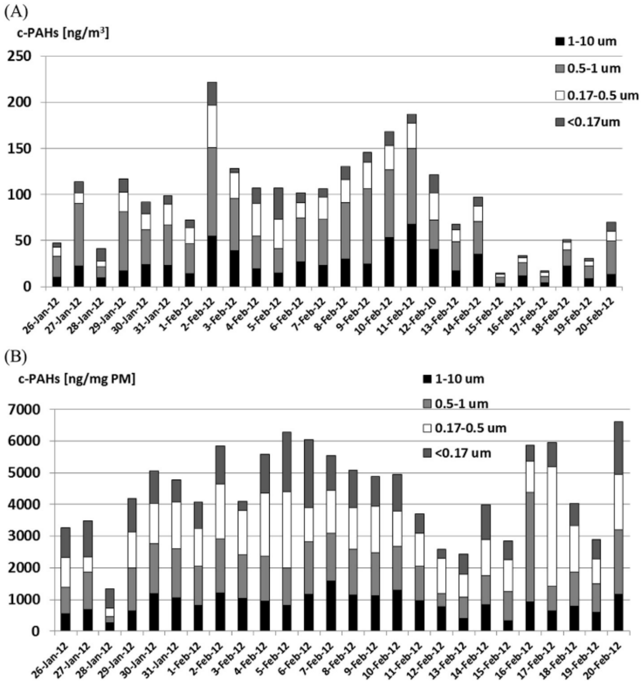

Fig. 2. Sum of concentrations of c-PAHs in four aerosol size fractions: per m^3 of sampled air (**A**) and per mg of the size fraction mass (**B**). c-PAHs include benz[a]anthracene, chrysene, benzo[b]fluoranthene, benzo[k]fluoranthene, benzo[a]pyrene, dibenz[a,h]anthracene, and indeno[1,2,3-cd]pyrene. The uncertainty of analysis was 30% of the measured value.

PAHs. Mean c-PAH levels per mg PM for the overall sampling period were lowest in the coarse fraction (885 ng/mg PM). The upper and lower accumulation fractions were both equally efficient c-PAH carriers (1278 and 1322 ng/mg PM), while the qUF fraction exhibited lower c-PAH levels by ~30% (957 ng/mg PM) (Table 1).

3.2. DNA adduct levels

DNA adduct analysis represents the method of choice to study genotoxicity induced by chemicals or by their mixtures. The method quantifies covalent binding of xenobiotics or their metabolites to DNA. DNA adducts may be removed by DNA repair machinery or may be fixed in DNA strand as mutations. These mutations (if they occur in the critical gene) are at the beginning of the multistep process of chemical carcinogenesis.

The autoradiographs obtained by ^{32}P-postlabeling analysis of CT DNA samples incubated for 24 h with 100 μg/ml of various EOMs from size-segregated aerosols, exhibited diagonal radioactive zones, representing the total DNA-adduct levels induced by the complex mixture of genotoxic EOM components (Fig. 3). The DNA adduct pattern for different sampling days was qualitatively very similar to that shown in Fig. 3. Since c-PAHs as well as other PAHs, heterocyclic aromatic compounds and PAH derivatives in EOMs require metabolic activation to exert their genotoxicity, we estimated the substantial contribution of c-PAHs in EOMs to the total genotoxicity from the much higher intensities of diagonal radioactive zones for samples incubated with the liver microsomal fraction (+S9) in comparison with samples without metabolic activation (−S9).

DNA adduct levels normalized per m^3 of air (Fig. 4) suggested a crucial contribution of the upper accumulation fraction to the total genotoxicity of the PM, irrespective of the presence/absence of metabolic activation by rat liver microsomal enzymes (+S9/−S9). The DNA adduct levels in samples with S9 metabolic activation were 3–5-fold higher than those without activation. As mentioned in the previous paragraph, these results indicate the substantial contribution of c-PAHs to PM genotoxicity. Coarse fraction contributed very significantly in the days, when the highest genotixic activity was found (January 29, February 2), especially after cotreatment with S9 mixture (Fig. 4A).

To reveal any association between the mass of size fractions of PM and their potential to induce genotoxicity, we expressed DNA adducts per mg of EOM for each individual fraction (Fig. 5A–B). The lower accumulation fraction (0.17–0.5 μm) was seen to be the most efficient in binding DNA-adduct-forming compounds in most sampling days. The qUF fraction exhibited significant, but lower genotoxicity. Generally, distribution of genotoxic activity among

(A) EOM from size-segregated aerosol (sampling date: January 29th, 2012)

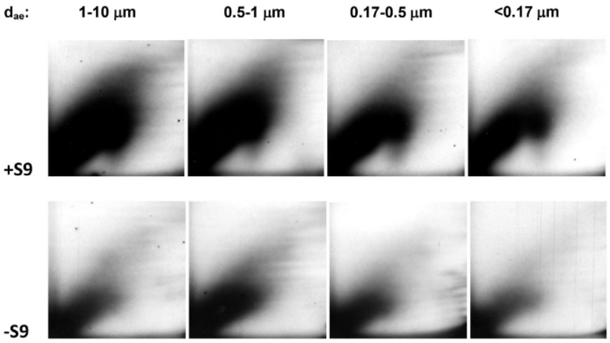

(B) Controls

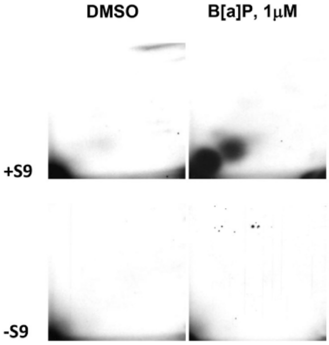

Fig. 3. Representative autoradiographs of TLC maps of ^{32}P-labeled DNA digests after incubation of calf-thymus DNA (±S9 fraction) with 100 µg/ml extractable organic matter (EOM) from size-segregated aerosols collected in Ostrava-Radvanice: January 29, 2012 (**A**); the control panels (**B**) depict analyses of calf-thymus DNA treated with B[a]P (1 µM) and DMSO (±S9). Screen-enhanced autoradiography was performed at −80 °C for 24 h.

the mass of size-segregated fractions was uniform at most of the sampling days.

3.3. Oxidative DNA damage

Similar to DNA adduct levels, we expressed 8-oxodG levels in CT DNA in two different ways. To model the effect of air pollution on humans as a result of breathing polluted air, we normalized 8-oxodG/10^5 dG per m^3 of air passed through filters (Fig. 6). To reveal any association between the mass of size fractions of PM and their potential to induce oxidative DNA damage, we expressed 8-oxodG/10^5 dG per µg of EOM for each individual fraction (Fig. 7).

In contrast to DNA adduct levels, the extent of oxidative DNA damage was distributed among all 4 PM size fractions, without apparent preference for specific PM fractions. No substantial differences were observed between samples with or without metabolic activation by the rat liver microsomal S9 fraction (Fig. 6). Interestingly, PM collected during the last sampling week, when the meteorological conditions substantially changed (temperature increased by 15–20 °C, snow) and the PM mass decreased several-fold (Fig. 1), the levels of 8-oxodG/mg EOM dramatically increased (Fig. 7). Oxidative damage was highest (3400 and 2900 8-oxodG/mg EOM with and without S9 metabolic activation, respectively) in the sample collected on February 17, the day the total PM mass was lowest (~20 µg/m^3). For all sampling days, the levels of 8-oxodG were independent of metabolic activation by the S9 fraction, indicating that oxidative damage was induced by other EOM components than PAHs.

3.4. Dioxin-like activity

The potency of individual compounds or complex mixtures to induce AhR-mediated reporter gene expression represents dioxin-like activity of complex environmental mixtures (Andrysík et al., 2011). The results of dioxin-like activity as detected by the DR-CALUX assay indicated high day-to-day variability as well as differences between individual size fractions (Fig. 8). Similar to the PM mass, PAH-content and DNA adduct levels, the highest toxic

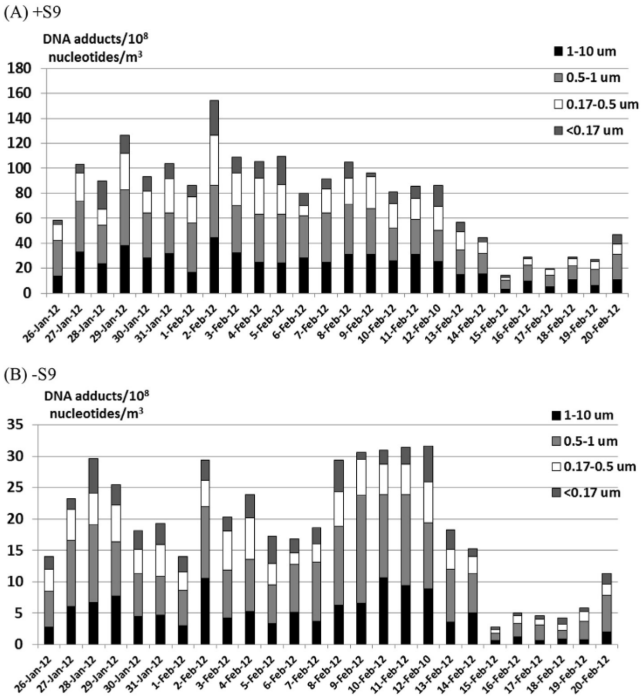

Fig. 4. Total DNA adduct levels induced by EOMs extracted from size segregated aerosol in an acellular system (calf thymus DNA) per m^3 of sampled air: with metabolic activation by the rat liver micromal S9-fraction (**A**); without metabolic activation by the S9-fraction (**B**). The values represent the means from two replicates varying by <±15%.

equivalency factor (TEQ) values were found in the upper accumulation fraction (~100–900 pg/m^3), while, with the exception of 2 sampling days (January 30 and February 20), the qUF PM fraction exhibited the lowest dioxin activity (~10–180 pg/m^3). AhR-mediated activity peaks (February 2 and February 10–12) showed significantly higher contribution of course fraction to the overall AhR-mediated activity. Extremely high TEQ values for sampling days January 27 and February 2 (Fig. 8) corresponded to high levels of c-PAHs in these days suggesting a key role of PAHs in the dioxin-like activity of PM organic extracts.

3.5. Correlation of selected toxicity markers with PM mass and c-PAHs

Relatively large data sets on day-to-day variability of the PM mass in 4 size fractions, c-PAH content, DNA adduct levels, oxidative DNA damage and dioxin-like activity enabled the analysis of the correlation between PM mass and its PAH content and toxicity markers as well as between individual toxicity markers with the aim of identifying the toxic endpoints closely related to c-PAH content (Table 2 A-D).

PM mass for all size fractions significantly correlated with B[a]P and c-PAH content. The correlation was strongest for the coarse aerosol fraction (R: 0.81 for B[a]P and 0.83 for c-PAHs; $p < 0.0001$), and weakest for the ultrafine PM fraction (R: 0.53 and 0.51; $p < 0.01$). A positive correlation was also found between PM mass and genotoxic potential (DNA adduct levels). Interestingly, EOMs metabolically activated by the microsomal S9 fraction exhibited a weaker correlation (R ranged between 0.49–0.71) than identical EOMs without S9 activation (R: 0.70–0.87). Similar positive correlations with the PM mass in all 4 fractions were observed for dioxin-like activity (R: 0.54–0.83), while DNA oxidative damage was generally unrelated to PM mass, despite S9 metabolic activation.

As expected, B[a]P and c-PAH levels were closely related (R: 0.993–0.998; $p < 0.0001$). The activation of c-PAHs, including B[a]P, by the S9 fraction to DNA reactive metabolites is likely the major reason for the stronger B[a]P correlation with DNA adduct levels (R: 0.59–0.81) than observed for PM mass. This correlation was even stronger for c-PAH content in EOMs vs. DNA adducts (R: 0.62–0.86). In contrast, in samples without metabolic activation other EOM components than PAHs (not requiring S9 metabolic activation) induced DNA adduct formation. The observed correlation of DNA adduct levels with B[a]P and other c-PAHs in EOMs is likely indirect, as maternal c-PAHs are known to be proportionally accompanied in EOMs by their derivatives not requiring S9 activation to elicit genotoxicity (nitro- and oxy-derivatives). Although dioxin-like activity of EOMs represents non-genotoxic effects and has been detected in different in vitro models, very similar correlations as for DNA adduct levels were observed for the dioxin activity of EOMs: a

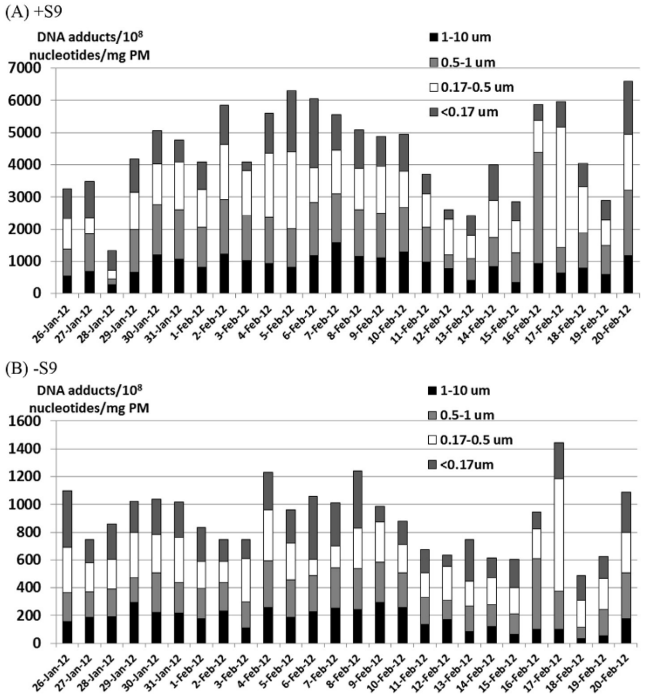

Fig. 5. Total DNA adduct levels induced by EOMs extracted from size-segregated aerosols in a cell-free system (CT DNA ± S9 fraction) per mg of sampled PM with metabolic activation by the rat liver micromal S9-fraction (**A**); without metabolic activation by the S9-fraction (**B**). The values represent the means from two replicates varying by <±15%.

close correlation with B[a]P content (R: 0.75–0.87) and slightly closer for c-PAHs (R: 0.76–0.89). This finding supported the hypothesis that PAHs are major contributors of AhR-mediated activity in airborne PM samples. The absence of any correlation of oxidative DNA damage with B[a]P and c-PAHs in S9-activated PAH metabolism together with a significant negative correlation of oxidative damage and PAH-content in samples without S9 activation (for accumulation fraction and ultrafine fraction) suggest the substantial role of S9-induced PAH metabolism in oxidative DNA damage.

In addition to the correlation of mass in 4 PM size fractions, B[a]P and c-PAH content vs. 3 analyzed toxicity markers, mutual correlations between DNA adducts, oxidative DNA damage and dioxin-like activities were studied. These correlations reflect the findings described in the previous paragraph: a positive correlation of DNA adducts and dioxin-like activity (R: 0.46–0.94 for S9 induced EOMs and R: 0.79–0.87 for EOMs without S9 metabolic activation). Interestingly, the closest correlation between genotoxic potential and dioxin-like activity was found for the S9-induced lower accumulation and qUF fractions (R: 0.93–0.94). Central role of the AhR-mediated activity, which is associated with both genotoxic and non-genotoxic effects of polyaromatic airborne contaminants (Andrysík et al., 2011), is apparent from Table 2A–D, summarizing correlations among chemical and biological parameters. In contrast to c-PAH-dependent genotoxicity and dioxin-like activity, oxidative DNA damage was either independent of the DNA adducts and dioxin-like activity (+S9-induced EOMs) or weaker, however, a significant negative correlation (-S9) was found (R: −0.40 to −0.49 for 8-oxodG vs. dioxin-like activity and R: −0.41 to −0.71 for 8-oxodG vs. DNA adducts).

4. Discussion

Distribution of polyaromatic compounds and their genotoxic and non-genotoxic toxic potencies in size-segregated airborne PM is currently subject of high interest. In contrast to our previous studies (Topinka et al., 2010, 2011) in which cumulative samples were analyzed, here we have shown the day-to-day distribution of mass and c-PAHs among four PM size fractions – coarse, lower- and upper-accumulation fractions and qUF particles collected during the smog period in industrial region of city of Ostrava, Czech Republic. Simultaneously, the temporal and PM size distribution of genotoxic potential, oxidative DNA damage and dioxin-like activity of organic extracts from size-segregated particles were analyzed.

High day-to-day variability of total PM_{10} mass (up to 10-fold difference between sampling days) and variability of mass in individual size fractions were observed. For example, the qUF fraction formed, depending on the sampling day, 12–31% of PM_{10}. Crucial effect of the meteorological conditions on this variability is clear from the comparison of PM10 levels within the inversion episode characterized by low temperature and low wind speed was

(A) +S9

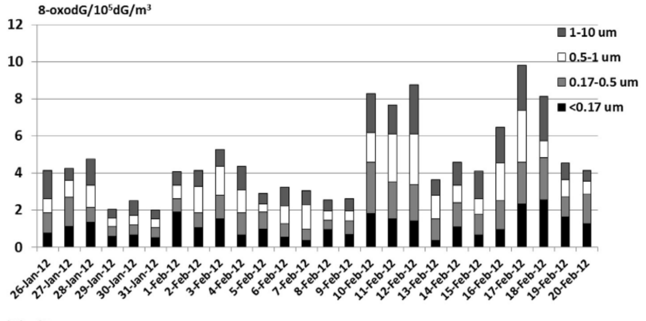

(B) -S9

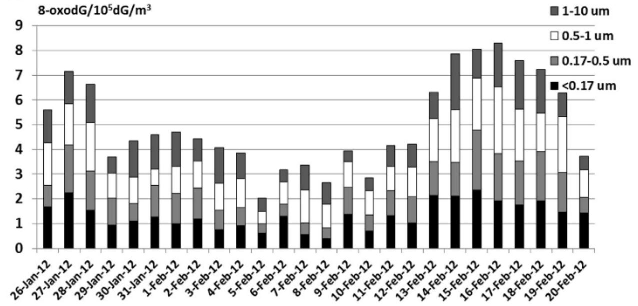

Fig. 6. Oxidative DNA damage detected as 8-oxodeoxyguanosine (8-oxodG) levels induced by EOMs extracted from size segregated aerosol in an acellular system (calf thymus DNA) per m^3 of sampled air: with metabolic activation by the rat liver micromal S9-fraction (**A**); without metabolic activation by the S9-fraction (**B**). The values represent the means from two replicates varying by <±15%.

prevailing (day 1–20) and the last week of sampling (day 21–26). The temperature increased during one day by 20° and high wind speed and snowing occurred. The most abundant qUF fraction was in the middle of an inversion episode, while in the middle of the last sampling week, the lowest levels of the qUF PM fraction were observed. Together with the analyses reported here, source apportionment of the size resolved PM was performed at the same sampling site and during the same sampling period (Pokorná et al., 2015). During the smog period, coal combustion and road dust contributed most to the overall aerosol mass, while during the last sampling week (post-smog period), the cold and hot phases of sinter production from the nearby metallurgy complex were found to contribute about 50% to the overall PM mass. These findings indicated that the different contributions of major PM sources, depending on meteorological conditions, were likely responsible for different relative abundance of PM size fractions.

Although the day-to-day variability of 7 c-PAHs in the qUF fraction was similar to that of the qUF fraction mass (~11–32%) and the highest levels of c-PAHs were observed during the inversion episode, the detailed distribution of PM mass and c-PAH levels was different, thus explaining their relatively low correlation. This finding confirmed previous findings that PM_{10} or $PM_{2.5}$ monitoring itself is not informative enough on toxic compounds bound to particles (Líbalová et al., 2012).

We found that c-PAH content per mg of PM varied from 0.2 to 0.6% of the total PM mass and on most sampling days the accumulation fraction was the major carrier of PM genotoxicity (Fig. 4) and dioxin-like activity (Fig. 8). On the other hand, differences of PAH concentrations per mg PM among size fractions were quite low, suggesting comparable efficiency of individual fractions to bind c-PAHs (Fig. 2B). With exception of several days, distribution of genotoxic activity of size-segregated fractions (expressed per mg PM) was also uniform (Fig. 5). However, the qUF fraction also plays a significant role as it bounds ~5–44% of total c-PAHs. Our recent data on transmission electron microscopy (TEM) of PM collected using a cascade impactor on PUFs and separated by extraction and ultrasonication suggested that the coarse fraction and accumulation fraction were mostly composed of agglomerates of ultrafine particles (manuscript under preparation). The particle agglomerates were decomposed during the separation from PUFs to ultrafine particles of uniform size in all PM fractions.

The overall evaluation of mutual correlations between the basic characteristics for PM size fractions (mass, c-PAH and B[a]P content) and toxicity markers (stable DNA adducts, oxidative DNA damage and dioxin-like activity) and between toxicity markers themselves allow us to draw some more general conclusions. Firstly, PM mass (frequently used for air pollution monitoring), does not sufficiently mimic the levels of B[a]P and c-PAHs, expected as major genotoxic PM components. The PM mass correlated well with levels of DNA adducts formed without S9 metabolic activation

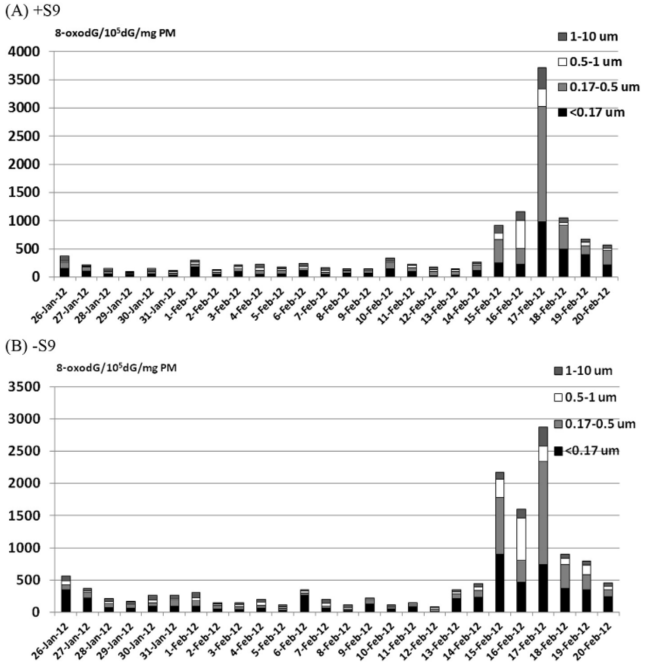

Fig. 7. Oxidative DNA damage as 8-oxodeoxyguanosine (8-oxodG) levels induced by EOMs extracted from size-segregated aerosols in a cell-free system (CT DNA ± S9 fraction) per mg of sampled PM with metabolic activation by the rat liver micromal S9-fraction (**A**); without metabolic activation by the S9-fraction (**B**). The values represent the means from two replicates varying by <±15%.

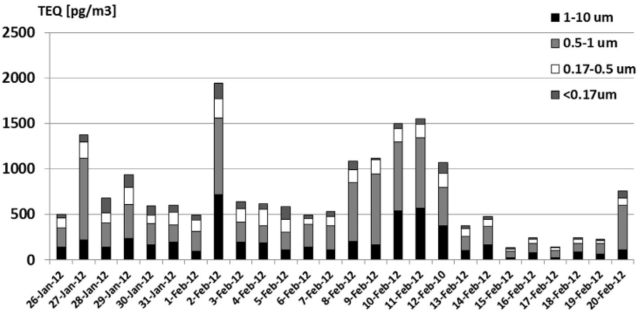

Fig. 8. Aryl hydrocarbon receptor-mediated activity induced by EOMs extracted from size-segregated aerosols collected daily for 26 consecutive days and expressed as TEQ [pg/m^3].

and only to less extent with concentrations of c-PAHs. The c-PAH concentrations were highly significantly associated with B[a]P concentrations and also with dioxin-like activities. Even c-PAHs do not sufficiently explain the day-to-day variability of DNA adduct levels. This suggests that many EOM components, other than c-PAH, induced DNA adducts, particularly without S9 metabolic activation, but also with S9 activation (required for c-PAH metabolic activation). The dioxin-like activity of EOMs, which is among other non-genotoxic effects connected with AhR-dependent induction of c-PAH metabolizing enzymes (Andrysík et al., 2011), exhibited an even higher positive correlation with the AhR agonists, B[a]P and c-PAHs, than DNA adduct levels. Thus, it is not surprising that DNA

Table 2

Pearson's correlation coefficients of PM mass, B[a]P and c-PAHs* content in EOMs extracted from various PM size (**d_{ae}**) fractions with dioxin-like activity (TEQ), genotoxicity (DNA adduct levels), oxidative DNA damage (8-oxodG levels).

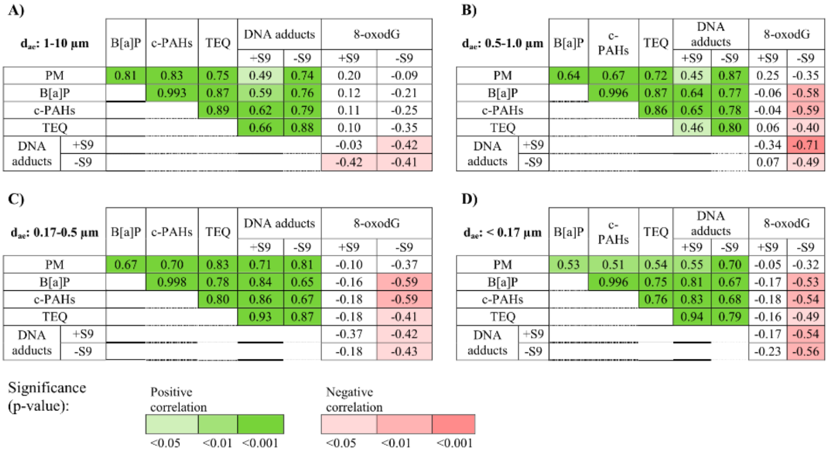

A)

d_{ae}: 1-10 µm		B[a]P	c-PAHs	TEQ	DNA adducts		8-oxodG	
					+S9	-S9	+S9	-S9
PM		0.81	0.83	0.75	0.49	0.74	0.20	-0.09
B[a]P			0.993	0.87	0.59	0.76	0.12	-0.21
c-PAHs				0.89	0.62	0.79	0.11	-0.25
TEQ					0.66	0.88	0.10	-0.35
DNA adducts	+S9						-0.03	-0.42
	-S9						-0.42	-0.41

B)

d_{ae}: 0.5-1.0 µm		B[a]P	c-PAHs	TEQ	DNA adducts		8-oxodG	
					+S9	-S9	+S9	-S9
PM		0.64	0.67	0.72	0.45	0.87	0.25	-0.35
B[a]P			0.996	0.87	0.64	0.77	-0.06	-0.58
c-PAHs				0.86	0.65	0.78	-0.04	-0.59
TEQ					0.46	0.80	0.06	-0.40
DNA adducts	+S9						-0.34	-0.71
	-S9						0.07	-0.49

C)

d_{ae}: 0.17-0.5 µm		B[a]P	c-PAHs	TEQ	DNA adducts		8-oxodG	
					+S9	-S9	+S9	-S9
PM		0.67	0.70	0.83	0.71	0.81	-0.10	-0.37
B[a]P			0.998	0.78	0.84	0.65	-0.16	-0.59
c-PAHs				0.80	0.86	0.67	-0.18	-0.59
TEQ					0.93	0.87	-0.18	-0.41
DNA adducts	+S9						-0.37	-0.42
	-S9						-0.18	-0.43

D)

d_{ae}: < 0.17 µm		B[a]P	c-PAHs	TEQ	DNA adducts		8-oxodG	
					+S9	-S9	+S9	-S9
PM		0.53	0.51	0.54	0.55	0.70	-0.05	-0.32
B[a]P			0.996	0.75	0.81	0.67	-0.17	-0.53
c-PAHs				0.76	0.83	0.68	-0.18	-0.54
TEQ					0.94	0.79	-0.16	-0.49
DNA adducts	+S9						-0.17	-0.54
	-S9						-0.23	-0.56

Significance (p-value):

Positive correlation			Negative correlation		
<0.05	<0.01	<0.001	<0.05	<0.01	<0.001

*) Carcinogenic PAHs include benz[a]anthracene, chrysene, benzo[b]fluoranthene, benzo[k]fluoranthene, benzo[a]pyrene, dibenz[a,h]anthracene, and indeno[1,2,3- cd]pyrene.

adduct levels correlated with the dioxin-like activity of EOMs. The correlation was much stronger for PM fractions <0.5 µm (S9 activated EOMs). Generally, the dioxin-like activity was strongly associated with PM mass, BaP and c-PAH concentrations and with levels of DNA adducts with/without S9 metabolic activation.

Although we did not find any correlation between PM mass and 8-oxodG levels for EOMs with/without S9 metabolic activation, a weak, but significant negative correlation was observed between B[a]P and c-PAHs content vs. 8-oxodG for EOM samples extracted from 3 submicron PM size fractions (accumulation and qUF fractions). This surprising finding can not be explained by the direct, antioxidant effect of c-PAHs. In contrast, c-PAHs have been shown to have the potential to induce oxidative stress, but for this activity they must be metabolized by aldo-keto reductases to *o*-quinones (Burczynski et al., 1998). Thus, it seems likely that other compound(s) with antioxidant properties are responsible for the negative correlation we observed. Our recent study on EOMs from the identical sampling site provides a detailed chemical analysis of EOMs from PM_{10} (Líbalová et al., 2014). The study demonstrated the presence of thousands of EOM components including PAHs, alkylated PAHs, oxidized PAHs, N- and S-heterocyclic PAHs, nitrated and dinitrated PAHs, phytosterols and many other contaminants bound to PM. The concentrations of these EOM components were mostly proportional to the 7 priority c-PAHs analyzed in this study. Some of those components may affect the redox potential of EOMs resulting in decreased levels of 8-oxodG seemingly related to c-PAH content. We hypothesize that phytosterols may be compounds with such activity. Indeed, it has been reported that these compounds have antioxidant effects and are potent free radical scavengers (Paniagua-Perez et al., 2008; Yokota et al., 2006; Yoshida and Niki, 2003). Based on these facts it is possible that the negative correlation between B[a]P and c-PAHs content vs. 8-oxodG levels in CT DNA is caused by the presence of phytosterols and/or other PM constituents that act as free radical scavengers and thus decrease oxidative DNA damage.

However, it should be noted that this effect is specific for samples without S9 activation, as S9 metabolic activation leads to a slight increase in oxidative damage and absence of the negative correlation with B[a]P and c-PAHs. It seems likely that the presence of metabolic enzymes in the S9 fraction partly caused an increased formation of *o*-quinones as mentioned above (Burczynski et al., 1998). We previously analyzed the effect of EOMs from size-segregated aerosol particles on oxidative damage to CT DNA and observed a significant positive correlation between concentrations of c-PAHs and 8-oxodG/10^5 dG levels in the presence of S9 metabolic activation (Rossner et al., 2010).

5. Conclusions

It can be concluded that high day-to-day variability of PM mass, B[a]P and c-PAH content, genotoxicity, oxidative DNA damage and dioxin-like activity and their relative distribution among size fractions of PM mainly depended on meteorological conditions. Based on data calculated per m^3 of sampled air, upper accumulation fraction was the major carrier of PM mass, c-PAHs, genotoxicity and dioxin-like activity. Daily levels of DNA adducts and dioxin-like activities were mostly related to c-PAH content and to some extent suggest a major role of upper accumulation PM fraction. In contrast, oxidative DNA damage by EOMs is not clearly PM size dependent, although it exhibited high day-to-day variability, and its weak negative correlation with c-PAHs suggests the possible antioxidant role of some other EOM components.

Acknowledgements

The study was supported by the Czech Science Foundation (CZ: P503/12/G147).

References

Andrysík, Z., Vondráček, J., Marvanová, S., Ciganek, M., Neča, J., Pěnčíková, K., Mahadevan, B., Topinka, J., Baird, W.M., Kozubík, A., Machala, M., 2011. Activation of the aryl h ydrocarbon receptor is the major toxic mode of action of an organic extract of a reference urban dust particulate matter mixture: the role of polycyclic aromatic hydrocarbons. Mutat. Res. 714, 53–62.

Binkova, B., Topinka, J., Sram, R.J., Sevastyanova, O., Novakova, Z., Schmuczerova, J., Kalina, I., Popov, T., Farmer, P.B., 2007. In vitro genotoxicity of PAH mixtures and organic extract from urban air particles. Part I: acellular assay. Mutat. Res. 620, 114–122.

Burczynski, M.E., Harvey, R.G., Penning, T.M., 1998. Expression and characterization of four recombinant human dihydrodiol dehydrogenase isoforms: oxidation of trans-7, 8-dihydroxy-7,8-dihydrobenzo[a]pyrene to the activated o-quinone metabolite benzo[a]pyrene-7,8-dione. Biochemistry 37, 6781–6790.

Fisher, T.T., Lawa, R.J., Rumneya, H.S., Kirbya, M.F., Kelly, C., 2011. Towards a scheme of toxic equivalency factors (TEFs) for the acute toxicity of PAHs in sediment. Ecotoxicol. Environ. Saf. 74, 2245–2251.

Gupta, R.C., 1985. Enhanced sensitivity of ^{32}P-postlabeling analysis of aromatic carcinogen: PM DNA adducts. Cancer Res. 45, 5656–5662.

Halek, F., Nabi, G., Kavousi, A., 2008. Polycyclic aromatic hydrocarbons study and toxic equivalency factor (TEFs) in Tehran. Iran. Environ. Monit. Assess. 143, 303–311.

Hanzalova, K., Rossner Jr., P., Sram, R.J., 2010. Oxidative damage induced by carcinogenic polycyclic aromatic hydrocarbons and organic extracts from urban air particulate matter. Mutat. Res. 696, 114–121.

Heyder, J., Gebhart, J., Rudolf, G., Schiller, C.F., Stahlhofen, W., 1986. Deposition of particles in the human respiratory tract in the size range 0.005–15 μm. J. Aerosol. Sci. 17, 811–825.

IARC, October 2013. Outdoor Air Pollution a Leading Environmental Cause of Cancer Deaths, Press Release No.221, IARC Lyon, France, vol. 17.

Leung, P.Y., Wan, H.T., Billah, M.B., Cao, J.J., Ho, K.F., Wong, C.K.C., 2014. Chemical and biological characterization of air particulate matter $_{10}$, collected from five cities in China. Environ. Pollut. 194, 188–195.

Líbalová, H., Uhlířová, K., Kléma, J., Machala, M., Šrám, R.J., Ciganek, M., Topinka, J., 2012. Global gene expression changes in human embryonic fibroblasts induced by organic extracts from respirable air particles. Part. Fibre Toxicol. 9, 1.

Líbalová, H., Krčková, S., Uhlířová, K., Kléma, J., Ciganek, M., Rössner Jr., P., Šrám, R.J., Vondráček, J., Machala, M., Topinka, J., 2014. Analysis of gene expression changes in A549 cells induced by organic compounds from respirable air particles. Mutat. Res. 770, 94–105.

Melendez-Colon, V.J., Luch, A., Seidel, A., Baird, W.M., 2000. Formation of stable DNA adducts and apurinic sites upon metabolic activation of bay and fjord region polycyclic aromatic hydrocarbons in human cell cultures. Chem. Res. Toxicol. 13, 10–17.

Paniagua-Perez, R., Madrigal-Bujaidar, E., Reyes-Cadena, S., Alvarez-Gonzalez, I., Sanchez-Chapul, L., Perez-Gallaga, J., Hernandez, N., Flores-Mondragon, G., Velasco, O., 2008. Cell protection induced by beta-sitosterol: inhibition of genotoxic damage, stimulation of lymphocyte production, and determination of its antioxidant capacity. Arch. Toxicol. 82, 615–622.

Park, J.H., Troxel, A.B., Harvey, R.G., Penning, T.M., 2006. Polycyclic aromatic hydrocarbon (PAH) o-quinones produced by the aldo-keto-reductases (AKRs) generate abasic sites, oxidized pyrimidines, and 8-oxo-dGuo via reactive oxygen species. Chem. Res. Toxicol. 19, 719–728.

Perrone, M.G., Gualtieri, M., Ferrero, L., Lo Porto, C., Udisti, R., Bolzacchini, E., Camatin, M., 2010. Seasonal variations in chemical composition and in vitro biological effects of fine PM from Milan. Chemosphere 78, 1368–1377.

Phillips, D.H., Castegnaro, M., 1999. Standardization and validation of DNA adduct postlabelling methods: report of interlaboratory trials and production of recommended protocols. Mutagenesis 14, 301–315.

Pokorná, P., Hovorka, J., Klán, M., Hopke, P.K., 2015. Source apportionment of size resolved particulate matter at a European air pollution hot spot. Sci. Total Environ. 502, 172–183.

Reddy, M.V., Randerath, K., 1986. Nuclease P1-mediated enhancement of sensitivity of 32P-postlabeling test for structurally diverse DNA adducts. Carcinogenesis 7, 1543–1551.

Rossner Jr., P., Milcova, A., Libalova, H., Novakova, Z., Topinka, J., Balascak, I., Sram, R.J., 2009. Biomarkers of exposure to environmental pollutants in mothers and their transplacental transfer to the foetus. Part II: oxidative damage. Mutat. Res. 669, 20–26.

Rossner Jr., P., Topinka, J., Hovorka, J., Milcova, A., Schmuczerova, J., Krouzek, J., Sram, R.J., 2010. An acellular assay to assess the genotoxicity of complex mixtures of organic pollutants bound on size segregated aerosol. Part II: oxidative damage to DNA. Toxicol. Lett. 198, 312–316.

Sanderson, J.T., Aarts, J.M., Brouwer, A., Froese, K.L., Denison, M.S., Giesy, J.P., 1996. Comparison of Ah receptor-mediated luciferase and ethoxyresorufin-Odeethylase induction in H4IIE cells: implications for their use as bioanalytical tools for the detection of polyhalogenated aromatic hydrocarbons. Toxicol. Appl. Pharmacol. 137, 316–325.

Topinka, J., Hovorka, J., Milcova, A., Schmuczerova, J., Krouzek, J., Rossner Jr., P., Sram, R.J., 2010. An acellular assay to assess the genotoxicity of complex mixtures of organic pollutants bound on size segregated aerosol. Part I: DNA adducts. Toxicol. Lett. 198, 304–311.

Topinka, J., Rossner Jr., P., Milcova, A., Schmuczerova, J., Svecova, V., Sram, R.J., 2011. DNA adducts and oxidative damage induced by organic extracts from PM$_{10}$ in an acellular assay. Toxicol. Lett. 202, 186–192.

Yokota, J., Takuma, D., Hamada, A., Onogawa, M., Yoshioka, S., Kusunose, M., Miyamura, M., Kyotani, S., Nishioka, Y., 2006. Scavenging of reactive oxygen species by *Eriobotrya japonica* seed extract. Biol. Pharm. Bull. 29, 467–471.

Yoshida, Y., Niki, E., 2003. Antioxidant effects of phytosterol and its components. J. Nutr. Sci. Vitaminol. (Tokyo) 49, 277–280.

6.6. APPENDIX F: Manuscript 6

Offer, S.; Hartner, E.; Di Bucchianico, S.; Bisig, C.; Bauer, S.; Pantzke, J.; Zimmermann, E. J.; Cao, X.; Binder, S.; Kuhn, E.; Huber, A.; Jeong, S.; Käfer, U.; Martens, P.; Mesceriakovas, A.; **Bendl, J.**; Brejcha, R.; Buchholz, A.; Gat, D.; Hohaus, T.; Rastak, N.; Jakobi, G.; Kalberer, M.; Kanashova, T.; Hu, Y.; Ogris, C.; Marsico, A.; Theis, F.; Pardo, M.; Gröger, T.; Oeder, S.; Orasche, J.; Paul, A.; Ziehm, T.; Zhang, Z.-H.; Adam, T.; Sippula, O.; Sklorz, M.; Schnelle-Kreis, J.; Czech, H.; Kiendler-Scharr, A.; Rudich, Y.; Zimmermann, R. Effect of Atmospheric Aging on Soot Particle Toxicity in Lung Cell Models at the Air-Liquid Interface: Differential Toxicological Impacts of Biogenic and Anthropogenic Secondary Organic Aerosols (SOAs). *Environmental Health Perspectives* **2022,** *130* (2), 27003; DOI 10.1289/EHP9413.

Effect of Atmospheric Aging on Soot Particle Toxicity in Lung Cell Models at the Air–Liquid Interface: Differential Toxicological Impacts of Biogenic and Anthropogenic Secondary Organic Aerosols (SOAs)

Svenja Offer,[1,2] Elena Hartner,[1,2] Sebastiano Di Bucchianico,[1] Christoph Bisig,[1] Stefanie Bauer,[1] Jana Pantzke,[1,2] Elias J. Zimmermann,[1,2] Xin Cao,[1,2] Stefanie Binder,[1,2] Evelyn Kuhn,[1] Anja Huber,[1] Seongho Jeong,[1,2] Uwe Käfer,[1,2] Patrick Martens,[2] Arunas Mesceriakovas,[3] Jan Bendl,[1,4,5] Ramona Brejcha,[1] Angela Buchholz,[6] Daniella Gat,[7] Thorsten Hohaus,[8] Narges Rastak,[1] Gert Jakobi,[1] Markus Kalberer,[9] Tamara Kanashova,[10] Yue Hu,[11] Christoph Ogris,[11] Annalisa Marsico,[11] Fabian Theis,[11] Michal Pardo,[7] Thomas Gröger,[1] Sebastian Oeder,[1] Jürgen Orasche,[1] Andreas Paul,[8] Till Ziehm,[8] Zhi-Hui Zhang,[9] Thomas Adam,[1,4] Olli Sippula,[3] Martin Sklorz,[1] Jürgen Schnelle-Kreis,[1] Hendryk Czech,[1,2] Astrid Kiendler-Scharr,[8] Yinon Rudich,[7] and Ralf Zimmermann[1,2]

[1]Joint Mass Spectrometry Center (JMSC) at Comprehensive Molecular Analytics, Helmholtz Zentrum München, Neuherberg, Germany
[2]JMSC at Analytical Chemistry, Institute of Chemistry, University of Rostock, Rostock, Germany
[3]Department of Environmental and Biological Sciences, University of Eastern Finland, Kuopio, Finland
[4]Institute for Chemistry and Environmental Engineering, University of the Bundeswehr Munich, Neubiberg, Germany
[5]Institute for Environmental Studies, Faculty of Science, Charles University, Prague, Czech Republic
[6]Department of Applied Physics, University of Eastern Finland, Kuopio, Finland
[7]Department of Earth and Planetary Sciences, Faculty of Chemistry, Weizmann Institute of Science, Rehovot, Israel
[8]Institute of Energy and Climate Research, Troposphere, Forschungszentrum Jülich GmbH, Jülich, Germany
[9]Department of Environmental Sciences, University of Basel, Basel, Switzerland
[10]Max-Delbrück-Centrum für Molekulare Medizin, Berlin, Germany
[11]Institute of Computational Biology, Helmholtz Zentrum München, Neuherberg, Germany

BACKGROUND: Secondary organic aerosols (SOAs) formed from anthropogenic or biogenic gaseous precursors in the atmosphere substantially contribute to the ambient fine particulate matter [PM ≤ 2.5 μm in aerodynamic diameter (PM$_{2.5}$)] burden, which has been associated with adverse human health effects. However, there is only limited evidence on their differential toxicological impact.

OBJECTIVES: We aimed to discriminate toxicological effects of aerosols generated by atmospheric aging on combustion soot particles (SPs) of gaseous biogenic (β-pinene) or anthropogenic (naphthalene) precursors in two different lung cell models exposed at the air–liquid interface (ALI).

METHODS: Mono- or cocultures of lung epithelial cells (A549) and endothelial cells (EA.hy926) were exposed at the ALI for 4 h to different aerosol concentrations of a photochemically aged mixture of primary combustion SP and β-pinene (SOA$_{\beta PIN}$-SP) or naphthalene (SOA$_{NAP}$-SP). The internally mixed soot/SOA particles were comprehensively characterized in terms of their physical and chemical properties. We conducted toxicity tests to determine cytotoxicity, intracellular oxidative stress, primary and secondary genotoxicity, as well as inflammatory and angiogenic effects.

RESULTS: We observed considerable toxicity-related outcomes in cells treated with either SOA type. Greater adverse effects were measured for SOA$_{NAP}$-SP compared with SOA$_{\beta PIN}$-SP in both cell models, whereas the nano-sized soot cores alone showed only minor effects. At the functional level, we found that SOA$_{NAP}$-SP augmented the secretion of malondialdehyde and interleukin-8 and may have induced the activation of endothelial cells in the coculture system. This activation was confirmed by comet assay, suggesting secondary genotoxicity and greater angiogenic potential. Chemical characterization of PM revealed distinct qualitative differences in the composition of the two secondary aerosol types.

DISCUSSION: In this study using A549 and EA.hy926 cells exposed at ALI, SOA compounds had greater toxicity than primary SPs. Photochemical aging of naphthalene was associated with the formation of more oxidized, more aromatic SOAs with a higher oxidative potential and toxicity compared with β-pinene. Thus, we conclude that the influence of atmospheric chemistry on the chemical PM composition plays a crucial role for the adverse health outcome of emissions. https://doi.org/10.1289/EHP9413

Introduction

Over the past decades, the impact of ambient fine particulate matter [PM ≤ 2.5 μm (PM$_{2.5}$)] on the global burden of disease has gained substantial attention. Epidemiological cohort studies have found significant correlations between the exposure to PM$_{2.5}$ and substantial effects on human health, such as respiratory and cardiovascular diseases, and increased morbidity and mortality (Brook et al. 2010; Cohen et al. 2017; Pope et al. 2020). It is well accepted that the toxicity of PM$_{2.5}$ varies between its sources and formation pathways. However, it is still largely unknown which PM properties—such as size, mass, shape, surface properties, or chemical composition—induce biological responses (Burkholder et al. 2017; Park et al. 2018; Wyzga and Rohr 2015). Furthermore, our knowledge is mostly limited to the effects of collected airborne particles under submerged exposure conditions rather than the direct deposition and interaction of aerosols with cell cultures (Ihantola et al. 2020; Oeder et al. 2015). Submerged exposures do not reflect the physiological condition of airway barriers because inhalation occurs by aerosol deposition onto airway epithelial cells that form, together with, for example, endothelial cells and basal membranes, a tissue layer enabling gas exchanges between the lungs and the blood circulation (Barosova et al. 2021). Air–liquid interface (ALI) aerosol exposures offer several advantages compared with submerged conditions. These include the preservation of the physicochemical characteristics of airborne PM and a higher sensitivity both in terms of effective doses, which are lower at the ALI, and in terms of transcripts regulation and protein enrichment, which are more pronounced in alveolar epithelial A549 cells

---

Address correspondence to Sebastiano Di Bucchianico, Joint Mass Spectrometry Center at Comprehensive Molecular Analytics, Helmholtz Zentrum München, Ingolstädter Landstr. 1, D-85764 Neuherberg, Germany. Email: dibucchianico@helmholtz-muenchen.de

Supplemental Material is available online (https://doi.org/10.1289/EHP9413).

All authors declare they have no actual or potential competing financial interests.

Received 31 March 2021; Revised 17 December 2021; Accepted 22 December 2021; Published 3 February 2022.

exposed at ALI compared with submerged exposures (Hilton et al. 2019; Lenz et al. 2013; Loret et al. 2016). It has been shown that ALI-cultured A549 cells retain more of the usual patterns of tight junction proteins, such as occluding, claudin-2, and zonula occludens-3, as well as show lower permeation coefficient values than the submerged cells, resulting in a clear and tighter epithelial phenotype (Rothen-Rutishauser et al. 2008).

Atmospheric aerosol particles may originate from primary sources (primary aerosols), but they are also formed and altered by oxidative gas-to-particle conversion in the atmosphere (secondary aerosols) as well as complex multiphase chemistry (aged primary aerosols) (Hallquist et al. 2009). The sources contributing to the global primary aerosol load are manifold and from both anthropogenic and natural origin, including industrial processes, traffic, sea spray, and wildfire burnings. Soot, or its related entities black carbon (BC) and elemental carbon (EC), is released from both anthropogenic (e.g., traffic, residential heating, industry) and naturally occurring (e.g., wildfire) combustion processes (Bond et al. 2013). In contrast to BC and EC, the term soot particles (SPs) is less specific and does not refer to carbon atoms only. Instead, it is described as black particles that can enter the atmosphere through combustion processes (Andreae and Gelencsér 2006), so it also includes organic and inorganic PM. SP has impacts on human health upon inhalation (Janssen et al. 2011); however, freshly emitted SP become very quickly coated by secondary aerosols in ambient air (Moore et al. 2014). Secondary aerosols are generated from volatile precursors by atmospheric oxidants, such as hydroxyl (OH), ozone (O_3), and nitrate radicals, or by photolysis in the atmosphere (Hallquist et al. 2009; Shakya and Griffin 2010). Secondary organic aerosols (SOAs) from the oxidative conversion of volatile organic compounds (VOCs) may increase levels of ambient $PM_{2.5}$ considerably, causing severe haze pollution episodes (Huang et al. 2014). Naphthalene and β-pinene were found to be substantial contributors to the anthropogenic (Jia and Batterman 2010) and biogenic (Guenther et al. 2012) global VOC emissions, respectively, with significant potential to form SOAs (Chen et al. 2016; Watne et al. 2017).

Naphthalene represents the smallest and most volatile polycyclic aromatic hydrocarbon (PAH) and is classified by the International Agency for Research on Cancer as probably carcinogenic to humans (Group 2B) (IARC 2010). It is mainly formed during combustion processes, such as fossil fuel combustion in engines, in particular diesel engines, biomass burning, or tobacco smoking, as well as in the chemical and metal industries (Jia and Batterman 2010; Qian et al. 2021; Wang et al. 2020). Because of its high vapor pressure, naphthalene is mainly in the gas phase at ambient conditions and thus undergoes homogeneous gas-phase reactions in the atmosphere, which can result in products of lower volatility accompanied with their conversion into the particle phase and the generation of SOAs (Williams et al. 2010). β-pinene is a monoterpene, one of the main compounds released by vegetation, such as by various coniferous plants (Faiola et al. 2015; Kleist et al. 2012). Its oxidation leads to substantial yields of SOAs (Sarrafzadeh et al. 2016; Xavier et al. 2019), including the formation of highly oxidized extremely low-VOCs (Ehn et al. 2014). On a global scale, biogenic VOCs largely exceed the emissions of anthropogenic VOCs; however, anthropogenic VOCs may regionally reach higher levels than biogenic VOCs (Guenther et al. 1995). In the case of biogenic VOCs (isoprene, terpenes) toxicity is generally enhanced by photochemical aging; however, there is an unambiguous effect of aging for PAHs and engine emissions (Weitekamp et al. 2020; Xu et al. 2022).

Depending on the size of the PM, their retention in the lung varies. Although inhaled particles between 5 and 10 μm in aerodynamic diameter typically affect only the upper airways and are removed by mucociliar clearance, particles in the range between 1 and 2.5 μm are able to penetrate deep into the respiratory regions and particles <1 μm can easily deposit on alveoli and be retained in the surfactant (Heyder 2004). Moreover, an *in vivo* study showed that not only can ultrafine PM [$PM \leq 0.1$ μm ($PM_{0.1}$)] enter extrapulmonary organs, but particles with an aerodynamic diameter of between 0.2 and 2 μm can also (Li et al. 2019). In addition to the direct harm of particles to the organs, several *in vitro* studies in human lung epithelial cells have shown that the $PM_{2.5}$ of SOA can trigger inflammation with systemic effects through the release of pro-inflammatory cytokines (Feng et al. 2016), an increase in reactive oxygen species (ROS) (Arashiro et al. 2018), and an impairment of the anti-oxidant system (Arashiro et al. 2018; Deng et al. 2013; Kouassi et al. 2010; Longhin et al. 2013). In response, oxidative stress further triggers inflammatory and mutagenic responses (Dergham et al. 2012; Lin et al. 2017; Longhin et al. 2013; Møller et al. 2014; Riediker et al. 2019). Beyond the size of ambient $PM_{2.5}$, its chemical composition is assumed to play an important role in the toxicity of the particles (Eaves et al. 2020; Sýkorová et al. 2016). Oxidation flow reactor (OFR) studies have revealed a greater toxic effect of higher photochemically aged α-pinene- and naphthalene-derived SOAs on A549 cells compared with their SOAs of lower photochemical age, which was attributed to the increased formation of ROS (Chowdhury et al. 2018, 2019).

Within the project aeroHEALTH (https://www.aerohealth.eu), the present study aimed to investigate the toxicological impacts of two model systems representing air pollution by primary combustion emissions (e.g., SPs) and atmospheric processing of a typical anthropogenic (e.g., naphthalene) or biogenic (e.g., β-pinene) VOC precursor. In the used experimental setup, the SOAs were generated in an OFR in the presence of freshly formed combustion soot, leading to coating SPs with condensed organic matter from naphthalene (SOA_{NAP}-SP) and β-pinene ($SOA_{\beta PIN}$-SP), respectively. Two different cell culture systems were exposed to these aerosols at the ALI. Increasing epidemiological and experimental evidences show that environmental exposure may disturb airway intercellular communication by indirect mechanisms, such as the release of inflammatory cytokines, or by direct mechanisms, including particles translocating from the lung into the circulation (Peters et al. 2021; Wang et al. 2019). Especially in the alveolar region, PAHs contained in the gas phase or detached from the particle surface may be displaced across the airway barriers and reach cells and secondary tissues that are not directly exposed (Låg et al. 2020). In view of the important role of these mechanisms, A549 human alveolar epithelial cells were grown either as a monoculture on an insert membrane or as a coculture model with microvascular endothelial EA.hy926 cells on the basolateral side of the membrane to mimic the blood–air barrier and to evaluate cell-to-cell interplay. We performed assays testing for aerosol-induced oxidative stress, inflammation, geno- and cytotoxicity, as well as to elucidate possible secondary effects derived from cellular interplay, according to adverse outcome pathways (Halappanavar et al. 2020). With this setup, we aimed to address the overarching scientific question whether atmospheric aging and the related formation and condensation of SOAs on SPs can increase the toxicity of the particles and whether the SOA precursor plays a decisive role in the biological response.

Material and Methods

Aerosol Generation and Characterization

Aerosol generation and sampling setup. SOAs of either naphthalene (Sigma-Aldrich; 147141-25G; 99%) or β-pinene (Sigma-Aldrich; 402753-10G; ≥99 %) were produced by mixing their pure vapor with SPs and subsequent processing in an OFR [i.e., a potential aerosol mass (PAM) reactor] (Bruns et al. 2015; Kang et al. 2007) for the simulation of atmospheric photooxidation (aging) by OH radicals. In addition, pure SPs were also fed into the PAM reactor without aging and used as the reference control. This was done because SPs and SOA precursors refer to primary compounds, which are simultaneously transformed by atmospheric aging. However, SOA rapidly starts to cover the surface of the SPs, and the particle constitution may be described by a core–shell model. Only particulate organic species at or near the particle surface are exposed to OH radicals, whereas the soot core of the particle is shielded against heterogeneous oxidation (Lim et al. 2017). Considering the generally slower reaction kinetics of heterogeneous oxidation compared with the homogeneous oxidation involved in SOA formation, we may assume that soot cores are oxidized to a negligible extent. Therefore, fresh SPs, rather than aged SPs, without the addition of SOA precursors were used as the reference. A simplified scheme of the setup is shown in Figure 1.

First, SPs, functioning as a condensation sink for SOAs, were produced by a CAST-Burner (Combustion Aerosol Standard; model 5201C; Jing) under lean combustion conditions (50 mL/min propane, 0 mL/min $MixN_2$, 1.42 L/min Oxid.Air, and 20 L/min Dil. Air) to minimize the organic content and generate EC-rich particles with a Gaussian size distribution (geometric mean ~100 nm). A custom-made porous tube diluter with a variable mass flow-controlled dilution ratio was applied as a first dilution step. Naphthalene or β-pinene vapors were produced using a custom-made diffusion source, placed in a temperature-controlled water bath, using nitrogen (99.999% purity) with a flow rate of 1 L/min. The length and diameter of the diffusion source, as well as the bath temperature, were adjusted for each VOC individually to maintain the same precursor concentration. The bath temperatures for VOC generation were ~40°C for β-pinene and ~60°C for naphthalene. Diameters of the diffusion source were 10 mm for β-pinene (length 40 mm) and 25 mm for naphthalene (length ~5 mm), with an additional 25 mm of frit to prevent turbulent mixing and reduce diffusion. The targeted VOC concentration of $4\ mg/m^3$ was adjusted every day before the experiment and verified after the experiment by a flame ionization detector (model 109A; J.U.M. Engineering). The mixture of soot and VOC was humidified during a second dilution step using an ejector diluter (Palas VKL 10; Palas GmbH) with a fixed 1:10 dilution ratio. Here, humidified air (moistened by a PermaPure humidifier FC125-240; Perma Pure), mixed with 0.3 mL/min nitrogen, containing deuterated butanol (D9-butanol; 98% isotopic purity; Sigma Aldrich) was used as dilution medium. Final concentrations entering the PAM reactor were $1\ mg/m^3$ soot, $4\ mg/m^3$ VOC, and 80 ppbV D9-butanol at 40% relative humidity (RH).

The PAM reactor (Bruns et al. 2015; Kang et al. 2007) refers to an OFR with an internal volume of 15 L and was operated at a flow rate of 8 L/min, resulting in a mean residence time of 113 s. It generates O_3 *in situ* and, subsequently, OH radicals from irradiating humid air by two ultraviolet (UV)-lamps (BHK Inc.) with emission

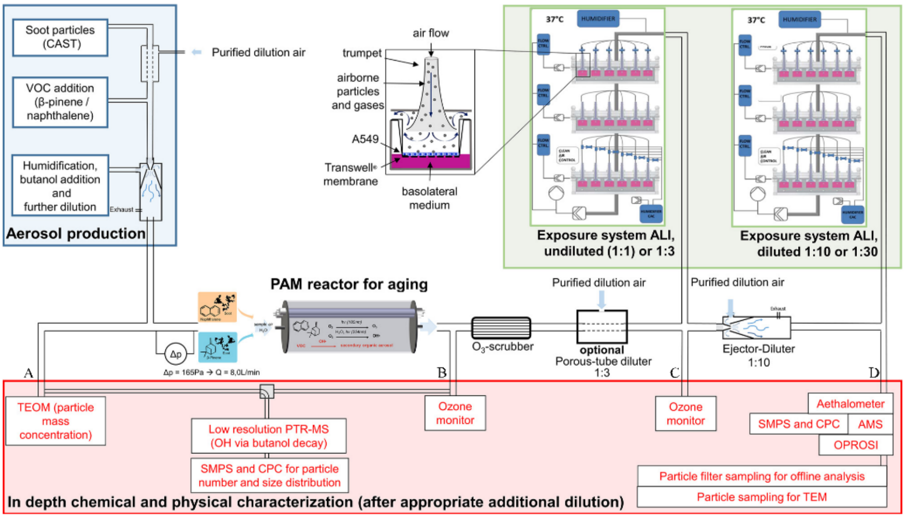

Figure 1. A schematic overview of the aerosol generation, sampling method, and ALI exposure system. SP (CAST soot; $1\ mg/m^3$) together with either β-pinene ($4\ mg/m^3$) or naphthalene ($4\ mg/m^3$) passed through a PAM reactor for photochemical aging by OH radicals after humidification and appropriate dilution. In addition, pure SP (CAST soot; $1\ mg/m^3$) were fed into the PAM reactor without aging and used as the reference control. O_3, which was produced *in situ* by the PAM reactor, was removed after the reactor by an O_3-scrubber to a level <10 ppb. State-of-the-art methods characterized the chemical and physical properties of the generated SOA [line A: TEOM; line A/B: PTR-MS, SMPS, CPC, O_3 monitor; line C: O_3 monitor; line D: Aethalometer, SMPS, AMS, OPROSI, offline sampling (VOC adsorber, TEM, GC × GC-TOFMS)]. Two ALI exposure systems were used in parallel. An optional 1:3 diluter in front of one ALI exposure system and a 1:10 diluter in front of the second ALI exposure system were applied to investigate different dilutions of the aerosol [undiluted (1:1), 1:3, 1:10, and 1:30]. The magnification of a single exposure position illustrates the air flow of the aerosol over the cells growing on the membrane of Transwell inserts and shows aerosol deposition by diffusion. Note: ALI, air-liquid interface; AMS, high-resolution time-of-flight aerosol mass spectrometer; CAST, combustion aerosol standard; CPC, condensation particle counter; Δp, change in pressure; GC × GC-TOFMS, comprehensive two-dimensional gas chromatography–time-of-flight mass spectrometer; OH, hydroxy; OPROSI, online particle-bound ROS (reactive oxygen species) instrument; ozone, O_3; PAM, potential aerosol mass; PTR-MS, quadrupole proton–transfer reaction mass spectrometer; SMPS, scanning mobility particle sizer; SOA, secondary organic aerosol; SP, soot particle; TEM, Transmission electron microscope; TEOM, tapered element oscillating microbalance; VOC, volatile organic compounds.

lines at 185 and 254 nm. We adjusted the UV lamp power to obtain similar photochemical ages (~ 3 d) of both types of SOAs, accounting for the different rate constants of naphthalene and β-pinene toward the OH radical (k_{OH} (naphthalene) $= 2.3 \times 10^{-11}$ s/cm^3; k_{OH} (β-pinene) $= 7.4 \times 10^{-11}$ s/cm^3 (Atkinson and Arey 2003). Although SOA-precursors and SP were exposed to O_3 concentrations of 6.0 ± 0.6 ppm (β-pinene) and 5.4 ± 0.3 ppm (naphthalene) for 113 s, the aging under the described conditions is strongly dominated by OH radical chemistry (Atkinson and Carter 1984; Sarrafzadeh et al. 2016). Fractional importance of non-OH fate, including photolysis at 185 and 254 nm, as well as reactions with $O(1^D)$, $O(3^P)$, and O_3, were found to be comparable to ambient air assessed by the PAM model of Peng et al. (2016). Furthermore, the surface oxidation of SP by O_3 is estimated to be negligible based on the kinetic data of Chughtai et al. (2003).

A ceramic honeycomb denuder, impregnated with sodium nitrite was installed downstream of the PAM reactor to remove O_3 to a level of <10 ppbV, and monitored by the O_3 monitor. In addition, a custom-made porous tube diluter (fixed at a 1:3 dilution) and an ejector diluter (1:10 dilution) (Palas) were installed in the sampling lines guided to the two ALI exposure systems to obtain the different dilution ratios [undiluted (1:1), 1:3, 1:10, and 1:30] for the cell exposures. All dilution steps were conducted with purified compressed laboratory air, compressed by an oil-free compressor (SF4; Atlas Copco) and purified by a modified catalytic converter (737-15; Aadco), which removed hydrocarbons, including methane, to a concentration of <10 ppbV.

Online aerosol measurements. Four sampling points were used for the online aerosol measurements (Figure 1). A detailed description of the respective methods are outlined in the below paragraphs.

Particle number and particle size distribution. A scanning mobility particle sizer (SMPS) comprised of an electrostatic classifier (TSI; model 3082) connected to a condensation particle counter (TSI; model 3750) was installed at line D. Multiple charge correction and diffusion loss correction were done using AIM software (version 10.3; TSI). A second electrostatic classifier (TSI; model 3082) connected to a 3025A CPC (TSI) was installed with the option to switch between line A or line B without additional dilution for monitoring the feed and aged aerosol properties.

BC and particle mass. A seven-wavelength aethalometer (model Magee AE33; Aerosol d.o.o.) was used at line D to confirm stable SP concentrations, measured as BC at 880 nm, whereas the difference of the PM concentration at 370 and 880 nm, denoted as brown carbon (BrC), confirmed the stable formation of SOA over the whole cell exposure time. In addition, a tapered element oscillating microbalance (TEOM 1400a; Rupprecht & Patashnick Co., Inc.) was used to determine the SP mass concentration at line A. Both instruments had own ejector diluters (1:10 dilution) (Palas), ensuring the appropriate concentrations.

Photochemical age. D9-butanol was used as a photochemical clock and was measured before and after the PAM reactor step by a quadrupole proton–transfer reaction mass spectrometer (PTR-MS; Ionicon). With a rate constant of 3.4×10^{-12} cm^3/s for D9-butanol and a mean PAM reactor residence time of 112.5 s, the OH radical exposure can be calculated and subsequently converted into an equivalent photochemical age (Barmet et al. 2012), assuming an average ambient OH radical concentration of 10^6 molecules/cm^3 (Prinn et al. 2001). The PTR-MS was installed in parallel to the second electrostatic classifier (switching between line A and line B) and setup in multiple ion detection mode, with an estimated detection limit of 0.5 ppb. For experiments with naphthalene: *m/z* 21 (primary water ion, $[H_2 18^O + H]^+$), 66 (D9-butanol fragment $[M\text{-}HDO + H]^+$), 129 (naphthalene $C_{10}H_8$, $[M+H]^+$, for quantification), and 159 (naphthoquinone $C_{10}H_6O_2$, $[M+H]^+$) were recorded. For experiments with β-pinene: *m/z* 21, 66, 137 (β-pinene $[M+H]^+$, for quantification), and 81 (β-pinene fragment $[M\text{-}C_4H_6 + H]^+$, as qualifier).

O_3, which was formed *in situ* by vacuum ultraviolet (VUV) radiation at 185 nm, was quantified after a 10-fold dilution with pure nitrogen by an O_3 monitor (model O_3 41 M; Environment S.A./Ansyco GmbH) at line B. A second O_3 monitor (model APOA 350E; Horiba) was installed at line C to guarantee that no O_3 reached the ALI systems.

Elemental ratios. A high-resolution time-of-flight aerosol mass spectrometer (AMS; Aerodyne Inc.) (DeCarlo et al. 2006) was operated at line D to determine ratios of the elements O/C and H/C, the total mass concentration, and a size distribution of the nonrefractory organic chemical composition. The instrument was run with a vaporizer temperature of 560°C, with an averaging time of 4 min. The resulting mass spectrum was analyzed in the *m/z* range of 12–220 amu because the fractions >200 amu have little to no impact on the total organic concentration or the elemental composition, given that we observed no $m/z > 200$ amu. Calibrations were preformed weekly using dried 350-nm ammonium nitrate particles, size selected based on mobility diameter with a differential mobility analyzer and a condensation particle counter (TSI; model 3786), as described previously (Jayne et al. 2000). The ionization efficiency was found to be 7.0×10^{-8} before experiments and 6.0×10^{-8} after the experiments. The collection efficiency, used to correct for nonunity collection, was calculated as the percentage of organics detected by the AMS compared with the CPC, assuming a density of 1.4 mg/m^3, and was found to be $\sim 70\%$. The method used to analyze the elemental composition of the aerosol is described in detail elsewhere (Canagaratna et al. 2015).

ROS measurement. An online particle-bound ROS instrument (OPROSI; University of Basel) was installed on line D with an 10-fold ejector diluter (Palas) to trace the oxidative potential as described previously by Wragg et al. (2016). The occurrence of ROS is based on H_2O_2 measurements.

Offline aerosol measurements. In parallel to the online chemical and physical characterization, $PM_{2.5}$ particles were sampled on prebaked (500°C) quartz fiber (QF) filters (Pall Corporation; Tissuquartz) for offline chemical characterization. Filters with a total sampling volume of 600 L were collected either at a 10-L/min flow rate (60 min collection time) or at a 5-L/min flow rate (120 min collection time), respectively.

Particulate carbon and chemical SOA composition. EC and organic carbon (OC) were determined from the QF filters using a thermal-optical carbon analyzer (Desert Research Institute model 2001A; Atmoslytic Inc.) following the IMPROVE_A protocol (Chow et al. 2007). The chemical SOA composition was investigated with two complementary MS techniques from particles collected on filters as described above: Direct inlet probe–high-resolution time-of-flight mass spectrometer (DIP-HRTOFMS; Pegasus GC-HRT 4D; LECO) (Käfer et al. 2019) and comprehensive two-dimensional gas chromatography (GC × GC)–TOFMS; Pegasus BT 4D GC × GC; LECO) with thermal desorption (TD). For DIP-HRTOFMS, round filter punches with a diameter of 2 mm were analyzed by TD in the ion source (40°C − 2/s − 400°C) in four replicates. Raw spectra were blank corrected, summed over the whole run, and found ions were assigned to elemental formulas limited to 1–50 carbon, 0–102 hydrogen, and 0–5 oxygen atoms within a relative mass error window of 5 ppm. Last, ions with odd nominal mass, which represent fragments from the electron ionization, were removed from the data set to focus on molecular ions. The TD-GC × GC-TOFMS was operated with an OPTIC-4 GC inlet system (GL Sciences), with helium (Helium 5.0; Linde AG) as the carrier gas and a GC column set consisting of an SGE BPX5 capillary column [5% phenyl polysilphenylene–siloxane, 60 m, 0.25 mm internal diameter (i.d.), 0.25 µm film thickness (df); SGE] in the first dimension (1D) and an SGE BPX50 capillary column [50% phenyl polysilphenylene–siloxane, 1.5 m, 0.1 mm i.d., 0.1 µm df; SGE] in the second dimension (2D). The desorbed semivolatile organic compounds (SVOCs) were cryogenically focused via the cryogenic trapping system Cryofocus-4 (GL Sciences) at −100°C using liquid nitrogen. The temperature for TD in the OPTIC-4 inlet system was gradually ramped at 2°C/s from 40°C to 300°C to gently introduce aerosol particle constituents onto the GC column with reduced thermal fragmentation. The inlet purge time was 100 s at a column flow of 1 mL/min and a split flow of 100 mL/min. The desorption flow rate was 2.6 mL/min in spitless mode. After TD, the column flow was adjusted to 1 mL/min, and the split flow to 100 mL/min, for the remainder of the measurement. After 10 min of holding the initial temperature of 40°C in the primary oven, it was ramped at 2°C/min from 40°C to 250°C, after which a gradient of 5°C/min was applied to 330°C and held for 10 min. The secondary oven was offset by +20 °C from the primary oven, and the modulator temperature was offset by 15°C to the secondary oven temperature. The modulation period was 5 s, with a hot pulse time of 1.5 s. The MS transfer line temperature was set to 300°C. Mass acquisition was done from 20 to 700 Da at 100 spectra/s. The electron energy was 70 eV, and the ion source temperature was 250°C. Data acquisition and processing was carried out using the ChromaTOF software (version 5.5; LECO). Postprocessing was done with a minimum peak signal-to-noise value (S/N) of 1,000, which resulted in a total peak number of 397 and 798 peaks for SOA_{NAP}-SP and $SOA_{\beta PIN}$-SP, respectively.

Transmission electron microscopy (TEM) images. Were taken for selected experiments by guiding a small volume (100 mL/min) of the aerosol flow for 2–10 min through a carbon sampling grid (400 mesh copper; Agar Scientific). Sampled grids were stored at room temperature (RT) at low humidity in a desiccator prior to analysis using a TEM (JEM-2100F; JEOL Ltd) at 200 kV.

ALI Exposure Systems and Cell Culture

ALI exposure. Two custom-made automated exposure systems (Vitrocell Systems) were used to expose cells at ALI at different dilutions of the aerosols [undiluted (1:1), 1:3, 1:10, and 1:30]. The tested aerosol was guided through a size-selective impactor that excluded particles with size fractions $>PM_{10}$, before entering the inlet of the ALI exposure system and the main reactor. The ALI exposure systems were operated with different settings compared with previous publications (Mülhopt et al. 2016; Oeder et al. 2015). The total aerosol flow (inlet) was reduced to 5 L/min owing to the limited aerosol flow through the PAM reactor. The cabinet was heated to a temperature of 39.4°C to reduce water condensation in the tubes. Both systems comprised three Vitrocell 6/6 CF Stainless modules, thus enabling the exposure of six inserts of a 6-well format per module. Every position in the module was supplied with separate air flow over a trumpet taken from the main reactor. Exposure to the tested aerosol was conducted in 12 positions per ALI exposure system, in which the aerosol was passed over the cells growing on Transwell inserts and deposition was controlled only by diffusion. A simplified scheme of the setup is shown in Figure 1. In addition to the aerosol exposures, each system had a separate clean air (CA; purified compressed laboratory air) exposure sector serving as controls (6 positions per ALI exposure system). Incubator control cell cultures were important to assess the impact of the ALI exposure system itself on the cultured cells. The temperature of each module containing the cells was continuously measured and controlled via external water baths, and although the cabinet was heated to 39.4°C, the modules themselves had to be cooled down to 37°C for optimal cell culture environment. Humidified aerosol and CA (85% RH) were operated with a 100-mL/min flow rate over every position in the ALI exposure system, as described by Mülhopt et al. (2016). Every evening the ALI exposure systems were dried using filtered ambient air, and the tubing to and from the modules was also dried by starting a filtered ambient air exposure (∼ 30% RH) with an increased flow rate of 200 mL/min for 20 min. Between different aerosol exposures, the reactors were taken apart and cleaned with 70% ethanol. The impactors were cleaned once a week, as well as before changing the aerosol.

Estimation of the particle deposition in ALI. The deposited PM mass per area was calculated using the following equation.

$$\textit{Deposited mass per area}\ [ng/cm^2] = \frac{\eta \times Q \times N \times t \times \rho_p \times V_p}{A},$$

where η is the deposition efficiency; Q is the aerosol flow; N is the particle number concentration (particle count per volume); t is the duration of the exposure; ρ_p is the particle density; V_p is the particle volume, assuming spherical particles; and A is the area of the deposition plate. The size-dependent deposition efficiency of particles (η) in the ALI exposure system is calculated using the theory described by Lucci et al. (2018). In the model, the deposition of particles is generally controlled by size-dependent diffusion and sedimentation mechanisms. Large particles deposit by sedimentation, whereas small particles deposit by diffusion. The particle deposition efficiency is controlled by various parameters (e.g., particle size and density, aerosol flow, temperature, pressure, and geometry of the system). In the present study, the size-dependent particle number concentration was used, which was measured by the SMPS at line D. The mean effective density of each aerosol type was calculated by forcing the mass concentration measured by SMPS to be equal to the mass concentration measured by a TEOM. Particle density influences the calculations in two ways: first, determining the deposition efficiency, and second, and more importantly, by converting the deposited number of particles to deposited mass. Aerosol flow and temperature were 100 mL/min and 37°C, respectively.

Cell lines and ALI exposure. A549 human alveolar epithelial cells (ATCC; CCL-185) and EA.hy926 hybrid human endothelial cells (kindly provided by Dr. S. Moertl, HelmholtzZentrum) were routinely cultured in high-glucose Gibco Dulbecco's Modified Eagle Medium: Nutrient Mixture F-12 (DMEM/F-12) (ThermoFisher Scientific; 31331-028) supplemented with 5% (vol/vol) fetal bovine serum (FBS) (ThermoFisher Scientific; 10500-064), and 100 U/mL penicillin and 100 µg/mL streptomycin (P/S; Sigma-Aldrich; P4333) in a humidified incubator at 37°C and 5% carbon dioxide (CO_2). For the mono- and coculture exposure experiments, A549 cells were seeded on the same day on transferrable 24-mm Transwell inserts with a polyester membrane (0.4−µm pore-size; type #3450; Corning) 96 h before the exposure experiments at a density of 1.8×10^5cells/mL per insert (3.8×10^4cells/cm^2 growth area) with 1.5 mL of cell culture medium provided at the basal compartment of the Transwell. Forty-eight hours after the initial cell seeding, the culture medium on the apical side for both cell models was removed to generate ALI conditions, and fresh cell culture medium was added in the basal compartment. Twenty-four hours later, the inserts for the coculture were inverted; 1×10^5 EA.hy926 cells per insert (0.21×10^4cells/cm^2 growth area) were seeded in 750 µL of medium; and after 1 h, the insert was turned back and fresh medium was added to the basolateral compartment of the Transwell. For the monoculture, the medium was renewed to ensure equal treatment of both cell culture models. On Day 5, the day of the exposure experiments, inserts with mono- and cocultures were placed in the exposure modules of the ALI exposure system (Vitrocell Automated Exposure Station Standard Version) with 1.8 mL serum-free DMEM/F12 medium supplemented with 1% P/S and 15 mM *N*-2-hydroxyethylpiperazine-*N*-2-ethane sulfonic acid (HEPES) buffer solution (ThermoFisher Scientific; 15630-056) at the basolateral compartment. Cells were then exposed for 4 h to the conditioned (85% RH, 37°C) and differently diluted aerosols [undiluted (1:1), 1:3, 1:10, and 1:30]. All experiments were performed in at least three independent exposures. After the exposure, the effects of the aerosols on the cells were examined with several assays, and the exposure medium was collected on ice for direct analyses or frozen at −80°C for later analyses.

Immunofluorescence

To check for a confluent cell monolayer, the membranes were cut out from the Transwell inserts on the day of the exposure and were washed twice in phosphate-buffered saline (PBS), fixed with 4% formaldehyde (Paraformaldehyde; Carl Roth; 4980.1) for 12 min, and washed three times in 0.1% bovine serum albumin (BSA) (Sigma-Aldrich; A8412) in PBS, before staining with Phalloidine A488 (1:100; Sigma-Aldrich; 49409) and 4′,6-diamidino-2-phenylindole (DAPI) (1:1,000; Sigma-Aldrich; D9542) in 1% BSA and 0.1% Triton-X in PBS for 1 h at RT. Membranes were washed three times in PBS, once in double-distilled water, and embedded in fluorescence mounting medium (Glycergel; DAKO; Agilent; C056330-2). Slides were observed on a Lionheart FX Automated Microscope and pictures captured for illustration.

Cell viability assay and live cell microscopy. To determine cell viability, immediately after the exposure, A549 inserts were transferred to a 6-well plate, washed once with PBS before adding 1 mL prewarmed fresh exposure medium (serum-free DMEM/F12+1% P/S and 15 mM HEPES) with 10% PrestoBlue HS Cell Viability Reagent (ThermoFisher Scientific; A13262) to the apical and basolateral compartments. After an incubation of 45 min at 37°C in the incubator, aliquots of the basal and apical medium were pipetted into a 96-well plate, and the quantification of metabolically active cells was performed by measuring the fluorescence at 570 nm with a spectrophotometer (MULTISKAN SKY Microplate Spectrophotometer; ThermoFisher Scientific). The results are presented as percentage cell viability compared with incubator control from at least four independent exposures and one technical replicate, respectively. After the PrestoBlue assay, inserts were washed twice with PBS before 600 μL of staining solution [Hoechst; 33342; 5 μg/mL (Sigma-Aldrich; B2261) and propidium iodide (PI), 25 μg/mL (Sigma-Aldrich; P41770) in serum-free cell culture medium (DMEM/F12+1 % P/S] was added for 45 min at 37°C. This was followed by two further PBS washing steps, the addition of prewarmed PBS below and above the insert, and the capturing of the image with a live cell microscope (Lionheart FX automated microscope) at 37°C.

Cell membrane damage assay. For assessing aerosol-induced membrane integrity as a measure of cytotoxicity, the release of lactate dehydrogenase (LDH) was immediately determined from the medium that had been directly collected after exposures by the Cytotoxicity Detection Kit^{Plus} (L-LDH; Roche; 11644793001) in a 96-well plate. Cell culture medium was used as the blank. The kit was used according to the manufacturer's recommendation with the addition of a LDH standard curve ranging from 4 to 250 mU/mL (L-LDH; Roche; 10127230001). After 10 min, the quantification of LDH release was performed by measuring the absorbance at 493 nm with a spectrophotometer (MULTISCAN SKY Microplate Spectrophotometer). The results are shown as LDH concentration in microunits per milliliter calculated with the help of standard curves from at least four independent exposures and, in each case, four (monoculture) or two (coculture) technical replicates.

Oxidative stress analysis. Malondialdehyde (MDA), an indicator of cellular oxidative stress, was measured from the frozen collected sample media using the liquid chromatographic (LC) MS/MS method (API 4000 Triple Quadrupole system, AB Sciex in positive MRM mode), as previously described by Wu et al. (2017b). Shortly afterward, frozen samples were thawed and 20 μL of cell culture medium was mixed with 25 μL of 100 ng/mL d_2-MDA and 500 μL of 0.5 mM 2,4-dinitrophenylhydrazine (DNPH; Sigma-Aldrich; D199303) in 1% formic acid solution. Derivatization was conducted at 37°C under 300 rpm for 70 min in a Thermomixer C (Eppendorf) before 700 μL of *n*-hexane (high-performance LC-grade; VWR) was added, shaken, and centrifuged at 9,390 × *g* for 5 min Heraeus Biofuge Pico Centrifuge (Thermo Scientific). The *n*-hexane supernatant was collected, and the extraction procedure was repeated once. Following this, the collected *n*-hexane supernatant was combined and dried by nitrogen in a Vapotherm Basis Mobil I (Barkey) at RT. The dried residue was redissolved in 50 μL of methanol:0.1% formic acid (80:20, vol/vol). After the liquid–liquid extraction, the MDA adduct was analyzed by LC-MS/MS (capillary voltage 4.5 kV, source temperature 350°C, column compartment set at 20°C) in multiple reaction, and the isocratic separation was conducted with a constant flow of 200 μL/min of mobile phase. Each sample was injected twice with 10 μL injection volume for each measurement. A standard calibration curve with standard concentrations of MDA ranging from 0.5 to 20 ng/mL was set up for quantification. Data are presented as MDA in nanograms per milliliter from at least three independent exposures with one technical replicate.

Comet assay. Immediately after the exposure, inserts were washed twice with PBS and cells were harvested with 0.5% Trypsin-ethylenediaaminetetraacetic acid (EDTA) (Sigma-Aldrich; T4174) for 3 min (for A549 cells) or 6 min (for EA.hy926 cells). Trypsin-EDTA was inhibited with FBS, and the cell types were collected separately. The cells were centrifuged at 0.2 × *g* and 4°C and then resuspended in 1 mL of cold PBS. Cells were counted with Trypan Blue in an automated cell counter (Luna-II; Logos Biosystems; BioCat). The alkaline version of the comet assay was performed according to the mini-gel comet assay method previously described (Di Bucchianico et al. 2017) to detect DNA single- and double-strand breaks, as well as alkaline labile sites. Cells exposed to 30 μM hydrogen peroxide for 5 min on ice were used as positive controls. On each slide, eight mini-gels were prepared, including untreated controls, exposed cells, and positive controls for both A549 and EA.hy926 cells. At least three independent slides per condition were prepared, and 100 nucleoids per mini-gel were scored using CometScore (version 2.0; TriTek Corp.) on 1:10.000-dilution SYBR Green (ThermoFisher Scientific; S7563) stained slides. A Lionheart FX automated microscope was used to take 20× magnification micrographs of the stained slides. Data are shown as percentage DNA breaks (% DNA in tail) from at least three independent exposures with two technical replicates.

IL-8 measurement. Aliquots of the collected and −80°C-stored exposure media were thawed and analyzed in a 96-well plate, using the enzyme-based immunosorbent assay (ELISA; R&D Systems; DY208) for the pro-inflammatory cytokine IL-8, according to manufacturer's instruction. In brief, a 96-well plate was coated with 100 μL of diluted human IL-8 capture antibody overnight at RT. On the next day, the plate was washed three times with wash buffer [0.05% Tween 20 (Santa Cruz; 9005-64-5) in PBS, pH 7.2–7.4], blocked with 300 μL block buffer (1% BSA, pH 7.2–7.4) for 1 h, after which the washing step was repeated. Thawed samples of the A549 monoculture were diluted 1:2 and samples of the coculture 1:3 in reagent diluent (0.1% BSA and 0.05% Tween 20 dissolved in PBS) and IL-8 standards were prepared (31–2,000 pg/mL). One hundred microliters of either the samples or the standards were added to the plate for 2 h at RT. After washing three times with wash buffer, the plate was incubated with 100 μL of detection antibody for 2 h at RT. The washing step was repeated, and 100 μL of streptavidin–horseradish peroxidase was added to each well for 20 min. After another washing step, 100 μL of 3,3′,5,5′-tetramethylbenzidine (TMB; Cell Signaling Technologies; 7004P6) was used as an substrate and incubated for 20 min before 50 μL of stop solution (sulfuric acid) was added, and the fluorescence was measured at 450 and 540 nm in a microplate reader (Varioskan Lux multimode microplate reader). Results are presented as IL-8 in picograms per milliliter from at least four independent exposures with one technical replicate.

Angiogenesis Assay

EA.hy926 cells were seeded at a density of 100,000 cells per well (2.6×10^4cells/cm^2 growth area) in a 12-well plate. After 24 h, the attached cells were treated with a 1:1 mixture of fresh medium and conditioned medium (CM) for 24 h. The CM represents the exposure medium that was collected and stored at −80°C after the 4-h exposure to the different undiluted aerosols. After 24 h, the cells were trypsinized and seeded in fresh cell culture medium at 2×10^4 cells per well (6.2×10^4cells/cm^2 growth area) in a 96-well plate precoated with a growth factor-reduced BME Matrigel (Cultrex *in vitro* angiogenesis assay; R&D Systems; 3470-096-K). Tube formation was captured 24 h after seeding (10× objective; Lionheart FX Automated Microscope; BioTek). The angiogenic potential, which indicates the capacity of a compound to increase or decrease the formation of capillary-like structures, was calculated with the formula established by Aranda and Owen (2009).

$$\textit{Angiogenic score} = \left(\frac{(\textit{No. of sprouting cells})\times1+(\textit{No. of connected cells})\times2+(\textit{No. of polygons})\times3}{\textit{Total number of cells}}\right) + (0,1\ \textit{or}\ 2)$$

The addition of 0, 1, or 2 to the total value depended on the presence of a complex mesh. No complex mesh is represented by the addition of 0 points; for the existence of luminal structures consisting of two to three cell layers, an addition of 1 point is necessary; and for luminal structures of greater than three cell layers, an additional value of 2 is added. Results are presented as Angiogenic score from at least three independent experiments and two technical replicates.

Statistical methods. Each experiment was performed at least in triplicate. The results of three or more independent experiments were expressed as the mean ± standard error of the mean (SEM). Differences between the groups were analyzed using one-way analysis of variance (ANOVA) with the Welch-Satterthwaite approximation for unequal variances (Welch 1947). Multiple comparisons using the Bonferroni correction to control the inflation of type I errors were conducted for all ANOVA results with a $p < 0.05$ as post hoc analysis for sample comparison. All data were analyzed with R environment (RStudioTeam 2019, http://www.rstudio.com/). Graphs were illustrated using GraphPad Prism for Windows (version 9.0.0; GraphPad Software).

Results

Characterization of the SOA Components of the Two Aerosol Types

All online instruments confirmed stable and reproducible aerosol feeds and aging conditions over the entire exposure period of 4 h (Figure S1A–E). Moreover, BC and OC concentrations were similar for both precursors. In addition, strong similarities between both precursors were observed for averages of geometric mean of particle size, equivalent photochemical ages, and OC fractions. An overview of the SOA concentrations and properties, as well as of the bare SPs, is compiled in Table 1. TEM micrographs of both SOAs revealed similar particle shapes of soot agglomerates coated with organic material, whereas pure SPs seemed to retain their more fractal structures (Figure S2). The particle number of $\mathrm{SOA_{NAP}}$-SP was slightly higher compared with $\mathrm{SOA_{\beta PIN}}$-SP (Table 1), and spontaneous nucleation of $\mathrm{SOA_{NAP}}$-SP, forming particles with a mobility diameter of <50 nm, occurred to a minor extent (Figure S1F). Consequently, the estimation of the particle mass deposition suggested a 1.5-fold higher deposition of $\mathrm{SOA_{NAP}}$-SP (28 ng/cm^2) compared with $\mathrm{SOA_{\beta PIN}}$-SP (17 ng/cm^2).

To explore how $\mathrm{SOA_{\beta PIN}}$-SP is chemically distinct from $\mathrm{SOA_{NAP}}$-SP, we performed untargeted GC × GC-TOFMS analysis for the SVOCs. The chemical composition of the two generated SOAs differed widely in individual molecular composition, compound classes, and oxidation state (Figure 2A–F). In GC × GC with a nonpolar column in the first and a polar column in the second

Table 1. Physical and chemical properties of unaged pure soot particles (SP, CAST soot; 1 mg/m^3) or atmospheric photooxidation (aging) by OH radicals in a potential aerosol mass (PAM) reactor of SP (CAST soot; 1 mg/m^3) together with either naphthalene (4 mg/m^3) or β-pinene (4 mg/m^3), forming $\mathrm{SOA_{NAP}}$-SP and $\mathrm{SOA_{\beta PIN}}$-SP, respectively.

		SP		$\mathrm{SOA_{NAP}}$-SP		$\mathrm{SOA_{\beta PIN}}$-SP	
Categories	Instrument	Mean ± SD	*n*	Mean ± SD	*n*	Mean ± SD	*n*
BC (mg/m^3)	Aethalometer	1.3 ± 0.1	7	1.5 ± 0.1	10	1.4 ± 0.1	11
BrC content (%)	Aethalometer	12 ± 1	7	32 ± 1	10	22 ± 1	11
Days atmospheric OH age [d (*n*)]^a	PTR-MS	0	7	2.9 ± 0.4	10	2.8 ± 0.2	11
Particle number concentration (n/cm^3)	CPC	$1.3\times10^6 \pm 0.3\times10^6$	7	$1.4\times10^6 \pm 0.2\times10^6$	10	$0.9\times10^6 \pm 0.2\times10^6$	11
Particle geometric mean diameter (nm)	SMPS	117 ± 1	7	114 ± 1	10	117 ± 1	11
Total EC (mg/m^3)	Carbon analyzer	0.7 ± 0.1	5	1.0 ± 0.2	10	0.7 ± 0.1	11
Total OC (mg/m^3)	Carbon analyzer	0.3 ± 0.2	5	1.1 ± 0.2	10	1.0 ± 0.2	11
OC_1 (mg/m^3)	Carbon analyzer	0.01 ± 0.01	5	0.2 ± 0.05	10	0.1 ± 0.03	11
OC_2 (mg/m^3)	Carbon analyzer	0.03 ± 0.02	5	0.3 ± 0.05	10	0.3 ± 0.05	11
OC_3 (mg/m^3)	Carbon analyzer	0.2 ± 0.3	5	0.5 ± 0.1	10	0.5 ± 0.1	11
OC_4 (mg/m^3)	Carbon analyzer	0.06 ± 0.08	5	0.1 ± 0.05	10	0.1 ± 0.04	11
Deposition (ng/cm^2)	Calculation	9 ± 1	5	28 ± 2	10	17 ± 2	11
H_2O_2-equivalent (μmol/m^3)	OPROSI	0.02 ± 0.05	3	14.1 ± 0.9	2	3.6 ± 0.5	3
O/C (ratio)	AMS	—	0	0.77 ± 0.06	10	0.61 ± 0.02	11

Note: Results are presented as mean ± SD. This reflects the reproducibility of *n* indicated independent experiments. —, no data available; AMS, high-resolution time-of-flight aerosol mass spectrometer; BC, black carbon; BrC, brown carbon; CPC, condensation particle counter; EC, elemental carbon; H_2O_2, hydrogen peroxide; OC, organic carbon; OH, hydroxy; PTR-MS, quadrupole proton–transfer reaction mass spectrometer; OPROSI, online particle-bound reactive oxygen species instrument; SD, standard deviation; SMPS, scanning mobility particle sizer.

[a] Assuming an average ambient hydroxyl radical concentration of 10^6molecules/m^3.

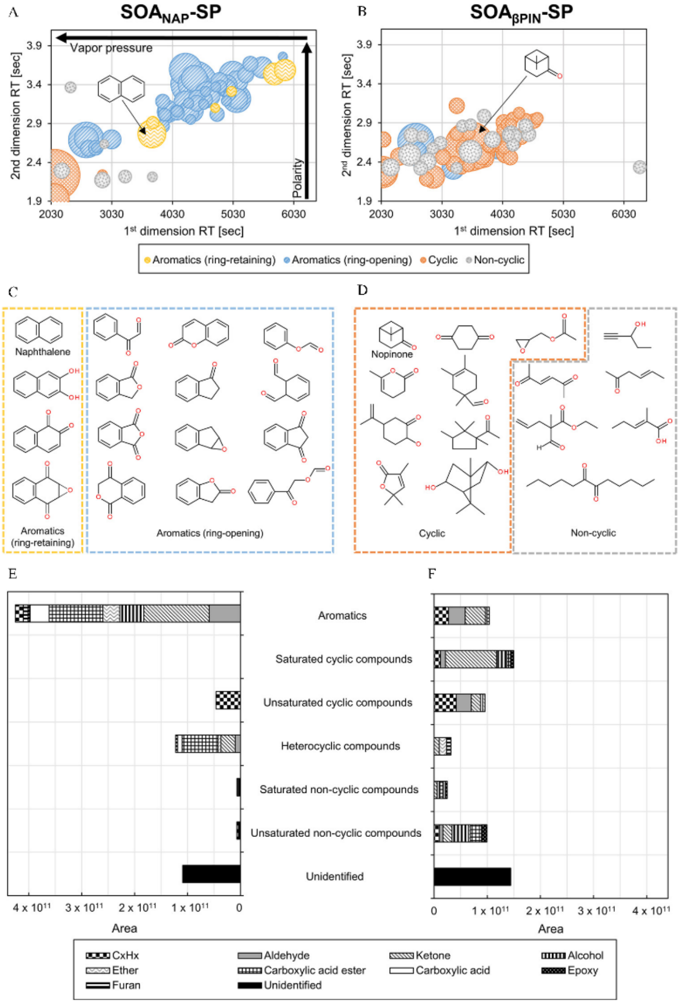

Figure 2. Chemical characterization of SOA_{NAP}-SP and $\text{SOA}_{\beta\text{PIN}}$-SP. (A,B) GC × GC-TOFMS bubble plots for SOA_{NAP}-SP (A) and $\text{SOA}_{\beta\text{PIN}}$-SP (B) at atmospheric OH age ≈ 3 d. Bubble sizes correspond to their respective peak areas. (C,D) Assignment of representative peaks from GC × GC-TOFMS for SOA_{NAP}-SP (C) and for $\text{SOA}_{\beta\text{PIN}}$-SP (D) to their molecular formulas via comparison with NIST mass spectral library and retention indices (excluding peaks with inconclusive MS spectra). (E,F) Areas of the 100 peaks with the highest signal intensities from GC × GC-TOFMS classified by compound classes and functional groups for SOA_{NAP}-SP (E) and for $\text{SOA}_{\beta\text{PIN}}$-SP (F). The classified 100 compounds account for 77.4% and 60.4% of the total abundance for SOA_{NAP}-SP and $\text{SOA}_{\beta\text{PIN}}$-SP, respectively. Corresponding numerical data for (A–D) are shown in Tables S1 and S2 and for (E,F) in Tables S3 and S4. Note: GC × GC-TOFMS, comprehensive two-dimensional gas chromatography–time-of-flight mass spectrometer; MS, mass spectrometer; NIST, National Institute of Standards and Technology; OH, hydroxyl; $\text{SOA}_{\text{NAP-SP}}/\text{SOA}_{\beta\text{PIN}}$-SP, soot particles (SP, CAST soot; $1\ \text{mg/m}^3$) together with either naphthalene ($4\ \text{mg/m}^3$) or β-pinene ($4\ \text{mg/m}^3$) photochemically aged with OH radicals in a potential aerosol mass reactor.

retention dimension, compounds were first separated according to their vapor pressures, corresponding to the respective carbon number and boiling point on the *x*-axis, and by polarity on the *y*-axis (Figure 2A,B). The compounds were classified into both ring-opening and -retaining aromatics, as well as cyclic and noncyclic compounds, based on their appearance in the 2D chromatogram and mass spectrometric signature (Figure S3). SOA_{NAP}-SP was clearly dominated by aromatic structures. Aromatic compounds, retaining the naphthalene carbon backbone of two six-rings, eluted slightly faster in the second dimension compared with the ring-opening aromatic compounds and, therefore, were located below the ring-opening aromatics in the 2D chromatogram. For SOA$_{\beta PIN}$-SP, the region between 3,000 and 5,000 s revealed peaks of highest abundance, corresponding to a boiling point range of ~170°C to 290°C for linear alkanes with a molecular weight of ~140–230 Da and carbon numbers between C_{10} and C_{16}. For SOA$_{NAP}$-SP, the region with peaks of highest abundance was between 3,700 and 6,000 s, corresponding to a boiling point range of ~220°C to 330°C for linear alkanes with a molecular weight of ~170–270 Da and carbon numbers between C_{12} and C_{19}.

In all aging experiments, we detected more individual compounds for SOA$_{\beta PIN}$-SP than for SOA$_{NAP}$-SP within the assessable boiling point range. At a minimum peak S/N of 1,000 the total peak number for SOA$_{NAP}$-SP and SOA$_{\beta PIN}$-SP was 397 and 798 peaks, respectively. The top 100 peaks with the highest peak intensities presented in Figure 2A,B,E,F contributed to 77.4% and 60.4% of the total peak intensity for SOA$_{NAP}$-SP and SOA$_{\beta PIN}$-SP, respectively (Figure S4, Tables S1 and S2). Furthermore, SOA$_{NAP}$-SP consisted of fewer, but more abundant, compounds in signal intensity (Figure S4A). Despite performing an elaborated cleaning procedure, carryover effects between experiments could not be fully avoided. However, Figure S4 illustrates that the carryover was limited when considering the chemical profiles and abundances, showing that the investigated two SOA types resulted in entirely different chemical species with respect to the detected molecular structures. For SOA$_{\beta PIN}$-SP, these compounds were mostly comprised of oxygenated cyclic and acyclic compounds (Figure 2D,F), whereas in SOA$_{NAP}$-SP, we mostly found aromatic structures (Figure 2C,E). DIP-HR-TOFMS measurements were performed for the analysis of higher oxidized compounds, exceeding the application range of GC×GC-TOFMS. Complex patterns of nonaromatic $(H/C > 1)$ oxidized fragments $(O/C > 0)$ with up to four oxygen atoms were recognized, although oligomers could not be unambiguously identified (Figure 3E,F). The DIP-HR-TOFMS measurements showed a lower H/C-ratio for SOA$_{NAP}$-SP, pointing again to its more aromatic structure compared with SOA$_{\beta PIN}$-SP. The resulting O/C values from the AMS measurements indicated a slightly higher photochemical oxidation of SOA$_{NAP}$-SP compared with SOA$_{\beta PIN}$-SP (Figure 3B,D). In addition, SOA$_{\beta PIN}$-SP appeared well within the triangular space spanned by the relative fractions of *m/z* 43 vs. *m/z* 44 (Figure S5).

Cytotoxic Effects after Exposure to Soot Aerosol Coated with SOAs

For our study we established two different cell culture models, one using an alveolar epithelial lung (A549) cell line as an ALI monoculture model and another using an A549/human endothelial (EA.hy926) cell line ALI coculture model (Figure 4A, graphical illustration). Immunofluorescence staining confirmed a confluent single cell layer in both cell culture models shortly before the aerosol exposure (Figure 4A, right panel). To explore how SOA$_{\beta PIN}$-SP and SOA$_{NAP}$-SP affect the cell culture models, we first performed a resazurin-based viability test on the A549 monoculture. Exposure to the undiluted pure SPs did not significantly decrease cell viability (Table S6). In addition, SOA$_{\beta PIN}$-SP did not significantly affect cell viability in all tested dilutions $(p > 0.05)$ and exhibited slightly

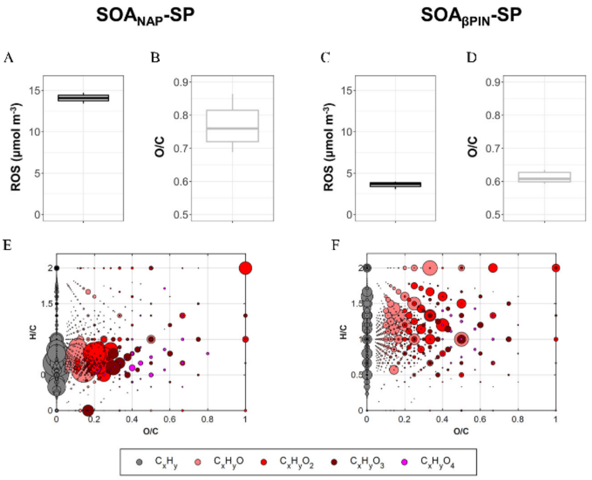

Figure 3. Oxidation state of SOA$_{NAP}$-SP and SOA$_{\beta PIN}$-SP. (A,C) Occurrence of reactive oxygen species (ROS) in SOA$_{NAP}$-SP (A) and SOA$_{\beta PIN}$-SP (C) by measuring H_2O_2 with an online particle-bound ROS instrument (OPROSI) in micromoles per meter cubed of *n* independent experiments (SOA$_{NAP}$-SP: $n = 2$, SOA$_{\beta PIN}$-SP: $n = 3$). (B,D) O/C ratios determined by AMS for SOA$_{NAP}$-SP (B) and SOA$_{\beta PIN}$-SP (D) of *n* independent experiments (SOA$_{NAP}$-SP: $n = 10$, SOA$_{\beta PIN}$-SP: $n = 11$). (A–D) The upper and lower hinges of the box plots represent the first and third quartiles (the 25th and 75th percentiles) of the distribution. The midline in the box is the median and the whiskers extend from the highest, respectively lowest, value that is within 1.5 × IQR of the hinge, where IQR is the distance between the first and third quartile. (E,F) Van-Krevelen Plots for DIP-HRTOFMS measurements (average of 4 independent experiments, respectively) of SOA$_{NAP}$-SP (E) and SOA$_{\beta PIN}$-SP (F). The size of the depicted circles represents the relative abundance of ions in the mass spectrum. Other than for the AMS, the mass fragments at *m/z* 43.9898 of CO_2^+ and *m/z* 27.9949 of CO^+ are not considered for the DIP results. Corresponding numerical data for (A–D) are shown in Table 1, and (E,F) in Excel Tables S7 and S8. Note: AMS, high-resolution time-of-flight aerosol mass spectrometer; CO_2, carbon dioxide; DIP-HRTOFMS, direct insertion probe high-resolution time-of-flight mass spectrometer; IQR, interquartile range; OH, hydroxyl;SOA$_{NAP\text{-}SP}$/SOA$_{\beta PIN}$-SP, soot particles (SP, CAST soot; 1 mg/m^3) together with either naphthalene (4 mg/m^3) or β-pinene (4 mg/m^3) photochemically aged with OH radicals in a potential aerosol mass reactor.

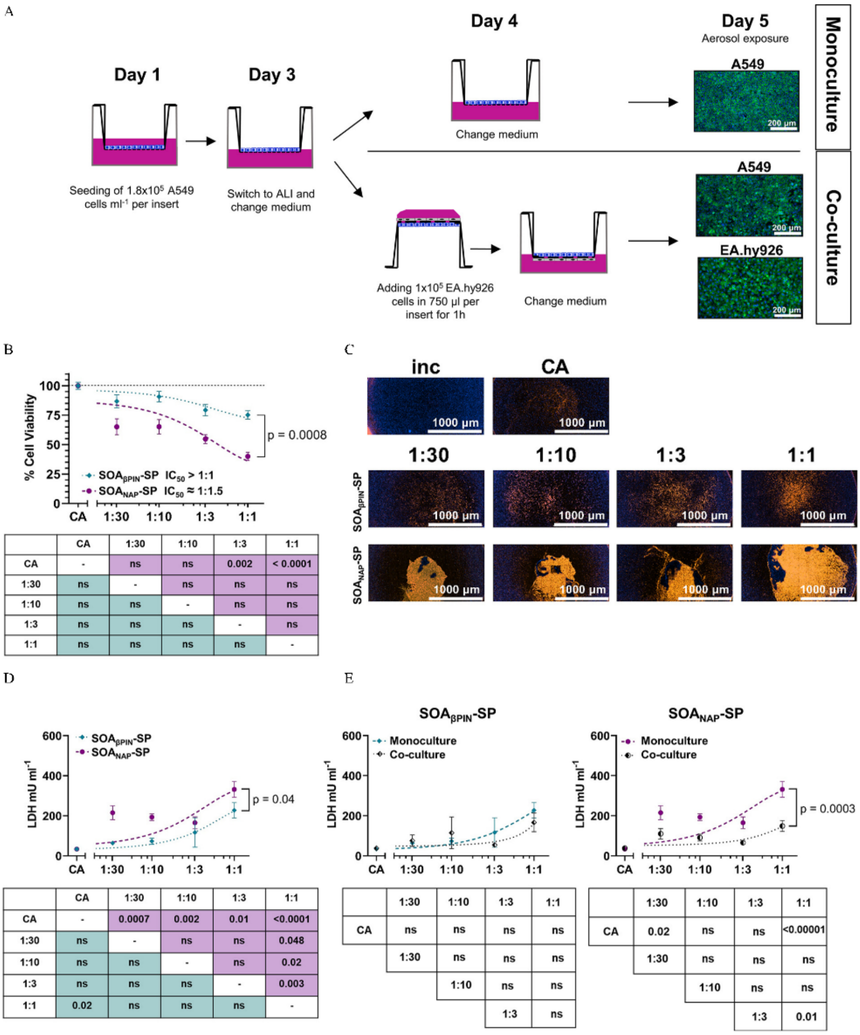

B

	CA	1:30	1:10	1:3	1:1
CA	-	ns	ns	0.002	< 0.0001
1:30	ns	-	ns	ns	ns
1:10	ns	ns	-	ns	ns
1:3	ns	ns	ns	-	ns
1:1	ns	ns	ns	ns	-

D

	CA	1:30	1:10	1:3	1:1
CA	-	0.0007	0.002	0.01	<0.0001
1:30	ns	-	ns	ns	0.048
1:10	ns	ns	-	ns	0.02
1:3	ns	ns	ns	-	0.003
1:1	0.02	ns	ns	ns	-

E (SOAβPIN-SP)

	1:30	1:10	1:3	1:1
CA	ns	ns	ns	ns
	1:30	ns	ns	ns
		1:10	ns	ns
			1:3	ns

E (SOANAP-SP)

	1:30	1:10	1:3	1:1
CA	0.02	ns	ns	<0.00001
	1:30	ns	ns	ns
		1:10	ns	ns
			1:3	0.01

Figure 4. Cell viability and LDH release after 4-h exposure to SOA_{NAP}-SP and $\text{SOA}_{\beta\text{PIN}}$-SP. (A) Schematic overview of the cell seeding procedure of mono- and coculture, as well as representative immunofluorescences images of mono- (A549; upper image) and coculture (A549/EA.hy926; lower image) on the day of aerosol exposure, stained for actin filaments (phalloidin, green) and nuclear stain (DAPI, blue). Scale bar: 200 μm. (B) Cell viability of A549 monoculture after the exposure to $\text{SOA}_{\beta\text{PIN}}$-SP and SOA_{NAP}-SP measured by resazurin-based assay. Results are presented as the mean cell viability compared with the incubator ctrl ± SEM of *n* independent experiments ($\text{SOA}_{\beta\text{PIN}}$-SP: $n = 4$, SOA_{NAP}-SP: $n = 5$ for all dilutions and CA ctrl: $n = 8$) and dotted lines denote the regression line for the respective SOA forced through the CA ctrl. (C) Propidium iodide staining (PI, red) of A549 monoculture after 4 h exposure with $\text{SOA}_{\beta\text{PIN}}$-SP and SOA_{NAP}-SP for all dilutions, as well as a CA ctrl. Hoechst nuclear stain (blue). Scale bar: 1,000 μm. Shown are representative images of at least three independent experiments. (D) LDH release (mU/mL) of A549 monoculture after the exposure to $\text{SOA}_{\beta\text{PIN}}$-SP and SOA_{NAP}-SP. (E) Comparison of LDH release (mU/mL) of the mono- and coculture after the exposure to $\text{SOA}_{\beta\text{PIN}}$-SP (left panel) and SOA_{NAP}-SP (right panel). (D,E) Results are presented as absolute values ± SEM of *n* independent experiments ($\text{SOA}_{\beta\text{PIN}}$-SP: $n = 4$, SOA_{NAP}-SP: $n = 5$ for all dilutions, and CA ctrl: $n = 9$) and dotted lines denote the regression line for the respective cell culture models and SOA forced through the CA ctrl. (B,D,E) Aerosol exposure groups were compared by performing a one-way ANOVA and statistical significance was calculated with multiple comparisons for the dilutions within one aerosol exposure group using the Bonferroni correction. *p*-Values are presented in the graph and in the tables below the graphs. Corresponding numerical data for (B,D,E) are shown in Tables S6 and S7. Note: ANOVA, analysis of variance; CA, clean air; ctrl, control; DAPI, 4′,6-diamidino-2-phenylindole; inc, incubator; LDH, lactate dehydrogenase; OH, hydroxyl; SEM, standard error of the mean; SOA, secondary organic aerosol; $\text{SOA}_{\text{NAP-SP}}/\text{SOA}_{\beta\text{PIN}}$-SP, soot particles (SP, CAST soot; 1 mg/m^3) together with either naphthalene (4 mg/m^3) or β-pinene (4 mg/m^3) photochemically aged with OH radicals in a potential aerosol mass reactor.

lower viability (78%) following undiluted aerosol exposures [half-maximal inhibitory concentration (IC_{50}) > 1:1 dilution; Figure 4B]. In contrast, cells exposed to SOA_{NAP}-SP had lower cell viability in the range from 70% cell viability for the 1:30 diluted aerosol to the significant ($p < 0.0001$) 40% for the undiluted aerosol ($IC_{50} = 1:1.5$; Figure 4B) compared with control cells. The undiluted SOA_{NAP}-SP aerosol cell exposures showed significantly lower viability than undiluted $SOA_{\beta PIN}$-SP treatments ($p = 0.0008$). This significant difference was also confirmed by normalizing to the deposition that is needed to achieve the respective IC_{50} values of $SOA_{\beta PIN}$-SP and SOA_{NAP}-SP. By liner regression analysis, the normalized mass deposition for SOA_{NAP}-SP ($R^2 = 0.6$, $p = 0.0005$) resulted in an IC_{50} value of $18\,ng/cm^2$, whereas the IC_{50} value for $SOA_{\beta PIN}$-SP ($SOA_{\beta PIN}$-SP: $R^2 = 0.7$, $p = 0.001$) did not even reach its highest concentration. No linear regression could be calculated for the exposure with SP ($R^2 = 0.01$) because of the similar results in all dilutions. No significant difference in cell viability was observed for the CA controls compared with the incubator controls (100% cell viability). The resazurin-based assay was not conducted with the coculture model owing to space limitations in the ALI exposure system. The results from the cell viability assay of the monoculture were also corroborated by live cell microscopy, where we saw a higher number of dead cells after the exposure to SOA_{NAP}-SP than to $SOA_{\beta PIN}$-SP and only a slightly higher number of dead cells in the CA control compared with the incubator controls (Figure 4C).

The difference in cell viability prompted a further elucidation of how the tested biogenic and combustion-derived SOAs affected the used cell cultures. In the monoculture, a concentration-dependent ($R^2 = 0.5$, $p = 0.03$) difference in LDH level (higher in exposed cells vs. control) was detected following exposure with $SOA_{\beta PIN}$-SP, with the highest effect at dilution 1:1 (undiluted). Compared with $SOA_{\beta PIN}$-SP, the exposure to SOA_{NAP}-SP in the monoculture led to the release of higher LDH concentrations in all dilutions with ~200 mU/mL in dilutions 1:30, 1:10, and 1:3 and 330 mU/mL in dilution 1:1 (undiluted) (Figure 4D). These aerosol-specific effects on LDH release in the monoculture were confirmed by the results observed with the coculture system, in which we monitored the same trends with a lower magnitude, but with no statistically significant effect compared with the monoculture (Figure 4E). Model systems exposed to CA were not significantly different from each other in LDH release (33 mU/mL for monoculture; 38 mU/mL for coculture).

Effects on Oxidative Stress and Genotoxicity by Soot Aerosol Coated with SOAs

Next, we investigated why SOA_{NAP}-SP induced a higher cytotoxic effect compared with $SOA_{\beta PIN}$-SP. No organic or inorganic peroxides were present in the undiluted pure soot aerosol (Table 1), 3.6 $\mu mol/m^3$ hydrogen peroxide (H_2O_2)-equivalent in the undiluted $SOA_{\beta PIN}$-SP and 14.1 $\mu mol/m^3$ H_2O_2-equivalent in the undiluted SOA_{NAP}-SP, indicating a higher oxidative potential of SOA_{NAP}-SP with respect to $SOA_{\beta PIN}$-SP (Figure 3A,C). These results were corroborated through analysis of MDA, a marker for cellular oxidative stress. Both in the mono- (Figure 5A) and the coculture (Figure 5B), exposure to SOA_{NAP}-SP induced the highest release of MDA in all dilutions (concentration-dependent; $R^2 = 0.98$, $p = 0.0002$) with a peak at the undiluted (1:1) aerosol (45 ng/mL). The exposure with $SOA_{\beta PIN}$-SP resulted in a concentration-dependent ($R^2 = 0.8$, $p = 0.15$) higher release of MDA, with the greatest release of 23.3 ng/mL (monoculture) and 18 ng/mL (coculture) at dilution 1:1 (undiluted) (Figure 5A,B). Also here, the cells exposed to undiluted pure soot had only a slightly higher release of MDA in the monoculture (12 ng/mL; SP column in Table S6) and in the coculture (11 ng/mL; SP column in Table S7). These findings of elevated oxidative stress markers after SOA exposure motivated the genotoxicity investigation, given that oxidative stress can cause DNA damage. Interestingly, the exposure with $SOA_{\beta PIN}$-SP and SOA_{NAP}-SP resulted in a flatter response compared with the MDA results for the dilutions from 1:10 until 1:1 (undiluted) for $SOA_{\beta PIN}$-SP (9–11% DNA breaks) and from 1:30 until 1:1 (undiluted) for SOA_{NAP}-SP (13–16% DNA breaks) in A549 cells in both cell culture models (Figure 5C,D). Remarkably, after the exposure to SOA_{NAP}-SP, we detected a significantly higher percentage of DNA breaks in EA.hy926 cells that were not directly exposed to the aerosols [7% DNA breaks (1:3), $p = 0.02$ to 1:10 dilution; 8% DNA breaks (1:10), $p = 0.03$ to 1:10 dilution], suggesting possible secondary genotoxic effects. Because of space limitations in the ALI exposure system, the baseline of DNA breaks were defined from the incubator control, showing 4% of DNA breaks. Moreover, the exposure to undiluted SP resulted in 8% DNA breaks of A549 cells in both cell culture models and 4% for EA.hy926 cells (SP column in Tables S6 and S7).

Impacts on Inflammatory Response and Angiogenesis by Soot Aerosols Coated with SOAs

The exposure to $SOA_{\beta PIN}$-SP resulted in a non–concentration-dependent response with IL-8 concentrations between 335 pg/mL and 382 pg/mL in the monoculture. SOA_{NAP}-SP, however, induced a higher concentration-dependent ($R^2 = 0.92$, $p = 0.002$) IL-8 release with 600 pg/mL at the undiluted (1:1) aerosol (Figure 6A). The CA control was at 341 pg/mL and the exposure to undiluted SP showed no further difference in IL-8 release (360 pg/mL; SP column in Table S6). Contrary to the results regarding cytotoxicity and oxidative stress, SOA exposures of the coculture resulted in a significantly higher IL-8 release compared with the monoculture in both aerosols and all dilutions (Figure 6B). Exposure of the coculture to SP had no significant effect on IL-8 release (520 pg/mL; SP column in Table S7). Moreover, we wanted to elucidate how the greater secretion of inflammatory cytokines may directly regulate the functional crosstalk between A549 and EA.hy926 endothelial cells. By treating EA.hy926 cells with conditioned media from the A549 exposure to the different aerosols, we found that only media from the SOA_{NAP}-SP exposure induced a higher angiogenic potential of EA.hy926 (Figure 6C,D). We saw the same effect with the conditioned medium from the coculture exposed to SOA_{NAP}-SP, where we found a significant difference compared with the CA control and even $SOA_{\beta PIN}$-SP (Figure 6C,D). No angiogenic effect of the conditioned media collected after the exposure to SP from both cell culture models was observed (Tables S6 and S7).

Discussion

The present study provides new insights into the impact of SOA of anthropogenic and biogenic volatile organic precursors in the presence of soot core particles in airway ALI model systems at the cellular and molecular levels. It was observed that the formation of an SOA layer by adsorption and condensation on freshly emitted SP could cause a substantial aggravation of toxic effects, differing from combustion-only SP, which caused only slight toxic effects. Thus, it could be expected that the toxicity of primary particulate emissions in the ambient air during a medium strong atmospheric aging (e.g., equivalent to a range of a few days) was enhanced. Here, SOAs formed from a biogenic (β-pinene) or a combustion-related organic precursor component (naphthalene) were investigated and compared. We showed that an in-depth physicochemical aerosol characterization delivered relevant information for inhalation toxicology studies and that the different chemical identity of tested aerosols may explain the different toxicological outcomes. Cells exposed to SOA_{NAP}-SP—here as surrogate for atmospherically processed

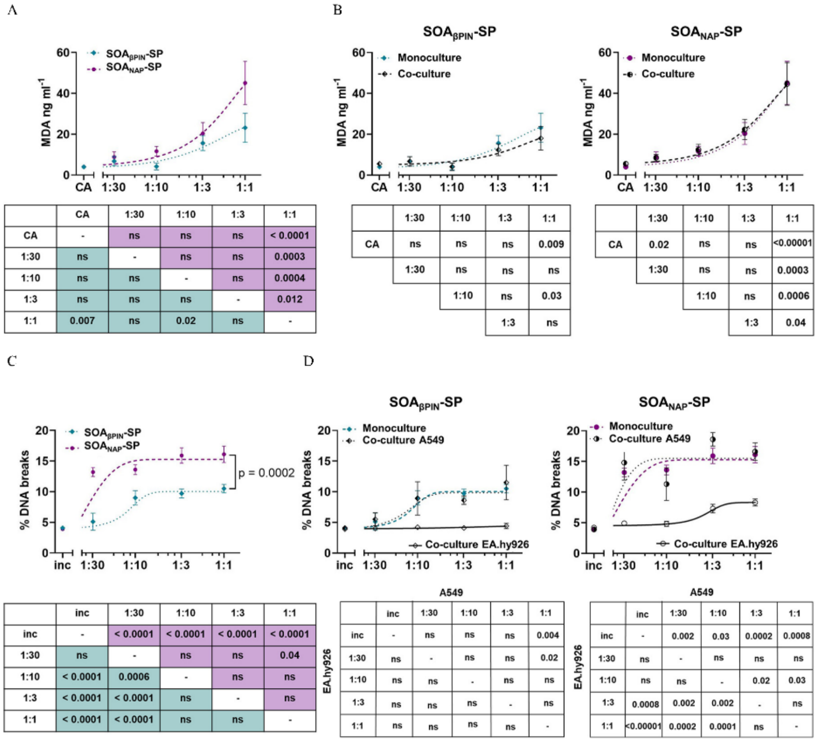

A

	CA	1:30	1:10	1:3	1:1
CA	-	ns	ns	ns	< 0.0001
1:30	ns	-	ns	ns	0.0003
1:10	ns	ns	-	ns	0.0004
1:3	ns	ns	ns	-	0.012
1:1	0.007	ns	0.02	ns	-

B, SOA$_{\beta PIN}$-SP

	1:30	1:10	1:3	1:1
CA	ns	ns	ns	0.009
	1:30	ns	ns	ns
		1:10	ns	0.03
			1:3	ns

B, SOA$_{NAP}$-SP

	1:30	1:10	1:3	1:1
CA	0.02	ns	ns	<0.00001
	1:30	ns	ns	0.0003
		1:10	ns	0.0006
			1:3	0.04

C

	inc	1:30	1:10	1:3	1:1
inc	-	< 0.0001	< 0.0001	< 0.0001	< 0.0001
1:30	ns	-	ns	ns	0.04
1:10	< 0.0001	0.0006	-	ns	ns
1:3	< 0.0001	< 0.0001	ns	-	ns
1:1	< 0.0001	< 0.0001	ns	ns	-

D, SOA$_{\beta PIN}$-SP (A549 / EA.hy926)

	inc	1:30	1:10	1:3	1:1
inc	-	ns	ns	ns	0.004
1:30	ns	-	ns	ns	0.02
1:10	ns	ns	-	ns	ns
1:3	ns	ns	ns	-	ns
1:1	ns	ns	ns	ns	-

D, SOA$_{NAP}$-SP (A549 / EA.hy926)

	inc	1:30	1:10	1:3	1:1
inc	-	0.002	0.03	0.0002	0.0008
1:30	ns	-	ns	ns	ns
1:10	ns	ns	-	0.02	0.03
1:3	0.0008	0.002	0.002	-	ns
1:1	<0.00001	0.0002	0.0001	ns	-

Figure 5. Induced oxidative stress and genotoxicity after 4-h exposure to SOA$_{NAP}$-SP and SOA$_{\beta PIN}$-SP. (A) MDA release (ng/mL) of A549 monoculture after the exposure to SOA$_{\beta PIN}$-SP and SOA$_{NAP}$-SP. (B) Comparison of MDA release (ng/mL) of the mono- and coculture after the exposure to SOA$_{\beta PIN}$-SP (left panel) and SOA$_{NAP}$-SP (right panel). Results are presented as absolute values ± SEM of *n* independent experiments (SOA$_{\beta PIN}$-SP: $n=3$, SOA$_{NAP}$-SP: $n=4$ for all dilutions, and CA ctrl: $n=7$) and dotted lines denote the regression line for the respective cell culture models and SOA forced through the CA ctrl (A,B). (C) DNA breaks (in %) of A549 monoculture after the exposure to SOA$_{\beta PIN}$-SP and SOA$_{NAP}$-SP. (D) Comparison of DNA breaks (in %) of the mono- and coculture (Coculture A549; Coculture EA.hy926) after the exposure to SOA$_{\beta PIN}$-SP (left panel) and SOA$_{NAP}$-SP (right panel). Results are presented as absolute values ± SEM of *n* independent experiments (SOA$_{\beta PIN}$-SP: $n=4$, SOA$_{NAP}$-SP: $n=5$ for all dilutions and inc ctrl: $n=3$) and dotted lines denote the regression line for the respective cell culture models and SOA forced through the CA ctrl (C and D). (A–D) Aerosol exposure groups were compared by performing a one-way ANOVA and statistical significance was calculated with multiple comparisons for the dilutions within one aerosol exposure group using the Bonferroni correction. *p*-Values are presented in the graph and in the tables below the graphs. Corresponding numerical data for (A–D) are shown in Tables S6 and S7. Note: ANOVA, analysis of variance; CA, clean air; ctrl, control; inc, incubator; MDA, malondialdehyde; SEM, standard error of the mean; SOA, secondary organic aerosol; SOA$_{NAP\text{-}SP}$/SOA$_{\beta PIN}$-SP, soot particles (SP, CAST soot; 1 mg/m^3) together with either naphthalene (4 mg/m^3) or β-pinene (4 mg/m^3) photochemically aged with OH radicals in a potential aerosol mass reactor.

combustion emissions—exhibited lower cell viability, higher oxidative stress, and genotoxicity and induced inflammatory and angiogenic responses compared with those exposed to SOA$_{\beta PIN}$-SP. In addition, concentration-dependent biological effects were observed following exposures to SOA$_{\beta PIN}$-SP and SOA$_{NAP}$-SP in several assays. Moreover, the different toxicological responses in the used mono- and coculture systems pointed out the importance of using multicellular *in vitro* models to improve the understanding of possible cellular crosstalk.

Chemical Distinct Characteristics of SOAs Responsible for Cellular Effects

Chemical and physical transformation of VOCs in the atmosphere lead to the formation of amorphous solid or semi-solid SOA particles (Dennis-Smither et al. 2014); however, investigations of the *in vitro* toxicity of primary combustion emissions (i.e., of SPs) photochemically aged in the presence of SOAs are scarce. The photochemical aging of both naphthalene and β-pinene in the presence of soot aerosols resulted in SPs coated with SOA materials that simulated aged atmospheric SPs. These aerosols had similar physicochemical characteristics in terms of mass, size distribution, particle number, particle geometric mean diameter, and atmospheric OH radical age, as well as EC and OC content. This is of great importance because it remains unclear whether SOAs with similar physical characteristics also cause similar biological effects (Burkholder et al. 2017; Künzi et al. 2015; National Academies of Sciences, Engineering, and Medicine 2016). The present study shows that SOA$_{NAP}$-SP compared with SOA$_{\beta PIN}$-SP had an adverse outcome on cell viability, oxidative stress, genotoxicity,

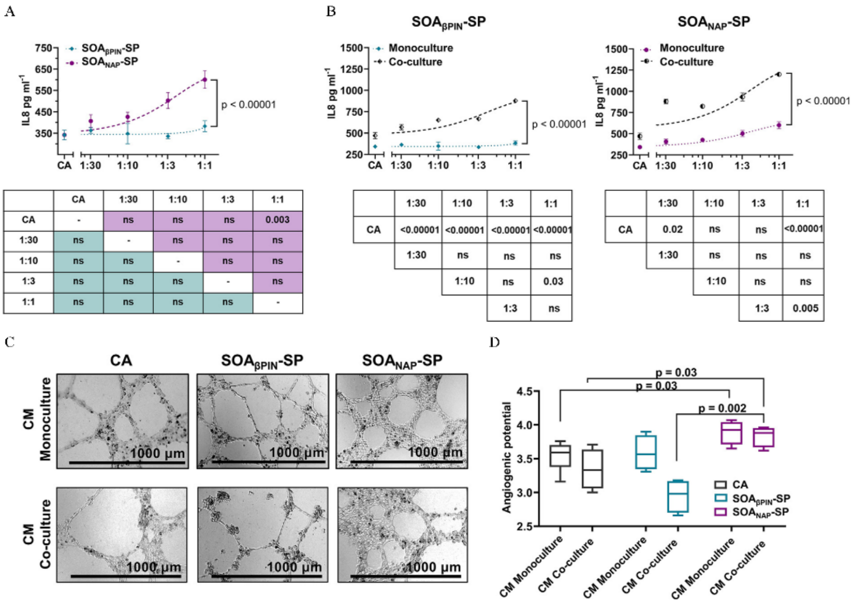

	CA	1:30	1:10	1:3	1:1
CA	-	ns	ns	ns	0.003
1:30	ns	-	ns	ns	ns
1:10	ns	ns	-	ns	ns
1:3	ns	ns	ns	-	ns
1:1	ns	ns	ns	ns	-

	1:30	1:10	1:3	1:1
CA	<0.00001	<0.00001	<0.00001	<0.00001
	1:30	ns	ns	ns
		1:10	ns	0.03
			1:3	ns

	1:30	1:10	1:3	1:1
CA	0.02	ns	ns	<0.00001
	1:30	ns	ns	ns
		1:10	ns	ns
			1:3	0.005

Figure 6. Inflammatory and angiogenic response triggered by SOA$_{NAP}$-SP and SOA$_{βPIN}$-SP. (A) IL-8 release (pg/mL) in A549 monoculture after the exposure to SOA$_{βPIN}$-SP and SOA$_{NAP}$-SP. (B) Comparison of IL-8 release (pg/mL) of the mono- and coculture after the exposure to SOA$_{βPIN}$-SP (left panel) and SOA$_{NAP}$-SP (right panel). (A,B) Results are presented as absolute values ± SEM of *n* independent experiments (SOA$_{βPIN}$-SP: $n = 4$, SOA$_{NAP}$-SP: $n = 5$ for all dilutions and CA ctrl: $n = 12$) and dotted lines denote the regression line for the respective cell culture models and SOA forced through the CA ctrl. Aerosol exposure groups were compared by performing a one-way ANOVA and statistical significance was calculated with multiple comparisons for the dilutions within one aerosol exposure group using the Bonferroni correction. *p*-Values are presented in the graph and in the tables below the graphs. (C,D) EA.hy926 cells were cultured for 24 h in media collected after the exposure to SOA$_{βPIN}$-SP and SOA$_{NAP}$-SP, as well as, CA control and then allowed to from tube structures on Matrigel for 24 h. Shown are representative images of EA.hy926 tubes from the indicated treatments (C) and quantification (D) of three independent experiments. Scale bar: 1,000 µm. Corresponding numerical data for (A–D) are shown in Tables S6 and S7. Note: ANOVA, analysis of variance; CA, clean air; CM, conditioned medium; ctrl, control; IL-8, interleukin-8; OH, hydroxyl; SEM, standard error of the mean; SOA, secondary organic aerosol; SOA$_{NAP}$-SP/SOA$_{βPIN}$-SP, soot particles (SP, CAST soot; 1 mg/m^3) together with either naphthalene (4 mg/m^3) or β-pinene (4 mg/m^3) photochemically aged with OH radicals in a potential aerosol mass reactor.

and inflammation consistent with previous studies (Chowdhury et al. 2018, 2019; Han et al. 2020) and, in addition, induced a pro-angiogenic potential in endothelial cells. This also holds true if we account for the calculated mass-specific cellular deposition, which was greater for SOA$_{NAP}$-SP. Even though this study confirmed the health risks of specific SOA compounds and pointed out the benefits of *in vitro* exposures in an ALI exposure system, it has its limitations. The applicability of ALI exposures to human exposures remains uncertain as long as it is difficult to determine respiratory tract deposition of airborne nanoparticles (Löndahl et al. 2014). However, calculations by Paur et al. (2011) for *in vitro* nanotoxicity studies suggested using ranges between 0.75 ng/cm^2 for realistic ambient exposure and 130 ng/cm^2 for worst-case occupational exposure representing daily dose levels. In the present study, the deposition ranged from 0.9 ng/cm^2 (1:30 dilution) to 28 ng/cm^2 (undiluted) for SOA$_{NAP}$-SP and from 0.6 ng/cm^2 (1:30 dilution) to 17 ng/cm^2 (undiluted) for SOA$_{βPIN}$-SP, covering realistic ambient exposure to mild occupational exposure conditions. Moreover, in a recent study, we showed that for aerosols with a comparable particle size distribution the difference between the deposition in lung tissue and ALI exposure system was less than a factor of 2 (Karg et al. 2020).

The chemical characterization revealed distinct qualitative differences in the chemical composition of SOA$_{βPIN}$-SP and SOA$_{NAP}$-SP, which is potentially responsible for the observed differences in the cellular toxicity. Thereby, the chemical composition of the derived SOA depended very much on the chemical functionality of the precursor and the low organic content of the SP seed. The detected chemical structures corresponded to typical first-generation degradation products of the respective precursor. For SOA$_{βPIN}$-SP, the major first-generation degradation product was nopinone in the particulate and acetone in the gas phase (Hohaus et al. 2015; Kaminski et al. 2017). In SOA$_{NAP}$-SP, we mostly found aromatic structures, which are well-known aging products originating from ring-opening and -retaining reactions of the aromatic precursors (Chan 2009). The photochemical degradation of naphthalene started with the addition of a OH radical, forming a hydroxyhexadienyl-type radical. From an intramolecular rearrangement, the first-generation product naphthol was formed. If the hydroxyhexadienyl-type radical reacts with oxygen, ring-opening structures may be formed, such as 2-formylcinnamaldehyde (Keyte et al. 2013). 1-Naphthol and 2-naphthol, which were generated in significant yields, may be further oxidized by other oxidants, such as hydroperoxides, and oxygen to naphthoquinones (Keyte et al. 2013). Upon further oxidation, early generation products increase in oxygen-containing moieties and could polymerize under the applied conditions (Kenseth et al. 2018; Sato et al. 2016).

Moreover, differences in volatility of the formed compounds from β-pinene and naphthalene aging could be derived from the GC × GC signatures, generally indicating more volatile compounds for $SOA_{\beta PIN}$-SP. In SOA_{NAP}-SP, the aromatic structure was usually maintained and dominated the SOA composition, for which toxic effects on human health are well documented and include carcinogenic and mutagenic effects, as well as reproductive defects (Drwal et al. 2019; Gaspari et al. 2003; Perera et al. 2002).

Concerning elemental aerosol particle composition, the O/C value for SOA_{NAP}-SP (0.77) exceeded that of $SOA_{\beta PIN}$-SP (0.61), agreeing with a previous study about the photooxidation of naphthalene and α-pinene (Chowdhury 2018). In addition, the average carbon oxidation state (OS_C), which is calculated as $2 \times O/C - H/C$ was higher for SOA_{NAP}-SP (0.5) than for $SOA_{\beta PIN}$-SP (–0.43). SOA_{NAP}-SP, with 0.3 to 0.7, showed a similar range of OS_C as reported in the literature for emissions from residential logwood combustion (Hartikainen et al. 2020) and gasoline direct injection vehicles (Pieber et al. 2018) of the same photochemical age (~3 equivalent days). The OS_C increases upon oxidation owing to the formation of carbon–oxygen bonds and/or the breaking of carbon–hydrogen bonds through, for example, functionalization or fragmentation reactions (Kroll et al. 2011). In this context, the oxidative addition of polar functional groups to the carbon backbone could be observed for both aerosol types.

We found that $SOA_{\beta PIN}$-SP appeared well within the triangular space spanned by the relative fractions of *m/z* 43 vs. *m/z* 44, representing ambient organic aerosols from global AMS field studies (Ng et al. 2011), thus supporting its use as a surrogate for atmospherically processed combustion emissions. The difference in O/C between SOA_{NAP}-SP and $SOA_{\beta PIN}$-SP might be a consequence of the slightly higher photochemical age of the SOA_{NAP}-SP or differences in formation pathways, including the release of secondary VOCs from fragmentation. In contrast to the data from AMS measurements, for which correction procedures were developed to improve the accuracy of the derived elemental ratios (Canagaratna et al. 2015), in the data evaluation from the DIP measurement the peak at *m/z* 43.9898 of CO_2^+, which increases from, for example, thermal decarboxylation of carboxylic acids in the SOAs, is not considered because of a too high peak intensity from background air and the associated high uncertainty of the result. Consequently, the result of higher O/C for $SOA_{\beta PIN}$-SP than for SOA_{NAP}-SP could indicate a higher abundance of carboxylic groups in SOA_{NAP}-SP, represented by the AMS, but not by DIP, measurements. Future studies beyond the scope of this manuscript will discuss data from AMS and DIP in more detail.

It is possible that the aerosol's toxicity largely depends on the degree of oxidation induced by atmospheric aging. Thus, the hazards of functional groups of the detected organic compounds could have a decisive impact. Studies on PAHs, such as naphthalene, have demonstrated specific toxic effects on cells (IARC 2010), and these effects may be enhanced by their oxidized derivatives (Chowdhury et al. 2018). However, it has to be noted that this increased toxicity reflected specific oxidation stages and could change with oxidation mechanism given that studies have also shown a declined toxicity during aging for naphthalene (Han et al. 2020) or hydrocarbons (Jiang and Jang 2018). For selected terpenes emitted from coniferous plants, including also β-pinene, no adverse cytotoxic or genotoxic effects in A549 human lung cells were found in an ALI exposure study by Gminski et al. (2010), although mutagenic and carcinogenic effects were described for specific compounds such as α, β-unsaturated aldehydes and 2-octen (Gminski et al. 2010). In our study, there were similarities between the abundance of most functional groups and related compound classes in $SOA_{\beta PIN}$-SP and SOA_{NAP}-SP, such as furans, aldehydes, and ketones. The oxidation of naphthalene may lead to first-generation open-ring dicarbonyl products and closed-ring epoxide products (Wang et al. 2007). A recent *in vitro* proteome-wide study by Han et al. (2020) pointed out the importance of short-lived unsaturated carbonyls in aged naphthalene as the main toxic components at the posttranslational level. Furthermore, the oxidation of furan-containing compounds favored the formation of epoxides, which are associated with enhanced harmful cellular effects (Peterson 2013; Tăbăran et al. 2019). The intracellular oxidation of aldehyde groups by enzymes of the aldehyde dehydrogenase family has been associated with adverse effects on various cell types, especially concerning tumor initiation, metastasis, and therapeutic resistance (Ma and Allan 2011; Rebollido-Rios et al. 2020; Rodriguez-Torres and Allan 2016). Photooxidation of β-pinene resulted in nopinone as a major first-generation product, which in a second step may form nine-carbon multifunctional compounds (Sato et al. 2016). In contrast to aldehydes, ketones are less reactive and less electrophilic, characteristics that can be associated with lower toxicological effects. However, minor changes in the molecular structure could be decisive for adverse outcomes (LoPachin and Gavin 2014; Schwöbel et al. 2011). Future studies are warranted to evaluate the particle cellular uptake of the tested aerosols to better understand the bioaccessibility of specific chemical compositions and their cellular effects.

Our results indicate that the differential toxicity of the precursors [half maximal oral lethal dose (LD_{50}) (rat) naphthalene: $2{,}000\,mg/m^3$ (U.S. EPA 2021b); oral LD_{50} (rat) β-pinene: $5{,}000\,mg/m^3$ (U.S. EPA 2021a)] was retained after an equivalent photochemical age of 3 d. However, depending on particle size, altitude, and atmospheric compartment, the lifetime of a particle spans a range from a few hours up to 2 wk (Raes et al. 2000; Williams et al. 2002). From a chemical perspective, atmospheric aging increased the O/C ratio of any organic aerosol constituent toward the limit of 2 determined by CO_2, steadily increasing their functionalization (Kroll et al. 2011); yet AMS analysis of organic aerosol from the Northern Hemisphere did not exceed O/C ratios of 1.2 (Ng et al. 2010), also not for highly oxidized molecules (Ehn et al. 2014). Moreover, atmospheric aging involves several processes and conditions, such as distinct differences during day- and nighttime or ambient levels and distributions of nitrogen oxides (NO_x) species, triggering different reaction pathways. There is particularly strong evidence that exposure to nitrogen dioxide is associated with adverse effects on human health (Atkinson et al. 2018; Mills et al. 2015) and leads to the formation of atmospheric mutagens from PAHs (Atkinson and Arey 1994). However, the general role of NO_x in atmospheric aging on the toxicity of SOA is in the early stage of research (Chowdhury et al. 2019). Hence, it remains an unanswered question if, when, and how different structural properties of SOA precursors are influencing the chemical and toxicological properties of the respective SOA during photochemical aging.

The Importance of Using Mono- and Coculture Systems in Aerosol Studies

Although monocultures provide information on direct toxicological effects of nanomaterials, recent studies have pointed out that multicellular culture systems are important tools for modeling an *in vivo* physiological cellular environment, including the interaction between different cell lines (Bengalli et al. 2013; Klein et al. 2013; Lacroix et al. 2018). It is well known that, apart from pulmonary adverse health effects, $\text{PM}_{2.5}$ can also induce an increased risk for cardiovascular morbidity and mortality (Brook et al. 2010). Dysfunction of endothelial cells in particular is suspected to play a major role in inducing cardiovascular injury after the inhalation of $\text{PM}_{2.5}$ in a cohort of healthy individuals (Pope et al. 2016), which highlights the importance of the used epithelial–endothelial coculture in our study to depict possible underlying mechanisms.

In our epithelial monoculture, SOA_{NAP}-SP induced a 10-fold higher, and $\text{SOA}_{\beta\text{PIN}}$-SP a 7-fold higher, release of LDH in the undiluted aerosol compared with CA controls. Interestingly, the relative difference in LDH was lower in our epithelial–endothelial coculture (5-fold) than in the monoculture after the exposure to both undiluted aerosols. It is conceivable that this effect was the result of an enhanced physical barrier due to the addition of endothelial cells on the basolateral side of the membrane. Notably, the diffusion of particle-related H_2O_2 content is presumed to represent a main pathway for inducing intracellular ROS formation (Liu et al. 2020). It was already shown that the SOA oxidative potential depends on the hydrocarbon precursor identity, with biogenic SOA having a lower water-soluble oxidative potential than anthropogenic SOA (Tuet et al. 2017). Indeed, we found a greater peroxide content in SOA_{NAP}-SP (~ 3.5 times higher compared with $\text{SOA}_{\beta\text{PIN}}$-SP) and a higher abundance of MDA (~ 2 times higher compared with $\text{SOA}_{\beta\text{PIN}}$-SP in the undiluted aerosol), which is an end product of the lipid peroxidation induced by free radicals (Ayala et al. 2014), in the cell culture medium of both mono- and cocultures. Assuming an enhanced physical barrier in the coculture system, but observing no differences in MDA release in the mono- and cocultures after the exposure to the tested SOAs, suggested an additional release of MDA from endothelial cells, possibly induced by oxidized phospholipids and cytotoxic compounds of the epithelial cells (Landar et al. 2006). Epidemiological and *in vivo* studies with $\text{PM}_{2.5}$ have identified inflammatory responses as a major adverse outcome pathway (Yan et al. 2016), and *in vitro* studies have highlighted the impact of endothelial cells in secreting pro-inflammatory mediators (Karki and Birukov 2020). In line with our observations of SOA_{NAP}-SP inducing cellular cytotoxicity and oxidative stress, we observed a greater release of IL-8 in the monoculture after the exposure to SOA_{NAP}-SP ($\approx$ 2-fold higher in the undiluted aerosol) compared with $\text{SOA}_{\beta\text{PIN}}$-SP (no difference in the undiluted aerosol). In addition, we showed higher secretion of IL-8 in the coculture compared with the monoculture system ($\approx$ 2-fold higher after the exposure to undiluted $\text{SOA}_{\beta\text{PIN}}$-SP and SOA_{NAP}-SP). Inflammation and oxidative stress are main drivers for the induction of DNA strand breaks (Møller et al. 2014). Consistent with our previous shown results on MDA and IL-8 release, we observed DNA breaks of $\approx 10\%$ for undiluted $\text{SOA}_{\beta\text{PIN}}$-SP and $\approx 16\%$ for undiluted SOA_{NAP}-SP in the monoculture. Moreover, experiments with conditioned media-based techniques revealed secondary genotoxic effects of nanomaterials (Åkerlund et al. 2019; Evans et al. 2019). To the best of our knowledge, this is the first study that showed secondary genotoxic effects on cells in a coculture system at ALI where a cell–cell interplay was provided. Here, we observed genotoxic effects on endothelial cells ($\approx 8\%$ DNA breaks) after the exposure with SOA_{NAP}-SP [undiluted (1:1) and 1:3 diluted] but not after $\text{SOA}_{\beta\text{PIN}}$-SP exposures. Further studies should investigate this observation to exclude a possible translocation of PM through the insert membrane and thus a direct effect on endothelial cells (Wang et al. 2019). However, the enhanced release of IL-8 in the coculture cell model compared with the monoculture following SOA_{NAP}-SP exposure, supported our assumption of secondary genotoxic effects given that cytokines may promote genomic instability and IL-8 is a pro-angiogenic factor, potentially explaining the observed cross-activation of endothelial cells (Aivaliotis et al. 2012; Heidemann et al. 2003). Furthermore, the angiogenesis assay with a conditioned media-based approach affirmed the cross-activation of endothelial cells after the exposure to SOA_{NAP}-SP. No difference in the angiogenic potential between the conditioned media of the mono- and cocultures was observed, indicating that besides IL-8 other pro-angiogenic factors and oxidative stress may also play a decisive role (Kim and Byzova 2014). The conditioned media of the coculture exposed to $\text{SOA}_{\beta\text{PIN}}$-SP induced a decreased angiogenic potential, whereas in the conditioned media of the monoculture, no difference from the control was detected. Future studies beyond the scope of this manuscript should investigate how $\text{SOA}_{\beta\text{PIN}}$-SP differently altered the angiogenic potential of endothelial cells in our experimental setup. In general, dysfunction of endothelial cells is associated with adverse health outcomes. Although a reduced angiogenic potential of endothelial cells after the inhalation of $\text{PM}_{2.5}$ has been observed in previous studies (Lan et al. 2020), and can be an indication for a compromised ventilation–perfusion ratio of the lung, an enhanced angiogenic potential is one of the hallmarks for several interstitial lung diseases (Ackermann et al. 2020).

Nonetheless, although coculture models are enhancing *in vitro* studies by including the interaction between cell types, to what extent this may reflect an *in vivo* physiological cellular environment is always of concern and further optimization and standardization are needed. For instance, although our coculture model focused on the deposition of inhaled $\text{PM}_{2.5}$ on epithelial cells, it is well accepted that resident immune cells are also directly targeted upon inhalation and thus, including immune competent cells would be an improvement of the model. Moreover, A549 cells at ALI are known to partially mimic the property of an alveolar epithelium (Wu et al. 2017a), but drawbacks include their low expression of tight junctions or adherence proteins and their inability to form a fully differentiated and polarized epithelium (Papazian et al. 2016). Therefore, the additional usage of different epithelial cells, which could represent a heterogeneous population of several different epithelial cell types, would have benefited our study. However, owing to the complexity of our experimental setup, we found with A549 a robust cell line that is suitable for large and repetitive studies. Further studies comparing simultaneous performed aerosol exposures *in vivo* with different *in vitro* cell culture systems should help to extrapolate within the framework of replacement, reduction, and refinement.

Conclusions

The ubiquitous layer of SOA components that condenses onto primary particles can have a strong impact on PM toxicity. In particular, SOA-coated combustion SPs showed higher toxicity compared with fresh combustion SPs. This emphasizes the importance of atmospheric transformations for the toxicity and adverse health effects of ambient aerosol particles and may help to explain the high numbers of air-pollution related mortality and morbidity cases identified by epidemiological studies. This study also demonstrated that different SOA precursors led to different toxicological outcomes at comparable exposure conditions. A typical anthropogenic, aromatic SOA precursor (naphthalene) mixed with SPs, led to condensation of higher oxidized, aromatic SOAs of higher oxidative potential on the SPs and induced stronger toxic effects in the investigated lung cell models. In contrast, a typical biogenic, aliphatic SOA precursor (β-pinene) led to condensation of less oxidized, aliphatic SOAs of lower oxidative potential on the SPs and induced milder toxic effects in the investigated lung cell models. Our findings highlight the role of different structural–chemical properties of photochemically aged SOAs for *in vitro* toxicological outcomes. Moreover, we emphasize the importance of multicellular culture systems to model a normal physiological cell environment with intercellular crosstalk. Future studies will also focus on an in-depth characterization of the used aerosols and of aerosol-specific effects on transcriptomic and proteomic outcomes.

Acknowledgments

S.D.B., H.C., T.H., A.K.-S., Y.R. and R.Z. conceived and supervised the study. S.Ba., S.Bi., J.B., C.B., S.D.B., R.B., A.B., X.C., H.C., T.G., G.J., S.J., E.H, T.H., A.H., U.K., M.K., T.K., A.K.-S., E.K., P.M., A.Me, S.Oe, S.O., J.O., J.P., A.P., N.R., Y.R., J.S.-K., O.S., M.S., Z.-H.Z., T.Z., E.J.Z. and R.Z. designed and performed the experiments. S.Ba., C.B., S.D.B., X.C., H.C., G.J., E.H, U.K., E.K., A.Ma, S.O., A.P., N.R. and M.S. analyzed and evaluated the data. A.K.-S., Y.R, and R.Z. provided funding; S.D.B., H.C., T.G., E.H, S.O., M.S. and R.Z. wrote the paper with input and approval from all the authors.

We thank the Helmholtz International Laboratory aeroHEALTH (InterLabs-0005; https://www.aerohealth.eu), the Helmholtz Association of German Research Centers and the Helmholtz Virtual Institute of Complex Systems in Environmental Health (InhaleHICE) for granting this project. Y.R. acknowledges support from the Estate of Raymond Lapon, the Estate of Betty Weneser, and Seed for Peace. Inc. C.B. acknowledges the support of the Swiss National Science Foundation (grant P2FRP3_178112). We also thank W.H. Brune (Pennsylvania State University) for providing the potential aerosol mass (PAM) reactor, which was funded by the University of Rostock.

References

Ackermann M, Stark H, Neubert L, Schubert S, Borchert P, Linz F, et al. 2020. Morphomolecular motifs of pulmonary neoangiogenesis in interstitial lung diseases. Eur Respir J 55(3):1900933, PMID: 31806721, https://doi.org/10.1183/13993003.00933-2019.

Aivaliotis IL, Pateras IS, Papaioannou M, Glytsou C, Kontzoglou K, Johnson EO, et al. 2012. How do cytokines trigger genomic instability? J Biomed Biotechnol 2012:536761, PMID: 22754280, https://doi.org/10.1155/2012/536761.

Åkerlund E, Islam MS, McCarrick S, Alfaro-Moreno E, Karlsson HL. 2019. Inflammation and (secondary) genotoxicity of Ni and NiO nanoparticles. Nanotoxicology 13(8):1060–1072, PMID: 31322448, https://doi.org/10.1080/17435390.2019.1640908.

Andreae MO, Gelencsér A. 2006. Black carbon or brown carbon? The nature of light-absorbing carbonaceous aerosols. Atmos Chem Phys 6(10):3131–3148, https://doi.org/10.5194/acp-6-3131-2006.

Aranda E, Owen GI. 2009. A semi-quantitative assay to screen for angiogenic compounds and compounds with angiogenic potential using the EA.hy926 endothelial cell line. Biol Res 42(3):377–389, PMID: 19915746, https://doi.org/10.4067/S0716-97602009000300012.

Arashiro M, Lin YH, Zhang Z, Sexton KG, Gold A, Jaspers I, et al. 2018. Effect of secondary organic aerosol from isoprene-derived hydroxyhydroperoxides on the expression of oxidative stress response genes in human bronchial epithelial cells. Environ Sci Process Impacts 20(2):332–339, PMID: 29292423, https://doi.org/10.1039/c7em00439g.

Atkinson R, Arey J. 1994. Atmospheric chemistry of gas-phase polycyclic aromatic hydrocarbons: formation of atmospheric mutagens. Environ Health Perspect 102(suppl 4):117–126, PMID: 7821285, https://doi.org/10.1289/ehp.94102s4117.

Atkinson R, Arey J. 2003. Atmospheric degradation of volatile organic compounds. Chem Rev 103(12):4605–4638, PMID: 14664626, https://doi.org/10.1021/cr0206420.

Atkinson RW, Butland BK, Anderson HR, Maynard RL. 2018. Long-term concentrations of nitrogen dioxide and mortality: a meta-analysis of cohort studies. Epidemiology 29(4):460–472, PMID: 29746370, https://doi.org/10.1097/EDE.0000000000000847.

Atkinson R, Carter WPL. 1984. Kinetics and mechanisms of the gas-phase reactions of ozone with organic compounds under atmospheric conditions. Chem Rev 84(5):437–470, https://doi.org/10.1021/cr00063a002.

Ayala A, Muñoz MF, Argüelles S. 2014. Lipid peroxidation: production, metabolism, and signaling mechanisms of malondialdehyde and 4-hydroxy-2-nonenal. Oxid Med Cell Longev 2014:360438, PMID: 24999379, https://doi.org/10.1155/2014/360438.

Barmet P, Dommen J, DeCarlo PF, Tritscher T, Praplan AP, Platt SM, et al. 2012. OH clock determination by proton transfer reaction mass spectrometry at an environmental chamber. Atmos Meas Tech 5(3):647–656, https://doi.org/10.5194/amt-5-647-2012.

Barosova H, Meldrum K, Karakocak BB, Balog S, Doak SH, Petri-Fink A, et al. 2021. Inter-laboratory variability of A549 epithelial cells grown under submerged and air-liquid interface conditions. Toxicol In Vitro 75:105178, PMID: 33905840, https://doi.org/10.1016/j.tiv.2021.105178.

Bengalli R, Mantecca P, Camatini M, Gualtieri M. 2013. Effect of nanoparticles and environmental particles on a cocultures model of the air-blood barrier. Biomed Res Int 2013:801214, PMID: 23509780, https://doi.org/10.1155/2013/801214.

Bond TC, Doherty SJ, Fahey DW, Forster PM, Berntsen T, DeAngelo BJ, et al. 2013. Bounding the role of black carbon in the climate system: a scientific assessment. J Geophys Res Atmos 118(11):5380–5552, https://doi.org/10.1002/jgrd.50171.

Brook RD, Rajagopalan S, Pope CA III, Brook JR, Bhatnagar A, Diez-Roux AV, et al. 2010. Particulate matter air pollution and cardiovascular disease: an update to the scientific statement from the American Heart Association. Circulation 121(21):2331–2378, PMID: 20458016, https://doi.org/10.1161/CIR.0b013e3181dbece1.

Bruns EA, El Haddad I, Keller A, Klein F, Kumar NK, Pieber SM, et al. 2015. Inter-comparison of laboratory smog chamber and flow reactor systems on organic aerosol yield and composition. Atmos Meas Tech 8(6):2315–2332, https://doi.org/10.5194/amt-8-2315-2015.

Burkholder JB, Abbatt JPD, Barnes I, Roberts JM, Melamed ML, Ammann M, et al. 2017. The essential role for laboratory studies in atmospheric chemistry. Environ Sci Technol 51(5):2519–2528, PMID: 28169528, https://doi.org/10.1021/acs.est.6b04947.

Canagaratna MR, Jimenez JL, Kroll JH, Chen Q, Kessler SH, Massoli P, et al. 2015. Elemental ratio measurements of organic compounds using aerosol mass spectrometry: characterization, improved calibration, and implications. Atmos Chem Phys 15(1):253–272, https://doi.org/10.5194/acp-15-253-2015.

Chan AWH, Kautzman KE, Chhabra PS, Surratt JD, Chan MN, Crounse JD, et al. 2009. Secondary organic aerosol formation from photooxidation of naphthalene and alkylnaphthalenes: implications for oxidation of intermediate volatility organic compounds (IVOCs). Atmos Chem Phys 9(9):3049–3060, https://doi.org/10.5194/acp-9-3049-2009.

Chen CL, Kacarab M, Tang P, Cocker DR III. 2016. SOA formation from naphthalene, 1-methylnaphthalene, and 2-methylnaphthalene photooxidation. Atmos Environ 131:424–433, https://doi.org/10.1016/j.atmosenv.2016.02.007.

Chow JC, Watson JG, Chen LWA, Chang MCO, Robinson NF, Trimble D, et al. 2007. The IMPROVE_A temperature protocol for thermal/optical carbon analysis: maintaining consistency with a long-term database. J Air Waste Manag Assoc 57(9):1014–1023, PMID: 17912920, https://doi.org/10.3155/1047-3289.57.9.1014.

Chowdhury PH, He Q, Carmieli R, Li C, Rudich Y, Pardo M. 2019. Connecting the oxidative potential of secondary organic aerosols with reactive oxygen species in exposed lung cells. Environ Sci Technol 53(23):13949–13958, PMID: 31652049, https://doi.org/10.1021/acs.est.9b04449.

Chowdhury PH, He QF, Male TL, Brune WH, Rudich Y, Pardo M. 2018. Exposure of lung epithelial cells to photochemically aged secondary organic aerosol shows increased toxic effects. Environ Sci Technol Lett 5(7):424–430, https://doi.org/10.1021/acs.estlett.8b00256.

Chughtai AR, Kim JM, Smith DM. 2003. The effect of temperature and humidity on the reaction of ozone with combustion soot: implications for reactivity near the tropopause. J Atmos Chem 45(3):231–243, https://doi.org/10.1023/A:1024250505886.

Cohen AJ, Brauer M, Burnett R, Anderson HR, Frostad J, Estep K, et al. 2017. Estimates and 25-year trends of the global burden of disease attributable to ambient air pollution: an analysis of data from the Global Burden of Diseases Study 2015. Lancet 389(10082):1907–1918, PMID: 28408086, https://doi.org/10.1016/S0140-6736(17)30505-6.

DeCarlo PF, Kimmel JR, Trimborn A, Northway MJ, Jayne JT, Aiken AC, et al. 2006. Field-deployable, high-resolution, time-of-flight aerosol mass spectrometer. Anal Chem 78(24):8281–8289, PMID: 17165817, https://doi.org/10.1021/ac061249n.

Deng X, Zhang F, Rui W, Long F, Wang L, Feng Z, et al. 2013. $PM_{2.5}$-induced oxidative stress triggers autophagy in human lung epithelial A549 cells. Toxicol In Vitro 27(6):1762–1770, PMID: 23685237, https://doi.org/10.1016/j.tiv.2013.05.004.

Dennis-Smither BJ, Marshall FH, Miles REH, Preston TC, Reid JP. 2014. Volatility and oxidative aging of aqueous maleic acid aerosol droplets and the dependence on relative humidity. J Phys Chem A 118(30):5680–5691, PMID: 25003240, https://doi.org/10.1021/jp504823j.

Dergham M, Lepers C, Verdin A, Billet S, Cazier F, Courcot D, et al. 2012. Prooxidant and proinflammatory potency of air pollution particulate matter ($PM_{2.5–0.3}$) produced in rural, urban, or industrial surroundings in human bronchial epithelial cells (BEAS-2B). Chem Res Toxicol 25(4):904–919, PMID: 22404339, https://doi.org/10.1021/tx200529v.

Di Bucchianico S, Cappellini F, Le Bihanic F, Zhang Y, Dreij K, Karlsson HL. 2017. Genotoxicity of TiO_2 nanoparticles assessed by mini-gel comet assay and micronucleus scoring with flow cytometry. Mutagenesis 32(1):127–137, PMID: 27382040, https://doi.org/10.1093/mutage/gew030.

Drwal E, Rak A, Gregoraszczuk EL. 2019. Review: polycyclic aromatic hydrocarbons (PAHs)—action on placental function and health risks in future life of newborns. Toxicology 411:133–142, PMID: 30321648, https://doi.org/10.1016/j.tox.2018.10.003.

Eaves LA, Smeester L, Hartwell HJ, Lin YH, Arashiro M, Zhang Z, et al. 2020. Isoprene-derived secondary organic aerosol induces the expression of microRNAs associated with inflammatory/oxidative stress response in lung cells. Chem Res Toxicol 33(2):381–387, PMID: 31765140, https://doi.org/10.1021/acs.chemrestox.9b00322.

Ehn M, Thornton JA, Kleist E, Sipilä M, Junninen H, Pullinen I, et al. 2014. A large source of low-volatility secondary organic aerosol. Nature 506(7489):476–479, PMID: 24572423, https://doi.org/10.1038/nature13032.

Evans SJ, Clift MJD, Singh N, Wills JW, Hondow N, Wilkinson TS, et al. 2019. In vitro detection of in vitro secondary mechanisms of genotoxicity induced by engineered nanomaterials. Part Fibre Toxicol 16(1):8, PMID: 30760282, https://doi.org/10.1186/s12989-019-0291-7.

Faiola CL, Jobson BT, VanReken TM. 2015. Impacts of simulated herbivory on volatile organic compound emission profiles from coniferous plants. Biogeosciences 12(2):527–547, https://doi.org/10.5194/bg-12-527-2015.

Feng S, Gao D, Liao F, Zhou F, Wang X. 2016. The health effects of ambient $PM_{2.5}$ and potential mechanisms. Ecotoxicol Environ Saf 128:67–74, PMID: 26896893, https://doi.org/10.1016/j.ecoenv.2016.01.030.

Gaspari L, Chang SS, Santella RM, Garte S, Pedotti P, Taioli E. 2003. Polycyclic aromatic hydrocarbon-DNA adducts in human sperm as a marker of DNA damage and infertility. Mutat Res 535(2):155–160, PMID: 12581533, https://doi.org/10.1016/S1383-5718(02)00297-8.

Gminski R, Tang T, Mersch-Sundermann V. 2010. Cytotoxicity and genotoxicity in human lung epithelial A549 cells caused by airborne volatile organic compounds emitted from pine wood and oriented strand boards. Toxicol Lett 196(1):33–41, PMID: 20362040, https://doi.org/10.1016/j.toxlet.2010.03.015.

Guenther A, Hewitt CN, Erickson D, Fall R, Geron C, Graedel T, et al. 1995. A global model of natural volatile organic compound emissions. J Geophys Res 100(D5):8873–8892, https://doi.org/10.1029/94JD02950.

Guenther AB, Jiang X, Heald CL, Sakulyanontvittaya T, Duhl T, Emmons LK, et al. 2012. The Model of Emissions of Gases and Aerosols from Nature version 2.1 (MEGAN2.1): an extended and updated framework for modeling biogenic emissions. Geosci Model Dev 5(6):1471–1492, https://doi.org/10.5194/gmd-5-1471-2012.

Halappanavar S, van den Brule S, Nymark P, Gaté L, Seidel C, Valentino S, et al. 2020. Adverse outcome pathways as a tool for the design of testing strategies to support the safety assessment of emerging advanced materials at the nanoscale. Part Fibre Toxicol 17(1):16, PMID: 32450889, https://doi.org/10.1186/s12989-020-00344-4.

Hallquist M, Wenger JC, Baltensperger U, Rudich Y, Simpson D, Claeys M, et al. 2009. The formation, properties and impact of secondary organic aerosol: current and emerging issues. Atmos Chem Phys 9(14):5155–5236, https://doi.org/10.5194/acp-9-5155-2009.

Han J, Wang S, Yeung K, Yang D, Gu W, Ma Z, et al. 2020. Proteome-wide effects of naphthalene-derived secondary organic aerosol in BEAS-2B cells are caused by short-lived unsaturated carbonyls. Proc Natl Acad Sci U S A 117(41):25386–25395, PMID: 32989125, https://doi.org/10.1073/pnas.2001378117.

Hartikainen A, Tiitta P, Ihalainen M, Yli-Pirilä P, Orasche J, Czech H, et al. 2020. Photochemical transformation of residential wood combustion emissions: dependence of organic aerosol composition on OH exposure. Atmos Chem Phys 20(11):6357–6378, https://doi.org/10.5194/acp-20-6357-2020.

Heidemann J, Ogawa H, Dwinell MB, Rafiee P, Maaser C, Gockel HR, et al. 2003. Angiogenic effects of interleukin 8 (CXCL8) in human intestinal microvascular endothelial cells are mediated by CXCR2. J Biol Chem 278(10):8508–8515, PMID: 12496258, https://doi.org/10.1074/jbc.M208231200.

Heyder J. 2004. Deposition of inhaled particles in the human respiratory tract and consequences for regional targeting in respiratory drug delivery. Proc Am Thorac Soc 1(4):315–320, PMID: 16113452, https://doi.org/10.1513/pats.200409-046TA.

Hilton G, Barosova H, Petri-Fink A, Rothen-Rutishauser B, Bereman M. 2019. Leveraging proteomics to compare submerged versus air-liquid interface carbon nanotube exposure to a 3D lung cell model. Toxicol In Vitro 54:58–66, PMID: 30243732, https://doi.org/10.1016/j.tiv.2018.09.010.

Hohaus T, Gensch I, Kimmel J, Worsnop DR, Kiendler-Scharr A. 2015. Experimental determination of the partitioning coefficient of β-pinene oxidation products in SOAs. Phys Chem Phys 17(22):14796–14804, PMID: 25975709, https://doi.org/10.1039/c5cp01608h.

Huang RJ, Zhang Y, Bozzetti C, Ho KF, Cao JJ, Han Y, et al. 2014. High secondary aerosol contribution to particulate pollution during haze events in China. Nature 514(7521):218–222, PMID: 25231863, https://doi.org/10.1038/nature13774.

IARC (IARC Working Group on the Evaluation of Carcinogenic Risks to Humans). 2010. Some non-heterocyclic polycyclic aromatic hydrocarbons and some related exposures. IARC Monogr Eval Carcinog Risks Hum 92:1–853, PMID: 21141735.

Ihantola T, Di Bucchianico S, Happo M, Ihalainen M, Uski O, Bauer S, et al. 2020. Influence of wood species on toxicity of log-wood stove combustion aerosols: a parallel animal and air-liquid interface cell exposure study on spruce and pine smoke. Part Fibre Toxicol 17(1):27, PMID: 32539833, https://doi.org/10.1186/s12989-020-00355-1.

Janssen NAH, Hoek G, Simic-Lawson M, Fischer P, van Bree L, ten Brink H, et al. 2011. Black carbon as an additional indicator of the adverse health effects of airborne particles compared with PM_{10} and $PM_{2.5}$. Environ Health Perspect 119(12):1691–1699, PMID: 21810552, https://doi.org/10.1289/ehp.1003369.

Jayne JT, Leard DC, Zhang XF, Davidovits P, Smith KA, Kolb CE, et al. 2000. Development of an aerosol mass spectrometer for size and composition analysis of submicron particles. Aerosol Sci Technol 33(1–2):49–70, https://doi.org/10.1080/027868200410840.

Jia C, Batterman S. 2010. A critical review of naphthalene sources and exposures relevant to indoor and outdoor air. Int J Environ Res Public Health 7(7):2903–2939, PMID: 20717549, https://doi.org/10.3390/ijerph7072903.

Jiang H, Jang M. 2018. Dynamic oxidative potential of atmospheric organic aerosol under ambient sunlight. Environ Sci Technol 52(13):7496–7504, PMID: 29772167, https://doi.org/10.1021/acs.est.8b00148.

Käfer U, Gröger T, Rüger CP, Czech H, Saraji-Bozorgzad M, Wilharm T, et al. 2019. Direct inlet probe–high-resolution time-of-flight mass spectrometry as fast technique for the chemical description of complex high-boiling samples. Talanta 202:308–316, PMID: 31171187, https://doi.org/10.1016/j.talanta.2019.05.030.

Kaminski M, Fuchs H, Acir IH, Bohn B, Brauers T, Dorn HP, et al. 2017. Investigation of the β-pinene photooxidation by OH in the atmosphere simulation chamber SAPHIR. Atmos Chem Phys 17(11):6631–6650, https://doi.org/10.5194/acp-17-6631-2017.

Kang E, Root MJ, Toohey DW, Brune WH. 2007. Introducing the concept of potential aerosol mass (PAM). Atmos Chem Phys 7(22):5727–5744, https://doi.org/10.5194/acp-7-5727-2007.

Karg EW, Ferron GA, Bauer S, Di Bucchianico S, Zimmermann R. 2020. Is the particle deposition in a cell exposure facility comparable to the lungs? A computer model approach. Aerosol Sci Technol 54(6):668–684, https://doi.org/10.1080/02786826.2020.1724868.

Karki P, Birukov KG. 2020. Oxidized phospholipids in healthy and diseased lung endothelium. Cells 9(4):981, PMID: 32326516, https://doi.org/10.3390/cells9040981.

Kenseth CM, Huang Y, Zhao R, Dalleska NF, Hethcox JC, Stoltz BM, et al. 2018. Synergistic O_3 + OH oxidation pathway to extremely low-volatility dimers revealed in β-pinene secondary organic aerosol. Proc Natl Acad Sci U S A 115(33):8301–8306, PMID: 30076229, https://doi.org/10.1073/pnas.1804671115.

Keyte IJ, Harrison RM, Lammel G. 2013. Chemical reactivity and long-range transport potential of polycyclic aromatic hydrocarbons—a review. Chem Soc Rev 42(24):9333–9391, PMID: 24077263, https://doi.org/10.1039/c3cs60147a.

Kim YW, Byzova TV. 2014. Oxidative stress in angiogenesis and vascular disease. Blood 123(5):625–631, PMID: 24300855, https://doi.org/10.1182/blood-2013-09-512749.

Klein SG, Serchi T, Hoffmann L, Blömeke B, Gutleb AC. 2013. An improved 3D tetraculture system mimicking the cellular organisation at the alveolar barrier to study the potential toxic effects of particles on the lung. Part Fibre Toxicol 10:31, PMID: 23890538, https://doi.org/10.1186/1743-8977-10-31.

Kleist E, Mentel TF, Andres S, Bohne A, Folkers A, Kiendler-Scharr A, et al. 2012. Irreversible impacts of heat on the emissions of monoterpenes, sesquiterpenes, phenolic BVOC and green leaf volatiles from several tree species. Biogeosciences 9(12):5111–5123, https://doi.org/10.5194/bg-9-5111-2012.

Kouassi KS, Billet S, Garçon G, Verdin A, Diouf A, Cazier F, et al. 2010. Oxidative damage induced in A549 cells by physically and chemically characterized air particulate matter ($PM_{2.5}$) collected in Abidjan, Côte D'Ivoire. J Appl Toxicol 30(4):310–320, PMID: 19943358, https://doi.org/10.1002/jat.1496.

Kroll JH, Donahue NM, Jimenez JL, Kessler SH, Canagaratna MR, Wilson KR, et al. 2011. Carbon oxidation state as a metric for describing the chemistry of atmospheric organic aerosol. Nat Chem 3(2):133–139, PMID: 21258386, https://doi.org/10.1038/nchem.948.

Künzi L, Krapf M, Daher N, Dommen J, Jeannet N, Schneider S, et al. 2015. Toxicity of aged gasoline exhaust particles to normal and diseased airway epithelia. Sci Rep 5:11801, PMID: 26119831, https://doi.org/10.1038/srep11801.

Lacroix G, Koch W, Ritter D, Gutleb AC, Larsen ST, Loret T, et al. 2018. Air–liquid interface *in vitro* models for respiratory toxicology research: consensus workshop and recommendations. Appl In Vitro Toxicol 4(2):91–106, PMID: 32953944, https://doi.org/10.1089/aivt.2017.0034.

Låg M, Øvrevik J, Refsnes M, Holme JA. 2020. Potential role of polycyclic aromatic hydrocarbons in air pollution-induced non-malignant respiratory diseases. Respir Res 21(1):299, PMID: 33187512, https://doi.org/10.1186/s12931-020-01563-1.

Lan Y, Ng CT, Ong RXS, Muniasamy U, Baeg GH, Ong CN, et al. 2020. Urban $PM_{2.5}$ reduces angiogenic ability of endothelial cells in an alveolar-capillary co-culture lung model. Ecotoxicol Environ Saf 202:110932, PMID: 32800216, https://doi.org/10.1016/j.ecoenv.2020.110932.

Landar A, Zmijewski JW, Dickinson DA, Le Goffe C, Johnson MS, Milne GL, et al. 2006. Interaction of electrophilic lipid oxidation products with mitochondria in endothelial cells and formation of reactive oxygen species. Am J Physiol Heart Circ Physiol 290(5):H1777–H1787, PMID: 16387790, https://doi.org/10.1152/ajpheart.01087.2005.

Lenz AG, Karg E, Brendel E, Hinze-Heyn H, Maier KL, Eickelberg O, et al. 2013. Inflammatory and oxidative stress responses of an alveolar epithelial cell line to airborne zinc oxide nanoparticles at the air-liquid interface: a comparison with conventional, submerged cell-culture conditions. Biomed Res Int 2013:652632, PMID: 23484138, https://doi.org/10.1155/2013/652632.

Li D, Li Y, Li G, Zhang Y, Li J, Chen H. 2019. Fluorescent reconstitution on deposition of $PM_{2.5}$ in lung and extrapulmonary organs. Proc Natl Acad Sci U S A 116(7):2488–2493, PMID: 30692265, https://doi.org/10.1073/pnas.1818134116.

Lim CY, Browne EC, Sugrue RA, Kroll JH. 2017. Rapid heterogeneous oxidation of organic coatings on submicron aerosols. Geophys Res Lett 44(6):2949–2957, https://doi.org/10.1002/2017GL072585.

Lin YH, Arashiro M, Clapp PW, Cui T, Sexton KG, Vizuete W, et al. 2017. Gene expression profiling in human lung cells exposed to isoprene-derived secondary organic aerosol. Environ Sci Technol 51(14):8166–8175, PMID: 28636383, https://doi.org/10.1021/acs.est.7b01967.

Liu F, Saavedra MG, Champion JA, Griendling KK, Ng NL. 2020. Prominent contribution of hydrogen peroxide to intracellular reactive oxygen species generated upon exposure to naphthalene secondary organic aerosols. Environ Sci Technol Lett 7(3):171–177, https://doi.org/10.1021/acs.estlett.9b00773.

Löndahl J, Möller W, Pagels JH, Kreyling WG, Swietlicki E, Schmid O. 2014. Measurement techniques for respiratory tract deposition of airborne nanoparticles: a critical review. J Aerosol Med Pulm Drug Deliv 27(4):229–254, PMID: 24151837, https://doi.org/10.1089/jamp.2013.1044.

Longhin E, Holme JA, Gutzkow KB, Arlt VM, Kucab JE, Camatini M, et al. 2013. Cell cycle alterations induced by urban PM2.5 in bronchial epithelial cells: characterization of the process and possible mechanisms involved. Part Fibre Toxicol 10:63, PMID: 24354623, https://doi.org/10.1186/1743-8977-10-63.

LoPachin RM, Gavin T. 2014. Molecular mechanisms of aldehyde toxicity: a chemical perspective. Chem Res Toxicol 27(7):1081–1091, PMID: 24911545, https://doi.org/10.1021/tx5001046.

Loret T, Peyret E, Dubreuil M, Aguerre-Chariol O, Bressot C, le Bihan O, et al. 2016. Air-liquid interface exposure to aerosols of poorly soluble nanomaterials induces different biological activation levels compared to exposure to suspensions. Part Fibre Toxicol 13(1):58, PMID: 27919268, https://doi.org/10.1186/s12989-016-0171-3.

Lucci F, Castro ND, Rostami AA, Oldham MJ, Hoeng J, Pithawalla YB, et al. 2018. Characterization and modeling of aerosol deposition in Vitrocell ® exposure systems—exposure well chamber deposition efficiency. J Aerosol Sci 123:141–160, https://doi.org/10.1016/j.jaerosci.2018.06.015.

Ma I, Allan AL. 2011. The role of human aldehyde dehydrogenase in normal and cancer stem cells. Stem Cell Rev Rep 7(2):292–306, PMID: 21103958, https://doi.org/10.1007/s12015-010-9208-4.

Mills IC, Atkinson RW, Kang S, Walton H, Anderson HR. 2015. Quantitative systematic review of the associations between short-term exposure to nitrogen dioxide and mortality and hospital admissions. BMJ Open 5(5):e006946, PMID: 25967992, https://doi.org/10.1136/bmjopen-2014-006946.

Møller P, Danielsen PH, Karottki DG, Jantzen K, Roursgaard M, Klingberg H, et al. 2014. Oxidative stress and inflammation generated DNA damage by exposure to air pollution particles. Mutat Res Rev Mutat Res 762:133–166, PMID: 25475422, https://doi.org/10.1016/j.mrrev.2014.09.001.

Moore RH, Ziemba LD, Dutcher D, Beyersdorf AJ, Chan K, Crumeyrolle S, et al. 2014. Mapping the operation of the miniature combustion aerosol standard (Mini-CAST) soot generator. Aerosol Sci Technol 48(5):467–479, https://doi.org/10.1080/02786826.2014.890694.

Mülhopt S, Dilger M, Diabaté S, Schlager C, Krebs T, Zimmermann R, et al. 2016. Toxicity testing of combustion aerosols at the air–liquid interface with a self-contained and easy-to-use exposure system. J Aerosol Sci 96:38–55, https://doi.org/10.1016/j.jaerosci.2016.02.005.

National Academies of Sciences, Engineering, and Medicine. 2016. *The Future of Atmospheric Chemistry Research: Remembering Yesterday, Understanding Today, Anticipating Tomorrow.* Washington, DC: National Academies Press.

Ng NL, Canagaratna MR, Jimenez JL, Chhabra PS, Seinfeld JH, Worsnop DR. 2011. Changes in organic aerosol composition with aging inferred from aerosol mass spectra. Atmos Chem Phys 11(13):6465–6474, https://doi.org/10.5194/acp-11-6465-2011.

Ng NL, Canagaratna MR, Zhang Q, Jimenez JL, Tian J, Ulbrich IM, et al. 2010. Organic aerosol components observed in Northern Hemispheric datasets from Aerosol Mass Spectrometry. Atmos Chem Phys 10(10):4625–4641, https://doi.org/10.5194/acp-10-4625-2010.

Oeder S, Kanashova T, Sippula O, Sapcariu SC, Streibel T, Arteaga-Salas JM, et al. 2015. Particulate matter from both heavy fuel oil and diesel fuel shipping emissions show strong biological effects on human lung cells at realistic and comparable *in vitro* exposure conditions. PLoS One 10(6):e0126536, PMID: 26039251, https://doi.org/10.1371/journal.pone.0126536.

Papazian D, Würtzen PA, Hansen SWK. 2016. Polarized airway epithelial models for immunological co-culture studies. Int Arch Allergy Immunol 170(1):1–21, PMID: 27240620, https://doi.org/10.1159/000445833.

Park M, Joo HS, Lee K, Jang M, Kim SD, Kim I, et al. 2018. Differential toxicities of fine particulate matters from various sources. Sci Rep 8(1):17007, PMID: 30451941, https://doi.org/10.1038/s41598-018-35398-0.

Paur HR, Cassee FR, Teeguarden J, Fissan H, Diabate S, Aufderheide M, et al. 2011. In-vitro cell exposure studies for the assessment of nanoparticle toxicity in the lung—a dialog between aerosol science and biology. J Aerosol Sci 42(10):668–692, https://doi.org/10.1016/j.jaerosci.2011.06.005.

Peng Z, Day DA, Ortega AM, Palm BB, Hu W, Stark H, et al. 2016. Non-OH chemistry in oxidation flow reactors for the study of atmospheric chemistry systematically examined by modeling. Atmos Chem Phys 16(7):4283–4305, https://doi.org/10.5194/acp-16-4283-2016.

Perera F, Hemminki K, Jedrychowski W, Whyatt R, Campbell U, Hsu Y, et al. 2002. *In utero* DNA damage from environmental pollution is associated with somatic gene mutation in newborns. Cancer Epidemiol Biomark Prev 11(10 pt 1):1134–1137, PMID: 12376523.

Peters A, Nawrot TS, Baccarelli AA. 2021. Hallmarks of environmental insults. Cell 184(6):1455–1468, PMID: 33657411, https://doi.org/10.1016/j.cell.2021.01.043.

Peterson LA. 2013. Reactive metabolites in the biotransformation of molecules containing a furan ring. Chem Res Toxicol 26(1):6–25, PMID: 23061605, https://doi.org/10.1021/tx3003824.

Pieber SM, Kumar NK, Klein F, Comte P, Bhattu D, Dommen J, et al. 2018. Gas-phase composition and secondary organic aerosol formation from standard and particle filter-retrofitted gasoline direct injection vehicles investigated in a batch and flow reactor. Atmos Chem Phys 18(13):9929–9954, https://doi.org/10.5194/acp-18-9929-2018.

Pope CA III, Bhatnagar A, McCracken JP, Abplanalp W, Conklin DJ, O'Toole T. 2016. Exposure to fine particulate air pollution is associated with endothelial injury and systemic inflammation. Circ Res 119(11):1204–1214, PMID: 27780829, https://doi.org/10.1161/CIRCRESAHA.116.309279.

Pope CA III, Coleman N, Pond ZA, Burnett RT. 2020. Fine particulate air pollution and human mortality: 25+ years of cohort studies. Environ Res 183:108924, PMID: 31831155, https://doi.org/10.1016/j.envres.2019.108924.

Prinn RG, Huang J, Weiss RF, Cunnold DM, Fraser PJ, Simmonds PG, et al. 2001. Evidence for substantial variations of atmospheric hydroxyl radicals in the past two decades. Science 292(5523):1882–1888, PMID: 11337586, https://doi.org/10.1126/science.1058673.

Qian Z, Chen Y, Liu Z, Han Y, Zhang Y, Feng Y, et al. 2021. Intermediate volatile organic compound emissions from residential solid fuel combustion based on field measurements in rural China. Environ Sci Technol 55(9):5689–5700, PMID: 33797233, https://doi.org/10.1021/acs.est.0c07908.

Raes F, Van Dingenen R, Vignati E, Wilson J, Putaud JP, Seinfeld JH, et al. 2000. Formation and cycling of aerosols in the global troposphere. Atmos Environ 34(25):4215–4240, https://doi.org/10.1016/S1352-2310(00)00239-9.

Rebollido-Rios R, Venton G, Sánchez-Redondo S, Iglesias I Felip C, Fournet G, González E, et al. 2020. Dual disruption of aldehyde dehydrogenases 1 and 3 promotes functional changes in the glutathione redox system and enhances chemosensitivity in nonsmall cell lung cancer. Oncogene 39(13):2756–2771, PMID: 32015486, https://doi.org/10.1038/s41388-020-1184-9.

Riediker M, Zink D, Kreyling W, Oberdörster G, Elder A, Graham U, et al. 2019. Particle toxicology and health—where are we? Part Fibre Toxicol 16(1):19, PMID: 31014371, https://doi.org/10.1186/s12989-019-0302-8.

Rodriguez-Torres M, Allan AL. 2016. Aldehyde dehydrogenase as a marker and functional mediator of metastasis in solid tumors. Clin Exp Metastasis 33(1):97–113, PMID: 26445849, https://doi.org/10.1007/s10585-015-9755-9.

Rothen-Rutishauser B, Blank F, Mühlfeld C, Gehr P. 2008. *In vitro* models of the human epithelial airway barrier to study the toxic potential of particulate matter. Expert Opin Drug Metab Toxicol 4(8):1075–1089, PMID: 18680442, https://doi.org/10.1517/17425255.4.8.1075.

Sarrafzadeh M, Wildt J, Pullinen I, Springer M, Kleist E, Tillmann R, et al. 2016. Impact of NO*x* and OH on secondary organic aerosol formation from β-pinene photooxidation. Atmos Chem Phys 16(17):11237–11248, https://doi.org/10.5194/acp-16-11237-2016.

Sato K, Jia T, Tanabe K, Morino Y, Kajii Y, Imamura T. 2016. Terpenylic acid and nine-carbon multifunctional compounds formed during the aging of β-pinene ozonolysis secondary organic aerosol. Atmos Environ 130:127–135, https://doi.org/10.1016/j.atmosenv.2015.08.047.

Schwöbel JAH, Koleva YK, Enoch SJ, Bajot F, Hewitt M, Madden JC, et al. 2011. Measurement and estimation of electrophilic reactivity for predictive toxicology. Chem Rev 111(4):2562–2596, PMID: 21401043, https://doi.org/10.1021/cr100098n.

Shakya KM, Griffin RJ. 2010. Secondary organic aerosol from photooxidation of polycyclic aromatic hydrocarbons. Environ Sci Technol 44(21):8134–8139, PMID: 20919733, https://doi.org/10.1021/es1019417.

Sýkorová B, Kucbel M, Raclavský K. 2016. Composition of airborne particulate matter in the industrial area versus mountain area. Perspect Sci (Neth) 7:369–372, https://doi.org/10.1016/j.pisc.2015.12.006.

Tăbăran AF, O'Sullivan MG, Seabloom DE, Vevang KR, Smith WE, Wiedmann TS, et al. 2019. Inhaled furan selectively damages club cells in lungs of A/J mice. Toxicol Pathol 47(7):842–850, PMID: 31426723, https://doi.org/10.1177/0192623319869306.

Tuet WY, Chen YL, Xu L, Fok S, Gao D, Weber RJ, et al. 2017. Chemical oxidative potential of secondary organic aerosol (SOA) generated from the photooxidation of biogenic and anthropogenic volatile organic compounds. Atmos Chem Phys 17(2):839–853, https://doi.org/10.5194/acp-17-839-2017.

U.S. EPA (Environmental Protection Agency). 2021a. EPA CompTox Chemicals Dashboard: Beta-pinene. https://comptox.epa.gov/dashboard/dsstoxdb/results?search=beta-pinene#toxicity-values [accessed 3 December 2021].

U.S. EPA. 2021b. EPA CompTox Chemicals Dashboard: Naphthalene. https://comptox.epa.gov/dashboard/dsstoxdb/results?search=DTXSID8020913#toxicity-values [accessed 3 December 2021].

Wang G, Zhang X, Liu X, Zheng J, Chen R, Kan H. 2019. Ambient fine particulate matter induce toxicity in lung epithelial-endothelial co-culture models. Toxicol Lett 301:133–145, PMID: 30481584, https://doi.org/10.1016/j.toxlet.2018.11.010.

Wang L, Atkinson R, Arey J. 2007. Dicarbonyl products of the OH radical-initiated reactions of naphthalene and the C_1- and C_2-alkylnaphthalenes. Environ Sci Technol 41(8):2803–2810, PMID: 17533842, https://doi.org/10.1021/es0628102.

Wang M, Li S, Zhu R, Zhang R, Zu L, Wang Y, et al. 2020. On-road tailpipe emission characteristics and ozone formation potentials of VOCs from gasoline, diesel and liquefied petroleum gas fueled vehicles. Atmos Environ 223:117294, https://doi.org/10.1016/j.atmosenv.2020.117294.

Watne ÅK, Westerlund J, Hallquist ÅM, Brune WH, Hallquist M. 2017. Ozone and OH-induced oxidation of monoterpenes: changes in the thermal properties of secondary organic aerosol (SOA). J Aerosol Sci 114:31–41, https://doi.org/10.1016/j.jaerosci.2017.08.011.

Weitekamp CA, Stevens T, Stewart MJ, Bhave P, Gilmour MI. 2020. Health effects from freshly emitted versus oxidatively or photochemically aged air pollutants. Sci Total Environ 704:135772, PMID: 31838301, https://doi.org/10.1016/j.scitotenv.2019.135772.

Welch BL. 1947. The generalisation of 'Student's' problems when several different population variances are involved. Biometrika 34(1–2):28–35, PMID: 20287819, https://doi.org/10.2307/2332510.

Williams BJ, Goldstein AH, Kreisberg NM, Hering SV. 2010. *In situ* measurements of gas/particle-phase transitions for atmospheric semivolatile organic compounds. Proc Natl Acad Sci USA 107(15):6676–6681, PMID: 20142511, https://doi.org/10.1073/pnas.0911858107.

Williams J, de Reus M, Krejci R, Fischer H, Ström J. 2002. Application of the variability-size relationship to atmospheric aerosol studies: estimating aerosol lifetimes and ages. Atmos Chem Phys 2(2):133–145, https://doi.org/10.5194/acp-2-133-2002.

Wragg FPH, Fuller SJ, Freshwater R, Green DC, Kelly FJ, Kalberer M. 2016. An automated online instrument to quantify aerosol-bound reactive oxygen species (ROS) for ambient measurement and health-relevant aerosol studies. Atmos Meas Tech 9(10):4891–4900, https://doi.org/10.5194/amt-9-4891-2016.

Wu J, Wang Y, Liu G, Jia Y, Yang J, Shi J, et al. 2017a. Characterization of air-liquid interface culture of A549 alveolar epithelial cells. Braz J Med Biol Res 51(2): e6950, PMID: 29267508, https://doi.org/10.1590/1414-431X20176950.

Wu X, Lintelmann J, Klingbeil S, Li J, Wang H, Kuhn E, et al. 2017b. Determination of air pollution-related biomarkers of exposure in urine of travellers between Germany and China using liquid chromatographic and liquid chromatographic-mass spectrometric methods: a pilot study. Biomarkers 22(6):525–536, PMID: 28330376, https://doi.org/10.1080/1354750X.2017.1306753.

Wyzga RE, Rohr AC. 2015. Long-term particulate matter exposure: attributing health effects to individual PM components. J Air Waste Manag Assoc 65(5):523–543, PMID: 25947312, https://doi.org/10.1080/10962247.2015.1020396.

Xavier C, Rusanen A, Zhou PT, Dean C, Pichelstorfer L, Roldin P, et al. 2019. Aerosol mass yields of selected biogenic volatile organic compounds—a theoretical study with nearly explicit gas-phase chemistry. Atmos Chem Phys 19(22):13741–13758, https://doi.org/10.5194/acp-19-13741-2019.

Xu J, Hu W, Liang D, Gao P. 2022. Photochemical impacts on the toxicity of $PM_{2.5}$. Crit Rev Environ Sci Technol 52(1):130–156, https://doi.org/10.1080/10643389.2020.1816126.

Yan Z, Jin Y, An Z, Liu Y, Samet JM, Wu W. 2016. Inflammatory cell signaling following exposures to particulate matter and ozone. Biochim Biophys Acta 1860(12):2826–2834, PMID: 27015762, https://doi.org/10.1016/j.bbagen.2016.03.030.